ROAD TO EQUILIBRIUM: STABLE ISOTOPE DISTRIBUTION IN GASEOUS ALKANES AND THERMAL HISTORY OF GEOLOGICAL HYDROCARBONS

Thesis by

Hao Xie

In Partial Fulfillment of the Requirements for

the degree of

Doctor of Philosophy

CALIFORNIA INSTITUTE OF TECHNOLOGY

Pasadena, California

2021

(Defended 03/10/2021)

Hao Xie
ORCID: 0000-0001-5656-2035

ACKNOWLEDGEMENTS

Thank you, John Eiler. I first heard about ‘clumped isotopes’ in my junior year of college and I feel lucky today to be one of the people to explore frontiers of this subject. Thank you very much for making this possible. Thank you for always being inspiring, motivating, and patient when we meet, whether it’s about a glitch on the mass spec or visualization ideas of a dataset. I am also extremely thankful to you for making me feel welcome in this country. Lastly, thanks for teaching me English idioms.

I really enjoyed the open and vibrant academic environment at Caltech. Thanks to the many faculty members of the GPS and CCE division who I interacted with, including members of my examination committee: Alex Sessions, Ken Farley, and Tom Miller. I’ll especially thank Alex Sessions for having me on your group meetings and group outings. I also want to thank a few other faculty members for either classes or advises, including George Rossman, Donald Burnett, Jess Adkins, Victoria Orphan, Jared Leadbetter, Paul Wennberg and John Seinfeld.

Thanks to Camilo Ponton for taking care of me like a big brother when I came here knowing very little about everything. Besides organic geochemical sciences, I also learned a lot of life philosophy from you. Thanks to members of our little ‘hydrocarbon geochemistry group’ within the Eiler Lab: Nivedita Thiagarajan, Guannan Dong, and Xavier Mangenot. Thanks to Nami Kitchen and Fenfang Wu, who can always make things happen in the lab. Thanks to many other fellows that show up in the Eiler Lab: Max,

Brooke, Emma, Uri, Sang, Elle, Renee, and Elliott. Thanks to the 2015-2016 pit members: Lee, Alex, Usha, Grey, Joe, and Maddie. You guys enriched my graduate school life a lot.

Thanks to colleagues and friends from the Exxon Mobile Corporation: Michael Formolo, Michael Lawson, David Wang, and Aaron Sattler. Your expertise and passion facilitated my work.

My thanks to Yuanlong Huang for being an intense climbing buddy and always being there to listen to my nonsense. Also, thank you for inviting me to your wedding in your hometown. Thanks to Antoine for being my surfing buddy and introducing me to the microbiological lab. Thanks to Weimeng (Stephanie) for being my surfing buddy, movie/concert buddy, and gossiping buddy. Thanks to members of our little 'GPS Chinese group': Yanzhe, Xunyi (Alison), Siteng, and Mingyan. Thanks to Baoyi, my ex-roommate and co-owner of our cute cat, Nana. Thanks to Nana for accompanying me and inspiring me with your curiosity. Thanks to Lefei Huang for being my roommate for the last two years and sharing delicious food with me all the time. My years in California would have be a lot duller without you all.

Lastly, thank you to my parents, Guangzhong Xie and Xiaohua Liu. I love you and am so proud of you.

ABSTRACT

Naturally occurring hydrocarbon fluids have economic, geological, and environmental significance. Most of the natural hydrocarbon on Earth is formed by thermal alteration of organic matter in the sedimentary basin. My dissertation study is motivated by this question: can we track generation, transformation, storage, and destruction of these subsurface hydrocarbon fluids with isotopic proxies? The conventional geochemical toolkit includes relative compositional abundances, such as wetness and C1/(C2+C3) ratio, and stable isotope ratios of $^{13}C/^{12}C$ and $^{2}H/^{1}H$, on both the bulk (material-average) and compound-specific (molecular-average) levels. However, these signatures often rely on empirical categorizations and calibrations, so they can be prone to ambiguities, errors, and inconsistencies. This thesis presents a series of work that develops and refines stable isotope proxies of gaseous hydrocarbon (C1-C5) molecules. My approaches overcome the problems in mainly two ways. (1) I add new analytical techniques to acquire isotopologue ratios of compounds. I establish two new analytical proxies, multiply substituted isotopologues (clumped isotopes) of methane, and position-specific isotope ratios of propane, using recently advanced high-resolution isotope ratio mass spectrometry. (2) I use rigorous thermodynamic and kinetic constraints of isotope distribution in hydrocarbon molecules to interpret isotopic data in natural samples. These constraints are determined by theories and experiments. For thermodynamic control, I conducted catalytic exchange experiments to calibrate equilibrium isotope effect for propane position-specific hydrogen isotopes (Chapter 2) and compound-specific hydrogen isotope fractionation between

alkanes (Chapter 4) and tested quantum chemical calculations. For expression of kinetic isotope effects, I implemented a statistical approach, the kinetic Monte Carlo method, to calculate the intramolecular and intermolecular stable isotope composition of alkanes generated by radical cracking mechanism in catagenesis (Chapter 6). I measured position-specific hydrogen isotopes of propane (Chapter 3) and methane clumped isotopes (Chapter 5) in natural gas samples from global reservoirs, and compiled compound-specific isotope data in the literatures (Chapter 5 and 6). Results show similarities in isotope ordering of these molecules, which is that gas formed at lower temperature/depth expresses kinetic isotope effects, but gas formed or buried at higher temperature for longer times is in equilibrium. The switch from kinetic control to thermodynamic control is likely a result of thermally activated hydrogen exchange. This trend provides the foundation for tracking generation and thermal evolution of subsurface hydrocarbons with stable isotope proxies.

PUBLISHED CONTENT AND CONTRIBUTIONS

Xie H., Ponton C., Formolo M. J., Lawson M., Peterson B. K., Lloyd M. K., Sessions A. L. and Eiler J. M. (2018) Position-specific hydrogen isotope equilibrium in propane. Geochim. Cosmochim. Acta 238, 193–207. doi: 10.1016/j.gca.2018.06.025.

H.X. participated in the conception of the project, conducted isotope exchange experiments, analyzed and interpreted the data, and participated in the writing of the manuscript.

Xie H., Ponton C., Formolo M. J., Lawson M., Ellis G. S., Lewan M. D., Ferreira A. A., Morais E. T., Spigolon A. L. D., Sessions A. L. and Eiler J. M. (2020) Position-specific distribution of hydrogen isotopes in natural propane: Effects of thermal cracking, equilibration and biodegradation. Geochim. Cosmochim. Acta 290, 235–256. doi: 10.1016/j.gca.2020.09.009.

H.X. participated in conducting isotope exchange experiments, analyzed data of isotope exchange experiments. H.X. interpreted the data of natural samples and hydrous pyrolysis experiments. H.X. wrote the numerical and analytical models and participated in the writing of the manuscript.

Table of Contents

NOMENCLATURE

C1. Methane.

C2. Ethane.

C3. Propane.

C4. Butane (including all isomers).

iC4. Isobutane (2-methylpropane).

nC4. n-Butane.

C5. Pentane (including all isomers).

iC5. Isopentane (2-methylbutane).

nC5. n-Pentane.

Chapter 1

Introduction

Low molecular weight (C1–C5) alkanes play important roles in Earth's crust, hydrosphere, and atmosphere. They are the major constituents of natural gas, a key energy and chemical-engineering resource projected to have growing demand in the next two decades (EIA 2018). Also, natural gas is promoted as a cleaner 'transition fuel' to replace more polluting and carbon-intensive coal and oil, before renewable energy overcomes technological and economical hurdles. C1–C5 alkanes also participate in the global biogeochemical cycle, as they can be produced and consumed by microbes in the shallow sediments or aqueous environments. In the atmosphere, methane is a potent greenhouse gas, causing immense radioactive forcing that is second only to CO_2 (IPCC 2014). Finally, light alkanes can be formed inorganically in submarine hydrothermal vents or fractured continental ultramafic rocks, which can potentially provide organic substrates for pre-biotic chemistry.

The scope of this thesis inclines towards hydrocarbon in the crustal subsurface, where overwhelming majority of alkanes are hosted on Earth. The primary goals of our study are to use chemical and isotopic properties to (1) understand the mechanisms of natural gas formation and (2) track the thermal evolution and fate of natural gas. These information are critical for predicting where it forms in economic volumes and recognizing its release to the environment. Also, they offer a window for probing basin geology, burial, and uplift with

hydrocarbons. Traditionally, geochemists have been extracting information from volatile alkanes with mainly two types of analytical attributes: compositional proportions (molar fraction of each compound) and stable isotope ratios (molecular average $^{13}C/^{12}C$ and D/H). These properties have been linked to processes that produce and alter these light alkanes. For example, $^{13}C/^{12}C$ and D/H of methane are commonly used to distinguish thermogenic vs. microbial sources (Schoell, 1980; Whiticar et al., 1986). $^{13}C/^{12}C$ of methane, ethane, and propane correlate with thermal maturity (the progress of thermally activated catagenesis reactions) of the source rock of natural gas (Berner and Faber, 1996). While these methods have been successful at providing useful information, there are also limitations. Most of these methods are based on empirical observations, so growth of the known dataset often changes the interpretation of geochemical tools. In the application of gas origin classification, a recent study (Milkov and Etiope, 2018) has shown that the actual ranges of the isotopic values and compositional ratios of each genetic gas types are much wider than previously thought, creating a lot of overlapping zone that can lead to ambiguous interpretations. For the $^{13}C/^{12}C$–maturity relationships, a handful of calibrations from different localities have been studied, but disagree with each other (Galimov, 2006).

I take two approaches to improve stable isotope geochemical toolkits. First, I add new analytical proxies. I develop and investigate utilities of new isotopic measurements: position-specific hydrogen isotope ratios of propane and clumped isotopes of methane. Compared to conventional molecular-average isotope ratios, these new proxies specify the

location and number of isotope substitution in molecules, and are more informative as constraints on chemical mechanisms and conditions of hydrocarbon forming reactions. Measurements of these isotopologue ratios require high mass resolving power, which became possible recently because of advances in modern mass spectrometry. I established methodology for measuring this isotopic information with gas-source high-resolution sector mass spectrometers. Second, I employ quantitative physical-chemical theories to interpret isotopic information. Specifically, I determine how stable isotopes fractionate in alkanes at both thermodynamic control (equilibrium isotope effect) and kinetic control, using quantum chemical and experimental methods. Knowing these effects allow us to examine the reversibility of hydrocarbon-formation chemistry in nature, which has been a subject of debates in the past. The conventional wisdom suggests that petroleum formation is a kinetic-controlled unidirectional process of breaking larger molecules to small molecules, mediated by the irreversible thermal cracking mechanisms (e.g., Tissot and Welte, 1978; Ungerer 1990). Field and experimental evidence lead several studies to challenge this view and argue that catagenic chemistry is partially or fully in equilibrium (James, 1983; Helgeson et al., 1993; Mango et al., 2009). Resolving this problem is essential for associating properties and quantities of hydrocarbons with physical and chemical attributes of their formation environment. Furthermore, isotopic geothermometer can be established because isotope effects are temperature dependent. The addition of these constraints also allow me to reexamine literature data of conventional compound-specific isotopic methods.

This thesis presents a series of subject-based projects that combine the two principal ideas: new analytical techniques plus physical-chemical theories. Although my research is on the context of hydrocarbon in sedimentary basins, the analytical methodology and theoretical framework for interpreting isotopic data are also applicable to other types of natural and artificial occurrences.

In Chapter 2, I present determination of equilibrium D/H fractionation factors between central (-CH_2-) and terminal (-CH_3) positions of propane, the smallest and most abundant natural gas component that has non-equivalent chemical sites. We develop a method to measure position-specific D/H differences of propane with molecular high-resolution gas source mass spectrometry (the Double Focusing Sector mass spectrometer). We perform laboratory exchange experiments using metal catalysts to exchange hydrogen isotope distribution in propane. An equilibrated (bracketed and time-invariant) intramolecular hydrogen isotope distribution is attained for propane with Pd/C catalyst at three temperatures, 30°C, 100°C and 200°C. We use this calibration to test the validity of prior published theoretical predictions, which suggests that the most sophisticated of these discrepant models (Webb and Miller, 2014) is most accurate; this conclusion implies that there is a combined experimental and theoretical foundation for an ‘absolute reference frame’ for position-specific H isotope analysis of propane.

In Chapter 3, I present a study that explore the controls on position-specific hydrogen isotope distribution in natural propane. We analyze propane samples from 10 different petroleum systems and from a shale hydrous pyrolysis experiment, with the same techniques used in Chapter 2. Our results show that hydrogen isotope structure of catagenic propane is largely controlled by irreversible processes, expressing kinetic isotope effects (KIEs). Propane sampled from unconventional shale fluids and hot conventional reservoirs have hydrogen isotope distribution at or close to equilibrium, presumably reflecting hydrogen isotope exchange during high temperature storage (100-150˚C). In relatively cold (<100 ˚C) conventional gas accumulations, propane can discharge from its source to a colder reservoir, rapidly enough to preserve disequilibrium signatures even if the source rock thermal maturity is high. These findings imply that long times at elevated temperatures are required to equilibrate the hydrogen isotopic structure of propane in natural gas host rocks and reservoirs. We further show that hydrogen in propane is exchangeable over laboratory time scales when exposed to clay minerals such as kaolinite. This implies rather rapid transfer of propane from sources to cold reservoirs in some of the conventional petroleum systems. Lastly, we found that biodegradation of propane in the Hadrian and Diana Hoover oil fields (Gulf of Mexico) results in strong increases in central—terminal hydrogen isotope fractionation, which reflects preferential attack on the central position in enzymatic degradation of propane.

In Chapter 4, I follow the experimental methodology in Chapter 2 to facilitate hydrogen exchange between light alkanes and calibrate intermolecular equilibrium isotope effects (i.e., equilibrium isotope fractionation between compounds). I prepared two alkane mixtures, one with C1/C2/C3 and another one with C2/C3/iC4/nC4/iC5/nC5, both of which are out of hydrogen isotope equilibrium. I tested the catalytic performance of a few metal catalysts, and eventually succeeded at attaining substantial hydrogen isotope exchange on both alkane mixtures. I compared the experimental equilibrium values with theoretical values and show that the harmonic theory of Urey-Bigeleisen-Mayor method is satisfactory for analytical precision of our analytical techniques, gas-chromatography/pyrolysis/isotope-ratio mass spectrometry (GC/Py/IRMS). The calibration of equilibrium isotope effects allows us to re-examine natural gas data in the literature, which will be presented in the next Chapter.

In Chapter 5, I explore isotope distribution in natural samples again, but shift to the subject of methane clumped isotopes (multiply-substituted isotopologues) and compound-specific hydrogen isotopes. We develop a method to measure relative abundances of $^{13}CH_3D$ and $^{12}CH_2D_2$ (along with other more major isotopologues) with molecular high-resolution gas source mass spectrometry (Ultra by Thermo Fischer Scientific). We analyze the stable isotope compositions of a suite of thermogenic gas samples that are globally distributed and cover a wide range in composition and thermal maturation, from dominantly unconventional shale gas formations and a few conventional gas plays. We show that

methane generated at early thermal maturity has a stable isotope composition governed by chemical kinetics, characterized by a pronounced deficit in $\Delta^{12}CH_2D_2$ (relative abundance of $^{12}CH_2D_2$ that is standardized to stochastic concentration, see Chapter 5 for full nomenclature). Methane from higher thermal maturity fluids increases in $\Delta^{12}CH_2D_2$, reaching equilibrium at vitrinite reflectance maturity (R_o) of approximately 1.5% (equivalent to 170–210 °C peak burial temperature) and higher, which is interpreted to be the result of isotope exchange erasing the disequilibrium signature of catagenetic chemistry. We further examined hydrogen isotope fractionations among methane, ethane and propane for a compiled global dataset and found that the intermolecular fractionation exhibits a trend similar to that seen for the $\Delta^{12}CH_2D_2$ value of methane, departing from equilibrium at low thermal maturities and moving towards equilibrium as maturity increases. These findings indicate that the inter- and intra-molecular hydrogen isotope structures of components of thermogenic natural gas transition from chemical-kinetic control at low thermal maturities toward thermodynamic control at higher thermal maturities, which could be used to identify the exact thermal maturation stages for natural gases and their associated fluids, especially for oil-associated gas at early maturation.

In Chapter 6, I present a theoretical and computational study to calculate molecular and isotopic information of the hydrocarbons formed by kinetic processes in catagenesis. We model the radical reaction network of thermal cracking with a kinetic Monte-Carlo method (kMC), a stochastic formulation of reactive systems. My kMC model integrates realistic

precursors, elementary reactions and patterns of inheritance, so it is able to output isotopologue abundances of hydrocarbons that are unavailable in conventional catagenesis modeling techniques. A simulation of the kMC model starts with initializing the parent organic molecules with isotopic substitutions, and then subject them to ‘cracking’ reactions (catagenetic thermal decomposition) in a many-step process. For each time step of the model, we determine the rate constants of included reactions for all non-isotope-substituted atomic sites in the parent molecules using an external kinetic database (reaction mechanism generator), and then compute the rates of those reactions for isotope-substituted sites using kinetic isotope effects (KIE). Every simulation composes a series of stochastic time steps, capturing a possible route of thermal degradation. The numbers of each unique isotopologue of product molecules of interest are tallied at the end. Our model results generally resemble patterns of compound-specific and position-specific isotope measurements of C1-C5 alkanes in natural gases. Via comparison of different chemistry schemes, we suggest that thermal cracking in natural hydrocarbon formation is mediated by full radical mechanisms.

References

Berner U. and Faber E. (1996) Empirical carbon isotope/maturity relationships for gases from algal kerogens and terrigenous organic matter, based on dry, open-system pyrolysis. In *Organic Geochemistry* pp. 947–955.

Galimov E. M. (2006) Isotope organic geochemistry. *Org. Geochem.* **37**, 1200–1262.

Helgeson H. C., Knox A. M., Owens C. E. and Shock E. L. (1993) Petroleum, oil field waters, and authigenic mineral assemblages Are they in metastable equilibrium in hydrocarbon reservoirs. Geochim. Cosmochim. Acta 57, 3295–3339.

James A. T. (1983) Correlation of Natural Gas By Use of Carbon Isotopic Distribution Between Hydrocarbon Components. Am. Assoc. Pet. Geol. Bull. 67, 1176–1191.

Mango F. D., Jarvie D. and Herriman E. (2009) Natural gas at thermodynamic equilibrium implications for the origin of natural gas. Geochem. Trans. 10, 1–12.

Milkov A. V. and Etiope G. (2018) Revised genetic diagrams for natural gases based on a global dataset of >20,000 samples. *Org. Geochem.* **125**, 109–120.

Schoell M. (1980) The hydrogen and carbon isotopic composition of methane from natural gases of various origins. *Geochim. Cosmochim. Acta* **44**, 649–661.

The Intergovernmental Panel on Climate Change (IPCC), 5th Assessment Report (2014). https://www.ipcc.ch/report/ar5/syr/

Tissot B. P. and Welte D. H. (1978) Petroleum Formation and Occurrence., Springer Berlin Heidelberg, Berlin, Heidelberg.

Sessions A. L., Sylva S. P., Summons R. E. and Hayes J. M. (2004) Isotopic exchange of carbon-bound hydrogen over geologic timescales. *Geochim. Cosmochim. Acta* **68**, 1545–1559.

Ungerer P. (1990) State of the art of research in kinetic modelling of oil formation and expulsion. Org. Geochem. 16, 1–25.

Whiticar M. J., Faber E. and Schoell M. (1986) Biogenic methane formation in marine and freshwater environments: CO2 reduction vs. acetate fermentation-Isotope evidence. *Geochim. Cosmochim. Acta*.

U.S. Energy Information Administration (EIA), Annual Energy Outlook (2018). https://www.eia.gov/pressroom/presentations/Capuano_02052018.pdf

Chapter 2

Position-Specific Hydrogen Isotope Equilibrium in Propane

Xie H., Ponton C., Formolo M. J., Lawson M., Peterson B. K., Lloyd M. K., Sessions A. L. and Eiler J. M. (2018) Position-specific hydrogen isotope equilibrium in propane. Geochim. Cosmochim. Acta 238, 193–207. doi: 10.1016/j.gca.2018.06.025.

Abstract

Intramolecular isotope distributions can constrain source attribution, mechanisms of formation and destruction, and temperature-time histories of molecules. In this study, we explore the D/H fractionation between central (-CH_2-) and terminal (-CH_3) positions of propane (C_3H_8) — a percent level component of natural gases. The temperature dependence of position-specific D/H fractionation of propane could potentially work as a geo-thermometer for natural gas systems, and a forensic identifier of specific thermogenic sources of atmospheric or aquatic emissions. Moreover, kinetically controlled departures from temperature dependent equilibrium might constrain mechanisms of thermogenic production, or provide indicators of biological or photochemical destruction. We developed a method to measure position-specific D/H differences of propane with high-resolution gas source mass spectrometry. We performed laboratory exchange experiments to study the

exchange rates for both terminal and central positions, and used catalysts to drive the hydrogen isotope distribution of propane to thermodynamic equilibrium. Experimental results demonstrate that D/H exchange between propane and water happens easily in the presence of either Pd catalyst or Ni catalyst. Exchange rates are similar between the two positions catalyzed by Pd. However, the central position exchanges 2.2 times faster than the terminal position in the presence of Ni catalyst. At 200°C in the presence of Pd catalyst, the e-folding time of propane-water exchange is 20 days and of homogeneous exchange (i.e., equilibrium between central and terminal positions) is 28 minutes. An equilibrated (bracketed and time-invariant) intramolecular hydrogen isotope distribution was attained for propane at three temperatures, 30°C, 100°C and 200°C; these data serve as an initial experimental calibration of a new position-specific thermometer with a temperature sensitivity of 0.25‰ per ˚C at 100 ˚C. We use this calibration to test the validity of prior published theoretical predictions. Comparison of data with models suggest the most sophisticated of these discrepant models (Webb and Miller, 2014) is most accurate; this conclusion implies that there is a combined experimental and theoretical foundation for an 'absolute reference frame' for position-specific H isotope analysis of propane, following principles previously used for clumped isotope analysis of CO2, CH4 and O2 (Eiler and Schauble, 2004; Yeung et al., 2014; Stolper et al., 2014).

1. Introduction

Non-statistical intramolecular distributions of stable isotopes have been recognized for decades. A few years after the discovery of deuterium, Koizum and Titani (1938) first studied deuterium transfer from the hydroxyl group to the benzene ring of phenol. The first study to examine natural position-specific isotopic variations in materials relevant to the Earth and life sciences measured the intramolecular carbon isotope variations of biosynthetic amino acids (Abelson and Hoering, 1961). This subject grew dramatically with the development of NMR techniques for measuring position-specific variations in D and ^{13}C abundances in organic molecules (Martin and Martin, 1981; Caytan et al., 2007). Such work has been applied to food-science, plant physiology, paleoenvironment reconstruction, and environmental contamination (Remaud et al., 1997; Gilbert et al., 2012; Ehler et al., 2015; Julien et al., 2015 and 2016). Intramolecular isotopic fractionations can reflect temperatures of molecular synthesis, mechanisms of formation, and/or source substrates (Martin et al., 2008; Eiler, 2013b).

Propane (C_3H_8) is a major constituent of thermogenic natural gas. It is also the smallest alkane that has chemically non-equivalent positions, making it an attractive test case for the broader subject of intramolecular isotopic ordering. Intramolecular isotope fractionations in propane (most simply, differences in ^{13}C or D content between the central methylene and terminal methyl groups) have potential to constrain mechanisms and conditions of its formation, the chemical and biological processes of its destruction, and the conditions of its migration and storage in the sub surface, as well as to add

forensic specificity to attempts to identify sources of fugitive atmospheric and aquatic emissions. (Gilbert et al., 2016; Gao et al., 2016; Piasecki et al., 2018). An additional motivation for this study is that recent theoretical models suggest the temperature dependence of site specific hydrogen isotope fractionation in propane has promising applications to geothermometry (Webb and Miller, 2014; Cheng and Ceriotti, 2016; Piasecki et al., 2016b). Here we present an experimental study of the position-specific fractionation of D/H ratios between terminal and central hydrogen positions in propane, including methods of mass spectrometric analysis, kinetics of exchange for a range of substrates and conditions, and initial calibration of the temperature dependence of the isotope exchange reaction:

$$^{12}CH_2D-{}^{12}CH_2-{}^{12}CH_3 \rightleftharpoons {}^{12}CH_3-{}^{12}CHD-{}^{12}CH_3 \quad (1)$$

2. Background

Natural variations in the D/H ratios of hydrocarbons provide proxies for environmental conditions and water sources of biosynthesis in biomolecules (Sessions 2016), source substrates and thermal maturities of catagenetically-formed oil and gas compounds (Li et al., 2001; Dawson et al., 2007), and forensic identification of environmental pollutants (Reddy et al., 2012). These stable isotope proxies are unusual both for the high amplitude of observed variations (reflecting the large relative difference in mass between H and D),

and for relatively high susceptibility to isotopic exchange of compounds with environmental water or other compounds after formation (Schimmelman et al., 2006).

Most prior research on the hydrogen isotope compositions of natural hydrocarbons has analyzed the molecule-averaged D/H ratios of either individual compounds or bulk organic matter. Such measurements observe the weighted average of D contents of the analyzed compounds, across all non-equivalent molecular positions and for all isotopologues. Thus, they do not contain any information that might be recorded in position-specific and/or 'clumped' (multiply substituted) variations. A substantial amount of prior research establishes that such intramolecular isotopic variations can constrain the substrates, mechanisms, and conditions of molecular formation, storage and destruction (e.g., Eiler, 2013b; Eiler et al., 2014). However, to-date there has been no effort to apply these principles to hydrogen isotope distributions in natural hydrocarbon gases other than methane. Here we develop a foundation to enable such studies of propane, with potential for extrapolation to other hydrocarbons.

Assuming one could observe the position-specific H isotope variations in natural propane, interpretation of such data would require at least two types of constraints: (1) the temperature dependent central-terminal fractionation at thermodynamic equilibrium, and (2) the rates of hydrogen isotope exchange between each position of propane and other materials, at naturally relevant conditions. Such data will inform the interpretation

of sample measurements in the context of each sample's temperature-time history and its approach to equilibrium. Equilibrium fractionations can serve either as a calibration for thermometry in equilibrated propane, or as a reference frame for identifying and interpreting kinetic fractionations in non-equilibrated propane.

The intramolecular isotope exchange equilibrium of interest to this study (Reaction 1) can be approached by theoretical calculations or equilibration experiments. Three recent studies have presented theoretical models of this reaction (Figure 2-A1; Webb and Miller, 2014; Cheng and Ceriotti, 2016; Piasecki et al., 2016b), using similar statistical mechanical approaches. Webb and Miller (2014) used both a Urey-Bigeleisen (i.e., rigid rotator and harmonic oscillator) model and a Path Integral Monte Carlo (PIMC) method to estimate the relevant equilibrium constant. Both methods are based on the potential energy surface (PES) used in the Chemistry at Harvard Macromolecular Mechanics (CHARMM) package. Piasecki et al. (2016b) used a Urey-Bigeleisen model, with a density function theory (DFT) model of molecular structure and vibrations. Cheng and Ceriotti (2016) used a Path Integral Molecular Dynamics (PIMD) approach, with a base molecular structure and force field that were based on the Adaptive Intermolecular Reactive Empirical Bond Order (AIREBO) force field, and which generated fundamental vibrational frequencies that differed significantly from the results of the other studies for some modes. The results of these studies are in substantial disagreement. Three of the four models (Webb and Miller, 2014 (PIMD); Webb and Miller, 2014 (Urey-Bigeleisen);

Piasecki et al. (2016b) (Urey-Bigeleisen)) indicate that deuterium will be enriched in the central CH_2 groups over the terminal CH_3 groups by an amount that diminishes monotonically with increasing temperature. In contrast, Cheng and Ceriotti, 2016 (PIMC) predict that the terminal methyl groups will be D enriched relative to the center position, with a more complex temperature dependence, increasing and then decreasing in amplitude with increasing temperature, with an inflection point near 500 K. Thus, if we can experimentally calibrate the position-specific D/H fractionation of propane as a function of temperature, we will both establish a new geo-thermometer and independently test the relative accuracies of these several statistical mechanical models.

The kinetics of position-specific hydrogen isotope exchange present a complex problem. Many environmental factors such as temperature, pressure, co-existing gas and fluid species, and availability and properties of catalytic substrates are all likely to affect exchange rates. Studies of molecule-average D/H ratios in natural samples suggest that aliphatic compounds are resistant to hydrogen isotope exchange at near-Earth-surface conditions (Sessions et al., 2016); however, the estimated exchange half-life of 10^5~10^8 years at 100°C (Sessions et al., 2004) implies that either or both positions in propane could be ‘open’ to exchange for a wide range of geological times in diagenetic, catagenetic and/or metamorphic conditions. Reeves et al. (2012) reported that substantial hydrogen isotope exchange between propane and water happened on the timescale of 300 days under simulated hydrothermal conditions (323 °C and 35–36 MPa). We are not

aware of any constraints on the kinetics of D/H exchange in propane at the conditions of catagenetic natural gas formation, migration, or accumulation (generally speaking, 50-200°C and 0–250 MPa).

3. Nomenclature

We report hydrogen isotope compositions using δD notation, which is defined as:

$$\delta \mathrm{D} = \frac{\left(\frac{\mathrm{D}}{\mathrm{H}}\right)_{\mathrm{Sample}}}{\left(\frac{\mathrm{D}}{\mathrm{H}}\right)_{\mathrm{Reference}}} - 1, \tag{2}$$

where the D/H value is the molar ratio between deuterium (D or ^{2}H) and protium (H or ^{1}H). The δD value is generally reported in units of per mille (‰), by multiplying the quantity calculated in Eqn. 2 by 1000. The reference material is either VSMOW (D/H=0.00015576) or another material specified in the text. The position-specific fractionation factor is the difference of D/H ratios between central position and terminal positions:

$$\varepsilon_{\mathrm{central-terminal}} = \frac{\left(\frac{\mathrm{D}}{\mathrm{H}}\right)_{\mathrm{Central}}}{\left(\frac{\mathrm{D}}{\mathrm{H}}\right)_{\mathrm{Terminal}}} - 1. \tag{3}$$

This quantity is also generally expressed in units of per mille after multiplication by 1000. Equation 3 assumes that D/H ratios of the central and terminal positions have been measured against the same reference composition, e.g., VSMOW. No position-specific standards are available for propane, making this approach problematic. We therefore also report a parameter for the position-specific hydrogen isotope composition of propane that can be directly related to our measurements, with minimal intervening calculations or assumptions. We report sample D/H ratios vs. our reference standard, CITP-1, which therefore has a $\delta D_{CITP\text{-}1}$ of 0 for all measured or calculated properties. In practice, we analyze the relative abundance of the singly D-substituted $C_2H_5^+$ fragment ion and molecular ion ($C_3H_8^+$), obtaining the ratios, $\left(\frac{C_2H_4D}{C_2H_5}\right)$ and $\left(\frac{C_3H_7D}{C_3H_8}\right)$. At the outset of this study, we had no constraints on this standard's position-specific hydrogen isotope composition, and so we recorded the difference in D/H ratio between the central and terminal hydrogen sites simply as the measured difference in D/H ratio of the two measured ion species, relative to our laboratory reference gas:

$$\varepsilon D_{C2H5-C3H8} = 1000 * \left(\frac{\left(\frac{C_2H_4D}{C_2H_5}\right)_{Sample}}{\left(\frac{C_2H_4D}{C_2H_5}\right)_{CITP-1}} \Big/ \frac{\left(\frac{C_3H_7D}{C_3H_8}\right)_{Sample}}{\left(\frac{C_3H_7D}{C_3H_8}\right)_{CITP-1}} - 1 \right). \quad (4)$$

Note that the difference in δD between the C_2H_5 and C_3H_8 species is directly related to the difference in D/H ratio between the central and terminal sites, but exhibits only 15% of the amplitude of $\varepsilon_{\mathrm{central-terminal}}$ because the C_2H_5 and C_3H_8 ion species both contain central and terminal hydrogens, simply in different proportions (Figure 2-1). Specifically, the central position makes up 25% of the hydrogen atoms in the $C_3H_8^+$ molecular ion, but 40% of the hydrogen atoms in the $C_2H_5^+$ fragment ion (this fact is demonstrated experimentally in in section 4.3). Therefore, both the amplitude and measurement error in the difference in D/H ratios between the molecular and fragment ions is multiplied by approximately a factor of 6.67 when converted into the amplitude and error in position-specific D/H fractionation. When the value $\varepsilon D_{C2H5\text{-}C3H8}$ is zero, it means that the sample has a central-to-terminal D/H fractionation identical to the reference propane (CITP-1). Positive values of this index indicate that the sample is higher in $\varepsilon_{\mathrm{central-terminal}}$ than the reference gas, and thus further to the right with respect to reaction 1(more deuteration in the central position), and vice versa.

The D/H ratios of the $C_2H_5^+$ and $C_3H_8^+$ ions can be converted into D/H ratios of the central and terminal hydrogen positions using principles of mass balance. Near the end of this chapter, we use our equilibrium experiments to calibrate the true position-specific composition of our reference gas, and at that point we re-calculate absolute $\varepsilon_{\mathrm{central-terminal}}$ and δD values of the central and terminal positions of select

experimental products in the VSMOW reference frame. The conversion equations are presented in Appendix 2.

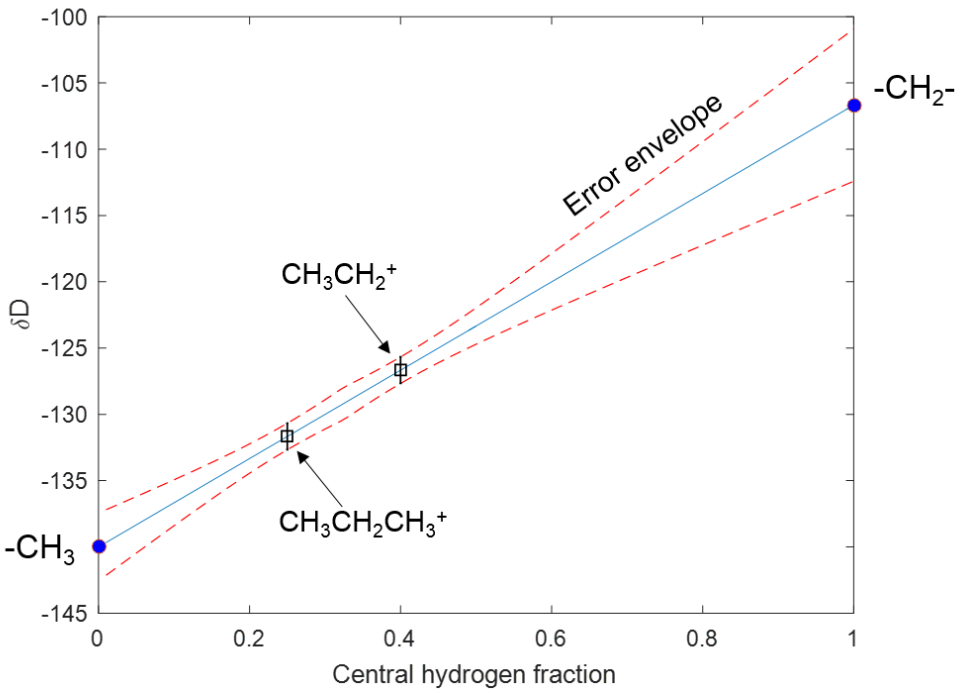

Figure 2-1: An illustration of the relationship between site-specific hydrogen isotope fractionation in propane and the isotopic contrast between molecular and ethyl fragment ions. The x-axis shows the fraction of hydrogen in a measured species that comes from the central site. The molecular ion contains 2/8=0.25 central hydrogen and the ethyl fragment contains 2/5=0.4 central hydrogen. A line connecting these two values can be extrapolated to obtain the endmember hydrogen isotope compositions of the central and terminal sites. This extrapolation leads to a magnification of analytical errors, as shown.

4. Experimental

We present a new method of mass spectrometric measurements constraining the position-specific D/H ratios of propane samples. We apply that method to propane subjected to incubations across a range of temperature-pressure conditions with a variety of substrates and catalysts. This section summarizes the materials, instruments, and methods used in these measurements and experiments.

4.1. Experimental Materials

4.1.1 Propane

We used two pure propane gas samples: (1) A reference propane, CITP-1, from a high-pressure cylinder of high purity propane (>99%) purchased from Air Liquide (UN1978); this is the same propane used as a reference standard by Piasecki et al., (2016a, 2018). Its bulk δD_{VSMOW} is -179±3‰, measured independently by GC-pyrolysis-MS. And (2) 98+ % pure $CH_3—CD_2—CH_3$ ('PROPANE (2,2-D2, 98%)') purchased from Cambridge Isotope Laboratories, Inc. This second propane was used as a deuterated 'spike' to examine the kinetics of the reaction:

$$C_3H_6D_2 + C_3H_8 \rightleftharpoons 2C_3H_7D. \quad (5)$$

We generally added 20 ppmv (by volume) of $C_3H_6D_2$ to CITP-1 for equilibrium calibration experiments on labeled gases, so that isotopic analyses of the products of these experiments would be broadly similar in molecular average D/H ratio to CITP-1. This is to minimize the effects of nonlinearity in instrumental mass fractionation (Dallas et al., 2018).

4.1.2 Water

Some experiments were conducted with deuterium-enriched water. The water was prepared by mixing 99.9 % D_2O (Cambridge Isotope Laboratories, Inc.) and deionized laboratory water by a ratio of 0.3 % volumetrically. We diluted this mixture with deionized water (reported δD_{SMOW} = -83.8 ‰) by a factor of 20.6 (by weight) in order to measure its δD on a water isotope spectroscopic analyzer (Los Gatos Research DLT-100). The measured δD_{SMOW} of the diluted mixture is 471.2±0.9 ‰, so the δD of the original mixture is 11419±31 ‰. This labeled water was used to examine the kinetics of hydrogen isotope exchange between water and propane through a reaction having a net stoichiometry (see section 4.2):

$$C_3H_8 + HDO \rightleftharpoons C_3H_7D + H_2O. \quad (6)$$

4.1.3 Metal Catalysts

Some experiments were performed using either a Pd or Ni catalytic substrate. The Pd catalyst is 10 wt. % Pd on carbon from Sigma Aldrich. It is matrix-activated and carbon-supported. The reported surface area of the support is 750–1000 m^2/g. The reported average particle size is 15μm. The Ni catalyst is 65 wt. % Ni from Sigma Aldrich. The support is silica/alumina. The surface area was measured by 11-point BET analysis to be 155.93 m^2/g. Catalysts were kept in an anaerobic chamber under an N_2+3%H_2 atmosphere.

4.2 Exchange Experimental Procedures

Isotope exchange experiments were conducted by incubating propane — either CITP-1, or labeled propane (2,2 D2), or a mixture of the two, alone or in the presence of deuterated water and/or one of the catalytic substrates (Table 2-1). Metal catalysts are loaded in the anaerobic chamber to minimize oxidation and deactivation. Each mixture of propane ± water ± substrate was placed in a 1-2 cc Pyrex® tube. We prepared 50–70 μmol of propane, and/or 500-600 μmol of water, and 40-60 mg of substrate for the hydrous experiments and 20-30 mg of substrate for the anhydrous experiments in each sample tube. The tube was then heated to a constant temperature between 30 and 200 °C in a resistance-heated furnace, for hours to weeks. The pressure inside the tube was not controlled, but depended in a calculable way on the amounts of propane ± water in each tube, the tube volume, and the temperature of the incubation. Prior to each experiment,

any catalytic substrate used in that experiment was heated by torch flame (500–600 °C) under vacuum to remove any adsorbed gas. We ceased heating when no detectable gas released from the catalyst accumulated in the gas line (<0.001 mbar in a 110 mL space for 10 seconds), which usually occurred 5-10 minutes after heating started. Then we condensed propane and water into the tube by vapor transfer through a vacuum line, with the tube immersed in liquid nitrogen. Once all reagents and catalysts were in the tube, it was flame-sealed, removed from the vacuum line, and allowed to warm to room temperature. Sealed tubes were then placed in a resistance-heated oven held at a constant, monitored temperature during the incubation period. After incubation, tubes were removed from the oven and quenched in liquid nitrogen. The tubes were then opened using a tube cracker attached to a vacuum line, and propane was passed through a dry ice-ethanol trap to remove remaining water vapor, and then condensed in a second glass tube at -196°C (immersed in liquid N_2). This second tube was then flame-sealed and removed from the vacuum line for mass spectrometric analysis.

Table 2-1: A list of exchange experiments

Substrate	Propane	Water	Temperature
Ni catalyst	CITP-1	Heavy water	200°C
Pd catalyst	CITP-1	Heavy water	200°C
Pd catalyst	CITP-1	None	30°C, 100°C and 200°C

Pd catalyst	Spiked CITP-1	None	30°C, 100°C and 200°C

4.3 Mass spectrometry

All isotopic analyses of propane starting materials and experimental products were performed using a high-resolution, doubly focusing, reverse geometry, sector mass spectrometer with electron impact ionization source (a modified version of the Thermo Fischer DFS™). This instrument and its use for high-precision isotope ratio analysis are described in detail in Dallas et al. (2018). All measurements presented here used an electron impact energy of 54 eV and a filament current of 1.0 or 1.5 mA. Typically, we prepare 50–70 μmol of propane for one sample and that results in a source pressure of 6×10^{-7}~9×10^{-7}mbar.

Since this study only involves laboratory materials, our propane samples are mostly pure. Nevertheless, we confirm each sample's purity prior to isotope ratio acquisitions. First, we scan across a narrow mass range (~0.1 Dalton) at m/z=28 to monitor N_2 and CO, which are the two most common contaminants. The most abundant ion species at nominal mass 28 is $C_2H_4^+$, so we evaluate concentrations of N_2 and CO via normalizing their signal to $C_2H_4^+$. We consider the sample contaminated by N_2 or CO if $[^{14}N_2^+]/[^{12}C_2H_4^+]$

or $[^{12}C^{16}O^+]/[^{12}C_2H_4^+]$ is higher than 1×10^{-2}. Second, we check the signal intensity of the propane molecular ion, which is $^{12}C_3H_8^+$, for the sample and CITP-1 at balanced ion source gas pressure, which can be read from the ion source gauge. Source pressure can be easily adjusted by varying inlet bellow volume. If $^{12}C_3H_8^+$ signal of the sample is within 95~100% of that of CITP-1, the discrepancy is smaller than the error of the source gauge (±5%) and we conclude that the sample is basically as clean as CITP-1. If a sample satisfies both requirements, it is ready for isotope ratio measurements. If not, we determine what the contaminant is by examining the full mass spectrum, and discard the sample.

In order to constrain the position-specific isotope difference between terminal and central hydrogen positions in propane (i.e., between CH_3— and —CH_2— groups), we require two independent observations of molecular or fragment ion species that sample different proportions of these positions (much as Yoshida (1999) and Piasecki et al. (2016a) have shown previously for position-specific measurements of ^{15}N in N_2O or ^{13}C in propane). The measurements presented here examine the D/H ratios of the full molecular ion ($C_3H_8^+$) and the ethyl fragment ion ($C_2H_5^+$). We run the DFS mass spectrometer at a tuning that delivers a mass resolution of 35,000 (FWHM), such that isobaric interferences can be well separated (Figure 2-A2).

If $C_3H_8^+$ is produced by simple ionization and $C_2H_5^+$ is produced by simple cleavage, the full molecular ion has a ratio of terminal to central hydrogens of 3:1 and the ethyl fragment ion 3:2. A crucial requirement of our mass-spectrometric approach is to demonstrate that $C_3H_8^+$ and $C_2H_5^+$ consistently sample these expected population of hydrogen sites from the original molecule. In order to test the validity of $C_3H_8^+$, we analyzed a sample from a second tank of propane, EM-1, using both our DFS MID method and independently using GC-pyrolysis-IRMS. The resulting δD (VSMOW) is –161.0 ± 1.0 ‰ with the DFS and –163.6 ± 3.2 ‰ with the GC-pyrolysis-IRMS. A more extensive test of these methods is in Ponton et al. (2017), which presented a cross-plot between measured δD values of natural propane samples using the DFS MID method and externally reported values (generally from GC-pyrolysis-IRMS techniques). That study confirms that the methods used here are consistent with independent constraints over a range of propane isotopic compositions in natural samples. We assume that the $C_2H_5^+$ inherits 3 of its hydrogens from the terminal methyl group of propane and 2 from the central CH_2 group. We tested our assumption regarding the $C_2H_5^+$ fragment ion by labeling the central site with two deuterium atoms (creating a strong enrichment in the otherwise rare species, $CH_3CD_2CH_3$) and then measuring the ratio, $[CD_2CH_3^+]/[^{13}C^{13}CH_5^+]$ to determine whether it is present in the expected abundance. Specifically, we added 333 ppmv of $CH_3CD_2CH_3$ into CITP-1 (known via measurements of the final D/H ratio of the mixture by GC-pyrolysis IRMS). This leads to a predicted

ratio of $[CD_2CH_3^+]/[^{13}C^{13}CH_5^+]$ of 3.42. We measured this ratio at a range of source pressures spanning those commonly encountered during sample measurements (Figure 2-A3). It is observed that $[CD_2CH_3^+]/[^{13}C^{13}CH_5^+]$ is stable to less than 3%, relative, over the source pressures of our measurements, and in all cases within 3%, relative, of the predicted value.

We apply the electric scan method and the multiple ion detection (MID) method detailed in Dallas et al., 2018. Briefly, the electric scan method involves scanning a narrow window of the accelerating voltage, observing the ion intensity at several (typically ~100) points across a mass range containing two or more ion peaks. Each scan typically takes around 1 second, and we stack multiple scans to generate a peak shape curve. The resulting peak shape curve is modeled as an additive function of the intensities of two or more peaks, in which the mass differences between these peaks are constrained. The output is interpreted through a peak-integration algorithm to obtain the ion intensity isotopologue ratios such as $[^{12}C_2H_4D^+]/[^{13}C^{12}CH_5^+]$ and $[^{12}C_3H_7D^+]/[^{13}C^{12}C_2H_8^+]$.

The MID method uses a different strategy. In this technique, ion intensities are measured by ‘jumping’ the electric accelerating voltage to the mass of the target ion, ‘parking’ on this mass for a certain time while determining its intensity, before jumping to the next selected ion. By repeating cycles of electrical jumping, we can integrate intensities of all ion peaks of interest over time. At the start of each cycle of analysis, the local mass scale

is re-calibrated by two anchor peaks that envelope the target peaks. Therefore, the target mass can be jumped to precisely. In practice we use one measurement to focus on the ethyl ion isotopologues (including [$^{12}C_2H_5^+$], [$^{13}C^{12}CH_5^+$] and [$^{12}C_2H_4D^+$]) and another measurement to observe the molecular ion isotopologues (including [$^{12}C_3H_8^+$], [$^{13}C^{12}C_2H_8^+$] and [$^{12}C_3H_7D^+$]). We use $^{12}C_2H_4^+$ and O_2^+ as the anchor peaks for the ethyl ion measurement, and $^{12}C_3H_7^+$ and $^{13}C^{12}C_2H_8^+$ for the molecular ion measurement. With these measured intensities, we can calculate isotope ratios of $^{13}C/^{12}C$ and D/H independently.

Since the electric scan method measures a ratio of two near isobaric species, one containing D and the other containing ^{13}C, it is important to investigate the possibility that the carbon isotope compositions of our experimental products changed as a result of our heating and reaction protocols. We found that exchange experiments in this study appear to have negligible effects on altering carbon isotope compositions of either site, at least to within limits relevant to this study. For example, a sample of CITP-1 which was exposed to Pd catalyst at 200°C on 04/07/2016, had a measured shift (end product – starting material) in $\delta^{13}C$ for the molecular ion of 0.49 ± 1.00 ‰ (2 s.e.) and for the ethyl ion of -1.00 ± 1.00 ‰ (2 s.e.). Because CITP-1 is the dominant propane component (>99.95 %) in every sample, it is a reasonable assumption that all propane samples examined in this study are uniform and equal to CITP-1 in ^{13}C content at both positions; thus, the ratios of D-bearing to ^{13}C-bearing species measured via electric scan constrain

the sample/standard difference in D/H ratio for the ethyl fragment and molecular ion. In this study, most of the results are obtained via the electric scan method. The MID method is mainly used as an independent test of electric scan results.

Each measurement, using either the MID or electric scan method, comprises 10 acquisition cycles, each of which in turn spends 2.6 minutes observing the reference material (typically CITP-1, unless indicated). We obtain 10 measured sample-reference comparisons by bracketing the sample measurement with the adjacent CITP-1 measurements, and report the mean of these 10 bracketed comparisons. We report the external error of the measurement as the standard error of the ten values, as a 1 s.e. error. Each typically 1-hour measurement consumes 4–10μmol of sample gas.

5. Results

5.1 Analytical Precision and Experimental Reproducibility

Mass spectrometric precision dictates the lower limit of our analytical uncertainty. Dallas et al. (2018) showed that both the electric scan method and the MID method of isotopic analysis using the modified DFS mass spectrometer system can approach shot-noise error. Figure 2-A4 demonstrates that the measurement error of $[^{12}C_3H_7D^+]/[^{13}C^{12}C^{12}CH_8^+]$ is only slightly greater than counting statistics. Typically, in a

1-hour D/H measurement, standard error of the ten acquisition cycles is on the order of 1‰. Converting the δD measurements of the ethyl fragment and the molecular ion into δDs of the positions leads to around 6‰ error in the central position and 3‰ error in the terminal position (See Appendix 2 for conversion equation). Our long term analytical precision can be established by evaluating replicate measurements of the CITP-1 reference standard vs. itself (zero-enrichment tests). The measured mean δD_{C3H8} value of such tests from September 2015 to March 2017 is 0.11‰ (indistinguishable from zero), and 1 standard deviation is 1.73‰ (n=12).

Analytical reproducibility for unknown samples is established by replicating measurements of the same sample. For each sample, we repeat at least one 1-hour measurement on either the ethyl ion or the molecular ion. Sometimes a comparison between methods (electric scan method vs. MID method) is also conducted. We found that the results are replicable between measurements to within analytical error. The large majority of repeated measurement pairs have normalized error ($\frac{A-B}{\sqrt{\sigma_A^2+\sigma_B^2}}$, John and Adkins, 2010) smaller than 1.

Other possible experimental and analytical artifacts could include: (1) isotope exchange between propane and other pools of hydrogen, such as exchange with water vapor either in the incubation experiments or during ionization in the source, and exchange with absorbed hydrogen on metal catalytic surfaces; (2) loss of propane through thermal

degradation, via decomposition reactions such as $C_3H_8 \rightarrow C_2H_4 + CH_4$ (Gilbert et al., 2016); and (3) vapor loss of propane. The first source of error is controlled by passing prepared propane samples through a dry ice-ethanol cold trap. The second and the third sources of error are minimized by monitoring propane yields. We manometrically quantify the amount gas at the beginning and end of each experiment. If the pressure loss is higher than 3%, relative, we discard the sample (i.e., we only use experimental data with gas yields >97%). The purity test, as mentioned in the previous section, can also serve as a proof of sample validity.

We further characterized experimental reproducibility by repeatedly analyzing a gas prepared by adding 20 ppmv (by volume) of $CH_3CD_2CH_3$ to CITP-1. Over the course of ~1 year, we repeatedly sampled the same mixture into Pyrex tubes and equilibrated them in the presence of Pd catalyst at either 30°C, 100°C or 200°C. After exchange, the majority (>99.9%) of deuterium exchanges to singly-deuterated propane (C_3H_7D; this is confirmed by monitoring the $C_3H_6D_2$ peak as a function of reaction time). We measured these heated labeled gases against CITP-1. The main goal was to calibrate the position-specific D/H fractionation thermometer, but these data also constrain our full procedural experimental reproducibility. The difference in D/H between the equilibrated labeled gas and CITP-1, obtained by measuring [$^{12}C_3H_7D^+$] is summarized in Table 2-2, which includes data of such measurements from May 2016 to April 2017.

Table 2-2: Experimental data set of equilibrated mixture (heated gas)

Experiment date	δD_{C3H8}	2s.e.
05/31/2016	38.1	1.5
07/31/2016	41.6	2.9
08/12/2016	37.0	3.1
08/13/2016	38.2	2.4
08/18/2016	35.2	2.6
08/20/2016	42.4	2.2
10/07/2016	37.7	2.0
11/01/2016	40.5	1.7
03/11/2017	38.9	1.8
04/03/2017	37.7	1.5

The measured replicate δD values are essentially consistent with an average of 38.74‰ (1 standard deviation = 2.19 ‰). The standard deviation does not differ significantly from the long-term instrumental precision (1.73‰, from the zero-enrichment tests), demonstrating that our catalyzed exchange experiments do not entail experimental artifacts or errors significantly in excess of mass spectrometric errors. Both heated-gas

and zero-test errors are higher than the average standard error of each individual measurement (1.09‰). We suspect imperfect pressure balancing between samples and standard as a possible cause, because the software we use to control the modified DFS mass spectrometer does not support automatic pressure-adjustment.

5.2 C_3H_8-H_2O exchange

At 200 °C, propane (CITP-1) was found to incorporate hydrogen from water over timescales of approximately 1-5 weeks in the presence of either the nickel catalyst or palladium catalyst. When exposed to deuterated water (δD=11419±31 ‰) the D/H ratio of both the central position and the terminal position increases (Figure 2-2). In the presence of Ni catalyst, the central hydrogens exchange significantly faster than the terminal hydrogens. In the presence of Pd catalyst there is little difference between

exchange rates of the propane hydrogen positions. Hydrogen exchange in the presence of Pd catalyst is more effective than with Ni catalyst.

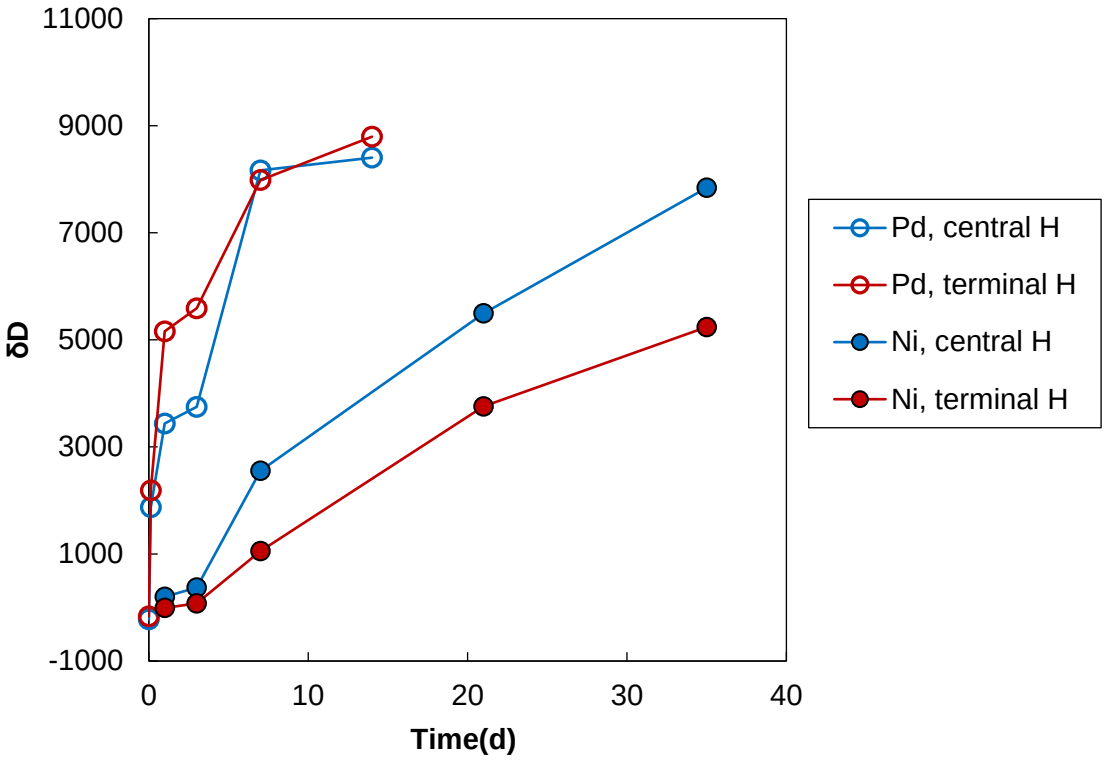

Figure 2-2 : δD values (vs. VSMOW) for central and terminal hydrogens of propane after reacting with deuterated water at 200°C, in the presence of Ni catalyst or Pd catalyst. We cannot confidently establish systematic errors associated with measurements of very D-rich samples, but estimate it could be as high as 100‰ for central H and 50‰ for

terminal H. The scale conversion from CITP-1 to VSMOW is done with the known position-specific D/H ratios of CITP-1; see Appendix 2 for details.

5.3 Internal equilibration in propane

In these experiments, two kinds of propane samples were prepared: pure CITP-1 and a mixture between CITP-1 and 20 ppmv centrally D_2-labled propane ($CH_3CD_2CH_3$). The $CH_3CD_2CH_3$ spike can provide a source of D to create a propane of different bulk hydrogen isotopic composition. In addition, it is a robust tracer for H exchange of propane, as its exchange with other propane molecules erases the excess of double-deuterated propane. By monitoring the concentration of $C_3H_6D_2$, we can assess the exchange reaction progress.

For those samples prepared from the spiked mixture, we observe decay of $C_3H_6D_2$ at all temperatures. (Figure 2-3) This proves that reaction 5 is progressing to the right, presumably catalyzed by Pd/C catalyst. At thermodynamic equilibrium the molar fraction of $C_3H_6D_2$ is predicted to be as low as 0.4 ppm. In these experiments we found that concentrations of $C_3H_6D_2$ reached this equilibrium value and stopped changing. Therefore, this is a strong line of evidence that the final time-invariant stages of our time-series represent the thermodynamic equilibrium state rather than the cessation of

exchange due to other artifacts such as deactivation of catalyst via coke formation (e.g., Albers et al., 2001). On this basis, we conclude that it is possible to equilibrate internal hydrogen isotope ordering of propane using Pd catalyst on laboratory time scales down to room temperatures. We also learned from these experiments that equilibrating D distribution within propane molecules in the presence of Pd/C catalyst but without water happens much faster than equilibrating the propane-water-Pd/C catalyst system. Using first-order kinetics the lifetimes (e-folding times) of the excess $CH_3CD_2CH_3$ are fit to be 0.020 d at 200°C, 0.093 d at 100°C and 9.9 d at 30°C (Figure 2-3). Fitting this temperature dependence to the Arrhenius equation results in an activation energy of 44 kJ/mol (R^2=0.97). Sárkány et al. (1978) studied hydrogen isotope exchange between propane and D_2 gas on Pd black catalyst (precipitated elemental Pd) and found an activation energy of 58 kJ/mol, which is broadly comparable with our findings.

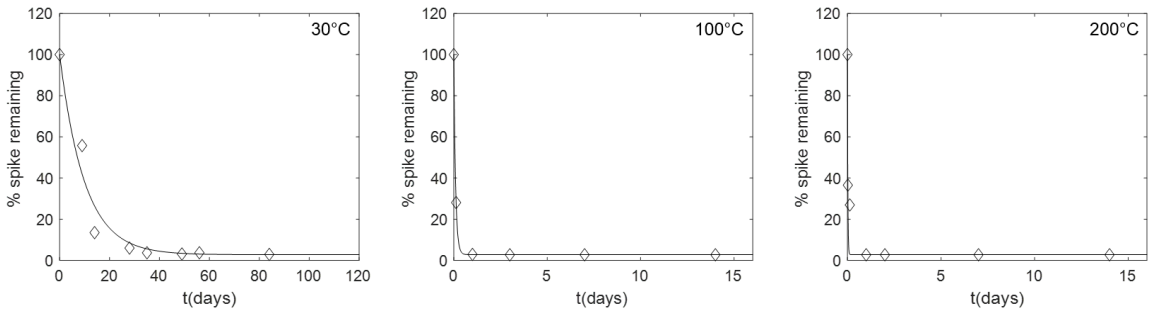

Figure 2-3: The change in concentrations of the spike $CH_3CD_2CH_3$ during anhydrous exchange experiments at three different temperatures. The spike concentrations are normalized to their original value prior to the experiments, i.e., $100\% \times [CH_3CD_2CH_3]_t/[CH_3CD_2CH_3]_0$. The diamonds are experimental data and the lines represent least square fits using first order kinetics.

We observe that propane samples of different initial isotopic composition (i.e., either CITP-1 alone or the mixture of CITP-1 and $CH_3CD_2CH_3$) converge to almost identical position-specific distribution (i.e., $\varepsilon D_{C2H5\text{-}C3H8}$) at each temperature (Figure 2-4). On this basis, we conclude that exposure of propane to Pd catalyst reaches a time-invariant and bracketed, and thus equilibrated, state. The central-terminal fractionation appears to stabilize at a different equilibrium value for each of the three temperatures (Figure 2-3). To the first order, $\varepsilon D_{C2H5\text{-}C3H8}$ at equilibrium is lower at higher temperature. This

indicates that D/H distribution within propane promotes greater enrichment of D in the central H site at lower temperatures.

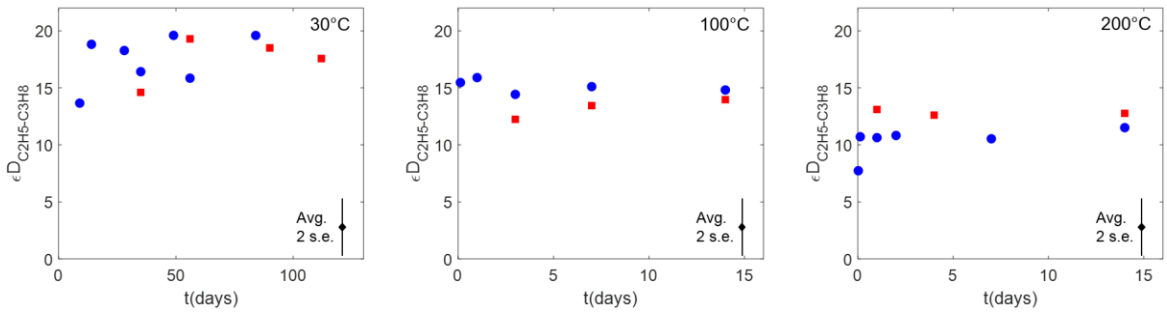

Figure 2-4: Time-series for measures of propane site-specific hydrogen isotope fractionation over the course of experiments in which propane is exposed to Pd catalyst at each of three controlled temperatures. Two initial propane compositions are used: CITP-1 (solid squares) and CITP-1 spiked with 20ppmv $CH_3CD_2CH_3$ (solid circles). The vertical axis represents the difference in dD between the ethyl fragment and molecular ions, which is proportional to the difference in dD between the central and terminal hydrogen

sites. The average analytical uncertainty, reported as 2 standard errors (±2.8‰), is shown in the bottom right corner of each panel.

We further tested this conclusion by creating a third, more deuterated sample by spiking the mixture with an additional 20ppmv $CH_3CD_2CH_3$ and exposing it to Pd catalyst at 200°C for 7 days. The $C_3H_6D_2$ concentration of this sample collapsed to a stochastic distribution, suggesting this mixture underwent quantitative D redistribution. Its $\varepsilon D_{C2H5\text{-}C3H8}$ is indistinguishable from the equilibrated original mixture and CITP-1. Table 2-3 lists the hydrogen isotope data for this sample and equilibrated samples of both the unspiked CITP-1 and the original 20 ppmv $C_3H_6D_2$ spiked mixture for comparison.

Table 2-3: Comparison of Equilibrium states of different propane samples at 200°C

Gas sample	$\delta D_{C3H8\ vs.\ CITP\text{-}1}$	1 s.e.	$\varepsilon D_{C2H5\text{-}C3H8}$	1 s.e.
CITP-1	0	N/A	12.7	1.0
CITP-1+20ppmv spike	38.0	0.8	11.2	1.2
CITP-1+40ppmv spike	74.7	1.3	11.0	2.2

6. Discussion

6.1 Position-specific exchange mechanisms

If the kinetics of hydrogen isotope exchange are treated using a pseudo first-order approximation (Robert and Urey, 1939; Sessions et al., 2004), D/H exchange rate and lifetime can be estimated through this expression:

$$e^{-kt} = \frac{F_t - F_e}{F_i - F_e}, \quad (6)$$

where F is the fraction of D among all hydrogen atoms (D/(D+^{1}H)). F_t is that fraction at time t, F_e is the fraction at equilibrium and F_i is the initial fraction. t is time, and k is the exchange rate constant, and 1/k is the e-folding time (lifetime) of this reaction. Using this equation to fit the data in Figure 2-2, we can obtain propane-water exchange reaction lifetimes. The molecule-averaged lifetime of exchange between propane and water is 2.8 days in the presence of Pd catalyst and 30.5 days in the presence of Ni catalyst at 200°C. Exchange rates for central position and terminal position appear to be different: In the presence of Ni catalyst, the central H exchange rate is faster than the terminal H exchange rate by a factor of 2.2. In the presence of Pd catalyst, terminal H exchanges faster by a factor of 1.3 — i.e., selectivity is detectable but reversed and less significant than for Ni catalyzed exchange. Figure 2-5 illustrates this difference by plotting the progress of the exchange reaction for the central site vs. that for the terminal positions. Our results for Ni

catalyzed exchange are similar to what Kauder and Taylor (1951) discovered in propane-D_2 exchange. They found that the central position exchanges with D_2 gas about 3 times as fast as the terminal position exchanges in the presence of Pt catalyst.

Table 2-4: Fitted Propane-water hydrogen isotope exchange life times (in days) for different positions and catalysts at 200°C. R^2 indicates the goodness of fit of the first-order rate law to the data.

	Central position	R^2	Terminal position	R^2
Pd catalyst	3.4	0.899	2.6	0.975
Ni catalyst	18.4	0.982	39.1	0.996

Three possible mechanisms have been proposed for the isotopic exchange of carbon-bound hydrogen in the light n-alkanes. The first is a radical exchange mechanism, in which the position-specific exchange rates are dependent on the bond dissociation energies (BDE) for each position. The BDE difference between central position and terminal position of propane is -10.7 kJ/mol (Luo, 2007). Under this scenario, we can estimate the ratio of position-specific exchange rates using the Arrehnius equation,

$$\frac{K_{central}}{k_{terminal}} = \frac{A_{central}}{A_{terminal}} e^{\frac{E_{terminal}-E_{central}}{RT}}, \quad (7)$$

where E stands for the activation energy for each hydrogen position, and A the frequency factors for the positions. It has been shown that frequency factor ratios are generally close to one (e.g., Ranzi et al., 1997), so we assume that the frequency factors are the same between the central position and the terminal position. Taking the BDE difference into account and assuming a temperature of 200 °C, we obtain that $k_{central}/k_{terminal} = 15.2$. The central hydrogen exchange is strongly favored in this case since the secondary alkyl radical (i.e., –CH·–) is much more stable than the primary radical (i.e., $–CH_2·$). A second possibility is di-adsorption, which includes αα, αβ and αγ types(Sattler, 2018). Bond (2006) suggests that αβ is the favored exchange mechanism for small straight-chain alkanes. Under this mechanism, each swap of hydrogen atoms involves one central hydrogen position and one terminal hydrogen position. Since the symmetry number ratio between central position and terminal position is 2/6, $k_{central}/k_{terminal}=3$. Thus, this mechanism also predicts faster central exchange and slower terminal exchange. A third possibility is ionic exchange, which is involves the dissociation of either proton or hydride (Schimmelmann et al., 2006; Sattler, 2018). Alexander et al. (1984) reported that alkyl H exchange happens exclusively on the position adjacent to the position that is more stable for carbocation. Since the secondary carbocation is much more stable than primary, the mechanism favors the exchange on the terminal position. Robertson et al.

(1975) studied ionic exchange between propane and D_2 on the surface of γ-alumina and found that the central position of propane exchanges 170 times faster than the terminal position. Hence, ionic exchange is the only plausible mechanism that would prefer terminal exchange over central exchange.

We plotted the predicted trajectories for these mechanisms in a plot of the δD of CH_2 groups vs. δD for methyl groups in Figure 2-5. We conclude from the data presented in Figure 2-5 that metal-catalyzed exchange is a mixture of multiple mechanisms. The Ni catalyzed exchange experiments has $k_{central}/k_{terminal}=2.2$, closely approaching the predictions of the αβ di-adsorption mechanism ($k_{central}/k_{terminal}=3$), suggesting it dominates on that catalyst, but is perhaps accompanied by a minor contribution of ionic exchange. This is consistent with Bond's (2006) review. The Pd catalyzed experiments suggest a greater role for ionic exchange and reduced importance of radical or αβ di-adsorption mechanisms. However, other combinations of these three mechanisms are permitted by our data.

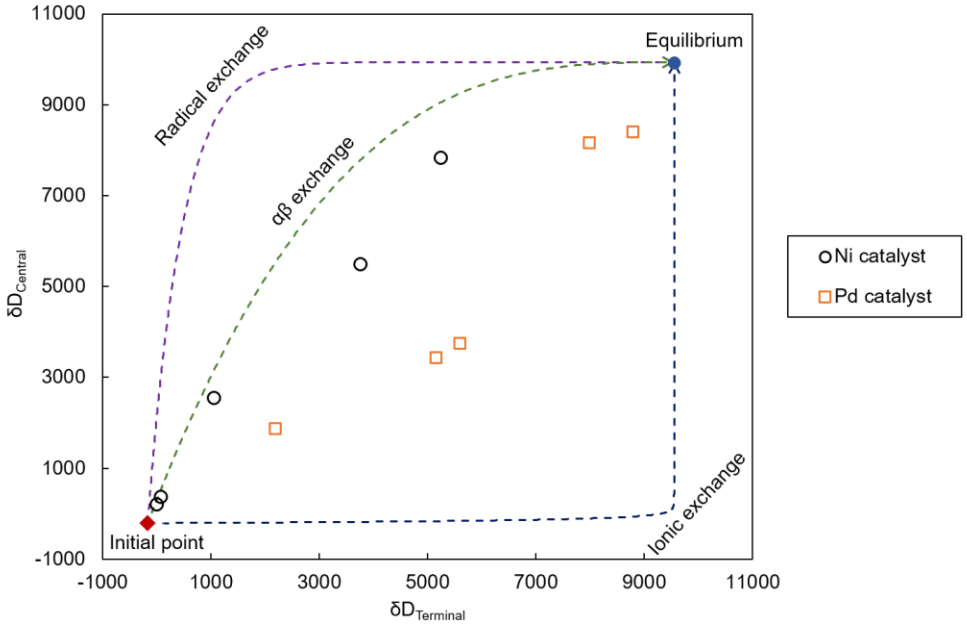

Figure 2-5: Evolution in the δD of terminal and central hydrogen sites of propane, observed in our experiments, and predicted trajectories for three proposed mechanisms of hydrogen isotope exchange: (1) radical exchange, (2) αβ di-adsorption, and (3) ionic exchange. The hydrogen isotope composition of propane in equilibrium with water vapor is calculated using results of Piasecki et al., 2016b and Richet et al., 1977.

6.2 Position-specific hydrogen isotope fractionation at thermodynamic equilibrium

We conclude that our exchange experiments examining internal hydrogen isotope exchange of propane constrain the equilibrium central-terminal fractionation to be the

final, common value to which both the CITP-1 and spiked CITP-1 experimental series converge. This allows us to obtain the equilibrium $\varepsilon D_{C2H5\text{-}C3H8}$ values. In order to determine when the propane samples are equilibrated for each temperature, we use the exchange rates learned from observing decay of $CH_3CD_2CH_3$ (Figure 2-3). We use the filter of >5 e-folding times to select the equilibrated samples, which is equivalent to >99.3% completion of exchange reaction. As a result, we have 6 data points for 30°C, 7 for 100°C and 8 for 200°C. We average these 'equilibrated' experiments at each temperature.

Figure 2-6 presents our experimental data along with all four previously published theoretical predictions for the center-terminal hydrogen isotope fractionation in propane, using units that allow us to directly compare all five sets of constraints (four models and our data) on a common plot. A comparison of these data is informative despite the fact that our measurements describe only relative differences between experimental products and an intralaboratory standard. In the left panel of Figure 2-6, we re-normalize all four theoretical predictions and our experiment to each of their fractionation at a temperature of 200˚C, and then examine the changes in predicted and observed values for the fractionation at lower temperatures. Three of the four predictions are within 2s.e. errors of our experimental data: both models presented by Webb and Miller (2014) and the model presented by Piasecki et al. (2016b). Cheng and Ceriotti's result falls outside the 2s.e. error limits of our data at both 30˚C and 100˚C.

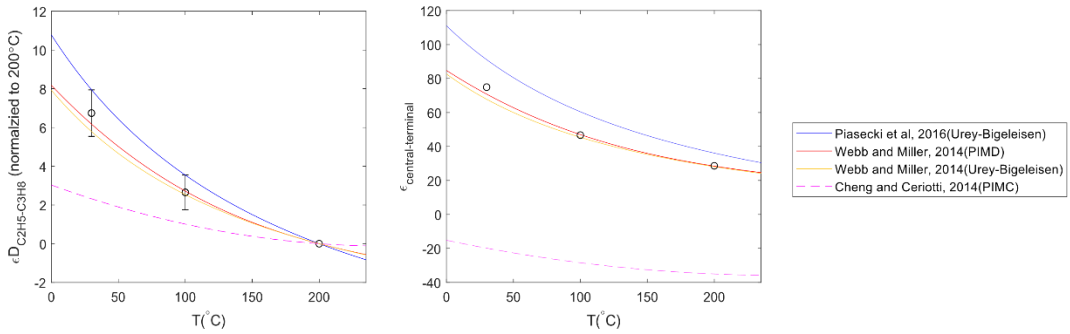

Figure 2-6: The measured equilibrium site-specific hydrogne isotope fractionation in propane plotted vs. temperature and compared to various theoretical predictions. The left panel shows the difference between the ethyl and molecular ions, which is normalized to such difference at 200°C in order to remove the dependence on the assumed intramolecular D/H fractionation in the CITP-1 standard. The right panel expresses these same data as the equilvant difference in D/H between the central and terminal positions, assuming the central position of CITP-1 has a $\delta D_{VSMOW} = -208.3‰$ and the terminal position of CITP-1 has $\delta D_{VSMOW} = -169.2‰$. (see text for details). Error bars reflect 2 standard errors of the mean of the equilbrated samples at each temperature. (n=6 for 30°C data, n=7 for 100°C data and n=8 for 200°C data). The path-integral methods (PIMC and PIMD) only report fractionation factors for 3-6 temperature points, so we fitted their data to second order polynomial functions to interpolate fractionation factors at all temperatures in this range.

There are several possible explanations for the difference between the Cheng and Ceriotti model and the other three we consider, but there is reason to believe it reflects an error in the potential energy surface (PES) in the model of Cheng and Ceriotti. The models of Webb and Miller (2014) and Cheng and Ceriotti (2014) used path-integral methods, but employed different PESs for integration. Cheng and Ceriotti (2014) used the Adaptive Intermolecular Reactive Empirical Bond Order (AIREBO) force field whereas Webb and Miller (2014) used the Chemistry at Harvard Macromolecular Mechanics (CHARMM) PES. These two models derive dramatically different vibrational frequencies for the fundamental modes of propane. In Table 2-A1 we list the vibrational frequencies of propane isotopomers derived from the two PESs (AIREBO and CHARMM), as well as those predicted by a density function theory with a B3LYP-6311G** basis set, shown for comparison. The CHARRMM frequencies are generally consistent with those predicted by B3LYP-6311G**. In the modes 5-19, there is a large difference between frequencies calculated by the AIREBO model and the other two model estimates. AIREBO frequencies can be as much as 500 cm^{-1} higher than CHARRMM frequencies. Such a conflict is beyond the magnitude of common errors. Additionally, we compared AIREBO frequencies of $^{12}C_3H_8$ with spectroscopically measured fundamental modes for propane (Table 2-A1) and the same discrepancy exists. The AIREBO frequencies are much higher than observation in the middle frequency range. We suggest that the AIREBO PES used

by Cheng and Ceriotti is likely responsible for the discrepant behavior of Cheng and Ceriotti's PIMC calculations.

Three observations suggest that our experimental data serve as a calibration of the propane D/H position-specific thermometer: Our findings are time-independent after an initial exchange period; our findings are bracketed (independent of initial composition); and the temperature-dependence of the fractionation we observe is consistent with the consensus of several theoretical predictions (recognizing the one discrepant prediction). We conclude that at thermodynamic equilibrium, D prefers to be in the central position of propane, and the central-terminal enrichment decreases with increasing temperature. The model that most closely matches our experimental findings is the PIMC model presented by Webb and Miller (2014). If we use our experimental products as a reference frame (following the reasoning behind the clumped isotope absolute reference frames for CO_2, CH_4, N_2O and O_2 (Eiler and Schauble, 2004; Yeung et al., 2014; Stolper et al., 2014)), we can calculate the hydrogen isotope structure of CITP-1: $\delta D_{central\_SMOW} = -208.3 \pm 6.6‰$ and $\delta D_{terminal\_SMOW} = -169.2 \pm 3.5‰$ and $\varepsilon_{central-terminal} = -47.1 \pm 8.9‰$.

6.3 A kinetic model of metal catalyzed exchange processes

Our experimental findings indicate hydrogen isotope exchange involving propane molecules over laboratory time scales at temperatures of 30-200 ˚C in the presence of Pd/C catalyst. However, it is difficult to use these results as precise constraints on the rate constants of this exchange both because some combinations of time and temperature have little data coverage (e.g., 30 ˚C at short times), and because multiple reaction mechanisms may be involved in re-distributing D within and between propane molecules. Nevertheless, it is worth asking whether our results are consistent with a defined set of exchange reactions having rates and activation energies broadly consistent with the results of our kinetic experiments (above). For this reason, we present a hypothesized model for the mechanisms and rates of H isotope exchange in propane, and examine whether that model is internally consistent and matches our experimental findings.

We constructed a three-box model to simulate the exchange kinetics and equilibria. The three boxes represent three hydrogen pools: the central position of propane, the terminal position of propane and absorbed hydrogen on a catalytic metal surface.

In this model, we describe hydrogen isotopic exchange on a Pd surface as governed by the following isotopic exchange reactions:

$$CH_3CD_2CH_3 + Pd-H \rightleftarrows CH_3CHDCH_3 + Pd-D \qquad (k1, 8)$$

$$CH_3CHDCH_3 + Pd-H \rightleftarrows CH_3CH_2CH_3 + Pd-D \qquad (k2, 9)$$

$$CH_3CH_2CH_2D + Pd - H \rightleftarrows CH_3CH_2CH_3 + Pd - D. \qquad (k3, 10)$$

Please note that each of these reactions represent net reactions of several elementary steps. For example, the forward reaction of k1 is combined from of two elementary steps: $CH_3CD_2CH_3 + Pd \rightarrow CH_3CDPdCH_3 + Pd\text{-}D$ and $CH_3CDPdCH_3 + Pd\text{-}H \rightarrow CH_3CHDCH_3 + Pd$. We define k_n and K_n to be the forward rate constants and equilibrium constants for the n^{th} reaction. The following differential equations can be derived:

$$\frac{d[CH_3CD_2CH_3]}{dt} = k_1[CH_3CD_2CH_3][Pd - H] - \frac{k_1}{K_1} * [CH_3CHDCH_3][Pd - D] \qquad (11)$$

$$\frac{d[CH_3CHDCH_3]}{dt} = -k_1[CH_3CD_2CH_3][Pd - H] + \frac{k_1}{K_1} * [CH_3CHDCH_3][Pd - D]$$
$$-k_2[CH_3CHDCH_3][Pd - H] + \frac{k_2}{K_2} * [CH_3CH_2CH_3][Pd - D] \qquad (12)$$

$$\frac{d[CH_3CH_2CH_2D]}{dt} = -k_3[CH_3CH_2CH_2D][Pd - H] + \frac{k_3}{K_3} * [CH_3CH_2CH_3][Pd - D] \qquad (13)$$

$$\frac{d[Pd-D]}{dt} = k_1[CH_3CD_2CH_3][Pd-H] - \frac{k_1}{K_1} * [CH_3CHDCH_3][Pd-D]$$
$$+k_2[CH_3CHDCH_3][Pd-H] - \frac{k_2}{K_2} * [CH_3CH_2CH_3][Pd-D]$$
$$+k_3[CH_3CH_2CH_2D][Pd-H] - \frac{k_3}{K_3} * [CH_3CH_2CH_3][Pd-D]. \quad (14)$$

We numerically solved this family of equations with MATLAB®. The unknown variables in this model include k_1, k_2, k_3, K_1, K_2, K_3 and relative sizes of the absorbed hydrogen reservoir. The constraints that permit us to solve for these variables are as follows:

First, exchange rate constants of the central position and the terminal position have been reported in Section 6.1. We assume the reaction rate ratio between the central position and the terminal position does not depend on whether or not water is present and is independent of temperature. Therefore, we can apply the same relationship, $k_2/k_3 = 0.76$ (Table 2-4), here. Second, k_2/k_1 is an H/D secondary kinetic isotope effect, because it describes the effect of isotopic substitution on one of the central positions on the dissociation rate of the other. For covalent C-H bonds, the secondary kinetic isotope effect is close to unity, commonly in the range of 0.8~1.2 (e.g., Lu et al., 1990), so we set k_2/k_1 equal to 1 in the model. Finally, for this purpose the effect of isotope clumping (i.e., the propensity of heavy isotopes to bond together) is trivial. We approximate that

equilibrium concentrations of isotopologues follow the stochastic rule. This approximation adds a constraint on the equilibrium constants: $K_2/K_1=4$.

With these controls, there are four free variables left: k_1, K_1, K_3 and the relative size of the surface hydrogen reservoir. We fit the model to the experimental data set (i.e., time variations in abundances of the various measured species). Results are shown in Figure 2-7. The model outputs are consistent with the data within experimental precision. This model predicts that CH_3CHDCH_3 will rise faster than $CH_3CH_2CH_2D$ when $CH_3CD_2CH_3$ is being consumed. It is because the first step of $CH_3CD_2CH_3$ exchange with the catalyst-bound H pool generates a CH_3CHDCH_3 molecule. This leads to faster changes in the $\varepsilon D_{C2H5\text{-}C3H8}$ value of spiked gas relative to un-spiked gas, with even a slight overshoot in the early period of spiked gas exchange. The faster rise of $\varepsilon D_{C2H5\text{-}C3H8}$ value of spiked gas is well observed in experimental data. (Figure 2-7).

We re-iterate that the details of our model are under constrained with respect to time and temperature sampling points and should be considered only an approximate statement about the rate constants for D/H exchange within and between propane molecules. However, this exercise shows that our experimental findings are internally consistent with a simple and intuitive description of the family of reaction steps involved in this process.

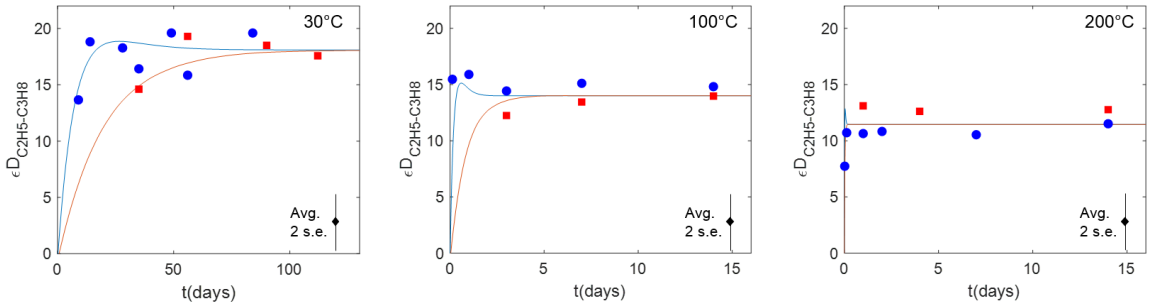

Figure 2-7: Fits of our three-box model to experimental results. The solid circles and solid squares represent the position-specific hydrogen isotope fractionation of spiked CITP-1 and pure CITP-1, respectively. The solid blue lines and solid red lines represent the optimized model for position-specific hydrogen isotope fractionation of spiked CITP-1 and pure CITP-1, respectively (converted into the units used for the Y axis, i.e., expressed as the difference between ethyl and molecular ions, normalized to CITP-1).

6.4 Implications for the interpretation of data for natural propanes

This study examines hydrogen isotope exchange of propane in the presence of artificial metal catalysts that are not common in nature. Therefore, it is reasonable to consider whether propane is too refractory to H isotope exchange to equilibrate its isotopic structure in natural settings. Interpretation of the bulk molecular D/H ratio of propane (and other natural gas hydrocarbons) assumes this property is immune to hydrogen isotope exchange between hydrocarbon molecules and molecular positions (e.g., Tang et

al., 2005; Ni et al., 2011). However, our findings indicate that intramolecular exchange of H between terminal and central positions in propane under anhydrous conditions occurs orders of magnitude faster than exchange between propane and water in the presence of metal catalysts. Thus we might expect that propane in natural crustal environments could internally re-equilibrate its position-specific hydrogen isotope structure even in the absence of changes in molecule averaged δD. We should also consider that even if propane fails to reach H isotope exchange equilibrium with co-existing hydrous compounds in geological conditions, our findings indicate that partial exchange may lead to a signature in hydrogen isotope site preference that constrains the thermal stress (time-at-temperature) and/or exposure to catalysts propane experienced since its formation. We show that intermolecular hydrogen isotope exchange rates (i.e., between propane and water) can differ between central and terminal hydrogen positions, depending on the co-existing catalysts. In particular, the central position exchanges hydrogen isotopes approximately twice as fast as the terminal position when Ni catalyst is present. The difference in exchange rates of the positions can lead to significant variance in central-to-terminal fractionation as propane approaches equilibrium with water (or perhaps another hydrous compound; Figure 2-5). Interpretation of natural propane samples' position-specific D/H will have to take this phenomenon into account. Future studies should examine the exchange kinetics for propane in the presence of

natural catalysts (e.g., minerals or rocks) to establish whether these conclusions based on metal catalyzed experiments are truly generalizable.

More generally, we anticipate that several processes will complicate the interpretation of position-specific hydrogen isotope fractionation in propane as a thermometer to natural systems. Radical chain reactions involving other hydrocarbons (Xiao, 2001) and microbial gas degradation (Jaekel et al., 2014) are two common processes that likely involve irreversible, isotopically fractionating elementary kinetic steps. In fact, we should expect that some small amount of propane destruction by irreversible 'cracking' occurred during our experiments, but had no apparent isotopic effects because the accompanying equilibration reactions happened on much faster timescales than propane destruction (this is demonstrably obvious; our experiments lose a negligible fraction of propane over a time scale equivalent to many e-folding times of exchange – see Figure 2-3). It also should be noted that even in natural systems dominated by irreversible elementary kinetic reactions, an interconnected network of such reactions can drive systems to or near equilibrium molecular and isotope distributions if they indirectly interconvert different compounds (and their isotopic forms). Such systems are said to have reached 'metathetic equilibrium', and are hypothesized to be common in natural gas forming systems (Mango et al., 2010). This study provides a foundation to test these hypotheses with measurements of position-specific hydrogen isotope fractionations in propane from natural gases and pyrolysis experiments. Our reference propane, CITP-1, which comes

from a commercial gas supplier, is significantly D-depleted in the central position relative to its terminal position ($\varepsilon_{\mathrm{central-terminal}}$ = -47.1±8.9‰). Its position-specific D/H distribution is far from internal equilibrium. This finding is comparable to NMR results from Liu et al. (2018), where they measured $\delta D_{central}$- $\delta D_{terminal}$ = –26.4±8.8‰ in a commercially obtained propane. These data suggest that some common process can easily generate large position-specific disequilibria. This phenomenon strengthens the prospect of applying this tool to study the origin and evolution of natural propane, as it suggests that both non-equilibrium and equilibrium signatures are possible (and thus might distinguish between different formation mechanisms and environments).

7. Conclusions

We have developed a method to analyze position-specific D/H variations of propane via high-resolution mass spectrometry. The same methodology, which involves measuring D/H ratios of specific fragment ions, should be amenable to the measurement of other small hydrocarbon molecules.

In a series of incubation experiments, we measured catalyzed hydrogen exchange kinetics of propane. Our results document differences in effectiveness between Ni and Pd catalysts and differences in the relative rates of exchange for the two non-equivalent

hydrogen positions. The exchange rates we observe do not exactly match any one previously proposed mechanism, suggesting our experiments involved exchange by two or more mechanisms. We also observed that the exchange between propane and water is slower than propane internal exchange in an anhydrous environment. We experimentally produced propane with an equilibrated position-specific hydrogen isotopic structure. The position-specific hydrogen isotope equilibrium in propane was shown to be time-invariant, composition-bracketed, and mass-balanced to within a few percent at three temperatures. Our results are able to discriminate between several different theoretical predictions, ruling out the one that predicts terminal position D enrichment. We conclude that our data serve as a calibration of the position-specific propane D/H thermometer. In the range of natural gas formation and storage, the fractionation factor is highly sensitive to temperature (around 0.25‰ per ˚C at 100 °C). With commercially available multi-collector high resolution mass spectrometers (e.g., Eiler et al., 2013a), we anticipate that we will be able to improve the precision of position-specific measurements by approximately an order of magnitude relative to the work presented here, and therefore should be able to apply this thermometer with a precision of 2~5°C in the range of geological relevant temperatures.

Acknowledgements

This research is supported by an NSF-EAR instruments and facilities grant and Caltech. Additional funding is provided by Exxon Mobil. We thank Michael Webb and Thomas Miller for helpful discussions and for providing the vibrational frequency calculations for the empirical PES. We thank Aaron Sattler and Michele Paccagnini for insightful advices on catalytic chemistry. We thank Nami Kitchen for advice and assistance with the experimental setup and the operation of the DFS mass spectrometer.

References

Abelson P. H. and Hoering T. C. (1961) Carbon isotope fractionation in formation of amino acids by photosynthetic organisms. Proceedings of the National Academy of Sciences. 47(5): 623-32.

Albers P., Pietsch J. and Parker S. F. (2001) Poisoning and deactivation of palladium catalysts. J. Mol. Catal. A Chem. 173, 275–286.

Alexander R., Kagi R. I. and Larcher A. V (1984) Clay catalysis of alkyl hydrogen exchange reactions—reaction mechanisms. Org. Geochem. 6, 755–760.

Bond G. C. (2005) Metal-catalysed reactions of hydrocarbons., Springer.

Caytan E., Remaud G. S., Tenailleau E. and Akoka S. (2007) Precise and accurate quantitative 13 C NMR with reduced experimental time. Talanta 71, 1016–1021.

Cheng B. and Ceriotti M. (2014) Direct path integral estimators for isotope fractionation ratios. J. Chem. Phys. 141, 244112.

Dallas B., Eiler J. M., Clog M., Ponton C., Xie H., Griep-Raming J., Schweiters J. and Kitchen N. (submitted) High precision stable isotope analysis of molecular and fragment ions using a high resolution, single-collector mass spectrometer. (2017)

Dawson D., Grice K., Alexander R. and Edwards D. (2007) The effect of source and maturity on the stable isotopic compositions of individual hydrocarbons in sediments and crude oils from the Vulcan Sub-basin, Timor Sea, Northern Australia. Org. Geochem. 38, 1015–1038.

Ehlers I., Augusti A., Betson T. R., Nilsson M. B., Marshall J. D. and Schleucher J. (2015) Detecting long-term metabolic shifts using isotopomers: CO2-driven suppression of photorespiration in C3 plants over the 20th century.

Eiler J. M. (2013) The isotopic anatomies of molecules and minerals. Annu. Rev. Earth Planet. Sci. 41, 411–441.

Eiler J. M., Bergquist B., Bourg I., Cartigny P., Farquhar J., Gagnon A., Guo W., Halevy I., Hofmann A. and Larson T. E. (2014) Frontiers of stable isotope geoscience. Chem. Geol. 372, 119–143.

Eiler J. M., Clog M., Magyar P., Piasecki A., Sessions A., Stolper D., Deerberg M., Schlueter H.-J. and Schwieters J. (2013) A high-resolution gas-source isotope ratio mass spectrometer. Int. J. Mass Spectrom. 335, 45–56.

Eiler J. M. and Schauble E. (2004) 18 O 13 C 16 O in Earth's atmosphere. Geochim. Cosmochim. Acta 68, 4767–4777.

Gao L., He P., Jin Y., Zhang Y., Wang X., Zhang S. and Tang Y. (2016) Determination of position-specific carbon isotope ratios in propane from hydrocarbon gas mixtures. Chem. Geol. 435, 1–9.

Gilbert A., Yamada K., Suda K., Ueno Y. and Yoshida N. (2016) Measurement of position-specific 13 C isotopic composition of propane at the nanomole level. Geochim. Cosmochim. Acta 177, 205–216.

Jaekel U., Vogt C., Fischer A., Richnow H.-H. and Musat F. (2014) Carbon and hydrogen stable isotope fractionation associated with the anaerobic degradation of propane and butane by marine sulfate-reducing bacteria. Environ. Microbiol. 16, 130–140.

John S. G. and Adkins J. F. (2010) Analysis of dissolved iron isotopes in seawater. Mar. Chem. 119, 65–76.

Julien M., Nun P., Robins R. J., Remaud G. S., Parinet J. and Höhener P. (2015) Insights into Mechanistic Models for Evaporation of Organic Liquids in the Environment Obtained by Position-Specific Carbon Isotope Analysis. Environ. Sci. Technol. 49, 12782–12788.

Julien M., Nun P., Höhener P., Parinet J., Robins R. J. and Remaud G. S. (2016) Enhanced forensic discrimination of pollutants by position-specific isotope analysis using isotope ratio monitoring by 13 C nuclear magnetic resonance spectrometry. Talanta 147, 383–389.

Kauder L. N. and Taylor T. I. (1951) Experiments on the Catalytic Exchange of Acetone and Propane with Deuterium. Science 113(2931), 238-241.

Koizumi M. and Titani T. (1938) Austauschreaktion der Kernwasserstoffatome des Phenols. I. Austauschreaktion in alkalischer Lösung. Bull. Chem. Soc. Jpn. 13, 681–690.

Li M., Huang Y., Obermajer M., Jiang C., Snowdon L. R. and Fowler M. G. (2001) Hydrogen isotopic compositions of individual alkanes as a new approach to petroleum correlation: case studies from the Western Canada Sedimentary Basin. Org. Geochem. 32, 1387–1399.

Liu C., Mcgovern G. P. and Horita J. (2015) Position-Specific Hydrogen and Carbon Isotope Fractionations of Light Hydrocarbons by Quantitative NMR. In AGU Fall Meeting Abstracts

Lorant F., Prinzhofer A., Behar F. and Huc A.-Y. (1998) Carbon isotopic and molecular constraints on the formation and the expulsion of thermogenic hydrocarbon gases. Chem. Geol. 147, 249–264.

Lu D. H., Maurice D. and Truhlar D. G. (1990) What is the effect of variational optimization of the transition state on. alpha.-deuterium secondary kinetic isotope effects? A prototype: CD3H+ H. dblarw. CD3+ H2. J. Am. Chem. Soc. 112, 6206–6214.

Luo Y.-R. (2007) Comprehensive handbook of chemical bond energies., CRC press.

Mango F. D. and Jarvie D. M. (2010) Metathesis in the generation of low-temperature gas in marine shales. Geochem. Trans. 11, 1.

Martin G. J. and Martin M. L. (1981) Deuterium labelling at the natural abundance level as studied by high field quantitative 2H NMR. Tetrahedron Lett. 22, 3525–3528.

Martin G. J., Martin M. L. and Remaud G. (2008) SNIF-NMR—Part 3: From Mechanistic Affiliation to Origin Inference. In Modern Magnetic Resonance Springer. pp. 1669–1680.

Ni Y., Ma Q., Ellis G. S., Dai J., Katz B., Zhang S. and Tang Y. (2011) Fundamental studies on kinetic isotope effect (KIE) of hydrogen isotope fractionation in natural gas systems. Geochim. Cosmochim. Acta 75, 2696–2707.

Park R. and Epstein S. (1961) Metabolic fractionation of C13 & C12 in plants. Plant Physiol. 36, 133.

Piasecki A., Sessions A., Lawson M., Ferreira A. A., Neto E. V. S. and Eiler J. M. (2016a) Analysis of the site-specific carbon isotope composition of propane by gas source isotope ratio mass spectrometer. Geochim. Cosmochim. Acta 188, 58–72.

Piasecki A., Sessions A., Lawson M., Ferreira A. A., Neto E. V. S., Ellis G. S., Lewan M. D. and Eiler J. M. (2018) Position-specific 13C distributions within propane from experiments and natural gas samples. Geochim. Cosmochim. Acta 220, 110–124.

Piasecki A., Sessions A., Peterson B. and Eiler J. (2016b) Prediction of equilibrium distributions of isotopologues for methane, ethane and propane using density functional theory. Geochim. Cosmochim. Acta 190, 1–12.

Ponton C., Xie H., Lawson M., Formolo M., Peterson B., Sattler A. & Eiler J. (2017) Goldschmidt Abstracts, 2017 3194

Ranzi E., Faravelli T., Gaffuri P., Garavaglia E. and Goldaniga A. (1997) Primary pyrolysis and oxidation reactions of linear and branched alkanes. Ind. Eng. Chem. Res. 36, 3336–3344.

Reddy C. M., Arey J. S., Seewald J. S., Sylva S. P., Lemkau K. L., Nelson R. K., Carmichael C. A., McIntyre C. P., Fenwick J. and Ventura G. T. (2012) Composition and fate of gas and oil released to the water column during the Deepwater Horizon oil spill. Proc. Natl. Acad. Sci. 109, 20229–20234.

Reeves E. P., Seewald J. S. and Sylva S. P. (2012) Hydrogen isotope exchange between n-alkanes and water under hydrothermal conditions. Geochim. Cosmochim. Acta 77, 582–599.

Remaud, G.S., Martin, Y.L., Martin, G.G. and Martin, G.J., 1997. Detection of sophisticated adulterations of natural vanilla flavors and extracts: application of the SNIF-NMR method to vanillin and p-hydroxybenzaldehyde. Journal of Agricultural and food Chemistry 45(3), pp.859-866.

Richet P., Bottinga Y. and Javoy M. (1977) A Review of Hydrogen, Carbon, Nitrogen, Oxygen, Sulphur, and Chlorine Stable Isotope Fractionation Among Gaseous Molecules. Annu. Rev. Earth Planet. Sci. 5, 65–110.

Roberts I. and Urey H. C. (1939) Kinetics of the exchange of oxygen between benzoic acid and water. J. Am. Chem. Soc. 61, 2580–2584.

Robertson P. J., Scurrell M. S. and Kemball C. (1975) Exchange of alkanes with deuterium over [gamma]-alumina. A Bronsted linear free energy relationship. J. Chem. Soc. Faraday Trans. 1 Phys. Chem. Condens. Phases 71, 903–912.

Sattler A. (2018) Hydrogen/Deuterium (H/D) Exchange Catalysis in Alkanes. ACS Catal. 8, 2296–2312.

Sárkány A., Guczi L. and Tétényi P. (1978) Reactions of some alkanes on palladium black catalyst. ACTA Chim. Acad. Sci. HUNGARICAE 96, 27–37.

Schimmelmann A., Sessions A. L. and Mastalerz M. (2006) Hydrogen isotopic (D/H) composition of organic matter during diagenesis and thermal maturation. Annu. Rev. Earth Planet. Sci. 34, 501–533.

Sessions A. L., Sylva S. P., Summons R. E. and Hayes J. M. (2004) Isotopic exchange of carbon-bound hydrogen over geologic timescales. Geochim. Cosmochim. Acta 68, 1545–1559.

Sessions A. L. (2016) Factors controlling the deuterium contents of sedimentary hydrocarbons. Org. Geochem. 96, 43–64.

Shimanouchi, T. (1972) Tables of Molecular Vibrational Frequencies Consolidated Volume I; National Bureau of Standards: Washington, DC 126.

Stolper D. A., Sessions A. L., Ferreira A. A., Neto E. V. S., Schimmelmann A., Shusta S. S., Valentine D. L. and Eiler J. M. (2014) Combined 13 C–D and D–D clumping in methane: Methods and preliminary results. Geochim. Cosmochim. Acta 126, 169–191.

Tang Y., Huang Y., Ellis G. S., Wang Y., Kralert P. G., Gillaizeau B., Ma Q. and Hwang R. (2005) A kinetic model for thermally induced hydrogen and carbon isotope fractionation of individual n-alkanes in crude oil. Geochim. Cosmochim. Acta 69, 4505–4520.

Webb M. A. and Miller III T. F. (2014) Position-specific and clumped stable isotope studies: Comparison of the Urey and path-integral approaches for carbon dioxide, nitrous oxide, methane, and propane. J. Phys. Chem. A 118, 467–474.

Xiao Y. (2001) Modeling the Kinetics and Mechanisms of Petroleum and Natural Gas Generation: A First Principles Approach. Rev. Mineral. Geochemistry 42, 383–436.

Yeung L. Y., Ash J. L. and Young E. D. (2014) Rapid photochemical equilibration of isotope bond ordering in O 2. J. Geophys. Res. Atmos. 119, 10552–10566.

Appendix 2

Converting δD_{C2H5} and δD_{C3H8} into absolute position-specific D/H ratios based on our calibration.

Neglecting the trivial effects of non-stochastic distribution of multiply D-substituted isotopologues in the un-spiked gases, we have:

$$\left(\frac{C_2H_4D}{C_2H_5}\right) = \frac{5 * \left(\frac{H}{D+H}\right)^4_{C2H5} \left(\frac{D}{D+H}\right)_{C2H5}}{\left(\frac{H}{D+H}\right)^5_{C2H5}} = 5 * \left(\frac{D}{H}\right)_{C2H5}$$

$$\left(\frac{C_3H_7D}{C_3H_8}\right) = \frac{8 * \left(\frac{H}{D+H}\right)^7_{C3H8} \left(\frac{D}{D+H}\right)_{C3H8}}{\left(\frac{H}{D+H}\right)^8_{C3H8}} = 8 * \left(\frac{D}{H}\right)_{C3H8}.$$

Therefore,

$$\left(\frac{D}{H}\right)_{C2H5} = \frac{1}{5} * \left(\frac{C_2H_4D}{C_2H_5}\right) = \frac{1}{5} * \frac{\delta D_{C2H5} + 1000}{1000} * \left(\frac{C_2H_4D}{C_2H_5}\right)_{CITP-1}$$

$$= \frac{\delta D_{C2H5} + 1000}{1000} * \left(\frac{D}{H}\right)_{C2H5(CITP-1)}$$

$$\left(\frac{\mathrm{D}}{\mathrm{H}}\right)_{\mathrm{C3H8}} = \frac{1}{8} * \left(\frac{\mathrm{C_3H_7D}}{\mathrm{C_3H_8}}\right) = \frac{1}{8} * \frac{\delta \mathrm{D_{C3H8}} + 1000}{1000} * \left(\frac{\mathrm{C_3H_7D}}{\mathrm{C_3H_8}}\right)_{\mathrm{CITP-1}}$$

$$= \frac{\delta \mathrm{D_{C3H8}} + 1000}{1000} * \left(\frac{\mathrm{D}}{\mathrm{H}}\right)_{\mathrm{C3H8(CITP-1)}}.$$

In section 6.2, we concluded that

$$\left(\frac{\mathrm{D}}{\mathrm{H}}\right)_{\mathrm{C2H5(CITP-1)}} = 0.00012696$$

$$\left(\frac{\mathrm{D}}{\mathrm{H}}\right)_{\mathrm{C3H8(CITP-1)}} = 0.00012786.$$

so we can calculate D fractions based on δDs:

$$\left(\frac{\mathrm{D}}{\mathrm{D+H}}\right)_{\mathrm{C2H5}} = \frac{\frac{\delta \mathrm{D_{C2H5}} + 1000}{1000}\left(\frac{\mathrm{D}}{\mathrm{H}}\right)_{\mathrm{C2H5(CITP-1)}}}{\frac{\delta \mathrm{D_{C2H5}} + 1000}{1000}\left(\frac{\mathrm{D}}{\mathrm{H}}\right)_{\mathrm{C2H5(CITP-1)}} + 1}$$

$$\left(\frac{\mathrm{D}}{\mathrm{D+H}}\right)_{\mathrm{C3H8}} = \frac{\frac{\delta \mathrm{D_{C3H8}} + 1000}{1000}\left(\frac{\mathrm{D}}{\mathrm{H}}\right)_{\mathrm{C3H8(CITP-1)}}}{\frac{\delta \mathrm{D_{C3H8}} + 1000}{1000}\left(\frac{\mathrm{D}}{\mathrm{H}}\right)_{\mathrm{C3H8(CITP-1)}} + 1}.$$

In section 4.3 we demonstrated that these ions inherit the isotopic composition of the molecule, so

$$\left(\frac{\mathrm{D}}{\mathrm{D}+\mathrm{H}}\right)_{\mathrm{Central}} = 5\left(\frac{\mathrm{D}}{\mathrm{D}+\mathrm{H}}\right)_{\mathrm{C2H5}} - 4\left(\frac{\mathrm{D}}{\mathrm{D}+\mathrm{H}}\right)_{\mathrm{C3H8}}$$

$$\left(\frac{\mathrm{D}}{\mathrm{D}+\mathrm{H}}\right)_{\mathrm{Terminal}} = \frac{8}{3}\left(\frac{\mathrm{D}}{\mathrm{D}+\mathrm{H}}\right)_{\mathrm{C3H8}} - \frac{5}{3}\left(\frac{\mathrm{D}}{\mathrm{D}+\mathrm{H}}\right)_{\mathrm{C2H5}}.$$

Finally,

$$\delta\mathrm{D}_{\mathrm{Central}} = 1000 * \left(\frac{\left(\frac{\mathrm{D}}{\mathrm{D}+\mathrm{H}}\right)_{\mathrm{Central}}}{1-\left(\frac{\mathrm{D}}{\mathrm{D}+\mathrm{H}}\right)_{\mathrm{Central}}} / \left(\frac{\mathrm{D}}{\mathrm{H}}\right)_{\mathrm{VSMOW}} - 1\right)$$

$$\delta\mathrm{D}_{\mathrm{Terminal}} = 1000 * \left(\frac{\left(\frac{\mathrm{D}}{\mathrm{D}+\mathrm{H}}\right)_{\mathrm{Terminal}}}{1-\left(\frac{\mathrm{D}}{\mathrm{D}+\mathrm{H}}\right)_{\mathrm{Terminal}}} / \left(\frac{\mathrm{D}}{\mathrm{H}}\right)_{\mathrm{VSMOW}} - 1\right),$$

in which

$$\left(\frac{\mathrm{D}}{\mathrm{H}}\right)_{\mathrm{VSMOW}} = 0.00015576.$$

Appendix Figures

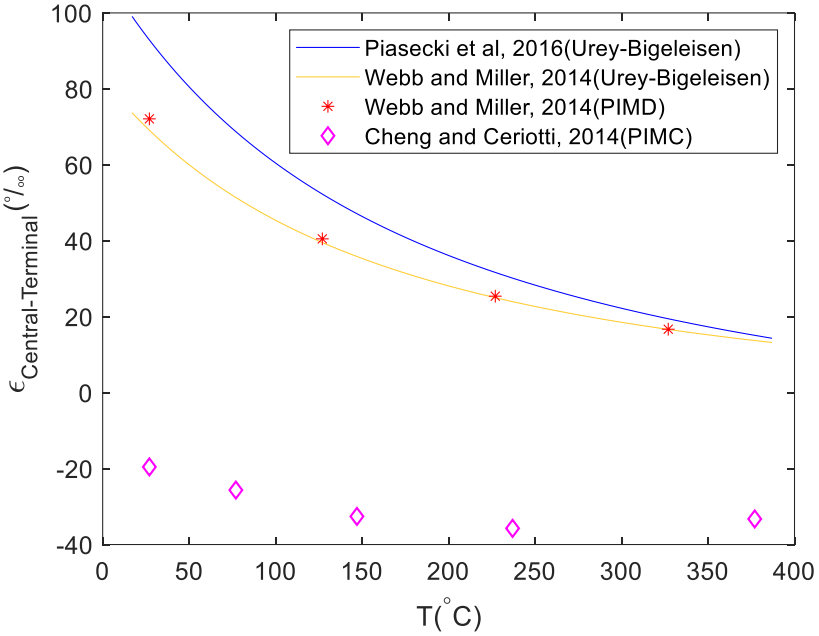

Figure 2-A1: Comparison of model predictions of the temperature dependence of the central-to-terminal hydrogen isotope fractionation factors for propane. PIMD stands for “Path Integral Molecular Dynamics” and PIMC stands for “Path Integral Monte Carlo”.

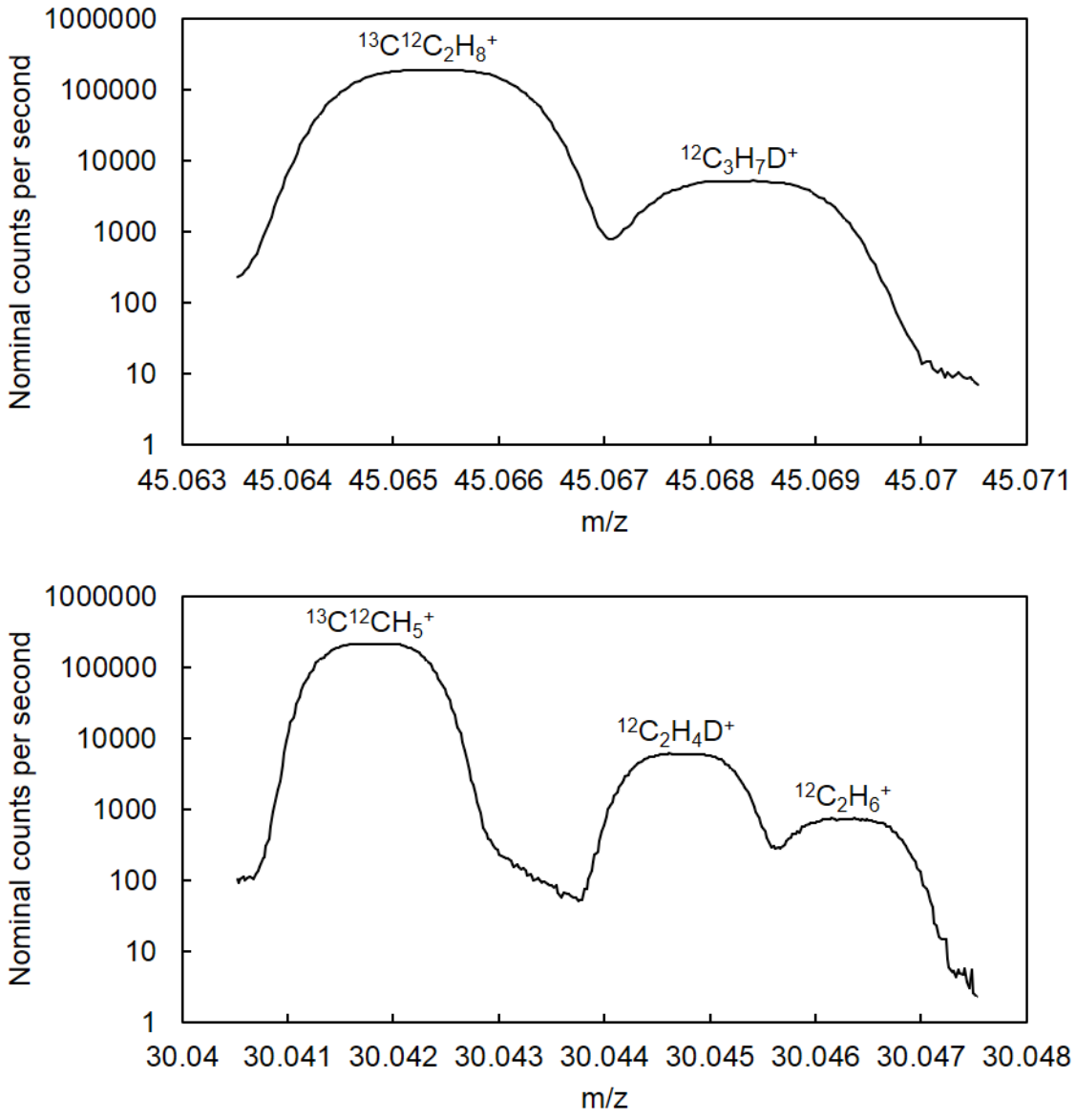

Figure 2-A2: Local mass spectrum of m/z=45 species (up) and m/z=30 species (bottom).

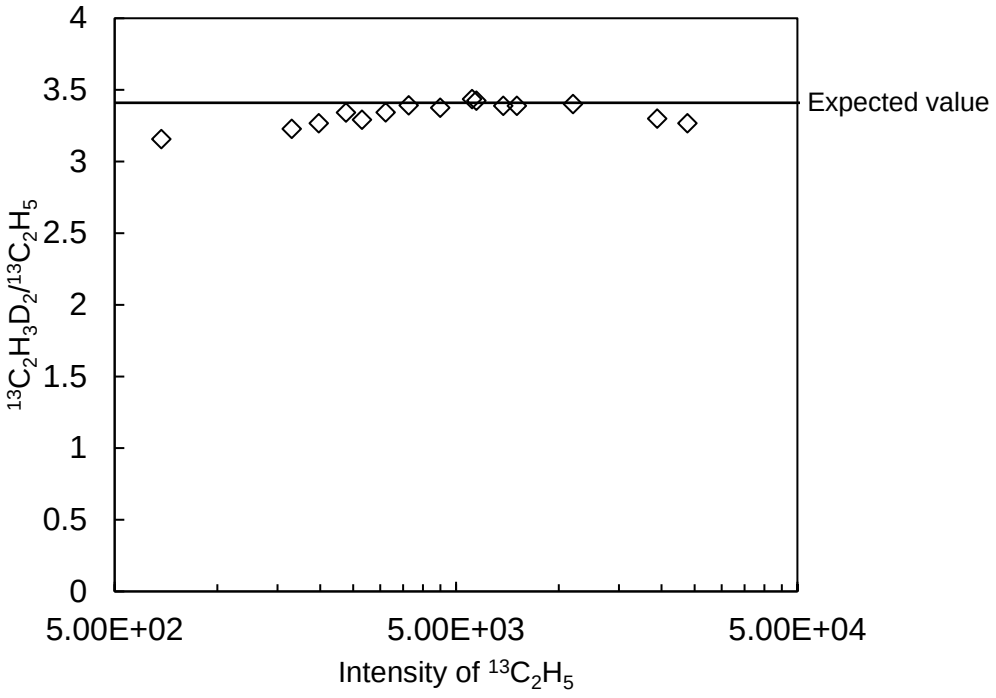

Figure 2-A3: Tests of our hypothesis regarding the sources of hydrogen (central vs. terminal sites) in the ethyl fragment ion. The X-axis is the intensity in units of counts/s. and the Y-axis is the relative concentration of $^{13}C_2H_3D_2$. We varied the pressure in the ion source to generate a range in ion intensity. Open squares are measurements and the horizontal solid line is calculated based on the known mixing ratio of $CH_3CD_2CH_3$ in the analyzed gas.

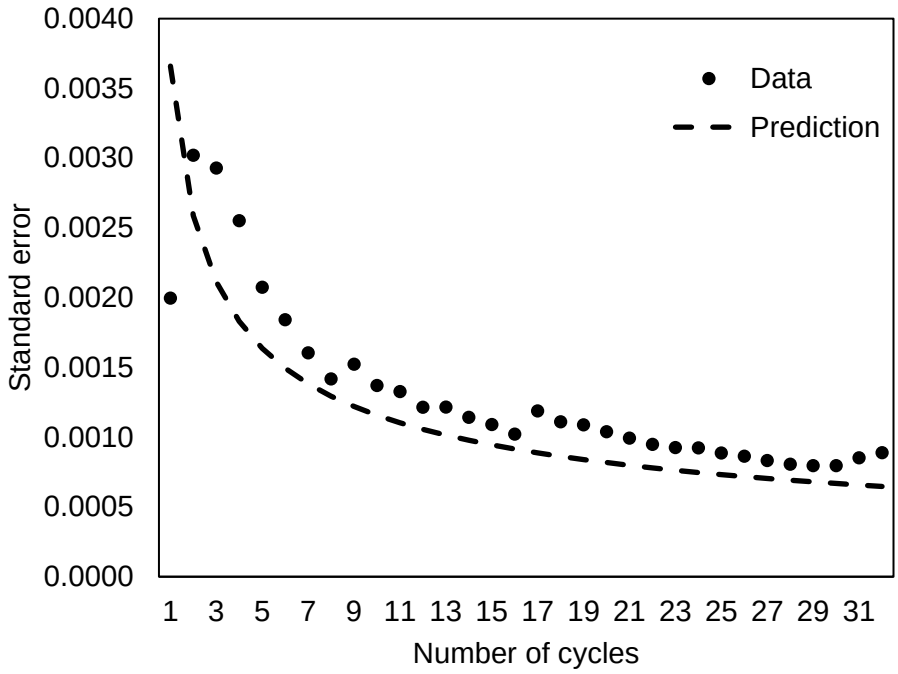

Figure 2-A4: The results of a test of whether the measurement error is limited by counting statistics. The plots show the external error of the measured $[^{12}C_3H_7D^+]/[^{13}C^{12}C^{12}CH_8^+]$ ratio, made via the electric scan method; the dashed curve indicates the predicted evolution of errors across multiple analytical cycles for the case where errors are shot noise limited. Each cycle is 2.3 minutes.

Appendix Tables

Table 2-A1: A comparison of harmonic wavenumbers (in cm^{-1}) of the vibrational modes of the D-substituted isotopomers of propane derived from different theoretical models. Data for AIREBO and CHARMM are from private communications with Michael Webb. Data for B3LYP-6311G** are from Piasecki et al., 2016. Data for spectroscopic observation of $CH_3CH_2CH_3$ is from Shimanouchi, 1972.

	CH3CH2CH3				CH3CH2CH2D (gauche)			CH3CHDCH3		
Mode#	AIREBO	CHARMM	B3LYP-6311G**	Observation[#]	AIREBO	CHARMM	B3LYP-6311G**	AIREBO	CHARMM	B3LYP-6311G**
1	233.2801	232.2719	219.3189	216	214.8174	211.3712	201.6949	233.2581	232.2682	219.3109
2	291.8998	252.7020	269.3751	268	281.8471	243.8475	259.6141	287.1524	249.8656	265.5630
3	483.5978	357.1896	366.3376	369	470.9414	350.5004	355.1954	480.9210	355.5481	364.2611
4	928.1719	794.7737	755.0908	748	925.4947	741.1732	707.1277	911.7060	696.0663	670.0738

5	1089.9861	869.4822	870.5537	869	1009.2690	789.7555	843.4579	992.7312	835.8072	807.7772
6	1121.4818	941.1163	914.6184	922	1096.6659	915.7384	869.2711	1059.8019	866.8711	866.2395
7	1323.9384	955.4877	933.0299	940	1213.7890	937.9711	915.3735	1215.4265	941.1710	929.0753
8	1361.5076	1038.1633	1057.1314	1054	1337.1719	1016.4346	1051.0626	1336.3636	965.4336	1003.4322
9	1434.1405	1090.6866	1175.4568	1158	1412.3653	1079.7758	1131.1886	1410.1030	1052.9224	1148.3138
10	1525.5459	1096.4099	1213.4906	1192	1489.7217	1084.2881	1175.5615	1411.8567	1092.8598	1168.3591
11	1616.9838	1192.9895	1319.0383	1278	1610.5415	1191.5593	1292.2171	1483.0419	1099.2627	1148.3138
12	1833.0848	1347.2850	1369.3555	1338	1650.4847	1257.6407	1313.4902	1659.2029	1298.2072	1168.3591
13	1837.8554	1374.6729	1406.3648	1378	1770.5301	1269.4655	1337.9457	1767.6480	1309.9798	1184.3088
14	1889.5793	1376.1386	1422.7910	1392	1833.6242	1348.4257	1379.8585	1888.8074	1374.6354	1348.3862
15	1895.2791	1426.2129	1491.5498	1451	1862.0255	1375.3538	1415.2113	1895.1594	1376.0552	1350.1473
16	1908.9366	1432.9691	1494.1528	1462	1892.3633	1414.8275	1475.4962	1908.9350	1432.9683	1405.0679
17	1917.0021	1433.5834	1499.4081	1464	1911.0449	1429.8859	1495.5279	1916.1495	1433.1805	1422.7455
18	1965.9111	1433.6414	1509.0365	1472	1923.1246	1433.6123	1502.0424	1960.7536	1433.3214	1491.1184
19	1991.8852	1455.6168	1515.3801	1476	1981.5624	1453.5816	1510.8227	1973.9382	1435.0417	1498.2997
20	2829.4751	2888.9245	3013.9862	2887	2140.8002	2159.2835	2237.7277	2144.3139	2142.9936	1508.3642
21	2829.5387	2897.6960	3014.6985	2887	2829.5067	2890.9130	3014.0343	2829.4396	2895.7061	2225.9348
22	2864.8661	2907.4242	3018.5641	2962	2864.0677	2903.4671	3016.7095	2829.6950	2897.6880	3014.6950
23	2928.6849	2931.8140	3034.3976	2967	2867.7599	2922.3180	3031.3726	2899.2754	2918.0661	3018.2585
24	2930.1024	2958.4968	3071.6452	2968	2929.0335	2931.8128	3045.7754	2928.5264	2958.4792	3025.1715
25	2931.0105	2959.2253	3081.2045	2968	2930.0352	2959.1896	3076.8782	2931.0054	2959.1787	3071.6369
26	2931.2744	2960.4246	3083.4092	2973	2931.0517	2959.4802	3081.6484	2931.0904	2959.7395	3081.2034
27	2932.3160	2961.0526	3084.0759	2977	2931.8757	2961.0206	3083.7942	2932.1337	2960.5053	3083.9920

References in the Appendix

Piasecki A., Sessions A., Peterson B. and Eiler J. (2016) Prediction of equilibrium distributions of isotopologues for methane, ethane and propane using density functional theory. *Geochim. Cosmochim. Acta* **190**, 1–12.

Shimanouchi, T. (1972) *Tables of Molecular Vibrational Frequencies Consolidated Volume I*; National Bureau of Standards: Washington, DC 126.

Chapter 3

Position-specific Distribution of Hydrogen Isotopes in Natural Propane: Effects of Thermal Cracking, Exchange Equilibration and Biodegradation

Xie H., Ponton C., Formolo M. J., Lawson M., Ellis G. S., Lewan M. D., Ferreira A. A., Morais E. T., Spigolon A. L. D., Sessions A. L. and Eiler J. M. (2020) Position-specific distribution of hydrogen isotopes in natural propane: Effects of thermal cracking, equilibration and biodegradation. Geochim. Cosmochim. Acta 290, 235–256. doi: 10.1016/j.gca.2020.09.009.

Abstract

Intramolecular isotope distributions, including isotope clumping and position specific fractionation, can provide proxies for the formation temperature and formation and destruction pathways of molecules. In this study, we explore the position-specific hydrogen isotope distribution in propane. We analyzed propane samples from 10 different petroleum systems with high-resolution molecular mass spectrometry. Our results show that the hydrogen isotope fractionation between central and terminal positions of natural propanes ranges from -102‰ to +205‰, a much larger range than that expected for thermodynamic equilibrium at their source and reservoir temperatures

(36-63‰). Based on these findings, we propose that the hydrogen isotope structure of catagenic propane is largely controlled by irreversible processes, expressing kinetic isotope effects (KIEs). Kinetic control on hydrogen isotope composition of the products of thermal cracking is supported by a hydrous pyrolysis experiment using the Woodford shale as substrate, in which we observed isotopic disequilibrium in the early stage of pyrolysis. We make a more general prediction of KIE signatures associated with kerogen cracking by simulating this chemistry in a kinetic Monte-Carlo model for different types of kerogens. In contrast, unconventional shale fluids or hot conventional reservoirs contain propane with an isotopic structure close to equilibrium, presumably reflecting internal and/or heterogeneous exchange during high temperature storage (ca. 100-150˚C). In relatively cold (<100 ˚C) conventional gas accumulations, propane can discharge from its source to a colder reservoir, rapidly enough to preserve dis-equilibrium signatures even if the source rock thermal maturity is high. These findings imply that long times at elevated temperatures are required to equilibrate the hydrogen isotopic structure of propane in natural gas host rocks and reservoirs. We further defined the kinetics of propane equilibration through hydrogen isotope exchange experiments under hydrous conditions; these experiments show that hydrogen in propane is exchangeable over laboratory time scales when exposed to clay minerals such as kaolinite. This implies rather rapid transfer of propane from sources to cold reservoirs in some of the conventional petroleum systems. Propane is also susceptible to microbial degradation in

both oxic and anoxic environments. Biodegradation of propane in the Hadrian and Diana Hoover oil fields (Gulf of Mexico) results in strong increases in central–terminal hydrogen isotope fractionation. This reflects preferential attack on the central position, consistent with previous studies.

1. Introduction

Natural propane and other volatile hydrocarbons in the subsurface are of great economic value and environmental significance. Compositional and stable isotope properties of these gases have been widely used to help trace their origins and fates (e.g., Berner and Faber, 1996; Whiticar, 1999). Recent studies of the intramolecular isotope structures of these gaseous compounds bring novel constraints to these processes (Stolper et al., 2014a; Wang et al., 2015; Young et al., 2017; Eiler et al., 2018; Piasecki et al., 2018; Clog et al., 2018; Xia and Gao, 2019). These new methods are revealing fundamental geochemical processes that control the geological distributions of hydrocarbons.

Propane (C_3H_8, or CH_3—CH_2—CH_3) has two chemically non-equivalent sets of atomic sites: the central CH_2 group and the terminal CH_3 groups. The carbon and/or hydrogen isotope differences between these two positions have been analyzed by GC-pyrolysis-GC-irMS (Gilbert et al., 2016; Li et al., 2018), biochemical degradation with GC-irMS

(Gao et al., 2016), high resolution direct molecular mass spectrometry (Piasecki et al., 2016a; Xie et al., 2018) and Nuclear Magnetic Resonance (Liu et al., 2018). It has been shown that site-specific isotopic measurements are able to differentiate abiotic propane sources from common thermogenic propane (Suda et al., 2017), track thermal maturation (Piasecki et al., 2018; Liu et al., 2019; Julien et al., 2020) and identify residues of subsurface microbial degradation (Gilbert et al., 2019). Position-specific hydrogen isotopes are especially interesting because hydrogen may undergo isotopic exchange at the conditions of some gas reservoirs, potentially driving propane to intramolecular hydrogen isotope equilibrium. The temperature dependence of equilibrium isotope fractionation between the central and terminal hydrogen positions has been theoretically predicted (Webb and Miller, 2014; Piasecki et al., 2016b) and experimentally calibrated (Xie et al., 2018). Therefore, position-specific hydrogen isotope distribution in propane can potentially work as a 'geothermometer' that could track the equilibration temperature at which propane has been generated and/or stored. And, because the approach to equilibrium may be time dependent, it is possible that site specific hydrogen isotope fractionation may serve as a kind of 'geospeedometer' for evaluating gas reservoir storage times. This kinetic property in the carbonate geothermometer has been shown to have significant value for constraining thermal histories of rock samples (e.g., Passey and Henkes, 2012; Shenton et al., 2015; Stolper and Eiler, 2015; Lawson et al., 2018; Mangenot et al., 2019; Ingalls, 2019). If such a property was demonstrated in propane, it

would provide an opportunity to assess the thermal histories of fluids that migrate within sedimentary systems.

In this study, we explore what controls the position-specific hydrogen isotope distribution in propane via natural observations and laboratory experiments. We present a dataset of measurements of propane from produced natural gases in 10 different, globally distributed petroleum systems. In addition, we report isotope exchange experiments and hydrous pyrolysis experiments designed to investigate the timescales and mechanisms of isotope exchange and the position-specific isotope effects of thermal cracking. Finally, we construct a model of the position-specific isotopic fractionations associated with kerogen cracking as a means of interpreting and extrapolating from laboratory cracking experiments. We show that the geochemistry of the source rock determines the primary position-specific hydrogen isotope signature in propane immediately after formation by kerogen cracking, that exchange in relatively hot reservoirs brings the position-specific hydrogen isotope structure of propane close to equilibrium, and that biodegradation in shallow reservoirs leads to distinctive central — terminal hydrogen isotope fractionations.

2. Samples

We examined natural gas samples from 18 different wells belonging to the following 10 petroleum fields: Diana Hoover (U.S. Gulf of Mexico), Galveston 209 (U.S. Gulf of Mexico), Genesis (U.S. Gulf of Mexico), Hadrian North and South (Gulf of Mexico), Hogsback (Wyoming, USA), Eagle Ford (Texas, USA), Briggs (Texas, USA), Santa Ynez Unit (SYU) (California, USA), Sleipner Vest (North Sea, Europe), and Potiguar basin (Brazil). Sampled well depths range from 1880 to 4618 meters with reservoir temperatures ranging from 42°C to 143°C.

All the gas samples come from conventional reservoirs (where gas migrated from the source rock is trapped in permeable formation) except those from the Eagle Ford shale (where gas is retained in the impermeable source rock). One of the samples from Eagle Ford (Las Raices 22H) and samples from Sleipner Vest and Hogsback are non-associated gases (free gas not dissolved in oil). The rest of our samples are oil-associated solution gases.

3. Methods

3.1. Nomenclature

The hydrogen isotope fractionation between central and terminal positions of propane (or, the ‘central—terminal fractionation’) can be expressed by the epsilon notation:

$$\varepsilon D_{C-T} = 1000 * \left(\frac{\left(\frac{D}{H}\right)_C}{\left(\frac{D}{H}\right)_T} - 1 \right), \quad (1)$$

where $\left(\frac{D}{H}\right)_C$ and $\left(\frac{D}{H}\right)_T$ are the hydrogen isotope ratios of the central and terminal positions, respectively. Neglecting the non-statistical distribution of multiply deuterated propane (a trivial contribution to overall D abundance in natural samples, e.g., a 10 ‰ enrichment in the doubly deuterated propane would only increase $\varepsilon D_{C\text{-}T}$ by 0.005‰), the above nomenclature is equivalent to the following function based on the concentrations of specific singly-deuterated isotopomers:

$$\varepsilon D_{C-T} = 1000 * \left(\frac{3[CH_3CHDCH_3]}{[CH_2DCH_2CH_3]} - 1 \right), \quad (2)$$

where 3 is the symmetry number ratio between CH_3CHDCH_3 and $CH_2DCH_2CH_3$. Note that D/H is synonymous to the $^2H/^1H$ nomenclature suggested by IUPAC (Dukov, 2007). We opt to use D instead of ^2H throughout this chapter for consistency with our previous publications.

3.2. Sample purification

Propane is generally a minor component (<5%) of natural gases and needs to be isolated prior to mass spectrometric analysis. We perform an initial purification via cryogenic distillation using a vacuum line consisting of calibrated volumes, cryogenic traps and a liquid-helium-cooled cryostat (CTI-Cryogenics and Janis Research Co.). Using a previously described protocol of cryostat cooling and warming cycles (Stolper et al., 2014b; Piasecki et al., 2016a) H_2, He, N_2 are pumped away and pure fractions of CH_4, and C_2H_6 are isolated. The residual fraction containing CO_2 and the series of $\geq C_3$ alkanes is transferred into a second glass vacuum line where CO_2 is removed by adsorption to an Ascarite II (NaOH-coated-silica) trap as described by Piasecki et al. (2016a). This refined gas fraction is collected in a pre-evacuated glass U-tube with a valve and polytetrafluoroethylene (PTFE) septum.

The final sample preparation step uses gas chromatography with cryogenic fraction collection to isolate propane from the remaining $\geq C_4$ alkanes. Samples for this study are prepared on a HP 5890 gas chromatograph instrument equipped with a Restek ShinCarbon packed column (ST 80/100, 2 mm ID, 1/8" OD, 2 m length). The gas sample is transferred from the glass u-tube into the GC injector (splitless) via gas-tight syringe (15-20 ml injections). Pure He at 30ml/min is used as the carrier gas and the GC oven was kept isothermal at 40 ^{o}C for 90 min. Under these conditions, the retention time for propane is 24.4 min. From 22-26 min after the sample injection all column gas flow is

diverted into a LN_2 trap to collect the purified propane. The LN_2 trap is then connected to the glass vacuum line and the propane transferred into a flame-sealed glass tube.

Piasecki et al. (2016a) tested the cryogenic separation and Ascarite II clean up with artificial mixtures of propane, ethane and CO_2. They concluded that both procedures are highly efficient (>97% recovery) and observed no carbon isotope fractionation of the purified propane when compared to the starting propane. We carried out additional tests using a laboratory reference gas mixture simulating a natural gas composition (80% C_1, 10% C_2, 5% C_3, and 5% CO_2) and found that the cryogenic separation and CO_2 adsorption procedures together have a recovery efficiency for propane of 93-103%. We observed no significant difference in molecular hydrogen isotope ratio between the starting propane and the final propane isolate. We conclude that this propane purification procedure is effectively quantitative and isotopically non-fractionating.

Upon analysis, each sample is carefully examined for contamination via a wide-range mass scan on a double focusing sector mass spectrometer (the Thermo Scientific DFS described below). The most common contaminants are butane ($C_4H_{10}^+$ at m/z=58.0777), ethane ($C_2H_6^+$ at m/z=30.03017) and CO_2 (m/z=43.98943). We consider a propane sample gas to be clean when ion beams corresponding to each of the contaminants are less than 1% of that for propane, which has been tested in Piasecki et al. (2016a). In cases

where severe contamination is identified, we either repeat the cryogenic and CO_2 cleanup procedures (above) until the gas is nominally pure or discarded the sample.

3.3. Measurements

3.3.1. Position-specific hydrogen isotope analysis

We analyze purified propane samples for their position-specific hydrogen isotope ratios on the Thermo Scientific Double Focusing Sector (DFS) mass spectrometer. Propane gases are introduced to the ion source through the bellows and metal capillaries of a dual-inlet system adapted from a Thermo Scientific Delta Plus IRMS. All sample measurements are made by sample/standard bracketing, referenced to an intra-laboratory working gas, CITP-1. CITP-1 has a δD of -179‰ and $\varepsilon D_{C\text{-}T}$ of -26‰ (Xie et al., 2018). The DFS can render very high mass-resolution ($M/\Delta M$ ~ 80-100,000), though we operate it at resolutions of 35,000 (full-width half-maximum definition) for propane analysis.

Each sample measurement examines two isotopologue ratios, $[C_2H_4D]/[C_2H_5]$ (i.e., the D/H ratio of the C_2H_5 fragment ion) and $[C_3H_7D]/[C_3H_8]$ (the D/H ratio of the full molecular ion), to constrain position-specific hydrogen isotope distribution. Each isotope ratio measurement is made using either of two mass-spectrometric methods: electric scan or multiple ion detection (MID). In an electric scan analysis, we vary the accelerating

voltage across a narrow range to rapidly scan the isotopologue ions of interest across the single detector. We derive the peak areas of each isotopic species by fitting the shape and height of the resulting mass spectra (i.e., a plot of intensity vs. mass) and use them to calculate isotopologue ratios. In an MID analysis, the magnet current is repeatedly jumped to translate two or more ion beams into positions where they intercept the detector, and the intensity ratios of these measurements constrain the abundance ratios of the species of interest. Both $[C_2H_4D]/[C_2H_5]$ and $[C_3H_7D]/[C_3H_8]$ ratios can be determined directly by this method.

Because an electric scan examines only a narrow mass range (~0.1 AMU), it is capable of constraining $[C_2H_4D]/[^{13}C^{12}CH_5]$ but not $[C_2H_4D]/[C_2H_5]$, and similarly constrains $[C_3H_7D]/[^{13}C^{12}C_2H_8]$ but not $[C_3H_7D]/[C_3H_8]$. For this reason, electric-scan data can be interpreted as constraints on the site-specific hydrogen isotope structure only when combined with independent constraints on the ratios: $[^{13}C^{12}CH_5]/[C_2H_5]$ and $[^{13}C^{12}C_2H_8]/[C_3H_8]$. In two samples, we combined $[C_2H_4D]/[^{13}C^{12}CH_5]$ and/or $[C_3H_7D]/[^{13}C^{12}C_2H_8]$ ratios measured by electric scan with $[^{13}C^{12}CH_5]/[C_2H_5]$ and/or $[^{13}C^{12}C_2H_8]/[C_3H_8]$ ratios measured for the same gases from Piasecki et al. (2018). In another four samples, we combined $[C_2H_4D]/[^{13}C^{12}CH_5]$ and $[C_3H_7D]/[^{13}C^{12}C_2H_8]$ ratios measured by electric scan with $[^{13}C^{12}CH_5]/[C_2H_5]$ and $[^{13}C^{12}C_2H_8]/[C_3H_8]$ ratios measured by MID method (above). Data for the rest of the samples are acquired by MID

method directly. Specific methods for data acquisition of each sample are labeled in Table 3-1.

Regardless of the mass spectrometric method used, we typically prepare 50 μmol of propane for each sample. Acquisition of either [C_2H_4D]/[C_2H_5] and [C_3H_7D]/[C_3H_8] ratios lasts 1 hour, achieving a standard error of around 1‰ (Table 3-1). $\varepsilon D_{C\text{-}T}$ is calculated from constraints on [C_2H_4D]/[C_2H_5] and [C_3H_7D]/[C_3H_8] ratios using the data processing methods detailed in Xie et al. (2018).

Table 3-1: Position-specific hydrogen isotope measurement results for natural gas samples analyzed in this study. $\delta D_{molecular}$ and δD_{ethyl} are the hydrogen isotope values of the molecular ion and the ethyl fragment, respectively, normalized to those of the reference gas (CITP-1). GOM= Gulf of Mexico. MID= multiple ion detection.

Sample	Basin	Well	$\delta D_{molecular}$	error	Method	δD_{ethyl}	error	Method	$\varepsilon D_{C\text{-}T}$	error
SD1	Diana Hoover-GOM	SD1	81.2	0.7	MID	106.3	1.7	MID	108.0	10.2
DB2	Diana Hoover-GOM	DB2-ST4	72.2	1.8	MID	111.6	3.0	MID	205.3	18.4
Las Raices 21H	Eagleford	Las Raices 21H	100.5	1.3	MID	118.1	1.1	MID	58.7	9.4
IS1H_R	Eagleford	Irvin South	82.1	1.1	E-scan+Piasecki	91.0	1.7	E-scan+Piasecki	6.1	11.6
GI-BD7	Galveston Island-GOM	BD7	76.3	0.7	MID	105.4	1.6	MID	135.0	9.2
GenA12_ST4_R	Genesis-GOM	5909 A12 ST4	72.9	0.6	MID	84.3	0.8	MID	22.2	5.6
GenA15_ST1	Genesis-GOM	5909 A15 ST1	64.1	0.8	MID	93.8	0.9	MID	141.5	6.4
KC919	Hadrian-GOM	Hadrian-6	78.7	0.9	MID	97.4	1.3	MID	67.5	8.6
KC5499_R	Hadrian-GOM	Hadrian-2	109.1	0.8	MID	139.6	0.6	MID	138.0	5.1
KC5500_R	Hadrian-GOM	Hadrian-2	123.1	0.7	MID	165.2	1.8	MID	209.9	9.7
H68-23	Hogsback	H68-23	7.5	1.6	MID	15.7	1.3	MID	5.6	12.1
PT-2	Potiguar		53.9	1.6	E-scan+Piasecki	45.0	1.0	E-scan+Piasecki	-101.9	11.5
B17-T2	Spleipner Vest	15/19 B17	47.7	1.1	E-scan+MID	63.1	1.5	E-scan+MID	49.2	10.6
B14-T2	Spleipner Vest	15/19 B14	51.0	0.8	MID	69.1	2.2	E-scan+MID	66.6	13.7

B1-T1-A1r	Spleipner Vest	15/19 B1	50.7	1.3	MID	71.4	1.9	E-scan+MID	83.8	13.2
5A-5L	SYU-Pescado	HE024	23.7	1.1	MID	28.4	1.4	E-scan+MID	-17.9	10.9
Holcomb 6	Briggs	Holcomb 6	86.4	0.9	MID	101.5	1.2	MID	44.2	8.1
McGee 4_R	Briggs	Scott McGee 4	114.3	0.7	MID	141.3	0.9	MID	115.2	5.9

3.3.2 Gas compositional analysis and compound-specific isotope analysis

A separate split of each gas sample was sent to Stratum Reservoir Services (formerly Isotech Laboratories) in Champaign, Illinois for both molecular compositional analysis and compound-specific isotope analysis ($\delta^{13}C$ and δD). For molecular compositional analysis, gas samples were injected into a GC system equipped with both thermal conductivity detector and flame ionization detector. Relative precision was typically ±5% relative for C_1-C_3 hydrocarbon abundance and ±10% relative for C_4-C_5 hydrocarbon abundance.

A gas-chromatography pyrolysis isotope-ratio mass spectrometer (GC-P-IRMS) system was used for δD analysis. In a GC-P-IRMS, gas mixtures were separated by the GC and pyrolyzed to H_2 for D/H ratio measurement with an IRMS. Typical precision for these analyses is ±5‰. We report δD values vs. the Vienna Standard Mean Ocean Water (VMOW) standard. A gas-chromatography combustion isotope-ratio mass spectrometer (GC-C-IRMS) system was used for $\delta^{13}C$ analysis. The GC system separates the individual hydrocarbons that are then combusted by a cupric oxide furnace into CO_2 for $^{13}C/^{12}C$ ratio measurement with an IRMS. Typical precision for these analyses is ±0.3‰. We report $\delta^{13}C$ values vs. the Vienna PeeDee Belemnite (VPDB) standard.

3.3.3 Methane clumped isotope analysis

For each gas sample, a separate aliquot is taken and cryogenically purified to recover methane, which was then measured for Δ_{18} on the prototype 253 Ultra at Caltech (Eiler et al., 2013). Gas purification and handling protocols, mass spectrometry methods, and protocols for data standardization follow Stolper et al. (2014b).

3.3.4 Well temperature measurements

A borehole temperature is measured at each natural gas well using standard petroleum-industry methods. However, the measured temperature is usually colder than actual formation temperature, due to invasion of drilling fluid. During drilling the borehole temperature reaches steady state in which cooling effects of the drilling fluid are balanced by the heat flow from the surrounding warmer formation. Therefore, we apply the Horner correction (Dowdle and Cobb, 1975) to raw measured bore-hole temperatures, or a 10°C increase when the Horner correction is not available.

3.4. Pyrolysis experiments

Hydrous pyrolysis can simulate formation of petroleum from source rock, as well as effects of maturation and expulsion (Lewan et al., 1979; Lewan, 1985; Lewan, 1997; Lewan and Ruble, 2002; Spigolon et al., 2015). In this study, hydrous pyrolysis experiments were done at the United States Geological Survey in Denver, Colorado. The experimental equipment, starting materials and protocols have been previously described in detail by Stolper et al. (2014a) and Piasecki et al. (2018). Briefly, an organic rich sample from the Woodford Shale was heated under a helium environment. The shale was heated stepwise at 330, 360, 390, and 415°C for 72 hours at each temperature to simulate maturation. Mixed gases were sampled at each temperature. Experimental procedures followed Lewan (1997). We extracted and analyzed propane from these mixed gas samples with the same methods in sections 3.2. and 3.3.1.

3.5 Isotope exchange experiments

In isotope exchange experiments, we incubated propane (CITP-1) with a deuterium source that is either deuterated water (diluted to $\delta D = 11419 \pm 31$ ‰) or $CH_3CD_2CH_3$ ('propane 2,2-D2, 98%' from Cambridge isotope laboratory), in the presence of one of three catalytic substrates described below. In the hydrous experiments, we prepared 50–70 μmol of propane, 500-600 μmol of D_2O and 40-60 μg of catalysts in each 1-2 ml Pyrex® tube. In the anhydrous experiments, the deuterated water is replaced with pre-

mixed 170 ppmv of $CH_3CD_2CH_3$ into CITP-1. The three catalytic substrates were kaolinite (from Wards Natural Science Establishment Inc.), montmorillonite (from Clay Minerals Society, University of Missouri; detailed in Sessions et al. (2004)) or pulverized Green River Shale powder. Prior to each experiment, the substrate clay minerals were heated by torch flame (est. 500–600 °C) under vacuum for 10 mins to remove any adsorbed gas. The organic-rich Green River Shale powder was heated only with a heat gun at 100-150°C under vacuum to prevent thermal degradation of organic matter. Each sealed Pyrex tube containing propane ± water + catalyst was then heated at a constant temperature (160 or 200 °C) in a resistance-heated furnace, for hours to weeks. After incubation, tubes were quenched in liquid nitrogen and then thawed and opened to a glass vacuum gas line. Propane was passed through a dry ice-ethanol trap (-72°C) to remove remaining water vapor and then condensed in a second glass tube at -196°C (immersed in liquid N_2). This second tube was then analyzed on the DFS mass spectrometer as described above.

4. Results

Table 3-1 lists the position-specific hydrogen isotope compositions and Table 3-2 lists other geochemical data for the studied propane samples. $\delta^{13}C$ values of propane range from -34.8 to -22.7‰ and δD values of propane from -169 to -74‰. Gas dry ratios

($C_1/(C_2+C_3)$) range from 1.4 to 76. These relatively wide ranges in composition reflect the diverse source kerogens and maturities of these gases. Note that we report two independent measurements of molecular-average δD: one based on our direct mass spectrometric measurement of the molecular ion and one based on compound-specific GC-P-IRMS. These data are consistent with one another within their respective external errors (Figure 3-A1). The $\delta^{13}C$ and δD values of methane in the sample gases indicate that most are thermogenic in origin (Figure 3-1). Exceptions are gases from the Diana Hoover, Hadrian and Genesis wells (all from the Gulf of Mexico), which might contain a component of microbial methane (see supporting data and discussions in Thiagarajan et al., 2020a, b). Theses samples' compound-specific carbon isotope patterns of C1-C5 alkanes (i.e., methane through pentanes) show negative anomalies of methane's $\delta^{13}C$, which also support contribution of microbial methane (Figure 3-A2).

The central-terminal hydrogen isotope fractionation in propane from subsurface reservoirs displays a very wide range, from -102 to +205‰. This is 11 times larger than the range of equilibrium isotope effects at the temperatures of gas generation and storage in conventional reservoirs (estimated central—terminal fractionations of +36 to +63‰; Webb and Miller, 2014, Xie et al., 2018). The observed range is also much greater than previously studied gases from the Woodford shale, Eagle Ford shale, and Spraberry Formation of Permian Basin (Liu et al., 2018; Liu et al., 2019; Zhao et al., 2020). Samples from the Gulf of Mexico (Diana Hoover, Hadrian North and South, Genesis,

Galveston) have the most positive central-terminal hydrogen isotope fractionations, whereas a sample from the Potiguar Basin has the most negative central-terminal hydrogen isotope fractionation.

Table 3-2: Compound-specific isotope compositions and other geological and geochemical information of natural gases analyzed in this study.

Sample	Basin	Well	Well T °C	% C3	Gas type	Δ_{18}	error	C1/(C2+C3)	$\delta^{13}C_{C1}$	δD_{C1}	$\delta^{13}C_{C2}$	δD_{C2}	$\delta^{13}C_{C3}$	δD_{C3}	Gas isotope maturity R_0 %
SD1	Diana Hoover-GOM	SD1	59	2.04	Conventional oil associated	5.34	0.25	15.68	-56.6	-203.2	-28.8	-122.6	-26.6	-116	1.5
DB2	Diana Hoover-GOM	DB2-ST4	54	1.88	Conventional oil associated	4.86	0.24	17.10	-53.7	-195.0	-28.9		-26.5		1.5
Las Raices 21H	Eagleford	Las Raices 21H	143	4.05	Unconventional non-associated	2.52	0.23	5.28	-40.7	-181.3	-24.6		-22.7		2.4
IS1H_R	Eagleford	Irvin South	141	5.32	Unconventional solution gas	2.39	0.22	4.34	-47.4	-260.1	-32.2		-29.3		1.0
GI-BD7	Galveston Island-GOM	BD7	89	0.761	Conventional solution gas	3.59	0.39	25.45	-41.8	-164.7	-26.5	-128.9	-24.7	-118	1.9
GenA12_ST4_R	Genesis-GOM	5909 A12 ST4	79	4.41	Conventional solution gas	5.73	0.25	8.19	-63.2	-204.9	-33.3	-158.2	-29.6	-128	0.9
GenA15_ST1	Genesis-GOM	5909 A15 ST1	66	4.33	Conventional solution gas	4.09	0.25	7.12	-54.7	-209.1	-31.6	-150.0	-28.0	-122.7	1.1
KC919	Hadrian-GOM	Hadrian-6	64.4	7.88	Conventional solution gas	4.14	0.25	3.20	-55.6	-247.7	-40.5	-160.1	-32.0	-117.6	0.4
KC5499_R	Hadrian-GOM	Hadrian-2	48.3	0.471	Conventional oil associated	5.56	0.24	77.58	-58.0	-178.3	-39.7		-28.8		0.4
KC5500_R	Hadrian-GOM	Hadrian-2	42.2	1.067	Conventional oil associated	5.98	0.26	42.86	-60.4	-177.0	-40.4		-30.2		0.4
H68-23	Hogsback	H68-23	100	3.12	Conventional non-associated	3.26	0.36	9.20	-36.9	-185.7	-31.0	-178.9	-28.7	-166.9	1.2
PT-2	Potiguar		71	18.2	Conventional oil associated	3.03	0.27	1.42	-48.3	-206.8	-38.0	-196.3	-34.8	-134.9	0.5
B17-T2	Spleipner Vest	15/19 B17	121	4.64	Conventional non-associated	2.64	0.25	5.57	-39.9	-217.3	-28.0		-27.0		1.6
B14-T2	Spleipner Vest	15/19 B14	123	4.27	Conventional non-associated	2.68	0.25	5.97	-39.8	-221.0	-28.7		-27.1		1.5
B1-T1-A1r	Spleipner Vest	15/19 B1	123	18.2	Conventional non-associated	2.21	0.25	5.50	-40.9	-230.9	-29.1		-27.3		1.4
5A-5L	SYU-Pescado	HE024	105	4.23	Conventional solution gas	2.69	0.25	7.26	-38.3	-175.0	-31.3		-28.4		1.1
Holcomb 6	Briggs	Holcomb 6	120	3.62	Conventional non-associated	2.98	0.25	8.41	-44.0	-181.8	-27.9	-121.0	-25.7	-113.1	1.6
McGee 4_R	Briggs	Scott McGee 4	93	1.58	Conventional non-associated	3.15	0.30	14.42	-40.3	-160.6	-25.2	-110.4	-23.1	-100.3	2.2

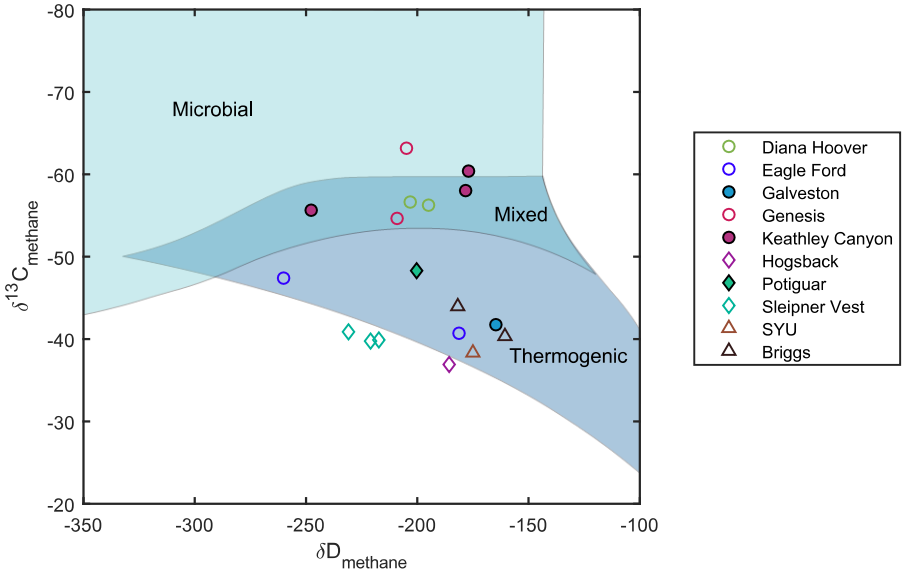

Figure 3-1: Isotopic composition of methane from natural gases examined in this study. δD is on VSMOW scale and $\delta^{13}C$ is on VPDB scale. Categorization areas are based on Whiticar (1999). Errors for these analyses are typically 0.3‰ for $\delta^{13}C$ and 3–5‰ for δD.

5. Discussion

5.1 Magnitude of fractionation

The wide range of central-terminal hydrogen isotope fractionation in propane indicates that isotope effects associated with irreversible, kinetically (rather than thermodynamically) controlled processes are common influences on propane hydrogen

isotope distribution and site-specific structure. Plausible contributing processes include thermal ‘cracking’ of propane precursors, destruction of propane during secondary cracking or biological consumption, transport (e.g., by diffusion), or phase transformations (e.g., ‘flashing’ of dissolved gases). Transport is not likely the key source of this signal because gas phase diffusion has been shown to fractionate carbon isotopes with no positional preference (Piasecki et al., 2016a), hence not changing ε values. This does not rule out condensed phase position–specific diffusive fractionations and hydrogen isotope effects (either in the vapor or condensed phase), but suggests that these processes are very unlikely to explain much, if any, of the several 100 ‰ range in site specific fractionation we observe. Phase change is also unlikely the cause for such a strong signature because D/H vapor-pressure isotope effects (VPIE) of similar hydrocarbon gases tend to be small. For example, D/H VPIE of ethane is only 10‰ at -73°C (Van Hook, 1966) and that of neopentane is only 7‰ at 9°C (Höpfner, 1969). We suspect that the VPIE for propane at reservoir temperatures will be smaller than these, making it negligible.

Despite the large observed range in position specific D/H ratio and diverse processes that may have contributed to it, subsets of the samples examined in this and previous studies are at or close to thermodynamic equilibrium with respect to their central-terminal hydrogen isotope fractionations (Figure 3-2). In some cases, this may be fortuitous, but this finding is sufficiently common and correlated with reservoir temperature (below) that

we think it is also plausible that it reflects equilibration through intra- or intermolecular hydrogen isotope exchange. The following sections further detail the role of each of several processes we hypothesize have contributed to observed position-specific hydrogen isotope fractionations in our sample set.

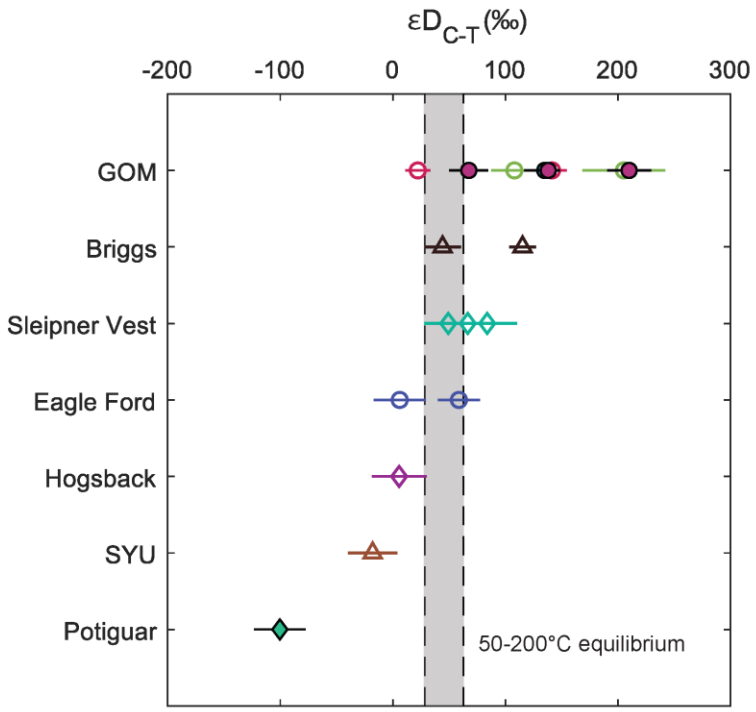

Figure 3-2: Central-terminal differences of D/H in natural propanes from this study. Error bars show 2 standard error of sample analysis. The coloring scheme in this figure is consistent with other figures in this chapter. GOM= Gulf of Mexico.

5.2 Effects of catagenic formation of propane

With exception of the occurrence of Fischer-Tropsch type ('FTT') synthesis of hydrocarbons in hydrothermal systems (e.g., Charlou et al., 2000; Proskurowski et al., 2008) and rare reports of anaerobic microbial production of ethane and propane in pore water (Hinrichs et al., 2006), it is accepted that subsurface hydrocarbon molecules larger than methane are generally derived from the thermal alteration of sedimentary organic matter under catagenic conditions (Peters et al., 2004). The isotopic structure of propane formed in this manner must reflect the intramolecular isotopic patterns of the parent molecules superposed by kinetic isotope effects associated with catagenic reactions (at least, immediately after formation and prior to any subsequent exchange or secondary 'cracking').

The formation of thermogenic hydrocarbons is believed to begin with thermally activated rupture of carbon-carbon and carbon-hydrogen bonds in macromolecular kerogen or higher order hydrocarbons (Ungerer, 1990; Savage, 2000; Xiao, 2001). In this scenario, the D/H ratios of hydrogen atoms adjacent to the carbon or carbons that participated in this bond cleaving event will be lower, on average, than those in the unreacted precursor

due to kinetic isotope effects (i.e., assuming the chemical kinetics involved follows patterns of 'normal' kinetic isotope effects rather than inverse isotope effects, such as those associated with sp3-sp2 reactions). Most earlier studies of the isotopic effect associated with catagenic gas generation (Chung et al., 1988; Tang et al., 2000) assume that cleavage of an n-alkane precursor (or, equivalently, an n-alkyl chain in macromolecules) dominates small alkane generation, leading to isotopic depletion in the terminal position of the product propane relative to the central position. However, macromolecular substrates (kerogen or bitumen) can have a large variety of structural components, such as hetero-atoms (N, O and S;), branched and cross-linked chains, aromatic and non-aromatic rings with alkyl chains connected to them (Burlingame and Simoneit, 1968; Curry and Simpler, 1988; Kelemen et al., 2007; Vandenbroucke and Largeau, 2007; Gao et al., 2017). In the cleavage of isoprenoid structures of kerogen, it can be speculated that propane could potentially be generated via bond breaking at the central position (i.e., forming an isopropyl radical), making the central position of the product ^{13}C and D depleted. Such patterns have also been observed, both in this work and past studies (Piasecki et al., 2018; Liu et al., 2019).

It is challenging to make quantitative predictions of the intramolecular isotope fractionations associated with propane formation by catagenesis of kerogen. One of the biggest hurdles is defining the diverse possible elementary reaction steps, reaction pathways and intermediate products. Peterson et al. (2018) introduced the kinetic Monte-

Carlo (kMC) method to approach a simplified version of this problem — homolytic cleavage of C-C bonds in initially isotopically homogeneous n-C_{20} alkane. Here we present a conceptually similar but more complex kMC model to describe the position-specific isotope distribution in propane produced from various types of macromolecular kerogens and oil mixtures. Note that we explore the kMC model in greater depth in Chapter 6 of this thesis. The parent substrates we considered include two sets of model kerogens: One set includes Type I, Type II and Type III kerogens (Ungerer et al., 2015) where each is described by a relatively small and structurally simple unit cell (200-350 carbon atoms each). It also includes four type II kerogen models of different maturity levels. The second set of model kerogens were created to describe the source kerogens of specific economically significant petroleum systems, including the Eagle Ford Shale, the Marcellus Shale, and a Middle East Shale (Bousige et al., 2016). These latter models have 4000-9000 carbon atoms per kerogen unit cell. In addition to these model kerogens, we also created models that describe catagenic cracking of n-alkanes and branched alkanes, which were mixed to mimic crude oil, and a molecular model of pure pristane to represent an isoprenoid endmember. Models of these simple molecules illuminate the relationships between molecular structure of reactants and isotopic structures of products.

We constructed a kMC model for each model substrate. Each model simulates an idealized reaction network that results from the thermal breakdown of precursors, as well as further breakdown of intermediate products (i.e., we describe both primary catagenesis

of bonds in the initial precursor and secondary catagenesis of the primary products). Each simulation starts with many units of the parent molecule, such that the model system contains more than 100,000 C atoms. Isotope substitution (^{13}C and D) is randomly populated across these molecules. In doing so, we assume that each position of the precursors has uniform stable isotope ratios. However, this might not be realistic, and the possible implications of this assumption are discussed later in this section. The system then goes through a multi-step bond cleavage process. In each step, the model randomly chooses one of bonds that are enabled to react (here we consider only homolytic cleavage of single bonds: C-C, C-N, C-O and C-S). The probability of choosing a given bond for cleavage is given by the rate for that particular bond (based on its structural position and the isotope effect if a ^{13}C or D is present) normalized by the sum of all events' rates. The rate of a bond-rupture event is based on the chemical type of the bond, determined for each using similar types of reactions that have been calculated by the RMG-Py rate rules from the Reaction Mechanism Generator (Gao et al., 2016). In the next step, we modify the reaction rates of bonds influenced by ^{13}C and/or D with KIEs. We use KIE values from previous ab initio calculations (Tang et al., 2000; Tang et al., 2005). We neglect tertiary or higher order KIEs for carbon and quaternary or higher order KIEs for hydrogen. The temperature of simulation is set at 180°C. The referenced values of KIEs are tabulated in Table 3- A1. The reaction process is propagated until 20% of the original single bonds are broken. During this process, the cleaved parts of the molecules remains

in the pool for iterative bond-breaking selections, therefore ‘secondary cracking’ of the intermediate products is allowed. At the end of each simulation, we count the number of produced propane molecules, and assess the proportions of its isotopomers. The precision of each isotope ratio increases with the number of the repetitions of the simulation. Typically, we run 10,000 to 200,000 simulations on each parent (depending on when the results converge to within 0.5 ‰ standard error in the D/H ratio of each site of product propane). The computer codes are written in Python and MATLAB and executed on the Caltech High Performance Cluster. This model is open source, available at https://github.com/1995123xh/kMC.

To simplify the chemistry and lower the computational demand, it is assumed that each radical formed by single bond dissociation is quenched by capping with an H atom immediately after the bond-breaking step. The isotopic signature of this H atom is set to be the average D/H produced by breaking the C-H bonds in the substrate, considering the primary KIE associated with C-H scission. This KIE is set equal to the reduced partition function ratio of the C-H bond (Wang et al., 2009). This is a substantial simplification of the real radical chemistry happening in organic matter, recognizing that there are also other reactions, such as radical propagation reactions, radical decomposition reactions and radical termination reactions without H radicals. We note that such simplifications could cause errors such as unrealistically high $\delta^{13}C$ values of C2+ alkanes at high

conversion ratios (Peterson et al., 2018). These other reactions might affect the carbon and hydrogen isotope composition of propane and need to be further explored.

In each simulation, we initiated precursors with uniform probability of isotope substitution across molecules. However, it has been widely expected and observed that biomolecules have non-stochastic intramolecular carbon and hydrogen isotope distribution (Abelson and Hoering, 1961; Monson and Hayes, 1982; Rossmann et al., 1991; Gilbert et al., 2012; Romek et al., 2015; Ehlers et al., 2015; Robins et al., 2017). Therefore, it is likely that sedimentary organic matter would have similarly non-even hydrogen isotope distributions. However, to our knowledge there is no sufficiently complete description of isotope distributions in organic structures of the size and complexity of kerogens. It is also questionable how much of this signature of the starting material can be transferred to the products (like propane), as the radical chemistry of thermal cracking involves random dissociation and re-combinations that tend to erase such biases. In order to explore the inheritance effects of isotopic structure, we experimented with an odd-even alternative pattern in n-alkanes that has been suggested to originate from biosynthesis of fatty acids (Monson and Hayes, 1982; Hayes, 2001; Gilbert et al., 2013). We initiated n-heptadecane with the even-numbered positions (2, 4, 6, …, 16) more enriched in D than the odd-number positions (1, 3, 5, …, 17) by 100 ‰. The propane product from cracking of n-heptadecane with this odd-even effect has $\varepsilon D_{C\text{-}T}$ value of 439‰, comparing to 392‰ when cracking n-heptadecane with homogeneously

distributed D in molecules. The difference is greater than the statistical error of simulations, and resolvable by our current instrumental precision. However, it is still second-order compared to the large effect of cracking reactions. In this example, the KIEs associated with radical initiation still dominates the position-specific hydrogen isotope signal in propane (though it remains true that inheritance of isotopic structures of precursors by products is a high priority for future study).

The propane produced by these simulations encompasses the range in position-specific hydrogen isotope structures we observe in natural samples (Figure 3-3 and Table 3-3). Overall the central-terminal difference in εD in propane is predicted to be positive for most source substrates, except for that sourced from pristane or the over-mature Type II kerogen model from Ungerer et al. (2015). Propane from pristane cracking is the most D-depleted in the central position. Propane from the oil cracking model is very D-enriched in the central position. Since oil in this model has a high abundance of *n*-alkanes, this contrast most likely reflects the difference between breaking straight chains and methyl-branched chains (isoprenoid structures). The cleavage of straight chains to generate propyl radicals always happens at a C-C bond that will place one of the reacted C sites (and its attached hydrogens) at the terminal position, but methyl-branched chains can often cleave in such a way that the reacted C site ends up in the central position of a propyl product. The model thus shows that molecular structure of the parent material exerts an important influence over the intramolecular isotope distribution of its products.

A plausible way of generating propane with D-depletion in the central position is by cracking precursors enriched in methyl-branched aliphatic chain structures.

Propane hydrogen isotope structures predicted by most of the kerogen models (8 of 9) are higher in $\varepsilon D_{C\text{-}T}$ than natural samples observed, in most cases by 200‰ or more. We consider several possible explanations for these discrepancies. First, they could be attributed to potential deficiencies of the kerogen models, such as under-representation of branched aliphatic structures. For example, a previous study simulated infrared spectra of all the larger kerogen models and the Type-I and Type-II smaller kerogen models used in this study, and found that the computed spectra are all in major disagreement with direct FTIR observations of the kerogens from the Mancos, Woodford, and Marcellus (directly described by one of the larger models) shales (Weck et al., 2017). The mismatch is likely attributable to inaccurate construction of functional groups or carbon backbones in the theoretical models. Second, isotopic discrepancies might reflect limitation of the model treatment of catagenetic chemistry. For example, it was suggested that beta-scission rather than homolytic cleavage can play an important role in hydrocarbon decomposition (Xiao, 2001). Besides thermal cracking, alternative mechanisms such as transition-metal catalysis (Mango et al., 2010) or sulfur radical catalysis (Lewan, 1998) have also been proposed to be responsible for short-chain hydrocarbon generation. These mechanisms could have isotope fractionations that differ from those of homolytic cleavage. Third, intra- or intermolecular hydrogen exchange of propane after its formation could erase the

primary KIE signature. It is possible that propane in most natural gases is subject to some level of hydrogen isotope exchange. Finally, yet importantly, the discrepancy might be due to sampling bias in our selection of kerogen model structures. We are limited by both the number of molecular models that exist and the sizes of those models, which are to some extent limited by computational resources. Future work exploring this technique needs to address these issues.

Table 3-3: Results of the kinetic Monte Carlo model for various molecular model inputs.

precursor	**source**	**Size(C atoms)**	**$\varepsilon D_{C\text{-}T}$**	**$\varepsilon^{13}C_{C\text{-}T}$**
pristane		19	-193	-1.7
oil		2206	326	10.0
kia*	Ungerer et al. (2015)	251	293	6.9
kiia	Ungerer et al. (2015)	252	417	9.9
kiib	Ungerer et al. (2015)	234	378	7.0
kiic	Ungerer et al. (2015)	242	304	7.2
kiid	Ungerer et al. (2015)	175	-31	-3.6
kiiia	Ungerer et al. (2015)	233	345	10.4
Eagle Ford Shale	Bousige et al. (2016)	3849	339	8.7

Middle East Shale	Bousige et al. (2016)	3995	303	8.5
Marcellus Shale	Bousige et al. (2016)	5160	235	5.2

*kia refers to the type I kerogen model in Ungerer et al. (2015). kiia, kiib, kiic, and kiid refers to the four type II kerogen models in Ungerer et al. (2015), ordered from least to most mature. kiiia refers to the type III kerogen model in Ungerer et al. (2015).

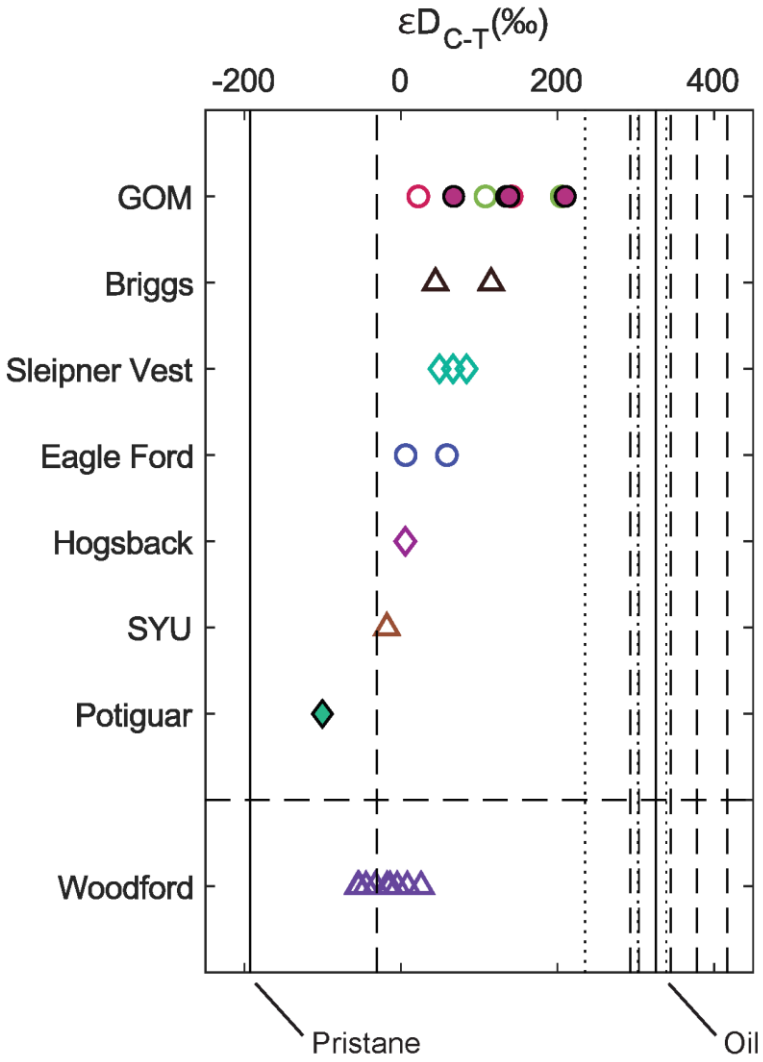

Figure 3-3: Comparison of kinetic Monte-Carlo model outputs with natural propane data. Dashed lines show results of the small kerogen models (Ungerer et al., 2015), dotted lines show results of the big kerogen models (Bousige et al., 2016) and solid lines show results

from pristane and oil. Propane isotope data of the Woodford shale is from Liu et al. (2019). GOM: Gulf of Mexico.

On the other hand, natural gas accumulations often represent a mixture of gas from multiple stages of charging, which might originate from different types of source kerogen and different thermal maturities. Unlike the clumped isotope signatures that show a non-linear anomaly associated with mixing isotopically distinct endmembers (Eiler, 2007), site-preference signatures tend to mix linearly (e.g., Piasecki et al., 2016a). Therefore, the position-specific hydrogen isotope composition of propane is expected to reflect a weighted average value of the accumulated gas; in some cases this could significantly impact the interpretation of gas measurements, .e.g., if a gas is a mixture of two end members, one from type II kerogen and one from type III kerogens (e.g., Dai et al., 2004), as these end members might differ in propane hydrogen isotope site preference.

5.3 Exchange and equilibration

It has previously been suggested that alkyl hydrogen can be susceptible to isotopic exchange over geological timescales under natural conditions (e.g., Sessions et al., 2004; Schimmelmann et al., 2006). Isotope exchange for both positions of propane with some

common pool, such as H_2O or other hydrocarbons should drive intramolecular hydrogen isotope fractionation towards thermodynamic equilibrium. Alternatively, propane may equilibrate its hydrogen isotope structure by intramolecular exchange between the CH_2 and CH_3 groups.

Previous studies have shown that certain reduced metals (e.g., Ni, Pd, Pt) and activated metal oxides such as Al_2O_3 can catalyze hydrogen isotope exchange of propane with or without D_2 gas, with apparent activation energies in the range of 30-90 kJ/mol (Sattler, 2018; Xie et al., 2018). And, in the absence of such solid catalysts, radical chain reactions, such as H-transfer reactions (e.g., Ungerer, 1990), could promote hydrogen exchange among coexisting alkanes at relatively high thermal maturation. But there is very little knowledge of the rates and conditions of hydrogen isotope exchange for propane, especially when water is present. To better quantify the exchangeability of hydrogen in natural propane, we conducted both hydrous and anhydrous hydrogen isotope exchange experiments on several substrates, including kaolinite, montmorillonite, and pulverized Green River shale powder (Table 3-4).

Table 3-4: Results of the isotope exchange experiments in this study. $\Delta\delta D$ is isotopic change of molecular/ethyl δD relative to the starting material. The ranges of exchanged halftime were calculated following the exchange kinetics expressed in $e^{-kt}=(F_e-F_t)/(F_e-F_0)$

(Sessions et al., 2004) using $\Delta\delta D_{molecular}$. All measurements here are made with the electronic scan method.

Catalysts	State	Temperature(°C)	Time(d)	$\Delta\delta D_{molecular}$	error	$\Delta\delta D_{ethyl}$	error	Estimated exchange halftime
Kaolinite	hydrous	200	7	4.0	1.6			20-83 yr
	hydrous	200	14	4.4	1.8			
	hydrous	160	21	1.8	3.0			>70 yr
Montmorillonite	hydrous	200	7	-2.3	1.7	-1.0	1.3	∞ yr
	anhydrous	200	7	14.7	1.1	34.0	0.9	100-110 d
Green River Shale	hydrous	200	7	1.6	1.7	3.4	1.3	>400 yr
	hydrous	200	21	2.3	1.3	2.6	2.0	
	hydrous	200	49	2.7	1.2	2.5	2.9	
	hydrous	200	56	0.6	0.9	1.8	1.9	

In the hydrous exchange experiments with labeled water as a deuterium source, some level of hydrogen isotope exchange between propane and water was observed on laboratory timescales at 200 °C. Experiments conducted in the presence of kaolinite exhibited the most significant exchange ($P<0.05$), whereas lower rates of exchange were observed in the presence of montmorillonite and shale powder. The shale powder catalyzed experiments did not produce statistically significant (>2σ) evidence of exchange. In the anhydrous experiments with montmorillonite substrate and $CH_3CD_2CH_3$ as a deuterium source, exchange happened much faster, with expected completion time of 500 days (5 half-lives). Hence, naturally occurring clay minerals can catalyze hydrogen isotope exchange both between water and propane and within propane (i.e.,

intermolecularly and/or between the central and terminal sites), at geological temperatures and timescales (Table 3-4). We suspect the slower rates of our hydrous experiments are more representative of natural behavior, as water is generally present in shallow crustal settings.

When the conditions are adequate for hydrogen exchange of propane (high enough temperature, presence of natural catalysts, long enough time at temperature), this exchange will tend to drive propane toward a site-specific hydrogen isotope structure consistent with equilibrium. Several suites of samples examined in this study are apparently at thermodynamic equilibrium at their current storage temperature (Figure 3-4). They include samples from Eagle Ford, Sleipner Vest, Briggs and one sample from Hadrian field. The Eagle Ford shale data presented is also consistent with previously published NMR measurements of site–specific hydrogen isotope structures of samples from the Eagle Ford system (Liu et al., 2018). Most of the conventional gases that closely approach equilibrium reside in relatively hotter reservoirs (>100 °C), and none of our gas samples that come from reservoirs this hot contains propane significantly out of equilibrium. We conclude that hydrogen exchange of propane drives it to an equilibrium isotopic structure in geological conditions at temperatures greater than 100 ˚C and timescales similar to the residence of gas in reservoirs from the studied systems (for example, $>10^7$ years for the equilibrated Eagle Ford Shale gas). In contrast, propanes sampled from reservoirs colder than 100 ˚C are frequently out of isotopic equilibrium,

leading us to suggest that below this temperature threshold hydrogen isotope exchange is too slow to equilibrate intramolecular D/H of propane readily on relevant geological timescales. (Below we consider the quantitative constraints on just what these timescales might be).

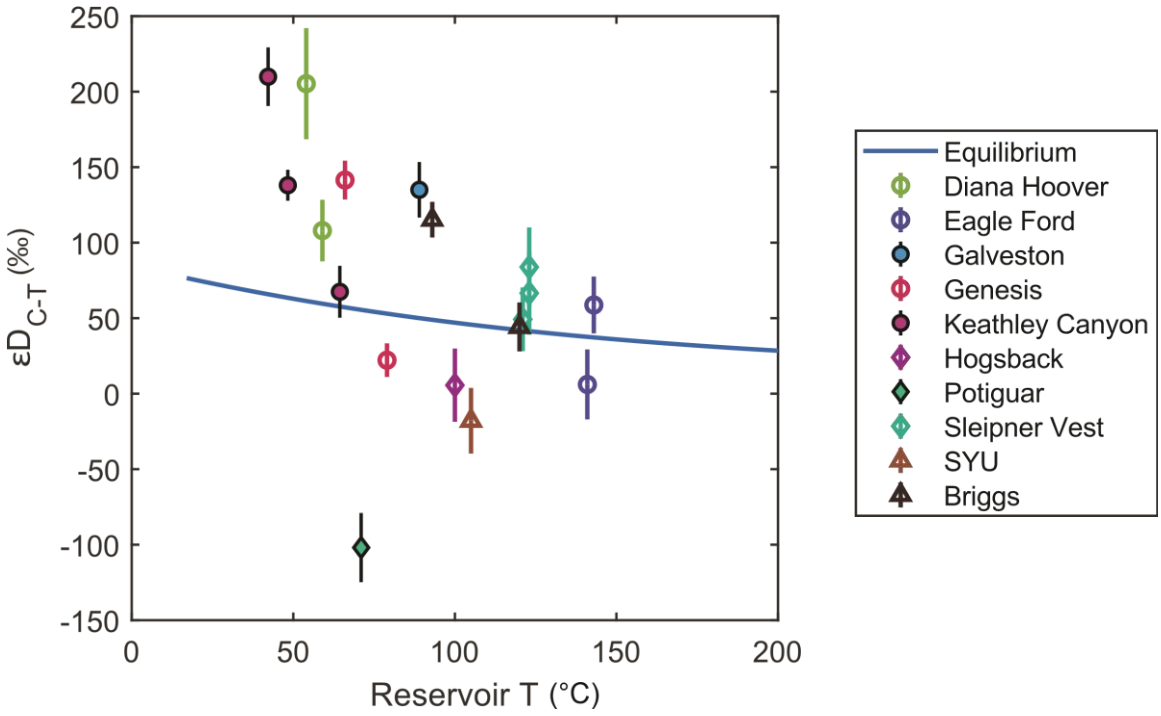

Figure 3-4: Central-terminal hydrogen isotope differences of natural propanes plotted vs. their reservoir temperatures. The temperatures were measured at the wells and adjusted.

Gases from unconventional reservoirs provide a natural field test of the role of hydrogen exchange in controlling propane isotopic structure, because these gases are retained in their source rocks, with residence times that are long and relatively predictable based on basin sequence stratigraphies and thermal histories. Fluid sampled from unconventional systems also may represent a more integrated composition as it doesn't migrate away. In these systems, thermal maturation of the gas can be determined via source shale analysis and molecular maturity evaluation of the fluids. We examined the response of the $\varepsilon D_{C\text{-}T}$ value for two unconventional reservoirs at a range of thermal maturity (based primarily on previous vitrinite reflectance data; Figure 3-5). The thermal maturity for the Eagle Ford samples shown here is based on molecular maturity indicators of biomarkers from co-produced oil or condensate (e.g., C_{29} sterane 20S/(20S+20R) and ββ/(ββ+αα); Peters et al., 2004). In the case of the Irvin Minerals gas from the Eagle Ford shale, this estimate is also consistent with observation of vitrinite reflectance at the depth of production. Both the Eagle Ford Shale (this study) and the Woodford Shale (Liu et al., 2019) produce propane in disequilibrium at the early thermal maturation stage. As maturity increases, the $\varepsilon D_{C\text{-}T}$ value for both formations also increases, eventually reaching equilibrium values at R_0>1.5. This is consistent with the conclusion that hydrogen isotopic exchange of propane is greater at higher storage temperatures and times. We suggest a value of $\%R_0$>1.5 may provide a good threshold

for the integrated time at temperature required for propane to equilibrate its isotopic structure in confined rock pore spaces and natural settings.

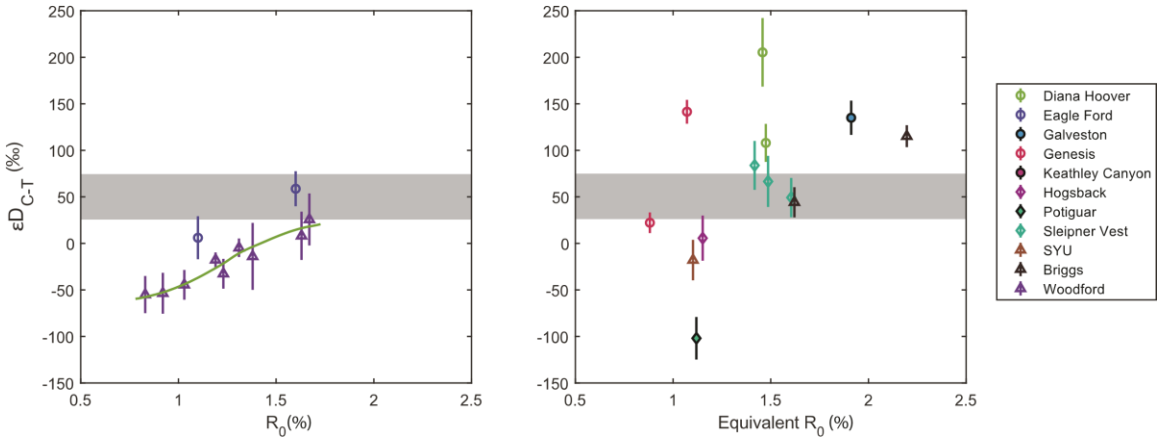

Figure 3-5: Left: $\varepsilon D_{C\text{-}T}$ plotted vs. mapped maturity (vitrinite reflectance) of the gases recovered from unconventional formations, the Eagle Ford Shale (this study) and the Woodford Shale (Liu et al., 2019). Right: $\varepsilon D_{C\text{-}T}$ plotted vs. gas maturity for the conventional hydrocarbon systems in this study. The solid line in the left panel represents the hydrogen exchange model with the best-fit parameters for the Woodford Shale series. The grey area shows isotope equilibrium at 50–200 °C.

The equilibration trend of propane from unconventional reservoirs occurs at maturation stages similar to equilibration of methane clumped isotopologues in similar samples (Xie

et al., 2019). This could reflect similarities between methane and propane in the mechanisms and kinetics of carbon-bound hydrogen equilibration. This could reflect the ability of both to undergo catalyst-mediated exchange, or that they are both participants in radical chain reactions that allow interconversion of molecules and radicals and exchange of atoms (Xia and Gao, 2018; Thiagarajan et al., 2020b).

Samples at $\%R_0<1.5$ from both the Eagle Ford and Woodford formations have $\varepsilon D_{C\text{-}T}$ lower than equilibrium, possibly related to the fact that they are sourced from Type II kerogens; it may also be relevant that some fraction of gas in these systems migrated out of the source rocks – i.e., we are looking at a residual fraction of partial loss (e.g., Zumberge et al., 2016). Isotope fractionation due to transport-related processes have been modeled and experimentally calibrated to be relatively small (Schloemer and Krooss, 2004; Xia and Tang, 2012), and should be negligible in the Eagle Ford formation, because it is estimated to have retained 40%-80% of hydrocarbons (Byrne et al., 2018). Additionally, transport processes such as molecular diffusion are also unlikely to have large positional preference in isotopic fractionations, as discussed earlier in the section.

Residual fluids in petroleum source rocks under partial expulsion may evolve in their molecular composition, meaning the source organic structures subjected to cracking differ between low and high maturities. Figure 3-3 illustrates that this factor may impact the isotope composition of propane, particularly as secondary cracking becomes a

significant propane source (see a fuller discussion of this issue below). However, source maturity is not correlated with the hydrogen isotopic structures of propanes from conventional reservoirs (Figure 3-5), where source rock thermal maturity, or 'Equivalent $\%R_0$' was estimated from the $\delta^{13}C$ values of ethane or propane; Whiticar, 1990). Many samples at higher maturity (Equivalent $\%R_0>1.5$) are still above equilibrium in position-specific D/H ratio of propane. We suggest this reflects preservation of the primary KIE signal associated with catagenic formation of propane, followed by relatively rapid discharge of gas to cool (< 100 ˚C) reservoirs. This interpretation is supported by data from the Briggs fields, where the colder wells with higher maturity gas are out of hydrogen isotope equilibrium whereas nearby hotter wells filled with lower maturity gases are at equilibrium. That is, the critical determinant of propane isotopic equilibration is long-term storage temperature, not generation temperature, suggesting hydrogen isotope exchange (with or without heterogeneous catalysts) controls the rate of approach to equilibrium.

This interpretation raises the possibility that the hydrogen isotopic structure of propane may provide a means of separately constraining temperature-time histories of fluids and their sources. The re-equilibration experiments we present provide a means of making initial estimates of the gas migration timescales implied by this interpretation. Our exchange experiments found that the timescale to reach equilibrium is likely short (Table 3-*4*), which limits the longest average time of these gases residing in the source rock (not

the time of charging the reservoir). At 200°C, the time required to erase disequilibrium signals (5 halftime) is 10^2~10^4 years. Since 200°C is near the high-end of the gas window (Hunt, 1996), longer timescales can be expected for colder environments. For instance, if source rock temperature is 150°C, and assuming a typical activation energy of 70kJ/mol (experimentally determined for natural existing materials such as Al_2O_3; Sattler, 2018) and first-order kinetics, we estimate an exchange half-time that is about 8 times longer, implying a timescale of generation and expulsion of 10^3~10^5 years. Either way, in these systems our laboratory exchange experiments imply that gas expulsion was geologically rapid compared to the time scales of source rock thermal evolution (10^6-10^7 years). This suggests that conventional gases that are found to be in disequilibrium (from Briggs, Galveston, Potiguar, SYU) were generated and expelled from their respective source rocks at those short timescales. It is worth noting that the source rock of the Potiguar gas (which is farthest away from equilibrium) is deposited during the Neocomian-Aptian rift phase of the basin evolution, when the heat flow increases very rapidly, allowing faster generation and expulsion (Trindade et al., 1992). We recognize that these estimations are based on the premise that clay minerals or other naturally occurring catalytic materials are available and as accessible to and catalytically active as those present in our experiments. If these assumptions are not true in the natural shale setting then expulsion timescales could have been longer.

Exchange rates also can be estimated by modeling exchange equilibration of propane in unconventional natural gas reservoirs. Liu et al. (2019) presented position-specific hydrogen isotope compositions of propane from the Woodford shale in the Arkoma basin, collected from source rocks spanning a range of thermal maturation. Assuming that the change of $\varepsilon D_{C\text{-}T}$ with increasing thermal maturation is controlled by hydrogen exchange, we created a numeric model to reconstruct the position-specific hydrogen isotope composition of propane as a function of temperature and time and fit that model to the data of Liu et al. We used a gas accumulation model determined with PetroMod (Higley et al., 2014) and thermal curves adapted from the burial and uplifting model of the Arkoma basin from Byrnes and Lawyer (1999). In this model, propane is generated and exchanged continuously, with first-order exchange kinetics (Sessions et al., 2004; Xie et al., 2018). We used a Monte-Carlo method to constrain the key kinetic parameters for hydrogen isotope exchange on the central position of propane (i.e., the activation energy, *Ea*, and pre-exponential frequency factor), obtaining a range of possible combinations of their distributions that are consistent with these data and the hydrogen-exchange hypothesis. The best-fit of those parameters (Ea=114 kJ/mol and A=4.9e5 yr^{-1}) accurately captures the measured values (Figure 3-5).

The posterior range of exchange half-time at 200°C from the Monte-Carlo simulation is 4.9-17 My (Figure 3-6). This is longer than those values obtained from clay-catalyzed experiments (10^2-10^4 years). This large discrepancy could be due to the lack of those

minerals and/or inhibition to the catalytic surfaces. Kaolinite appears as a minor mineral in the Woodford shale (Lewan, 1985), but natural shale conditions are unlikely to possess such high surface area/gas ratios as we created in the laboratory. Nevertheless, we compared the Monte-Carlo outcome of possible rates with kinetic data of laboratory experiments on a few other relevant processes (Figure 3-6). First of all, it was found that the predicted values are broadly consistent with (though a little slower than) exchange experiments between methane/hexane and water without catalysts (Koepp, 1978; Sessions et al., 2004). Secondly, the chemistry of either oil cracking (Ungerer et al., 1988) or hydrous pyrolysis (Lewan, 1985) would be faster than exchange processes if we extrapolate their high-temperature experiments to the temperatures of natural gas formation. This implies that the kinetic fractionation signatures of propane generation are not equilibrated over geologically brief times (i.e., less than a million years), explaining why such signals are preserved in so many conventional reservoirs with a wide range of source maturation. Lastly, the self-cracking kinetics of propane (Laidler et al., 1962), when extrapolated to gas window temperatures, would be slower than hydrogen exchange. Taken together, this suggests that during propane loss (transformation from wet gas to dry gas) propane should stay at intramolecular hydrogen isotope equilibrium.

When propane is equilibrated, $\varepsilon D_{C\text{-}T}$ constrains the equilibration temperature of the environment where isotope exchange happened. Unfortunately, the analytical precision of the NMR and DFS methods from this and previous studies is insufficient to usefully

constrain this apparent temperature. However, the recently developed multi-collector high-resolution gas source isotope ratio mass spectrometers (Eiler et al., 2013; Young et al., 2016) are capable of measuring δD of methane down to 0.05-0.1‰ precision. The application of such mass spectrometric techniques to propane site-specific D/H ratios could enable quantitatively useful geo-thermometry of gas storage. For example, a 0.05‰ error in hydrogen isotope ratios of both the ethyl fragment and molecular ion would be propagated to a 0.45‰ error in $\varepsilon D_{C\text{-}T}$ (for natural propane with typical hydrogen isotope composition), which could be translated to around 2°C inferred equilibrium temperature error in the relevant temperature range. The gases that yield propane in hydrogen isotope equilibrium in our study also yield methane in clumped-isotope equilibrium (Figure 3-7) with self-consistent (or higher) apparent temperatures of 150-220°C — generally in the gas window.

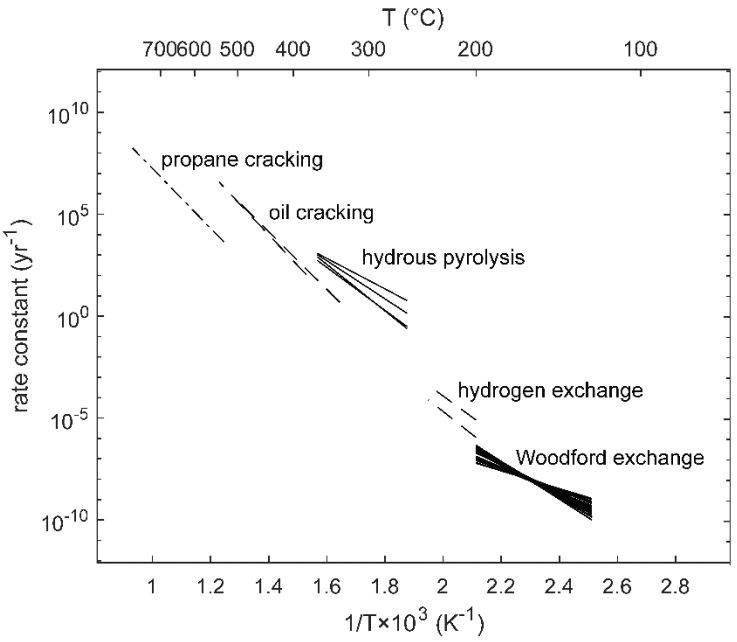

Figure 3-6: Arrhenius plot showing the result of modeling the hydrogen exchange rate constants of propane in Woodford Shale (labeled as 'Woodford exchange' in the figure) compared to various processes. The simulated activation energy is between 80–180 kJ/mol. Hydrogen exchange refers to D/H exchange experiments on methane and hexane (Koepp., 1978; Sessions et al., 2004). Hydrous pyrolysis refers to hydrous pyrolysis experiments on the Woodford, Alum, Phosphoria, and Monterey Shales (Lewan and Ruble, 2002). Oil cracking refers to oil-cracking experiments on the Boscan oil and Pematang oil (Ungerer et al., 1988). Propane cracking refers to propane pyrolysis experiments (Laidler et al., 1962).

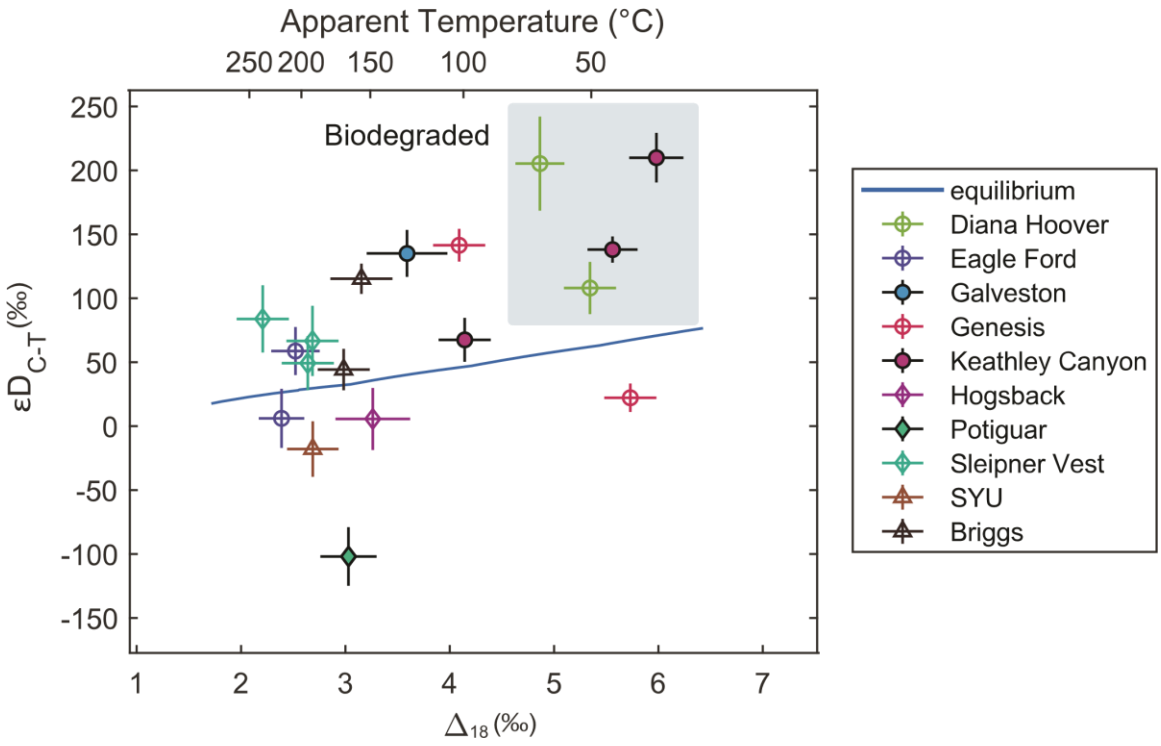

Figure 3-7: Position specific D/H fractionation in propane plotted vs. a measure of isotope clumping in methane. The equilibrium fractionation line and its apparent temperature (top horizontal axis) is based on ab initio calculations from Webb and Miller (2014) for propane and experimental calibration from Stolper et al. (2014b) for methane.

Propane from more mature fluids tend to have higher $\varepsilon D_{C\text{-}T}$ values in both unconventional and conventional reservoirs. It is possible that this is driven by a change

in cracking source material as thermal maturation proceeds (as mentioned above). As thermal maturity increases, the organic substrate that propane and other hydrocarbons derive from change to vary in their chemical composition and structure. Natural gases formed by direct thermal decomposition of kerogen at earlier maturation are often categorized as ‘primary gas’, distinguished from the ‘secondary gas’ that results from oil cracking at later stages of maturation. For Type I/II kerogens, oil-associated gases are commonly the primary gases of kerogen cracking, whereas non-associated gases are the secondary gases from further cracking of oil. The majority of our sample set are gases derived from type II kerogen, except for the Potiguar sample, which was generated by lacustrine section (Pendência formation of Lower Cretaceous (130 Ma)) mainly related to an organic–rich shale with type-I kerogen (Pestilho et al., 2018). The source origin of the non-associated Hogsback gas is unclear, though we favor an interpretation that it is a primary gas derived from a more gas-prone mixed Type II/III source rock, based on the Δ_{18} apparent temperature of its methane, compound specific $\delta^{13}C$ of methane, ethane and propane and biomarker data (not presented here) of co-produced condensate. With our background knowledge, samples from Potiguar, Diana Hoover, Genesis, Keathley Canyon, SYU and Irvin Minerals South of Eagle Ford Shale would be categorized as primary gas by this reasoning, and samples from Galveston, Sleipner Vest, Briggs and Las Raices 22H of Eagle Ford Shale would be classified as secondary gases. We found that $\varepsilon D_{C\text{-}T}$ of the secondary gases are observed to be higher than the equilibrium line,

whereas that of the primary gases can be either higher or lower. This is consistent with the oil-cracking signature predicted by the kMC model (Figure 3-*3*), where oil as a substrate produces propane with highly positive $\varepsilon D_{C\text{-}T}$. This interpretation is also consistent with observed trends of higher $\varepsilon^{13}C_{C\text{-}T}$ at higher maturation in both pyrolysis experiments and natural samples (Piasecki et al., 2018; Gilbert et al., 2019). When we examine the position-specific hydrogen isotope ratios of propane in the hydrous pyrolysis experiments of the Woodford shale, we also observed $\varepsilon D_{C\text{-}T}$ increases as experimental temperature increases and more secondary cracking is happening (Figure 3-8). However, this theory (i.e., change in $\varepsilon D_{C\text{-}T}$ is controlled by source maturation) requires hydrogen exchange rate to be very slow, which is not favored by experimental results reported earlier in this section. Propane sampled from more mature unconventional gases could provide evidence as to whether cracking chemistry or hydrogen exchange have stronger influences in this signature. If the hydrogen isotope structure of propane is primarily controlled by cracking chemistry, $\varepsilon D_{C\text{-}T}$ values would continue to increase with maturity to $\%R_0$ ~2 or above, but if it is primarily controlled by hydrogen exchange, $\varepsilon D_{C\text{-}T}$ values would remain in hydrogen isotope equilibrium as $\%R_0$ rises to extreme values.

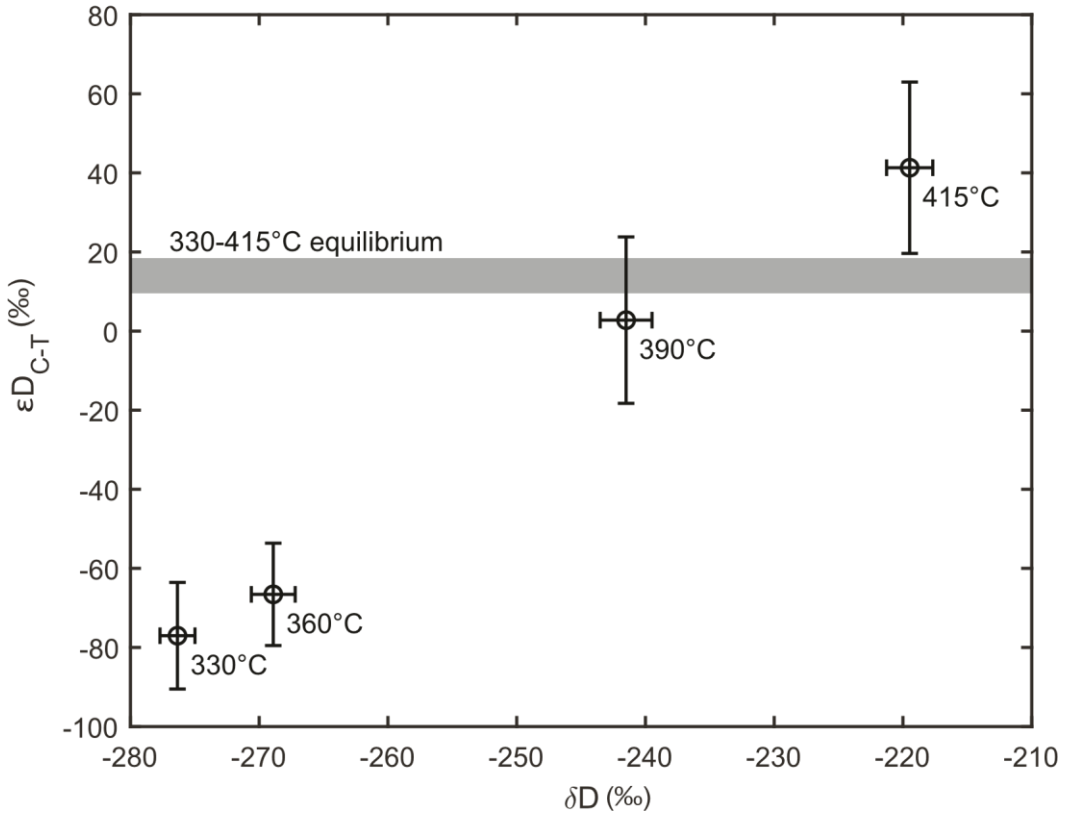

Figure 3-8: Propane isotope data for the hydrous pyrolysis experiments (horizontal axis is molecular average δD of propane). Equilibrium isotope effect at 330–415°C is extrapolated from Xie et al. (2018) and Webb and Miller (2014).

5.4 Propane destruction

5.4.1 Secondary cracking of propane

Secondary cracking of propane is associated with high-maturity cracking of hydrocarbons to destroy C_2-C_5 alkanes and increase the dryness (C_1 to C_{2+} ratio) of the system. Position-specific hydrogen isotope fractionation could be changed during this process, as different isotopomers have different cracking rates. We can calculate the isotopic structure of residual propane using KIEs associated propane cracking. We consider the homolytic cleavage of the C-C bond to be the primary mechanism that initiates secondary cracking of propane, as C-C breaking is approximately 5 orders of magnitude faster than C-H breaking at relevant temperatures (e.g., Dean, 1985). Deuterium KIEs predicted for homolytic cleavage of the C-C bond has been previously calculated using quantum chemical methods (Ni et al., 2011). It is found that this process enriches the central position in D faster than the terminal position, which could be explained by that there are twice as many terminal carbons and 3x more terminal hydrogens as central ones, but an equal number of each positions is involved in C-C cracking. We predict that $\varepsilon D_{C\text{-}T}$ increases by 53‰ after 1 e-folding time (63% reaction progress) of propane cracking at 200°C.

Results from hydrous pyrolysis experiments support this prediction (Figure 3-7 and Table 3-5). At lower temperature, pyrolytic propane has a relatively D-depleted central position. As temperature increases, both δD and $\varepsilon D_{C\text{-}T}$ rises. $\varepsilon D_{C\text{-}T}$ reaches equilibrium values at

390°C, but continue to rise as temperature increases to 415°C. At the temperature of 415°C, The data provide suggestive but not definitive evidence that at the maximum temperature of 415°C, $\varepsilon D_{C\text{-}T}$ just exceeds equilibrium isotope effects. If this is not simply a statistical anomaly (as it is just outside errors of equilibrium), it would suggest that the trend of rising $\varepsilon D_{C\text{-}T}$ with increasing maturity is at least influenced by kinetic isotope effects instead of (or perhaps in addition to) equilibration.

On the other hand, we do not see any natural samples from the unconventional reservoirs at higher fluid maturity with significantly elevated $\varepsilon D_{C\text{-}T}$ values (statistically above equilibrium). In fact, it is conceivable that H exchange, via either catalysis or other mechanisms, will play an important role in the maturation stage of gas cracking, as discussed in section 5.3 and Figure 3-6. That is, perhaps H exchange reactions are faster than secondary cracking of propane, erasing any kinetic fractionations resulting from secondary cracking in natural settings. This may be because the high activation energy of secondary cracking reactions renders them ineffective compared to exchange at geological temperatures (Figure 3-6).

Table 3-5: Results of the hydrous pyrolysis experiments in this study. All measurements here are made with the MID method.

Temperature(°C)	Propane data							Compound-specific isotope data			
	$\delta D_{molecular}$	error	δD_{ethyl}	error	εD_{C-T}	error	δD_{vsmow}	$\delta^{13}C_{C1}$	$\delta^{13}C_{C2}$	$\delta^{13}C_{C3}$	δD_{C1}
330	-118.6	0.7	-122.6	0.6	-77.0	6.7	-270	-42.87	-37.96	-35.62	-340
360	-109.5	0.9	-112.1	0.4	-66.6	6.5	-264	-44.38	-34.61	-33.51	-340
390	-76.1	1.0	-69.0	1.2	2.8	10.5	-239	-39.19	-31.9	-30.96	-336
415	-49.3	0.9	-36.5	1.4	41.3	10.8	-219	-33.11	-28.42	-25.54	-324

5.4.2 Biological degradation

In relatively cool (up to 80°C) reservoirs where biological activity could occur, propane is susceptible to microbial degradation both by aerobes (where suitable conditions exist) and — more commonly — anaerobes. Amongst C_2-C_5 hydrocarbons, propane is biodegraded most rapidly (Head et al., 2003). Biological consumption of propane expresses normal KIEs, leaving the residual propane more enriched in ^{13}C and D. The initiation step is binding either the central or terminal position of propane, and previous deuterium labeling studies have shown that the central position is preferentially (70%) attacked in the anaerobic oxidation of propane by a sulfate–reducing bacteria culture (Jaekel et al., 2014). This position preference would cause more rapid isotopic enrichment in the central position than the terminal position (both positions are enriched),

such that the central-terminal difference in both carbon and hydrogen isotopes increases as biodegradation intensifies. The greater enrichment of ^{13}C at the central position has been confirmed in both lab cultures and several natural gas basins for carbon isotopes (Gilbert et al., 2019), where it was estimated that 85% of attacks occur on the central position. It is also notable that a recent study has shown that thermophilic anaerobic methanotrophic archaea (ANME-1) can oxidize butane (and potentially propane) by methyl-CoM reductase (MCR). This mechanism attacks the terminal position, so it would lead to decrease in central-terminal difference that is opposite to bacterial degradation.

Moderately elevated $\varepsilon D_{C\text{-}T}$ values in propane samples retrieved from several wells in the Diana Hoover and Hadrian (GOM) fields — places known to contain biogenic methane — suggest that these gases could have been biodegraded. Since all of these gases are sampled from deep wells (>2000m), the potential biodegraders would be anaerobes. Several independent lines of evidence also support that these gases are biodegraded: (1) The propanes have high δD values (-120‰ to -80‰) compared to other samples from the Gulf of Mexico (-126‰ to -116‰). (2) Propane concentration is relatively low for the immature gases in these formations. (3) Methanogenesis is commonly associated with hydrocarbon biodegradation (sometimes referred to as ‘secondary methanogenesis’; e.g., Jones et al., 2008), and compound-specific stable isotope signatures indicate significant microbial input of methane. That is to say, δD and $\delta^{13}C$ of methane in these samples

match a microbial origin in a ‘Schoell/Whiticar diagram’ (Figure 3-1; Figure 3-A2; Whiticar, 1999), and $\delta^{13}C$ of methane has a negative anomaly (compared to $\delta^{13}C$ trend of C2+ alkanes) in a ‘Chung plot’ (Figure 3-A2). (4) apparent temperatures derived from Δ_{18} clumped isotope measurements of methane are between 30-68 °C, consistent with the reservoir temperatures of these wells (42-59 °C), suggesting that these methanes were formed (or microbially recycled) *in situ* (see Thiagarajan et al., 2020a). Although microbial methane is often in clumped isotope disequilibrium (Wang et al., 2015; Stolper et al., 2015; Douglas et al., 2016; Young et al., 2017), microbial methane found in marine and/or subsurface environments are usually in or close to equilibrium. It has been proposed that slow anaerobic coupled methanogenesis and methanotrophy in nature under low thermodynamic drive (e.g., H_2 supply) could drive methane to internal isotopic equilibrium at its environmental temperature (e.g., Gruen et al., 2018; Giunta et al., 2019; Douglas et al., 2020). Besides that, microbes degrading C_2–C_4 short alkanes have been found in the Gulf of Mexico sediments (Kniemeyer et al., 2007; Laso-Pérez et al., 2016; Chen et al., 2019).

The three samples from the Hadrian field provide suggestive evidence of the hydrogen isotope signature of the biodegradation progress: Their $\varepsilon D_{C\text{-}T}$ values increase with molecular δD values of propane (Figure 3-9). Assuming that biodegradation occurs as a closed system process, and that the amplitude of the KIE is similar between central and

terminal uptake, we can model the position-specific propane isotopic composition with a modified Rayleigh relationship:

$$\frac{\epsilon D_{C-T} + 1000}{\epsilon D_{C-T(0)} + 1000} = F^{x_C(\alpha-1)-(1-x_C)(0.5\alpha-0.5)}, \quad (3)$$

where x_C is the fraction of attack events on the central position and α is the primary KIE of methane binding with methane monooxygenase (MMO). Results of this model for the Hadrian field propanes are consistent with having a high central preference, with an x_C value between 80 and 90%.

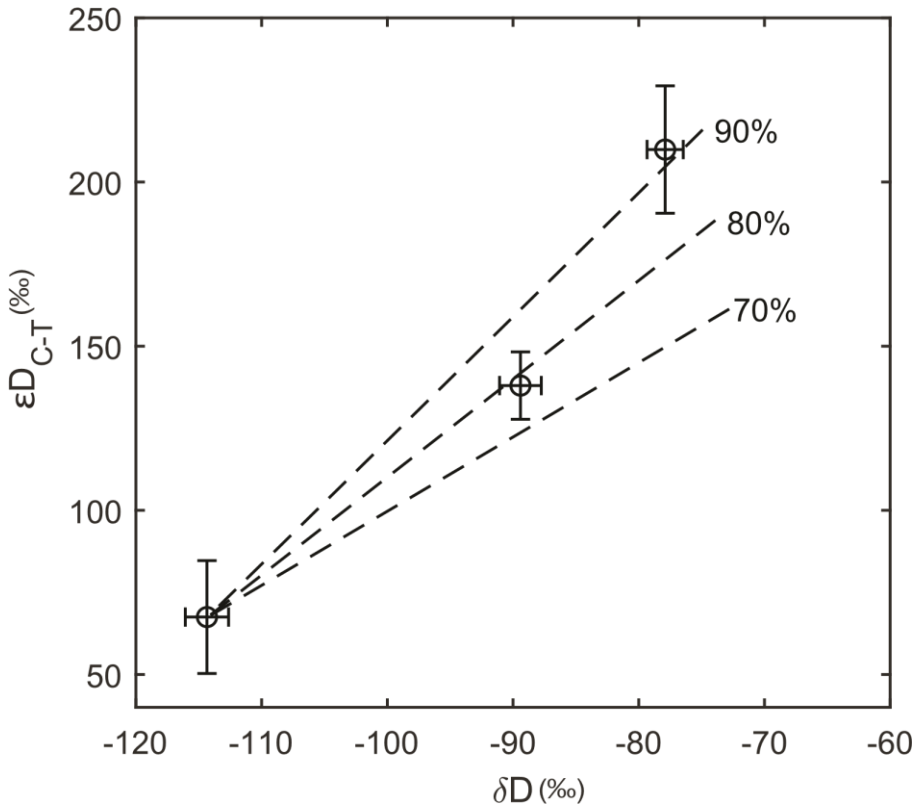

Figure 3-9: Isotopic constraints on the sites of propane decomposition associated with biodegradation in the Hadrian field gas samples (horizontal axis is molecular average δD of propane). Dashed lines represent modeled trends of the residual propane as biodegradation intensifies, where the numerical label notes the percentage of destroyed propane that was subject to attack at the central carbon site (x_C). Changes in the primary KIE of methane oxidation does not alter the modeled lines (assuming that KIE is closely similar for the terminal and central site mechanisms).

6. Conclusions

We used high-resolution mass spectrometry to examine the position-specific hydrogen isotope distribution in propane from a diverse set of natural gas samples and laboratory experiments. We explored the effects of various processes of propane formation, storage, and destruction on intramolecular isotope fractionation, via both theory and experiment. The wide range of this central-terminal difference in natural samples suggests that catagenesis is dominated by kinetic fractionations and forms propane out of H-isotopic equilibrium. Kinetic Monte-Carlo models reveal that structural properties of the organic precursors can control the direction and amplitude of intramolecular fractionation. Specifically, straight-chain precursors lead to center-site D enrichment, whereas branched precursors lead to terminal site D enrichment. Based on their position-specific hydrogen isotope ratios, natural propanes appear to sample branched precursors with greater frequencies than one might predict from some structural models of kerogen (Ungerer et al., 2015; Bousige et al., 2016), particularly in gases from unconventional reservoirs.

Once formed, propane can be subject to hydrogen exchange that will drive its site-specific isotopic distribution towards equilibrium. Results from laboratory isotope exchange experiments indicate that hydrogen isotope exchange can be catalyzed by clay minerals such as kaolinite. The exchange timescale estimated from these experiments can

be relatively short (10^2-10^4 yrs) in the presence of clays at 200°C. The natural observations show that higher maturity propane in non-associated gases sitting in relatively hot reservoirs (>100 ˚C) are nearly equilibrated (though this may or may not reflect the role of solid catalysts such as those used in our laboratory experiments). In unconventional reservoirs, position-specific hydrogen isotopes of propane in fluids with an integrated maturity of Ro < 1.5 % is out of equilibrium and tend to approach equilibrium as thermal maturity increases. If this is driven by exchange equilibration, the exchange half-time is estimated to be 5-17 My at 200 ˚C based on data from the Woodford Shale. In conventional reservoirs, propane can still be out of equilibrium despite having relatively high source maturity, suggesting fast (<10^5 years) expulsion from source formations and storage in cool (<100 ˚C) reservoirs. More generally, position-specific hydrogen isotope compositions of propane can be used to constrain the temperature-time histories of gas expulsion and migration.

It is worth mentioning that biodegradation can also impact $\varepsilon D_{C\text{-}T}$ values, as observed in two relatively cold reservoirs, Hadrian North and Diana Hoover. These elevated values reflect a strong central position preference in the chemical degradation reactions during biological uptake, consistent with previously reported carbon isotope behavior. Intramolecular isotope distributions for both ^{13}C and D in propane provide a distinct signature for subsurface hydrocarbon biodegradation.

Acknowledgements

This research is supported by an NSF-EAR instruments and facilities grant and Caltech. Additional funding is provided by Exxon Mobil. The kinetic Monte-Carlo computations were conducted on the Caltech High Performance Cluster, partially supported by a grant from the Gordon and Betty Moore Foundation. We thank Nami Kitchen for assistance with the operation of the DFS mass spectrometer.

References

Abelson P. H. and Hoering T. C. (1961) Carbon isotope fractionation in formation of amino acids by photosynthetic organisms. Proc. Natl. Acad. Sci. U. S. A. 47, 623–632.

Berner U. and Faber E. (1996) Empirical carbon isotope/maturity relationships for gases from algal kerogens and terrigenous organic matter, based on dry, open-system pyrolysis. In Organic Geochemistry pp. 947–955.

Bousige C., Ghimbeu C. M., Vix-Guterl C., Pomerantz A. E., Suleimenova A., Vaughan G., Garbarino G., Feygenson M., Wildgruber C., Ulm F. J., Pellenq R. J. M. and Coasne

B. (2016) Realistic molecular model of kerogen's nanostructure. Nat. Mater. 15, 576–582.

Burlingame A. L. and Simoneit B. R. (1968) Isoprenoid fatty acids isolated from the kerogen matrix of the Green River Formation (Eocene). Science (80-.). 160, 531–533.

Byrne D. J., Barry P. H., Lawson M. and Ballentine C. J. (2018) Determining gas expulsion vs retention during hydrocarbon generation in the Eagle Ford Shale using noble gases. Geochim. Cosmochim. Acta 241, 240–254.

Byrnes A. P. and Lawyer G. (1999) Burial, maturation, and petroleum generation history of the Arkoma Basin and Ouachita Foldbelt, Oklahoma and Arkansas. Nat. Resour. Res. 8, 3–26.

Charlou J. L., Donval J. P., Douville E., Jean-Baptiste P., Radford-Knoery J., Fouquet Y., Dapoigny A. and Stievenard M. (2000) Compared geochemical signatures and the evolution of Menez Gwen (35°50N) and Lucky Strike (37°17N) hydrothermal fluids, south of the Azores Triple Junction on the Mid-Atlantic Ridge. Chem. Geol. 171, 49–75.

Chen S. C., Musat N., Lechtenfeld O. J., Paschke H., Schmidt M., Said N., Popp D., Calabrese F., Stryhanyuk H., Jaekel U., Zhu Y. G., Joye S. B., Richnow H. H., Widdel F. and Musat F. (2019) Anaerobic oxidation of ethane by archaea from a marine hydrocarbon seep. Nature 568, 108–111.

Chung H. M., Gormly J. R. and Squires R. M. (1988) Origin of gaseous hydrocarbons in subsurface environments: Theoretical considerations of carbon isotope distribution. Chem. Geol. 71, 97–104.

Clog M., Lawson M., Peterson B., Ferreira A. A., Santos Neto E. V. and Eiler J. M. (2018) A reconnaissance study of 13C–13C clumping in ethane from natural gas. Geochim. Cosmochim. Acta 223, 229–244.

Curry D. J. and Simpler T. K. (1988) Isoprenoid constituents in kerogens as a function of depositional environment and catagenesis. Org. Geochem. 13, 995–1001.

Dai J., Xia X., Qin S. and Zhao J. (2004) Origins of partially reversed alkane δ13C values for biogenic gases in China. In Organic Geochemistry Pergamon. pp. 405–411.

Dean A. M. (1985) Predictions of pressure and temperature effects upon radical addition and recombination reactions.,

Douglas P. M. J., Gonzalez Moguel R., Walter Anthony K. M., Wik M., Crill P. M., Dawson K. S., Smith D. A., Yanay E., Lloyd M. K., Stolper D. A., Eiler J. M. and Sessions A. L. (2020) Clumped Isotopes Link Older Carbon Substrates With Slower Rates of Methanogenesis in Northern Lakes. Geophys. Res. Lett. 47.

Douglas P. M. J., Stolper D. A., Smith D. A., Walter Anthony K. M., Paull C. K., Dallimore S., Wik M., Crill P. M., Winterdahl M., Eiler J. M. and Sessions A. L. (2016) Diverse origins of Arctic and Subarctic methane point source emissions identified with multiply-substituted isotopologues. Geochim. Cosmochim. Acta 188, 163–188.

Dowdle W. L. and Cobb W. M. (1975) Static Formation Temperature From Well Logs - an Empirical Method. JPT, J. Pet. Technol. 27, 1326–1330.

Dukov I. L. (2007) Nomenclature of inorganic chemistry - IUPAC recommendations 2005. Chemistry (Easton).

Ehlers I., Augusti A., Betson T. R., Nilsson M. B., Marshall J. D. and Schleucher J. (2015) Detecting long-term metabolic shifts using isotopomers: CO2-driven suppression of photorespiration in C3 plants over the 20th century. Proc. Natl. Acad. Sci. U. S. A. 112, 15585–90.

Eiler J. M. (2007) “Clumped-isotope” geochemistry-The study of naturally-occurring, multiply-substituted isotopologues. Earth Planet. Sci. Lett. 262, 309–327.

Eiler J. M., Clog M., Lawson M., Lloyd M., Piasecki A., Ponton C. and Xie H. (2018) The isotopic structures of geological organic compounds. Geol. Soc. London, Spec. Publ. 468, 53–81.

Eiler J. M., Clog M., Magyar P., Piasecki A., Sessions A., Stolper D., Deerberg M., Schlueter H. J. and Schwieters J. (2013) A high-resolution gas-source isotope ratio mass spectrometer. Int. J. Mass Spectrom. 335, 45–56.

Gao C. W., Allen J. W., Green W. H. and West R. H. (2016) Reaction Mechanism Generator: Automatic construction of chemical kinetic mechanisms. Comput. Phys. Commun. 203, 212–225.

Gao L., He P., Jin Y., Zhang Y., Wang X., Zhang S. and Tang Y. (2016) Determination of position-specific carbon isotope ratios in propane from hydrocarbon gas mixtures. Chem. Geol. 435, 1–9.

Gao Y., Zou Y. R., Liang T. and Peng P. (2017) Jump in the structure of Type I kerogen revealed from pyrolysis and 13C DP MAS NMR. Org. Geochem. 112, 105–118.

Gilbert A., Lollar B. S., Musat F., Giunta T., Chen S., Kajimoto Y., Yamada K., Boreham C. J., Yoshida N. and Ueno Y. (2019) Intramolecular isotopic evidence for bacterial oxidation of propane in subsurface natural gas reservoirs. Proc. Natl. Acad. Sci. U. S. A. 116, 6653–6658.

Gilbert A., Robins R. J., Remaud G. S. and Tcherkez G. G. B. (2012) Intramolecular 13C pattern in hexoses from autotrophic and heterotrophic C3 plant tissues. Proc. Natl. Acad. Sci. U. S. A. 109, 18204–9.

Gilbert A., Yamada K., Suda K., Ueno Y. and Yoshida N. (2016) Measurement of position-specific 13C isotopic composition of propane at the nanomole level. Geochim. Cosmochim. Acta 177, 205–216.

Gilbert A., Yamada K. and Yoshida N. (2013) Exploration of intramolecular 13C isotope distribution in long chain n-alkanes (C11-C31) using isotopic 13C NMR. Org. Geochem. 62, 56–61.

Giunta T., Young E. D., Warr O., Kohl I., Ash J. L., Martini A., Mundle S. O. C., Rumble D., Pérez-Rodríguez I., Wasley M., LaRowe D. E., Gilbert A. and Sherwood Lollar B. (2019) Methane sources and sinks in continental sedimentary systems: New insights from paired clumped isotopologues 13 CH 3 D and 12 CH 2 D 2. Geochim. Cosmochim. Acta 245, 327–351.

Gruen D. S., Wang D. T., Könneke M., Topçuoğlu B. D., Stewart L. C., Goldhammer T., Holden J. F., Hinrichs K.-U. and Ono S. (2018) Experimental investigation on the controls of clumped isotopologue and hydrogen isotope ratios in microbial methane. Geochim. Cosmochim. Acta 237, 339–356.

Hayes J. M. (2001) Fractionation of Carbon and Hydrogen Isotopes in Biosynthetic Processes. Rev. Mineral. Geochemistry 43, 225–277.

Head I. M., Jones D. M. and Larter S. R. (2003) Biological activity in the deep subsurface and the origin of heavy oil. Nature 426, 344–352.

Higley D. K., Cook T. A. and Pawlewicz M. J. (2014) Petroleum Systems and Assessment of Undiscovered Oil and Gas in the Anadarko Basin Province, Colorado, Kansas, Oklahoma, and Texas — Woodford Shale Assessment Units. Higley, D.K., Compil. Pet. Syst. Assess. undiscovered oil gas Anadarko Basin Prov. Color. Kansas, Oklahoma, Texas - USGS Prov. 58 U.S. Geol. Surv. Digit. Data Ser. DDS-69-EE 58, 24.

Hinrichs K. U., Hayes J. M., Bach W., Spivackl A. J., Hmelo L. R., Holm N. G., Johnson C. G. and Sylva S. P. (2006) Biological formation of ethane and propane in the deep marine subsurface. Proc. Natl. Acad. Sci. U. S. A. 103, 14684–14689.

Van Hook W. A. (1966) Vapor Pressures of the Deuterated Ethanes. J. Chem. Phys. 44, 234–251.

Höpfner A. (1969) Vapor Pressure Isotope Effects. Angew. Chemie Int. Ed. English 8, 689–699.

Hunt J. (1996) Petroleum geology and geochemistry., Freeman, New York.

Ingalls M. (2019) Reconstructing carbonate alteration histories in orogenic sedimentary basins: Xigaze forearc, southern Tibet. Geochim. Cosmochim. Acta 251, 284–300.

Jaekel U., Vogt C., Fischer A., Richnow H.-H. and Musat F. (2014) Carbon and hydrogen stable isotope fractionation associated with the anaerobic degradation of propane and butane by marine sulfate-reducing bacteria. Environ. Microbiol. 16, 130–140.

Jones D. M., Head I. M., Gray N. D., Adams J. J., Rowan A. K., Aitken C. M., Bennett B., Huang H., Brown A., Bowler B. F. J., Oldenburg T., Erdmann M. and Larter S. R. (2008) Crude-oil biodegradation via methanogenesis in subsurface petroleum reservoirs. Nature 451, 176–180.

Julien M., Goldman M. J., Liu C., Horita J., Boreham C. J., Yamada K., Green W. H., Yoshida N. and Gilbert A. (2020) Intramolecular 13C isotope distributions of butane from natural gases. Chem. Geol. 541, 119571.

Kelemen S. R., Afeworki M., Gorbaty M. L., Sansone M., Kwiatek P. J., Walters C. C., Freund H., Siskin M., Bence A. E., Curry D. J., Solum M., Pugmire R. J., Vandenbroucke M., Leblond M. and Behar F. (2007) Direct characterization of kerogen by X-ray and solid-state 13C nuclear magnetic resonance methods. Energy and Fuels 21, 1548–1561.

Kniemeyer O., Musat F., Sievert S. M., Knittel K., Wilkes H., Blumenberg M., Michaelis W., Classen A., Bolm C., Joye S. B. and Widdel F. (2007) Anaerobic oxidation of short-chain hydrocarbons by marine sulphate-reducing bacteria. Nature 449, 898–901.

Koepp M. (1978) D/H isotope exchange reaction between petroleum and water : A contributory determinant for D/H-isotope ratios in crude oil? Short Pap. Fourth Int. Conf. Geochronology. Cosmochronol. Isot. Geol. 1978, 221–222.

Laidler K. J., Sagert N. H. and Wojciechowski B. W. (1962) Kinetics and mechanisms of the thermal decomposition of propane I. The Uninhibited of reaction. Proc. R. Soc. London. Ser. A. Math. Phys. Sci. 270, 242–253.

Laso-Pérez R., Wegener G., Knittel K., Widdel F., Harding K. J., Krukenberg V., Meier D. V., Richter M., Tegetmeyer H. E., Riedel D., Richnow H. H., Adrian L., Reemtsma T., Lechtenfeld O. J. and Musat F. (2016) Thermophilic archaea activate butane via alkyl-coenzyme M formation. Nature 539, 396–401.

Lawson M., Formolo M. J., Summa L. and Eiler J. M. (2018) Geochemical applications in petroleum systems analysis: New constraints and the power of integration. Geol. Soc. Spec. Publ. 468, 1–21.

Lewan M. D. (1985) Evaluation of petroleum generation by hydrous pyrolysis experimentation. Philos. Trans. R. Soc. London, 123–134.

Lewan M. D. (1997) Experiments on the role of water in petroleum formation. Geochim. Cosmochim. Acta 61, 3691–3723.

Lewan M. D. (1998) Sulphur-radical control on petroleum formation rates. Nature 391, 164–166.

Lewan M. D. and Ruble T. E. (2002) Comparison of petroleum generation kinetics by isothermal hydrous and nonisothermal open-system pyrolysis. Org. Geochem. 33, 1457–1475.

Lewan M. D., Winters J. C. and McDonald J. H. (1979) Generation of oil-like pyrolyzates from organic-rich shales. Science (80-.). 203, 897–899.

Li Y., Zhang L., Xiong Y., Gao S., Yu Z. and Peng P. (2018) Determination of position-specific carbon isotope ratios of propane from natural gas. Org. Geochem. 119, 11–21.

Liu C., Liu P., McGovern G. P. and Horita J. (2019) Molecular and intramolecular isotope geochemistry of natural gases from the Woodford Shale, Arkoma Basin, Oklahoma. Geochim. Cosmochim. Acta 255, 188–204.

Liu C., McGovern G. P., Liu P., Zhao H. and Horita J. (2018) Position-specific carbon and hydrogen isotopic compositions of propane from natural gases with quantitative NMR. Chem. Geol. 491, 14–26.

Mangenot X., Deçoninck J. F., Bonifacie M., Rouchon V., Collin P. Y., Quesne D., Gasparrini M. and Sizun J. P. (2019) Thermal and exhumation histories of the northern

subalpine chains (Bauges and Bornes—France): Evidence from forward thermal modeling coupling clay mineral diagenesis, organic maturity and carbonate clumped isotope (Δ 47) data. Basin Res. 31, 361–379.

Mango F. D., Jarvie D. M. and Herriman E. (2010) Natural catalytic activity in a marine shale for generating natural gas. Proc. R. Soc. A Math. Phys. Eng. Sci. 466, 3527–3537.

Monson K. D. and Hayes J. M. (1982) Carbon isotopic fractionation in the biosynthesis of bacterial fatty acids. Ozonolysis of unsaturated fatty acids as a means of determining the intramolecular distribution of carbon isotopes. Geochim. Cosmochim. Acta 46, 139–149.

Ni Y., Ma Q., Ellis G. S., Dai J., Katz B., Zhang S. and Tang Y. (2011) Fundamental studies on kinetic isotope effect (KIE) of hydrogen isotope fractionation in natural gas systems. Geochim. Cosmochim. Acta 75, 2696–2707.

Passey B. H. and Henkes G. A. (2012) Carbonate clumped isotope bond reordering and geospeedometry. Earth Planet. Sci. Lett. 351–352, 223–236.

Pestilho A. L. S., Monteiro L. V. S., Carbonezi C. A., Jorge S. B. and Santos Neto E. V. (2018) Linking the geochemistry of crude oils and petroleum inclusions in the Ubarana and Lorena oilfields, Potiguar Basin, Brazilian Equatorial Margin. Org. Geochem. 124, 133–150.

Peters K. E., Walters C. C. and Moldowan J. M. (2004) The Biomarker Guide., Cambridge University Press.

Peterson B. K., Formolo M. J. and Lawson M. (2018) Molecular and detailed isotopic structures of petroleum: Kinetic Monte Carlo analysis of alkane cracking. Geochim. Cosmochim. Acta 243, 169–185.

Piasecki A., Sessions A., Lawson M., Ferreira A. A., Neto E. V. S. and Eiler J. M. (2016a) Analysis of the site-specific carbon isotope composition of propane by gas source isotope ratio mass spectrometer. Geochim. Cosmochim. Acta 188, 58–72.

Piasecki A., Sessions A., Lawson M., Ferreira A. A., Santos Neto E. V., Ellis G. S., Lewan M. D. and Eiler J. M. (2018) Position-specific 13C distributions within propane from experiments and natural gas samples. Geochim. Cosmochim. Acta 220, 110–124.

Piasecki A., Sessions A., Peterson B. and Eiler J. (2016b) Prediction of equilibrium distributions of isotopologues for methane, ethane and propane using density functional theory. Geochim. Cosmochim. Acta 190, 1–12.

Proskurowski G., Lilley M. D., Seewald J. S., Früh-Green G. L., Olson E. J., Lupton J. E., Sylva S. P. and Kelley D. S. (2008) Abiogenic hydrocarbon production at lost city hydrothermal field. Science (80-.). 319, 604–607.

Robins R. J., Romek K. M., Remaud G. S. and Paneth P. (2017) Non-statistical isotope fractionation as a novel “retro-biosynthetic” approach to understanding alkaloid metabolic pathways. Phytochem. Lett. 20, 499–506.

Romek K. M., Nun P., Remaud G. S., Silvestre V., Taïwe G. S., Lecerf-Schmidt F., Boumendjel A., De Waard M. and Robins R. J. (2015) A retro-biosynthetic approach to the prediction of biosynthetic pathways from position-specific isotope analysis as shown for tramadol. Proc. Natl. Acad. Sci. U. S. A. 112, 8296–8301.

Rossmann A., Butzenlechner M. and Schmidt H. L. (1991) Evidence for a nonstatistical carbon isotope distribution in natural glucose. Plant Physiol. 96, 609–614.

Sattler A. (2018) Hydrogen/Deuterium (H/D) Exchange Catalysis in Alkanes. ACS Catal. 8, 2296–2312.

Savage P. E. (2000) Mechanisms and kinetics models for hydrocarbon pyrolysis. J. Anal. Appl. Pyrolysis 54, 109–126.

Schimmelmann A., Sessions A. L. and Mastalerz M. (2006) Hydrogen Isotopic (D/H) Composition of Organic Matter During Diagenesis and Thermal Maturation. Annu. Rev. Earth Planet. Sci. 34, 501–533.

Schloemer S. and Krooss B. M. (2004) Molecular transport of methane, ethane and nitrogen and the influence of diffusion on the chemical and isotopic composition of natural gas accumulations. Geofluids 4, 81–108.

Sessions A. L., Sylva S. P., Summons R. E. and Hayes J. M. (2004) Isotopic exchange of carbon-bound hydrogen over geologic timescales. Geochim. Cosmochim. Acta 68, 1545–1559.

Shenton B. J., Grossman E. L., Passey B. H., Henkes G. A., Becker T. P., Laya J. C., Perez-Huerta A., Becker S. P. and Lawson M. (2015) Clumped isotope thermometry in deeply buried sedimentary carbonates: The effects of bond reordering and recrystallization. Bull. Geol. Soc. Am. 127, 1036–1051.

Spigolon A. L. D., Lewan M. D., de Barros Penteado H. L., Coutinho L. F. C. and Mendonça Filho J. G. (2015) Evaluation of the petroleum composition and quality with increasing thermal maturity as simulated by hydrous pyrolysis: A case study using a Brazilian source rock with Type I kerogen. Org. Geochem. 83–84, 27–53.

Stolper D. A. and Eiler J. M. (2015) The kinetics of solid-state isotope-exchange reactions for clumped isotopes: A study of inorganic calcites and apatites from natural and experimental samples. Am. J. Sci. 315, 363–411.

Stolper D. A., Lawson M., Davis C. L., Ferreira A. A., Santos Neto E. V., Ellis G. S., Lewan M. D., Martini A. M., Tang Y., Schoell M., Sessions A. L. and Eiler J. M. (2014a) Formation temperatures of thermogenic and biogenic methane. Science (80-.). 344, 1500–1503.

Stolper D. A., Martini A. M., Clog M., Douglas P. M., Shusta S. S., Valentine D. L., Sessions A. L. and Eiler J. M. (2015) Distinguishing and understanding thermogenic and biogenic sources of methane using multiply substituted isotopologues. Geochim. Cosmochim. Acta 161, 219–247.

Stolper D. A., Sessions A. L., Ferreira A. A., Santos Neto E. V., Schimmelmann A., Shusta S. S., Valentine D. L. and Eiler J. M. (2014b) Combined 13C-D and D-D clumping in methane: Methods and preliminary results. Geochim. Cosmochim. Acta 126, 169–191.

Suda K., Gilbert A., Yamada K., Yoshida N. and Ueno Y. (2017) Compound– and position–specific carbon isotopic signatures of abiogenic hydrocarbons from on–land serpentinite–hosted Hakuba Happo hot spring in Japan. Geochim. Cosmochim. Acta 206, 201–215.

Tang Y., Huang Y., Ellis G. S., Wang Y., Kralert P. G., Gillaizeau B., Ma Q. and Hwang R. (2005) A kinetic model for thermally induced hydrogen and carbon isotope

fractionation of individual n-alkanes in crude oil. Geochim. Cosmochim. Acta 69, 4505–4520.

Tang Y., Perry J. K., Jenden P. D. and Schoell M. (2000) Mathematical modeling of stable carbon isotope ratios in natural gases. Geochim. Cosmochim. Acta 64, 2673–2687.

Thiagarajan N., Kitchen N., Xie H., Ponton C., Lawson M., Formolo M. and Eiler J. (2020a) Identifying thermogenic and microbial methane in deep water Gulf of Mexico Reservoirs. Geochim. Cosmochim. Acta 275, 188–208.

Thiagarajan N., Xie H., Ponton C., Kitchen N., Peterson B., Lawson M., Formolo M., Xiao Y. and Eiler J. (2020b) Isotopic evidence for quasi-equilibrium chemistry in thermally mature natural gases. Proc. Natl. Acad. Sci. 117, 3989–3995.

Trindade L. A. F., Brassell S. C. and Santos Neto E. V. (1992) Petroleum migration and mixing in the Potiguar Basin, Brazil. Am. Assoc. Pet. Geol. Bull. 76, 1903–1924.

Ungerer P. (1990) State of the art of research in kinetic modelling of oil formation and expulsion. Org. Geochem. 16, 1–25.

Ungerer P., Behar F., Villalba M., Heum O. R. and Audibert A. (1988) Kinetic modelling of oil cracking. Org. Geochem. 13, 857–868.

Ungerer P., Collell J. and Yiannourakou M. (2015) Molecular modeling of the volumetric and thermodynamic properties of kerogen: Influence of organic type and maturity. Energy and Fuels 29, 91–105.

Vandenbroucke M. and Largeau C. (2007) Kerogen origin, evolution and structure. Org. Geochem. 38, 719–833.

Wang D. T., Gruen D. S., Sherwood Lollar B., Hinrichs K. U., Stewart L. C., Holden J. F., Hristov A. N., Pohlman J. W., Morrill P. L., Könneke M., Delwiche K. B., Reeves E. P., Sutcliffe C. N., Ritter D. J., Seewald J. S., McIntosh J. C., Hemond H. F., Kubo M. D., Cardace D., Hoehler T. M. and Ono S. (2015) Nonequilibrium clumped isotope signals in microbial methane. Science (80-.). 348, 428–431.

Wang Y., Sessions A. L., Nielsen R. J. and Goddard W. A. (2009) Equilibrium 2H/1H fractionations in organic molecules. II: Linear alkanes, alkenes, ketones, carboxylic acids, esters, alcohols and ethers. Geochim. Cosmochim. Acta 73, 7076–7086.

Webb M. A. and Miller T. F. (2014) Position-specific and clumped stable isotope studies: Comparison of the urey and path-integral approaches for carbon dioxide, nitrous oxide, methane, and propane. J. Phys. Chem. A 118, 467–474.

Weck P. F., Kim E., Wang Y., Kruichak J. N., Mills M. M., Matteo E. N. and Pellenq R. J. M. (2017) Model representations of kerogen structures: An insight from density functional theory calculations and spectroscopic measurements. Sci. Rep. 7, 7068.

Whiticar M. J. (1990) A geochemial perspective of natural gas and atmospheric methane. Org. Geochem. 16, 531–547.

Whiticar M. J. (1999) Carbon and hydrogen isotope systematics of bacterial formation and oxidation of methane. Chem. Geol. 161, 291–314.

Xia X. and Gao Y. (2018) Depletion of 13C in residual ethane and propane during thermal decomposition in sedimentary basins. Org. Geochem. 125, 121–128.

Xia X. and Gao Y. (2019) Kinetic clumped isotope fractionation during the thermal generation and hydrogen exchange of methane. Geochim. Cosmochim. Acta 248, 252–273.

Xia X. and Tang Y. (2012) Isotope fractionation of methane during natural gas flow with coupled diffusion and adsorption/desorption. Geochim. Cosmochim. Acta 77, 489–503.

Xiao Y. (2001) Modeling the kinetics and mechanisms of petroleum and natural gas generation: A first principles approach. Rev. Mineral. Geochemistry 42, 382–436.

Xie H., Dong G., Thiagarajan N., Shuai Y., Mangenot X., Formolo M. J., Lawson M. and Eiler J. M. (2019) Methane Clumped Isotopologues With High-resolution Gas Source Isotope Ratio Mass Spectrometry. In AGU.

Xie H., Ponton C., Formolo M. J., Lawson M., Peterson B. K., Lloyd M. K., Sessions A. L. and Eiler J. M. (2018) Position-specific hydrogen isotope equilibrium in propane. Geochim. Cosmochim. Acta 238, 193–207.

Young E. D., Kohl I. E., Lollar B. S., Etiope G., Rumble D., Li (李姝宁) S., Haghnegahdar M. A., Schauble E. A., McCain K. A., Foustoukos D. I., Sutclife C., Warr O., Ballentine C. J., Onstott T. C., Hosgormez H., Neubeck A., Marques J. M., Pérez-Rodríguez I., Rowe A. R., LaRowe D. E., Magnabosco C., Yeung L. Y., Ash J. L. and Bryndzia L. T. (2017) The relative abundances of resolved l2CH2D2 and 13CH3D and mechanisms controlling isotopic bond ordering in abiotic and biotic methane gases. Geochim. Cosmochim. Acta 203, 235–264.

Young E. D., Rumble D., Freedman P. and Mills M. (2016) A large-radius high-mass-resolution multiple-collector isotope ratio mass spectrometer for analysis of rare isotopologues of O2, N2, CH4 and other gases. Int. J. Mass Spectrom. 401, 1–10.

Zhao H., Liu C., Larson T. E., Mcgovern G. P. and Horita J. (2020) Bulk and position-specific isotope geochemistry of natural gases from the Late Cretaceous Eagle Ford Shale, south Texas. Mar. Pet. Geol.

Zumberge J. E., Curtis J. B., Reed J. D. and Brown S. W. (2016) Migration happens: Geochemical evidence for movement of hydrocarbons in unconventional petroleum systems. In SPE/AAPG/SEG Unconventional Resources Technology Conference 2016 Unconventional Resources Technology Conference (URTEC).

Appendix 3

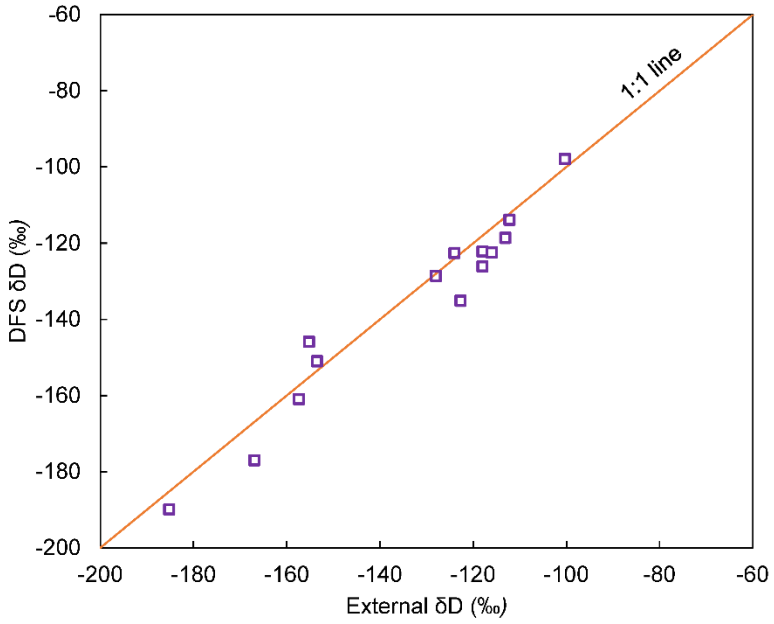

Figure 3-A1: A comparison of molecular δD_{VSMOW} of propane measured by DFS and in other laboratories ('external'). DFS results are based on molecular ion measurements ($[C_3H_7D^+]/[C_3H_8^+]$). External measurements were made with GC-py-IRMS, with expected 1σ error of 3-5‰.

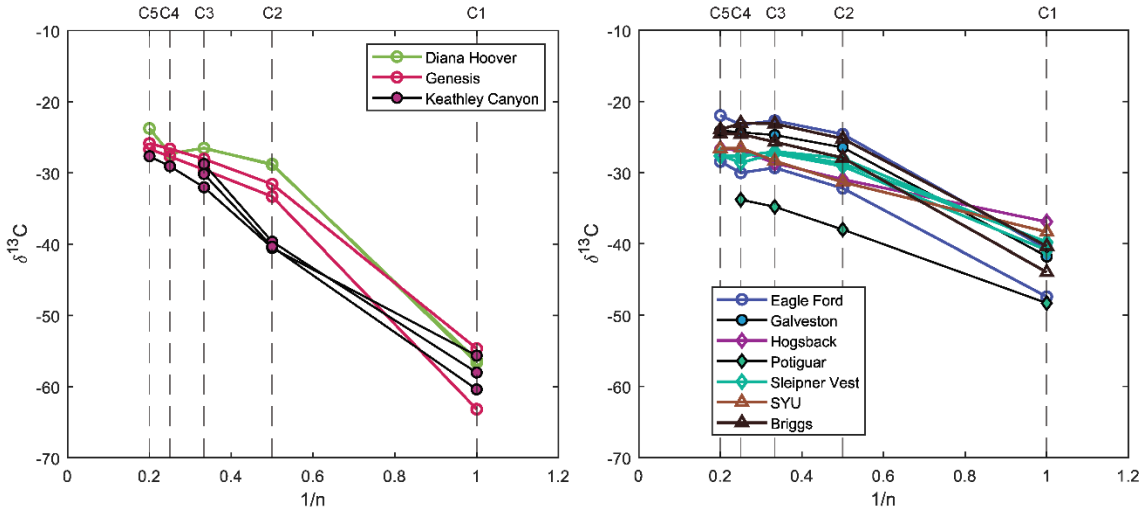

Figure 3-A2: Compound-specific carbon isotope data of studies natural gas samples in this study. The x-axis, 1/n, denote reciprocal of the alkane chain length. Left panel: gases with potential microbial methane input and/or hydrocarbon consumption. (See Thiagarajan et al. (2020a) and Section 5.4.2 of this chapter). Right panel: gases of thermogenic origin.

Table A1: Kinetic parameters for homolytic dissociation of single bonds in the kinetic Monte-Carlo model. Hydrogen KIE is for hydrogen bonded to the carbon position with asterisk. Temperature is set at 180 °C.

	Carbon KIE($k^{12}C/k^{13}C$)			Hydrogen KIE (kH/kD)		
Bond type	1°	2°	3°	1°	2°	3°
C*-C(aliphatic)	1.025	1.024	1.017	1.277	1.198	1.184
C*-C(aromatic)	1.024	1.014	1.010	1.242	1.165	1.151
C*-N	N/A					
C*-O	1.024	1.018	1.014	1.339	1.257	1.242
C*-S	1.013	1.019	1.015	1.267	1.189	1.175
Adjacent[#]	1.002	1.006	1.006	1.034	0.990	0.990

[#]This denotes KIE of isotopically substituting the C/H position adjacent to the cracking position, which is formally secondary KIE for carbon and tertiary KIE for hydrogen. The adjacent isotope KIE is treated to be the same for all bonding environments.

Chapter 4 Hydrogen Isotope Exchange Equilibrium in C1-C5 Alkanes

Abstract

Stable isotope ratios of C1–C5 alkanes, the major constituents of subsurface gaseous hydrocarbons, can provide valuable insights on their origins, transport, and fates. Equilibrium isotope effects are fundamental to interpreting stable isotope signatures, as recognition of them in natural materials indicates reversible processes and constrains the temperature of the equilibrating system. Hydrogen isotope equilibrium of C1–C5 alkanes is of particular interest because evidence shows that alkyl H can undergo isotopic exchange with coexisting compounds under subsurface conditions. Both the trajectory through isotope composition space associated with the exchange process and the final equilibrium state might be used to constrain the thermal evolution of fluids. Although the equilibrium isotope effects can be calculated with theoretical methods, systematic inaccuracies in such models make it necessary to determine and calibrate them accurately in laboratory experiments. We present the first experimental effort to exchange and equilibrate hydrogen isotope distribution of mixtures of these hydrocarbon molecules. We created two mixtures: one with C1, C2, and C3 (where C1 indicates methane, C2 ethane, etc.) and another one with C2, C3, iC4, nC4, iC5, and nC5; in both cases, the mixtures were created to be out of hydrogen isotope equilibrium. We conducted

laboratory experiments involving exposure of these mixtures to different metal catalysts at 100 or 200 ˚C for controlled times, after which we analyzed the compound-specific hydrogen isotope ratios of the product gases. We tested the performance of several metal catalysts. In the presence of Ru/Al_2O_3 catalyst, the C1–C3 mixture exchanges hydrogen isotopes among the co-existing compounds rapidly at 200°C. The isotope ratios remained unchanged after 72 hours of heating (up to 120 hours), indicating that a steady-state had been reached, consistent with full equilibration. The hydrogen isotopic ratios of C2 to C5 molecules shift substantially in a short amount of time in the presence of Rh/Al_2O_3 at 100°C. However, isotope ratios of ethane and propane are still changing between 12h and 48h of heating (the last time in this time series), i.e., steady state had not been reached by this point. However, we predicted the final hydrogen isotope compositions towards which C2 and C3 were evolving in these low-temperature experiments by evaluating the reaction progress of isotope exchange for each compound as a function of time, fitting a reaction-network model to experimental data. The model simulates the evolution of hydrogen isotope ratios and thus the trajectories samples follow through the composition space defined by the compound specific δD values, letting us extrapolate to the final equilibrium fractionation factors and errors associated with these factors. We executed the model for both the C1–C3 and C2–C5 mixture experiments. Model-estimated equilibrium isotope effects for every pair of compounds match theoretically predicted values in both experiments, which were calculated with the

Bigeleisen-Meyer theorem using vibrational frequencies derived from density functional theory (B3LYP/aug-cc-pVTZ level). Our study also reveals that hydrogen isotope ratios and inter-compound isotopic fractionations involving certain species do not always evolve monotonically towards equilibrium values during the exchange process; instead, it might depart from equilibrium in the early stage of reaction before finally approaching it.

1. Introduction

C1–C5 alkanes in the natural environment are important energy and chemical-engineering resources, potent pollutants, and microbial metabolites. Stable isotope ratios of these alkanes have been useful in tracing their sources, probing their formation pathways and environments, and discerning non-chemical processes such as mixing and transport. In subsurface petroleum reservoirs, stable isotope ratios indicate thermal maturity of gas generation (Berner and Faber, 1996), type of source organic matter (Galimov, 2006), and microbial degradation or methanogenesis (Whiticar, 1999; Boreham et al., 2008).

Compared to carbon isotopes, little attention has been focused on the study of hydrogen isotope ratios of these alkanes, especially for C2 and higher alkanes. Far fewer samples have been measured for compound specific D/H than for $^{13}C/^{12}C$ (Sherwood et al., 2017; Milkov and Etiope, 2018) and less is known about the information that can be deduced

from the hydrogen isotope data that do exist. However, we value hydrogen isotope data for two reasons. Firstly, the relative mass difference between protium (^{1}H) and deuterium (^{2}H) is the largest amongst all isotopes. Consequently, hydrogen isotope effects for chemical or physical processes are substantially larger than carbon isotope effects and create significant variations in natural samples. Secondly and more specifically, studies have shown experimental and observational evidence that alkanes can be susceptible to catalyzed H-isotope exchange at temperatures only slightly elevated compared to earth-surface conditions (Sessions et al., 2004; Schimmelmann et al., 2006; Xie et al., 2020). Hydrogen isotope exchange has the potential to drive intermolecular isotope fractionations towards equilibrium isotope distributions, which are controlled by thermodynamic equilibrium and therefore suitable for quantitative geothermometry. Moreover, it has been shown that even non-equilibrated isotopic distributions between and within hydrocarbons can usefully constrain geological histories, as the progress of isotope exchange (or departure from equilibrium isotope distributions) provides constraints on thermal maturity of natural gas (Xie et al., 2021).

Gauging extent of isotope exchange reactions and attainment of equilibrium distributions and use of isotopic data for equilibrated samples for geothermometry all require accurate constraints on equilibrium isotope effects. More generally, equilibrium isotope effects are fundamental constants of broad geochemical importance because they can be used to distinguish reversible processes from irreversible processes. Accurate equilibrium

hydrogen isotope effects of alkanes can serve as cornerstone for interpreting hydrogen isotope data in studies not limited to the topic of thermogenic natural gas, such as abiotic formation of hydrocarbons in hydrothermal fluids and microbial hydrocarbon recycling in the surface aqueous environments.

The purpose of this study is to experimentally create and analytically document hydrogen isotope equilibrium in C1–C5 alkanes. These alkanes include the isomers of butane and pentane (excepting neopentane, which is usually only a trace component of natural hydrocarbons). We use heterogeneous catalysts to promote hydrogen isotope exchange and compound-specific hydrogen isotope ratio mass spectrometry for analysis. We also compare the experimentally observed fractionations to theoretical values computed by quantum chemistry methods, both to assess the self-consistency of experiment and theory and as a basis for evaluating the accuracy of theory as a constraint on isotopic properties that have not yet been observed experimentally.

2. Methods

2.1. Nomenclature

We report hydrogen isotope ratios in units of δD (synonym of the IUPAC recommended δ^2H) on the VSMOW scale. We report the isotope fractionation between two compounds using the ε value:

$$\epsilon D_{A-B} = \frac{\left(\frac{D}{H}\right)_A}{\left(\frac{D}{H}\right)_B} - 1. \quad (1)$$

2.2. Calculation of equilibrium isotope effects

Equilibrium isotope effects between alkanes are calculated with the Bigeleisen-Mayer (B-M) method (Bigeleisen and Mayer, 1947), also known as Urey-Bigeleisen-Mayer method. Reduced partition function ratios (β values) are calculated for every singly substituted and non-substituted isotopologues of C1-5 alkanes from methane to n-pentane. The equilibrium isotope effect between two alkanes equals to the ratio between their molecule-average β values, which are averaged from β values of singly substituted isotopomers of each compound, with the number of equivalent positions as weights. Harmonic vibrational frequencies are computed using density functional theory (DFT) with the B3LYP hybrid functional and the Dunning correlation-consistent triple-zeta basis set with added diffuse functions: aug-cc-pVTZ, as reported in one of our previous studies (Thiagarajan et al., 2020).

The approach used here involves several approximations that may influence our results. The B-M theorem assumes harmonic vibration, rigid rotation, and the Born-Oppenheimer approximation. Prior studies have shown that partition function ratios for hydrogen isotopes can have nontrivial effects of vibrational anharmonicity and vibrational-rotational coupling (Bigeleisen and Mayer, 1947; Richet et al., 1977), although these error are substantially canceled when taking the ratio of β values. Corrections to the B-M theorem and alternative *ab initio* methods have been developed to account for these effects (Liu et al., 2010; Marklanda and Berneb, 2012; Webb and Miller, 2014; Webb et al., 2017). It has been previously shown that the hydrogen isotope fractionation between methylene and methyl moieties in propane, a system relevant to our research, suffers from a combined error of range from 1 to 3 ‰ at 0–200°C when calculated using the B-M equation (Webb and Miller, 2014; Liu et al., 2021). Such errors are smaller than the long-term analytical uncertainty of the method we use for compound specific dD measurement (5‰), so we consider the B-M theorem satisfactorily accurate for our study. Similarly, it was shown that harmonic theoretical values are reasonably consistent (within 10‰ at 0–100°C) with experimental values for hydrogen isotope equilibrium between water and ketone molecules (Wang et al., 2009a). We adopt a suggestion from Liu et al. (2010) to scale the zero point vibrational energies (ZPVE) terms in the B-M equation with a scale factor, λ=0.9867, that is specific to the

B3LYP/aug-cc-pVTZ level of theory (Sinha et al., 2004). Figure 4-1 shows intermolecular equilibrium isotope effects calculated with this approach.

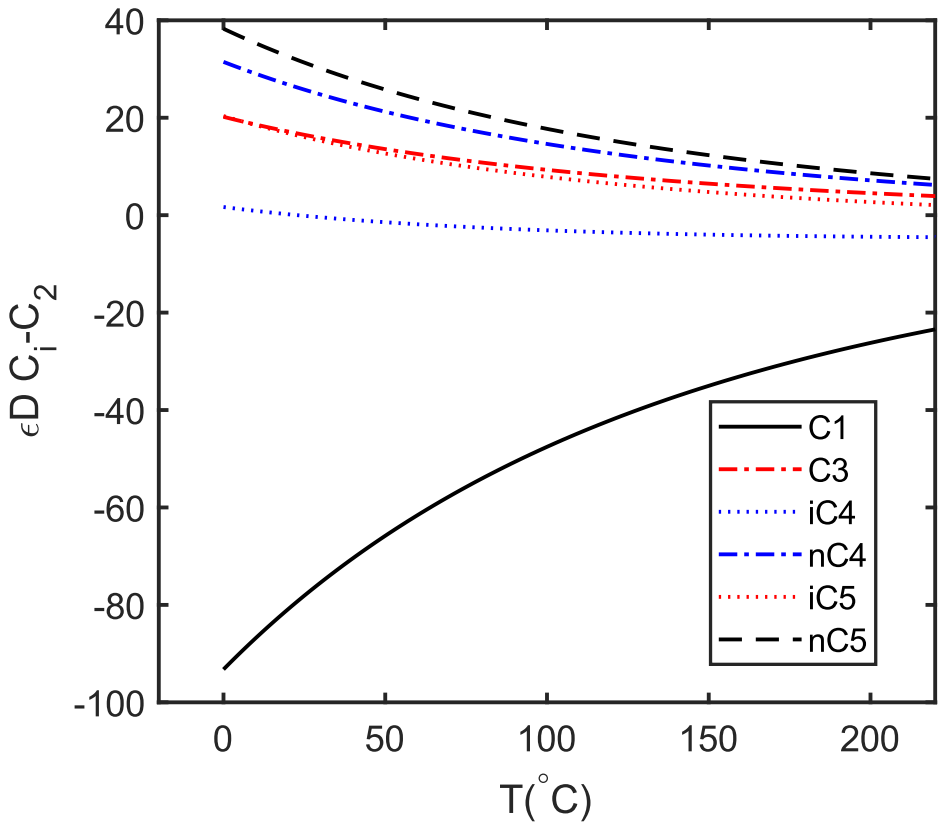

Figure 4-1. Theoretical predictions of equilibrium hydrogen isotope effects between alkanes, calculated with the B-M theorem and DFT at B3LYP/aug-cc-pVTZ settings (See methods section for details). All fractionation factors are referenced to ethane.

Piasecki et al. (2016) reported vibrational frequencies for isotopologues of methane, ethane and propane calculated from the B3LYP hybrid functional and a split-valence triple-zeta basis set: 6-311G**. Equilibrium isotope effects calculated from their frequencies are almost identical to those calculated with the aug-cc-pVTZ level theory, e.g., $\varepsilon D_{C3\text{-}C1}$ and $\varepsilon D_{C2\text{-}C1}$ values are within 0.2‰ between the two basis sets at relevant temperature. Wang et al. (2009b) presented equilibrium hydrogen isotope effects for primary, secondary and tertiary positions based on B-M theorem with the B3LYP/6-311G** level of theory using C_7 molecules as targets, but their values might not be applicable to C1–C5 alkanes because local chemical structures are different. It was demonstrated that accurate 'cutoff' calculations demand identical local structures within three bonds of the target position (He et al., 2020). Liu et al. (2021) reported equilibrium isotope effects for isotopologues of n-butane and i-butane from the coupled cluster method, CCSD(T), and 6-311G** basis set. They report an additional set of values with a series of corrections to the B-M theorem, including vibrational anharmonicity, vibrational-rotational coupling, quantum-mechanical rotation, centrifugal distortion, hindered internal rotation, and diagonal Born-Oppenheimer correction. For εD between n-butane and i-butane, B3LYP/aug-cc-pVTZ results are in minor disagreement with results from uncorrected and corrected CCSD(T)/6-311G** values. The biggest difference within these three sets is between B3LYP and CCSD(T) + corrections, which

is 6.9‰ at 100°C. However, this discrepancy is still less than 2σ error of our mass spectrometric analysis, and so it is unlikely we will resolve differences among these levels of theory (i.e., establishing which are closer or further from measured equilibrium fractionations) using our experimental data. However, we note for the purposes of possible future studies that high-resolution mass spectrometry is capable of measuring δD of alkanes with precisions as good as ~0.1 ‰, and so it is possible that one could experimentally test the relative accuracies of these various models.

2.3. Creation of alkane mixtures in isotope disequilibrium

We created two alkane mixtures, one with methane, ethane and propane (hereinafter called 'C1–C3 mixture') and another one with ethane, propane, iso-butane, n-butane, iso-pentane and n-pentane (hereinafter called 'C2–C5 mixture'). The main reason for doing two sets of exchange experiments separately is that hydrogen isotope exchange for ethane and higher alkanes have different kinetics and preference of catalysts as compared to methane (Bond, 2006). On metal catalysts, methane usually exchanges slower than C2+ alkanes (Sattler, 2018). Furthermore, we found that C4 and C5 alkanes tend to be significantly lost by destructive side reactions before reaching equilibrium at 200°C in early tests of catalysts, so lower temperature is required, making it difficult to simultaneously equilibrate methane and preserve C4-5 alkanes with a single catalyst and

temperature. Consequently, we performed C1–C3 experiments at 200°C and C2–C5 experiments at 100°C.

Methane, ethane and propane were sourced from commercial pure gas tanks (99%) from Air Liquide. Butanes and pentanes were from pure gas cylinders (99%) from Sigma Aldrich. All components except methane were cryogenically purified in a vacuum line at liquid nitrogen temperature to remove air before mixing. We attempted to mix each component in an amount that would contribute an even amount of hydrogen to the overall mixture, as opposed to mixing equal molar quantities (Table 4-1). The original methane had a $\delta D = -175‰$, which was too close to the projected equilibrium value. In order to ensure that methane had unambiguous hydrogen isotope change during the experiments, we added $^{12}CH_3D$ (99%, from Sigma Aldrich) spike to the mixture. The enriched mixture has $\delta D_{C1} = -125‰$. Both the C1–C3 and C2–C5 mixtures are significantly out of isotopic equilibrium prior to heating (Figure 4-2).

Table 4-1. Molecular and isotopic composition of the original alkane mixtures in our study.

		C1	C2	C3	i-C4	n-C4	i-C5	n-C5
C1–C3	% mol	0.57	0.20	0.23				
mixture	δD (initial)	-125	-105	-173				

	δD (equilibrium)	-152	-129	-125				
C2–C5 mixture	% mol		0.50	0.14	0.12	0.07	0.10	0.07
	δD (initial)		-114	-171	-153	-167	-106	-110
	δD (equilibrium)		-135	-127	-138	-122	-128	-118

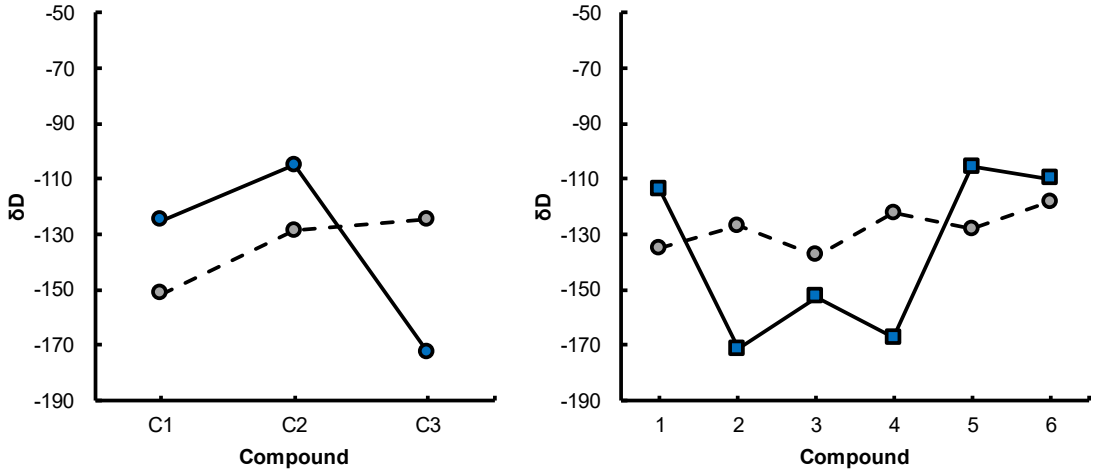

Figure 4-2. Initial hydrogen isotope compositions of our hydrocarbon mixtures and prediction of equilibrium composition. Blue squares and solid line show initial values; Gray circle and dashed line show expected equilibria.

2.4. Exchange experiments

Isotope exchange experiments were conducted by heating gas mixtures in the presence of metal catalyst in Pyrex tubes. Based on a literature review of the activities of heterogeneous catalysts (Bond, 2006; Sattler, 2018), we focused our study on five catalysts: Pd/C (10% loading, powder), Pd/Al_2O_3 (10% loading, powder), Rh/Al_2O_3 (5% loading, powder), Rh/Al_2O_3 (0.5% loading, pellet), and Ru/Al_2O_3 (5% loading, powder). All catalysts are commercial products from Sigma-Aldrich. Each tube (1–2cc) was loaded with 40-60mg of catalyst in an anaerobic environment. Catalyst was then degassed by heating with a torch flame (500–600°C) under vacuum for 3 minutes. One of the gas mixtures was then condensed into the tube at liquid nitrogen temperature, transferred through a glass vacuum line. We prepared 140 μmol of one or the other gas mixture in each sample tube. The tube was then flame sealed and placed in an oven for a controlled time varying from several hours to weeks. The oven has automatic temperature control that keeps the temperature within +/- 0.5 °C of the set point.

After heating, the pyrex tube was removed from the furnace and cooled to room temperature in air. We then cracked the pyrex tube under vacuum using a flexible tube cracker and transferred the evolved gas to a known volume in a glass vacuum line and recorded its total pressure (constraining the amount of gas remaining after heating). The gas was then transferred through the vacuum line to a second glass tube immersed in liquid nitrogen. For experiments with C1–C3 mixture, we put degassed 5A molecular sieve into the tube beforehand to trap methane. This second glass tube was then flame-sealed and moved to the gas chromatograph - mass spectrometer system (below) for isotopic analysis.

We conducted blank experiments to rule out experimental artifacts, such as losses and/or isotopic fractionations associated with gas handling or cracking or other side reactions. In these experiments, mixed gases are loaded into the tube with catalysts but kept at room temperature.

2.5. Molecular and hydrogen isotope analysis

Molecular compositions of the mixtures before and after heating were analyzed at Caltech on a quadruple gas chromatography/mass spectrometer (GC/MS) system, the Thermo Fischer Scientific ISQ. The GC uses an Agilent GS-GasPro column. We

standardized these measurements using a reference gas mixture made of 80% methane, 10% ethane, 5% propane, and 5% CO_2.

Compound-specific hydrogen isotope analysis of starting and post-heating gas mixtures was done at Caltech on a GC/pyrolysis/isotope ratio mass spectrometer (GC/Py/IRMS) system. The sample glass tube is cracked and gas expanded into a small volume (~2ml) that has a rubber septum on one end. For samples of the C2–C5 mixture, this volume was warmed to 80 °C to avoid partial condensation of C4 and C5 alkanes, which might lead to isotopic fractionation of remaining vapor. For samples of the C1–C3 mixture, the sample tube is heated at 150°C for two hours to desorb the alkanes from molecular sieve (Stolper et al., 2014). We use a gas-tight syringe to sample the gas from the septum. Around 10–100µL of gas is used per injection. For measurements of the C1–C3 mixture, a GS-GasPro column is used. For measurements of the C2–C5 mixture, either a GS-GasPro and a Zebron ZB-5ms column is used. The pyrolysis tube used to convert alkanes to H_2 for isotopic analysis is heated to 1375 °C. In-house H_2 gas or CH_4 gas injections bracket sample injections and serve as reference standards. 1–3 replicate measurements are made for each sample. Long term external precision for δD is 5‰ (1σ per injection).

3. Results

Results of both Rh and Pd blank experiments do not show change in hydrogen isotope compositions from those of the original mixtures (Table 4-2).

Table 4-2. Results from blank tests and exchange experiments.

Time(h)	C1	C2	C3			
0	-125	-105	-173			
12	-140	-117	-145			
24	-147	-132	-133			
72	-154	-134	-130			
120	-155	-132	-127			
	C2	C3	i-C4	n-C4	i-C5	n-C5
Original	-114	-171	-153	-167	-106	-110
Rh/Al2O3 blank	-111	-171	-147	-158	-105	-111
Pd/C blank	-115	-176	-153	-165	-103	-106
0	-114	-171	-153	-167	-106	-110
0.5	-114	-167	-152	-156	-117	-115
12	-122	-133	-131	-111	-115	-112
48	-142	-122	-135	-117	-125	-116

In experiments aimed at equilibrating the hydrogen isotope fractionations in the C2–C5 mixture, we found that Rh/Al_2O_3 (5% loading, powder) is the most active catalyst. At 100 °C, hydrogen isotope compositions of every component shifted toward the equilibrium composition over a few days (Figure 4-3). At the end of the longest of these experiments, δD_{C2} decreased by 28‰; δD_{C3} increased by 50‰; δD_{iC4} increased by 18‰; δD_{nC4} increased by 18‰; δD_{iC5} decreased by 19‰; and δD_{nC5} decreased by 6‰ (a negligible change, based on analytical uncertainties).

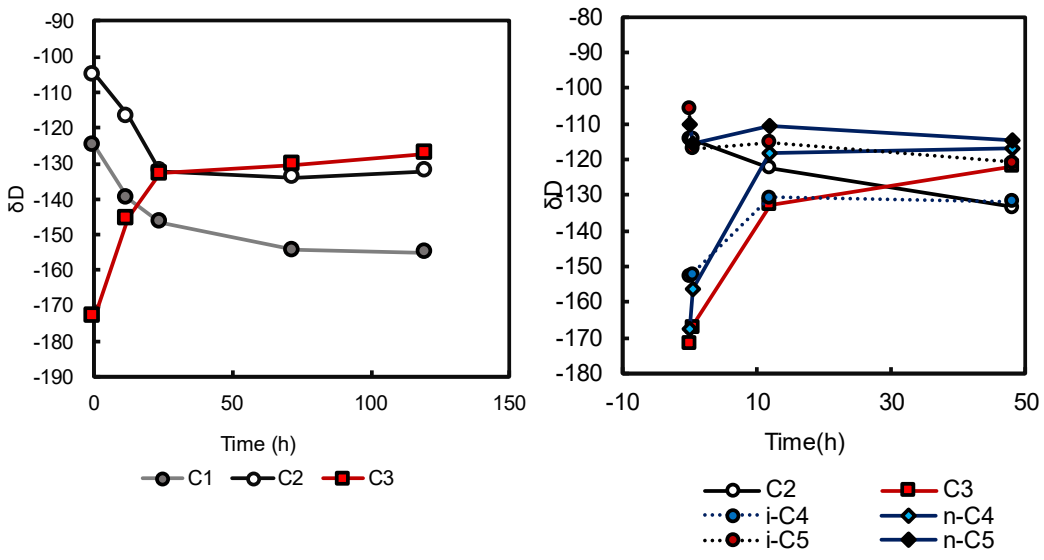

Figure 4-3. Left: evolution of hydrogen isotope composition in the C1–C3 mixture exchange experiment. T=200°C and catalyst is Ru/Al_2O_3. Right: evolution of hydrogen

isotope composition in the C2–C5 mixture exchange experiment. T=100°C and catalyst is Rh/Al_2O_3.

In the experiments aimed at equilibrating the C1–C3 mixture, we found that Ru/Al_2O_3 is the most active catalyst. At 200 °C, hydrogen isotope ratios changed significantly in a few days (Figure 4-3). At the end of the longest of these experiments, δD_{C1} decreased by 30‰; δD_{C2} decreased by 27‰; δD_{C3} increased by 46‰. The hydrogen isotope compositions are not distinguishable between the 72h sample and the 120h sample, indicating that the mixture had attained a steady-state, and so plausibly reached equilibrium.

We report results of these two series of experiments in Table 4-2. In Figure4-A.1 we report results from several experiments using less effective catalysts that did not undergo substantial hydrogen isotope exchange.

4. Discussion

4.1. Modeling isotopic evolution during the hydrogen isotope exchange process

We attained a steady-state, and therefore plausibly equilibrium state in the C1–C3 exchange experiments, so equilibrium isotope effects for C1/C2/C3 can be inferred from the final state of the time series. However, the C2–C5 experiments still show statistically meaningful changes in isotope ratios of some compounds between the last and second-to-last samples. Evaluation of the progress of exchange reactions for this time-series is needed if we are to use these data to estimate the equilibrium isotope effects that would eventually be attained with even longer heating. It is difficult to quantify the extent of reaction directly in a system where exchange happens simultaneously for many molecules. A common mathematical treatment of isotopic exchange is a pseudo-first order approximation, which has isotopic ratios or difference between isotopic ratios approach the equilibrium value via an exponential decay function (Roberts, 1939; Criss et al., 1987; Sessions et al., 2004; Labidi et al., 2020). However, this simplistic form does not apply to a multi-endmember exchange environment like our experiments. In our experiments, isotopic values and epsilon values can have non-monotonic paths to equilibrium because different compounds/moieties exchange at different rates. In the C2–C5 mixture experiment, C4 and C5 compounds exchange faster than C2 and C3. Hydrogen isotope compositions of C4 and C5 shift rapidly in the first 12 hours and the become invariant with time, while C2 and C3 seem to exchange steadily and continue to change their hydrogen isotope compositions between 12 and 48 hours. In the C1–C3 mixture experiment, fractionation between C2 and C3 approaches equilibrium around

twice as fast as do C1 and C2 or C1 and C3. The heterogeneity in exchange rates can produce non-monotonic trends in hydrogen isotope ratio evolution. This phenomenon has been observed in prior studies and has been attributed to a decrease in bond dissociation energies (BDE) with increasing carbon degrees (Sattler, 2018).

We develop a reaction network model to simulate the evolution of hydrogen isotope compositions in our experiments. This model allows us to evaluate the progress of hydrogen isotope exchange and constrain the equilibrium values that would be attained at longer times. This model considers the elementary reactions of chemisorption and desorption of alkanes on a metal surface:

$$R - H + M \rightleftharpoons R - M + M - H \quad (3)$$

Note that α-β, α-γ, and α-β-γ multi adsorptions are alternative mechanisms for C2 and higher order alkanes. Regrettably, there has been no quantitative estimation of the relative strengths of these mechanisms (Bond, 2006), so we do not include them in our model. This model has a total of 44 unique isotopologues of the various molecular species and 60 unique isotope exchange reactions. The molecules include gas-phase molecules with no isotopic substitutions and single-deuterium substitutions, metal-bound molecules with no substitutions and metal bound ^{1}H and D. The reactions include forward and backward reactions of varieties of eqn 3. The kinetic treatments of reactions are based on the observation that the activation energy of the desorption reaction is proportional to the

BDE of that C–H bond, as discussed earlier. We use the reaction of methane adsorption/desorption as the reference reaction. The rate constants of a non-methane reaction could then be calculated from

$$\frac{k}{k_0} = \exp\left(-\frac{sf * \Delta BDE}{RT}\right). \quad (4)$$

sf denotes a scale factor. BDE is 438.9 kJ/mol for methane, and 420.9/410.5/400.0 for primary/secondary/tertiary carbon positions, respectively (Luo, 2007). For the D-substituted version of reaction eqn. (3), we modify the reaction rate constant with a kinetic isotope effect (KIE). The KIE is treated as equal to the zero-point energy (ZPE) differences (ZPE_H-ZPE_D) in the reactants, as we are not aware of a previous quantitative simulation on the isotope substitution in the transition states. In practice, we set KIE(kD/kH) to equal to 1/β, where β is the reduced partition function ratio. This treatment also directly parameterizes the equilibrium isotope effects into the kinetic model.

There are two additional benefits of making this model. First, we can estimate uncertainty on the equilibrium isotope effects via creating noise in the experimental dataset with a Monte Carlo method and populate a distribution of fitted parameters. Second, we can establish a mechanistic framework for modeling alkyl-H exchange on catalytic surfaces

that could be applied to exchange in real environments, which will be discussed in the last section of the paper.

We initialize the model with only gas-phase molecules (adsorbed molecules and hydrogen atoms are set to have zero concentrations). The starting isotopic compositions of the gas molecules equals those of the initial gases in the prepared mixtures (Table 4-1). Initial intramolecular (position-specific) isotope distributions are assumed to be homogenous. The reaction network is modelled via a set of ordinary differential equations. We solve it numerically with a variable-step, variable-order solver based on the numerical differentiation formulas of orders 1 to 5 (MATLAB ode15s).

We fit parameters of the model to experimental data via the least square method. The fitted parameters are KIE values, the scale factor for activation energy to BDE relationships and rate constants of the reference methane exchange reaction. In KIE calculations, we constrain ZPE differences between two positions on the same molecule as equal to the quantum chemical predictions, as the intramolecular equilibrium isotope effects have been experimentally validated (Xie et al., 2018). For the scale factor, we allow it to vary from 0.05 to 0.4, which is based on the range of ratios between catalyzed activation energy (28–156 kJ/mol) and BDE (400–438 kJ/mol). We will also examine the C1–C3 experiment with this model, albeit the equilibrium state was attained at the end of these higher temperature experiments.

4.2. Model results and equilibrium values

The model succeeded in fitting our experimental data for both experiments (Figure 4-4). Reduced χ^2 of our model is 0.85 for the C1–C3 experiment and 0.81 for the C2–C5 experiment. We normalize all ε values to ethane in Figure 4-4, because ethane is present in both series of experiments. In the C1–C3 experiment series, it shows that both the 120h sample and the 72h sample should be indistinguishable from equilibrium. In the C2–C5 experiment, it shows that the 48h sample should be indistinguishable from equilibrium and the 12h sample is still away from equilibrium. The high goodness of fit between model trends and experimental data on the non-equilibrated part of the time series validate that exchange kinetics are controlled by BDE of C–H bonds. Model results reproduce non-monotonic trajectories of isotopic ratios during the exchange process. For example, the isotope fractionation between iC5 and C2 ($\varepsilon D_{iC5\text{-}C2}$) drops by 12‰ at from 0h to 0.5h and increases by 11‰ from 0.5h to 12h in this series of experiments. This feature is captured by a dip in the model curve and is likely caused by the fast exchange on the tertiary carbon position of iC5. At 100°C, the fitted scale factor yields that tertiary carbon positions exchange 2× faster than secondary carbon positions and 4× faster than primary carbon positions. Since iC5 has a relatively high hydrogen isotope ratio in the beginning of experiment, exchange in the early stage decreases its hydrogen isotope values. Therefore, a relatively fast exchange on the tertiary position creates a dip on the hydrogen isotope curve.

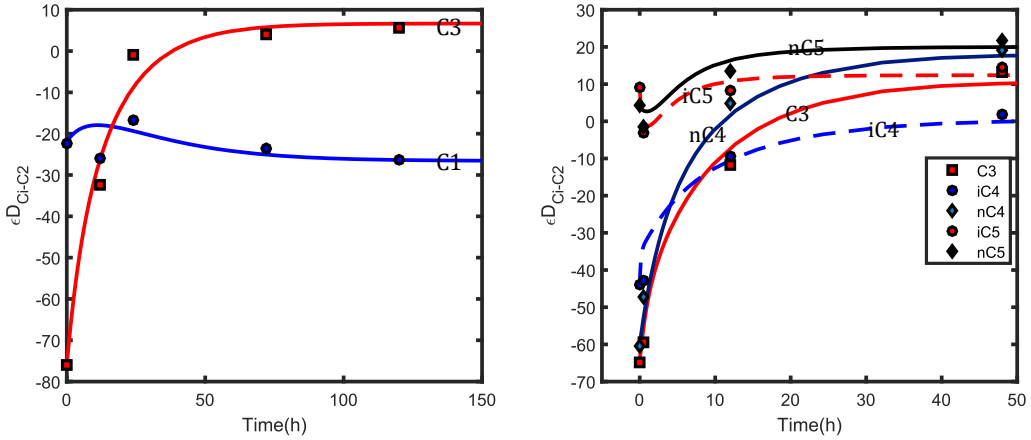

Figure 4-4. Hydrogen isotope fractionation normalized to ethane during experiments. Left: C1–C3 mixture exchange experiment. Right: C2–C5 mixture exchange experiment. Model results with best-fit parameters are shown in the curves.

The equilibrium isotope effects (normalized to C2, again) from the model best-fit parameters are reported in Table 4-3. We perform a Monte Carlo analysis to estimate their errors. We introduce noise to the experimental data set by generating normally distributed random deviations from the measured δD values. The magnitude of random deviation is set to follow a probabilistic normal distribution function with experimental

error (5‰) as sigma. This process is repeated to produce a distribution of model parameters that can be used to calculate error in equilibrium isotope effects (ε values). We visualize the results of this Monte Carlo analysis in Figure 4-5.

Table 4-3. Equilibrium isotope effects derived from experimental results, in comparison with theoretical predictions. B3LYP means results calculated with B-M equation and DFT at B3LYP/aug-cc-pVTZ settings. CCSD(T)corr denotes results calculated with corrections to B-M theorem and CCSD(T)/6-311G** (Liu et al., 2021).

	C1-C2	C3-C2	iC4-C2	nC4-C2	iC5-C2	nC5-C2	nC4-iC4
100C exp.		10.4	0.3	17.8	12.4	20.0	17.5
1σ		6.7	6.2	6.6	5.7	6.0	7.0
B3LYP		9.3	-3.1	14.6	7.9	17.7	17.8
CCSD(T)corr							10.9
200C exp.	-26.5	6.6					
1σ	5.3	5.7					
B3LYP	-26.2	4.5					

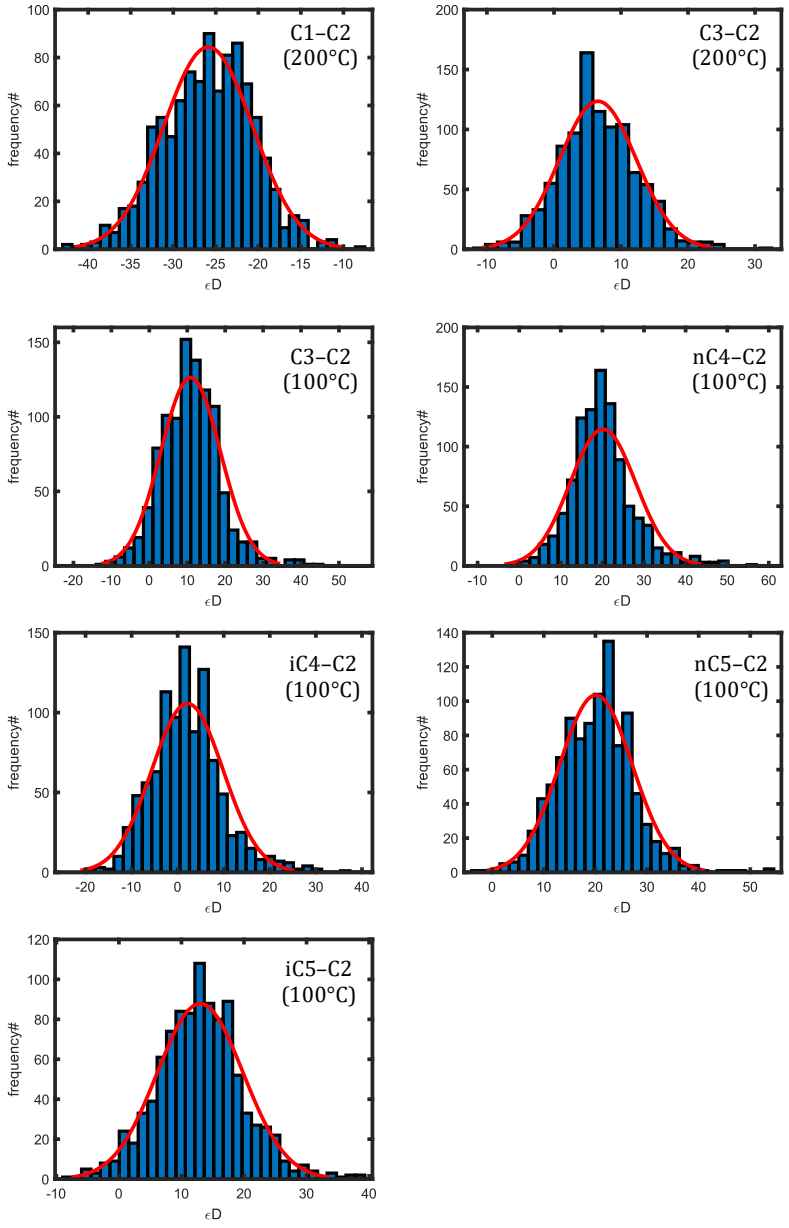

Figure 4-5. Bootstrap Monte Carlo sampling results of noise in equilibrium isotope effects for multiple molecular pairs in our study. N=1000 for both experiments.

We compare our experimental results on equilibrium isotope effects with theoretical predictions in Figure 4-6. They are overall in good agreement (<1σ) with B3LYP results for both series of experiments (100°C and 200°C). For the molecule pair of nC4–iC4, the theoretical value of ε from CCSD(T)/6-311G** with B-M corrections is also within uncertainty of experimental result. This agreement demonstrates that results from B-M theorem with harmonic vibration and rigid rotation are satisfactory for the current precision of online GC/Py/IRMS analysis. Alternative analytical techniques can reduce uncertainty — the offline reduction method (Schimmelmann, 1991) can achieve an uncertainty of 1–2‰ and the direct molecular method (Stolper et al., 2014) can achieve an uncertainty of 0.1–0.2‰. When these more precise techniques are applied, the nuanced differences in theory will be important.

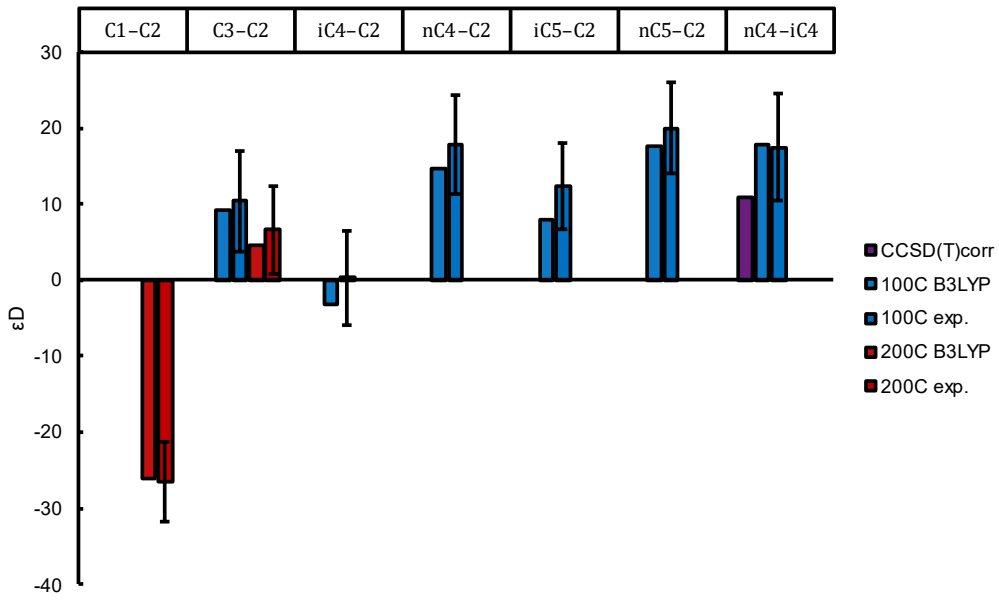

Figure 4-6. Experimental vs. theoretical equilibrium isotope effects. Error bar on the experimental results denotes 1 sigma error, estimated with the Monte Carlo analysis. B3LYP denotes theoretical values calculated from the BM theorem and DFT with B3LYP functional and aug-cc-pVTZ basis set (see methods section for details). CCSD(T)corr denotes theoretical values calculated with the corrections to BM theorem and CCSD(T) method on 6-311G** basis set (Liu et al., 2021).

4.3. Implications

Prior analysis of compound specific hydrogen isotope compositions of C1-C3 compounds in natural gases have shown that they are generally disequilibrated at lower thermal maturity and equilibrated at higher maturity (Xie et al., 2021); thus, the approach to intramolecular hydrogen isotope equilibrium can serve as a maturity indicator. This study strengthens the foundation of that application by validating prior theoretical predictions of the equilibrium fractionations. Additionally, the same argument now can be expanded to consider the evolution in hydrogen isotope compositions of iC4, nC4, iC5, and nC5.

We put forward a reaction network model that outputs the trajectory gases are expected to follow through the composition space defined by the hydrogen isotope ratios due to isotope exchange processes, which can be used to constrain time-at-temperature for geological fluids. This model successfully reproduces the isotope ratio evolution in our experiments by asserting that activation energy is controlled by BDE. It also shows that certain δD and εD values do not approach the equilibrium value in a straightforward, monotonic way at all times.

We note that hydrogen isotope exchange can be catalyzed by mechanisms other than metal-organic bonding, and the order of rates with respect to C degree (i.e., tertiary>secondary>primary) reported in our experiments might not apply to other scenarios. Catalysis by metal oxides (Al_2O_3) is suggested take the carbanion mechanism

that favors exchange on lower degree carbons (i.e., acidity controls) (Sattler, 2018). Catalysis by clay mineral is suggested to take the carbocation mechanism, which favors exchange on the position adjacent to carbocation-stable positions (Alexander et al., 1984). Finally, the radical-molecule reaction of H-abstraction has also been proposed to enable hydrogen exchange at higher thermal maturity (Xia and Gao, 2019; Thiagarajan et al., 2020). The H-abstraction reactions have the same kinetic trend (tertiary>secondary>primary) as metal catalysis (Tsang, 1990). Nevertheless, the modeling framework that we presented can be easily adapted to these scenarios to reflect the change of kinetic rules.

Acknowledgements

This work was supported by Caltech, ExxonMobil Upstream Integrated Solutions, the Caltech Joint Industry Partnership for Petroleum Geochemistry, and the Department of Energy BES program. We thank Camilo Ponton, Fenfang Wu, Nami Kitchen, and Guannan Dong for advice on experiments and measurements. We thank Brian Peterson for discussion of quantum chemical methods.

Appendix 4

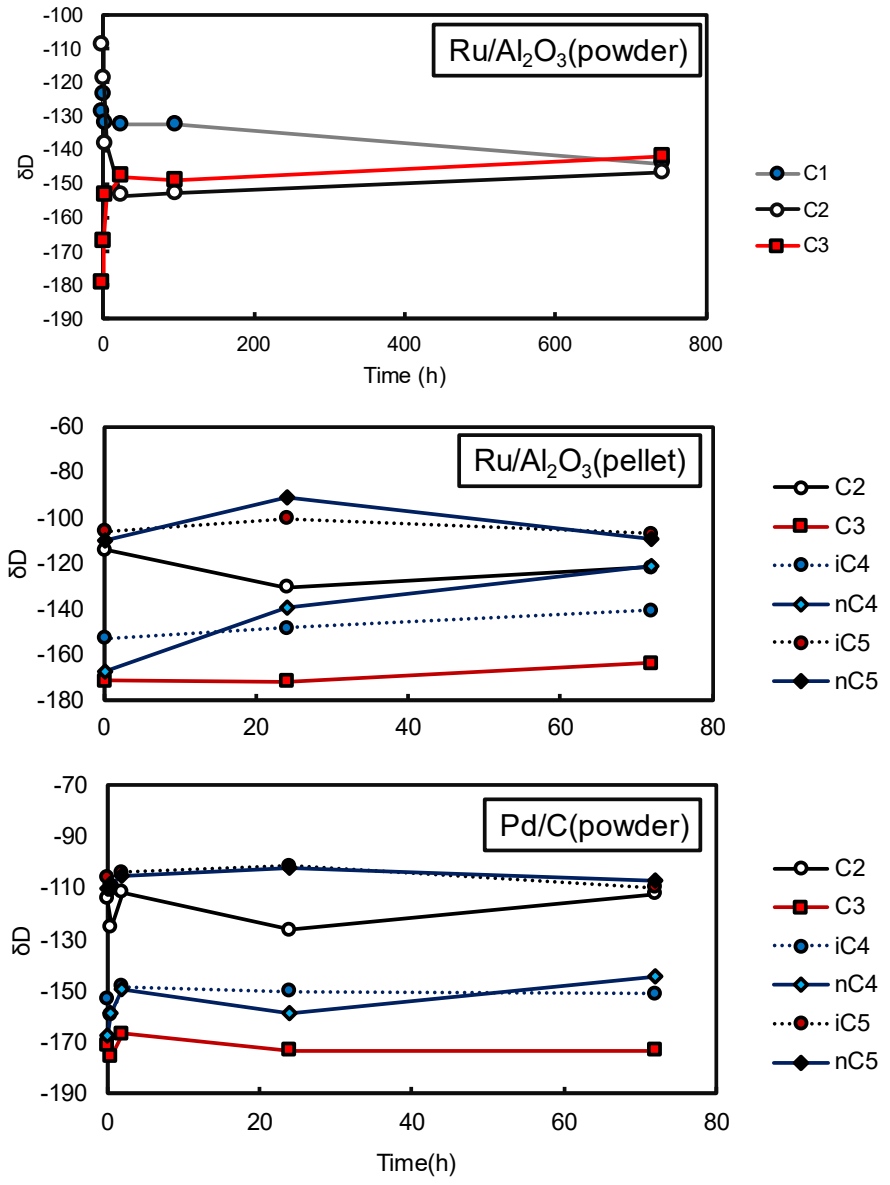

Figure 4-A.1. Examples of unequilibrated exchange experiments.

References

Alexander R., Kagi R. I. and Larcher A. V. (1984) Clay catalysis of alkyl hydrogen exchange reactions-reaction mechanisms. *Org. Geochem.* **6**, 755–760.

Berner U. and Faber E. (1996) Empirical carbon isotope/maturity relationships for gases from algal kerogens and terrigenous organic matter, based on dry, open-system pyrolysis. In *Organic Geochemistry* pp. 947–955.

Bigeleisen J. and Mayer M. G. (1947) Calculation of Equilibrium Constants for Isotopic Exchange Reactions. *J. Chem. Phys.* **15**, 261–267.

Bond G. C. (2006) *Metal-catalysed reactions of hydrocarbons*., Springer.

Boreham C. J., Edwards D. S., Hope J. M., Chen J. and Hong Z. (2008) Carbon and hydrogen isotopes of neo-pentane for biodegraded natural gas correlation. *Org. Geochem.* **39**, 1483–1486.

Criss R. E., Gregory R. T. and Taylor H. P. (1987) Kinetic theory of oxygen isotopic exchange between minerals and water. *Geochim. Cosmochim. Acta* **51**, 1099–1108.

Galimov E. M. (2006) Isotope organic geochemistry. *Org. Geochem.* **37**, 1200–1262.

He Y., Bao H. and Liu Y. (2020) Predicting equilibrium intramolecular isotope distribution within a large organic molecule by the cutoff calculation. Geochim. Cosmochim. Acta 269, 292–302.

Labidi J., Young E. D., Giunta T., Kohl I. E., Seewald J., Tang H., Lilley M. D. and Früh-Green G. L. (2020) Methane thermometry in deep-sea hydrothermal systems: Evidence for re-ordering of doubly-substituted isotopologues during fluid cooling. *Geochim. Cosmochim. Acta* **288**, 248–261.

Liu Q., Tossell J. A. and Liu Y. (2010) On the proper use of the Bigeleisen-Mayer equation and corrections to it in the calculation of isotopic fractionation equilibrium constants. *Geochim. Cosmochim. Acta* **74**, 6965–6983.

Liu Q., Yin X., Zhang Y., Julien M., Zhang N., Gilbert A., Yoshida N. and Liu Y. (2021) Theoretical calculation of position-specific carbon and hydrogen isotope equilibriums in butane isomers. *Chem. Geol.* **561**, 120031.

Luo Y. R. (2007) *Comprehensive handbook of chemical bond energies*., CRC press.

Marklanda T. E. and Berneb B. J. (2012) Unraveling quantum mechanical effects in water using isotopic fractionation. *Proc. Natl. Acad. Sci. U. S. A.* **109**, 7988–7991.

Milkov A. V. and Etiope G. (2018) Revised genetic diagrams for natural gases based on a global dataset of >20,000 samples. *Org. Geochem.* **125**, 109–120.

Piasecki A., Sessions A., Peterson B. and Eiler J. (2016) Prediction of equilibrium distributions of isotopologues for methane, ethane and propane using density functional theory. *Geochim. Cosmochim. Acta* **190**, 1–12.

Richet P., Bottinga Y. and Javoy M. (1977) A Review of Hydrogen, Carbon, Nitrogen, Oxygen, Sulphur, and Chlorine Stable Isotope Fractionation Among Gaseous Molecules. *Annu. Rev. Earth Planet. Sci.* **5**, 65–110.

Roberts I. (1939) Kinetics of the Exchange of Oxygen Between Organic Compounds and Water. *Ann. N. Y. Acad. Sci.* **39**, 375–394.

Sattler A. (2018) Hydrogen/Deuterium (H/D) Exchange Catalysis in Alkanes. *ACS Catal.* **8**, 2296–2312.

Schimmelmann A. (1991) Determination of the Concentration and Stable Isotopic Composition of Nonexchangeable Hydrogen in Organic Matter. *Anal. Chem.*

Schimmelmann A., Sessions A. L. and Mastalerz M. (2006) Hydrogen Isotopic (D/H) Composition of Organic Matter During Diagenesis and Thermal Maturation. *Annu. Rev. Earth Planet. Sci.* **34**, 501–533.

Sessions A. L., Sylva S. P., Summons R. E. and Hayes J. M. (2004) Isotopic exchange of carbon-bound hydrogen over geologic timescales. *Geochim. Cosmochim. Acta* **68**, 1545–1559.

Sherwood O. A., Schwietzke S., Arling V. A. and Etiope G. (2017) Global inventory of gas geochemistry data from fossil fuel, microbial and burning sources, version 2017. *Earth Syst. Sci. Data* **9**, 639–656.

Sinha P., Boesch S. E., Gu C., Wheeler R. A. and Wilson A. K. (2004) Harmonic vibrational frequencies: Scaling factors for HF, B3LYP, and MP2 methods in combination with correlation consistent basis sets. *J. Phys. Chem. A* **108**, 9213–9217.

Stolper D. A., Sessions A. L., Ferreira A. A., Santos Neto E. V., Schimmelmann A., Shusta S. S., Valentine D. L. and Eiler J. M. (2014) Combined 13C-D and D-D clumping in methane: Methods and preliminary results. *Geochim. Cosmochim. Acta* **126**, 169–191.

Thiagarajan N., Xie H., Ponton C., Kitchen N., Peterson B., Lawson M., Formolo M., Xiao Y. and Eiler J. (2020) Isotopic evidence for quasi-equilibrium chemistry in thermally mature natural gases. *Proc. Natl. Acad. Sci.*, 201906507.

Tsang W. (1990) Chemical Kinetic Data Base for Combustion Chemistry Part 4. Isobutane. *J. Phys. Chem. Ref. Data* **19**, 1–68.

Wang Y., Sessions A. L., Nielsen R. J. and Goddard W. A. (2009a) Equilibrium 2H/1H fractionations in organic molecules: I. Experimental calibration of ab initio calculations. Geochim. Cosmochim. Acta 73, 7060–7075.

Wang Y., Sessions A. L., Nielsen R. J. and Goddard W. A. (2009b) Equilibrium 2H/1H fractionations in organic molecules. II: Linear alkanes, alkenes, ketones, carboxylic acids, esters, alcohols and ethers. Geochim. Cosmochim. Acta 73, 7076–7086.

Webb M. A. and Miller T. F. (2014) Position-specific and clumped stable isotope studies: Comparison of the urey and path-integral approaches for carbon dioxide, nitrous oxide, methane, and propane. *J. Phys. Chem. A* **118**, 467–474.

Webb M. A., Wang Y., Braams B. J., Bowman J. M. and Miller T. F. (2017) Equilibrium clumped-isotope effects in doubly substituted isotopologues of ethane. *Geochim. Cosmochim. Acta* **197**, 14–26.

Whiticar M. J. (1999) Carbon and hydrogen isotope systematics of bacterial formation and oxidation of methane. *Chem. Geol.* **161**, 291–314.

Xia X. and Gao Y. (2019) Kinetic clumped isotope fractionation during the thermal generation and hydrogen exchange of methane. *Geochim. Cosmochim. Acta* **248**, 252–273.

Xie H., Dong G., Formolo M. J., Lawson M., Liu J., Cong F., Mangenot X., Shuai Y., Ponton C. and Eiler J. M. (2021) The evolution of intra- and inter-molecular isotope equilibria in natural gases with thermal maturation. *Submitt. to GCA*.

Xie H., Ponton C., Formolo M. J., Lawson M., Ellis G. S., Lewan M. D., Ferreira A. A., Morais E. T., Spigolon A. L. D., Sessions A. L. and Eiler J. M. (2020) Position-specific distribution of hydrogen isotopes in natural propane: Effects of thermal cracking, equilibration and biodegradation. *Geochim. Cosmochim. Acta* **290**, 235–256.

Xie H., Ponton C., Formolo M. J., Lawson M., Peterson B. K., Lloyd M. K., Sessions A. L. and Eiler J. M. (2018) Position-specific hydrogen isotope equilibrium in propane. *Geochim. Cosmochim. Acta* **238**, 193–207.

Chapter 5: The Evolution of Intra- and Inter-molecular Isotope Equilibria in Natural Gases with Thermal Maturation

Abstract

Naturally occurring hydrocarbon fluids in sedimentary basins have economic, geological and environmental significance. Connecting sedimentary basin temperature-time evolution with petroleum generation and transformation is a long-studied problem. In this study, we investigate the use of a novel tool – multiply substituted isotopologues of methane, for distinguishing between different chemical mechanisms in catagenesis and for characterizing the extent of thermal maturation of thermogenic natural gases. We analyze the stable isotope compositions of a suite of thermogenic gas samples that are globally distributed and cover a wide range in composition and thermal maturation, from dominantly unconventional shale gas formations and a few conventional gas plays. Our data show that methane generated at early thermal maturity has a stable isotope composition governed by chemical kinetics, characterized by a pronounced deficit in $\Delta^{12}CH_2D_2$; this signature can be explained by its formation chemistry that combines a more D-rich methyl radical pool and more D-poor H radical pool. Methane from higher thermal maturity fluids increases in $\Delta^{12}CH_2D_2$, reaching equilibrium at vitrinite reflectance maturity (R_o) of approximately 1.5% (equivalent to 170–210 °C peak burial temperature) and higher, which is interpreted to be the result of isotope exchange erasing

the disequilibrium signature of catagenetic chemistry, mediated by C-H activation during either radical chain reactions or organic-inorganic interactions on mineral surfaces. We further examined hydrogen isotope fractionations among methane, ethane and propane for a compiled global dataset and found that the intermolecular fractionation exhibits a trend similar to that seen for the $\Delta^{12}CH_2D_2$ value of methane, departing from equilibrium at low thermal maturities and moving towards equilibrium as maturity increases. These findings indicate that the inter- and intra-molecular hydrogen isotope structures of components of thermogenic natural gas transition from chemical-kinetic control at low thermal maturities toward thermodynamic control at higher thermal maturities, mediated by hydrogen exchange reactions. We propose that these systematic relationships could be used to identify the exact thermal maturation stages for natural gases and their associated fluids, especially for oil-associated gas at early maturation.

1. Introduction

Petroleum formation is the result of decomposition of organic matter that is exposed to increasing thermal stress in a sedimentary basin. The quantity and chemical and isotopic composition of petroleum accumulations are related to both the properties of the source materials and the thermal history of burial, as well as post-generation processes of expulsion, migration, and trapping. These relationships can form the basis of useful

geochemical tools for predicting and characterizing occurrences of petroleum and their relationships to basin geology, burial, and uplift. Proxies linking petroleum fluid characteristics (molecular composition, stable isotope ratios, and biomarkers) with features of basin geology (burial depth, source rock organic matter type and depositional environment, and structural activity) have been widely examined and applied, but they often rely on empirical calibrations or extrapolation of the kinetics of catagenetic reactions from the high-temperatures of pyrolysis experiments to lower natural temperatures, potentially leading to errors and inconsistencies. Moreover, accurate models of hydrocarbon maturation require knowledge of the specific chemical reactions of catagenesis, which are poorly defined or debated. One of the most important uncertainties is whether petroleum formation is controlled by chemical kinetics (as is generally assumed) or stable or metastable equilibria (as has been sometimes suggested), and, if the equilibrium petroleum chemistry is possible, where the transitions between kinetic and equilibrium control can occur.

The prevailing paradigm of catagenic chemistry describes the formation of oil and gas as being kinetically controlled and governed by many parallel irreversible radical reactions (Tissot and Welte, 1978; Burnham et al., 1987; Tissot et al., 1987; Burnham et al., 1988; Ungerer, 1990; Hunt, 1996; Xia, 2014). Under this paradigm, isotope fractionation during alkane formation is usually treated as kinetic isotope effects associated with thermal dissociation of C-C bonds to form free radicals (Sackett et al., 1966; Galimov, 1975;

Chung et al., 1988; Tang et al., 2000; Tang et al., 2005; Ni et al., 2011; Xia and Gao, 2017). This theory is challenged by field and laboratory evidence showing that the transformation of precursors to alkanes could be controlled by thermodynamic equilibrium, metastable equilibrium, or quasi-equilibrium created by cycles of reactions that are individually irreversible but together mediate interconversion and exchange of co-existing molecules to attain chemical and/or isotopic equilibrium (James, 1983; Helgeson et al., 1993; Helgeson et al., 2009; Mango et al., 2009; Mango, 2013; Wei et al., 2018). In all of these cases, speciation of compounds and distribution of stable isotopes favor minimization of Gibbs free energy**.** A more recent work (Thiagarajan et al., 2020b) uses stable isotope evidences to argue that natural gas formation at early maturation is kinetically controlled, but that metastable equilibrium can be reached as thermal maturation increases. Overall, it remains uncertain how extensive the thermodynamic control is and what time-temperature condition is required to equilibrate (if, in fact, stable or metastable equilibrium is attainable); the answers to both of these questions are critical for quantitative reconstruction of thermal history and its relationship to petroleum formation.

These questions could potentially be re-examined using intramolecular stable isotope ratios of natural hydrocarbon compounds, including multiply substituted isotopologues (‘clumped isotopes’) and position-specific isotope variations, which can be observed using several recently developed analytical techniques. (Gilbert et al., 2013; Stolper et al.,

2014b; Ono et al., 2014; Gilbert et al., 2016; Suda et al., 2017; Eiler et al., 2018; Piasecki et al., 2018; Clog et al., 2018; Liu et al., 2018; Gilbert et al., 2019; Gonzalez et al., 2019; Thiagarajan et al., 2020a). These methods provide novel insights into processes controlling the formation, accumulation and destruction of petroleum hydrocarbons, as they are more informative as constraints on chemical mechanisms and conditions of petroleum forming reactions than average isotopic contents across a range of compounds. And, when an intramolecular isotopic property is controlled by equilibrium isotope effects, it can provide the basis for stable isotope geothermometry. Amongst these novel intramolecular isotope distributions, clumped isotopes of methane have been studied most extensively (Stolper et al., 2014a; Wang et al., 2015; Douglas et al., 2016a; Young et al., 2017; Stolper et al., 2018; Wang et al., 2018; Giunta et al., 2019; Giunta et al., 2021). Technical advancements in gas-source high-resolution mass spectrometry allow precise measurements of two clumped isotopologues of methane, $^{13}CH_3D$ and $^{12}CH_2D_2$. Because abundances of these two species are governed by two independent intramolecular exchange reactions, the integration of both measurements provides a test for whether or not methane has a clumped isotope composition consistent with intramolecular isotope equilibrium (i.e., whether relative proportions of both species are consistent with equilibrium at the same temperature). Previous studies observed that relative abundances of one or both of $^{13}CH_3D$ and $^{12}CH_2D_2$ isotopologues in thermogenic natural gases conform to isotopic equilibrium and that the inferred temperatures derived

from this proxy were consistent with the canonical ‘oil window’ and ‘gas window’ maturity ranges (Stolper et al., 2014a; Wang et al., 2015; Stolper et al., 2015; Young et al., 2017; Douglas et al., 2017; Giunta et al., 2019). These findings are unexpected by canonical kinetic models of gas generation (though in the absence of further information it is imaginable that chemical-kinetic controls might mimic equilibrium clumped isotope abundances). However, two recent sets of observations question the finding that thermogenic methane is always at clumped isotope equilibrium. Firstly, it has been shown that laboratory pyrolysis experiments can produce methane out of clumped isotope equilibrium. During coal pyrolysis experiments, Δ_{18} of methane departed to values below those consistent with equilibrium at the experimental temperatures, even reaching negative values inconsistent with equilibrium at any temperature (Shuai et al., 2018). In another pyrolysis experiment using n-octadecane as the substrate, large (10’s of ‰) deficits in $^{12}CH_2D_2$ relative to equilibrium were observed, despite the fact that $^{13}CH_3D$ abundances were close to equilibrium (Dong et al., 2020). Secondly, it was found that some natural gases have clumped isotope abundances suggesting anomalously high (>300 °C) apparent temperatures (based on Δ_{18} measurements, i.e., combined measurement of $^{13}CH_3D$ and $^{12}CH_2D_2$ at mass 18), although it was also proven that at least part of this anomaly is due to physical isotope fractionation associated with laboratory extraction of gas at room temperature (Douglas et al., 2017; Stolper et al., 2018). These gases also tend to be oil-associated shale gases that are ‘wet’ (low

C1/(C2+C3) ratio), which indicate oil-window stage thermal maturity and make the high apparent temperatures unrealistic. These observations and experiments point towards the potential violation of equilibrium control in thermogenic methane generation. It has been suggested that this conflict can be reconciled by a kinetic gas generation model coupled with a hydrogen exchange process (Xia and Gao, 2019).

In this study, we investigate the clumped isotope compositions, including relative abundances of $^{13}CH_3D$ and $^{12}CH_2D_2$, for methanes sampled from thermogenic natural gases covering a wide range in thermal maturity and geographical location. Most of these samples come from unconventional shales with the exception of one conventional gas from Sleipner Vest and three conventional gases from the Paris Basin; we focus on shale gases because they have simpler migration histories so that source rock thermal history provides an independent constraint on petroleum thermal maturity. We show that oil-associated natural gases formed at early maturation can be out of clumped isotope equilibrium in a $\Delta^{13}CH_3D$ and $\Delta^{12}CH_2D_2$ space, which disagrees with the existing thought that clumped isotopes of thermogenic methane are always equilibrated, but is consistent with laboratory pyrolysis experiments and kinetic gas generation models (Shuai et al., 2018; Xia and Gao, 2019; Dong et al., 2020). As thermal maturity increases, proportions of clumped isotope species in thermogenic methanes approach thermodynamic equilibrium, eventually reaching and maintaining equilibrium at and above the threshold around a thermal maturity equivalent to a vitrinite reflectance value

of R_o=1.5%. Moreover, we show that the intermolecular hydrogen isotope fractionations between methane, ethane and propane exhibit a behavior similar to that of methane clumped isotope abundances, based on compiled literature data documenting compound-specific hydrogen isotope compositions of thermogenic natural gases. We then discuss the thermodynamic and kinetic controls of stable isotope partitioning in these compounds. Our results provide new understanding to gas formation mechanisms and new tools for constraining thermal maturation of petroleum basins and their evolved fluids.

2. Methods and materials

2.1. Methane preparation and analysis

Methane samples are extracted from natural gas cylinders using a cryogenic trap. Before we expand a gas to the glass vacuum line, we heat the high-pressure cylinder to 80˚C for 1 hour in order to minimize potential fractionation in cylinder (Douglas et al., 2017). The expanded gas is frozen at 20K into a cold head and cycled between 45K and 80K to remove volatile components (N_2, O_2, CO). Methane is thawed at 70K and transferred to another cold trap of molecular sieve in liquid nitrogen bath. Finally, we flame-seal the

Pyrex tube that traps methane. For each clumped isotope analysis, around 160 µmol of methane gas is needed.

Methane's isotopologue ratios are analyzed on a Thermo Scientific Ultra (commercial version) at Caltech. A detailed protocol has been previously reported (Thiagarajan et al., 2020a), so we give a synopsis of our methodology here. We introduce a gas sample into a dual-inlet system to be measured against a CIT-1 reference ($\delta^{13}C$=-42.88‰, δD=-175.5‰, $\Delta^{13}CH_3D$ =2.90‰, $\Delta^{13}CH_2D_2$=7.6‰). The sample tube is heated at 150°C for 1 hour before expansion to minimize fractionation via adsorption, and we use the bellow motor to compress and release the bellow 15 times to homogenize gas between the sample tube and internal compartments. Each sample is examined carefully in the mass range of 27.9–28.1 for the presence of common contaminants (N_2, CO and C_2H_4) and we only measure methane that is > 99% pure. Isotopologue ratio analysis is divided into 3 'analytical' blocks. In the first block, we measure $^{12}CH_2D_2/^{12}CH_4$. In the second block, we measure $^{13}CH_3D/^{12}CH_4$ and $^{13}CH_4/^{12}CH_4$. In the last block, we measure $^{12}CH_3D/^{12}CH_4$. These four isotopologue ratios are converted to $\delta^{13}C$, δD, $\Delta^{13}CH_3D$, and $\Delta^{12}CH_2D_2$ as given below:

$$\delta^{13}C + 1 = \frac{[^{13}CH_4]/[^{12}CH_4]}{R^{13}_{VPDB}}$$

$$\delta D + 1 = \frac{1}{4} * \frac{[^{12}CH_3D]/[^{12}CH_4]}{R^{D}_{VPDB}}$$

$$\Delta_{^{13}CH_3D} + 1 = \frac{[^{13}CH_3D] * [^{12}CH_4]}{[^{13}CH_4] * [^{12}CH_3D]} = \frac{[^{13}CH_3D]}{[^{12}CH_4]} / (\frac{[^{13}CH_4]}{[^{12}CH_4]} * \frac{[^{12}CH_3D]}{[^{12}CH_4]})$$

$$\Delta_{^{12}CH_2D_2} + 1 = \frac{3}{8} * \frac{[^{12}CH_2D_2] * [^{12}CH_4]}{[^{12}CH_3D]^2} = \frac{3}{8} * \frac{[^{13}CH_3D]}{[^{12}CH_4]} / (\frac{[^{13}CH_4]}{[^{12}CH_4]} * \frac{[^{12}CH_3D]}{[^{12}CH_4]})$$

1/4 and 3/8 are symmetry number ratios. Note that standard $\delta^{13}C$, δD definitions account for $^{13}C/^{12}C$ and D/H in the form of all isotopologue species, so the treatment of the first two equations (that only involve singly substituted species) lead to small discrepancies in the isotopologue abundances causing deviation from the stochastic distribution. We note that the error of this approximation scales with the amplitudes of the deviation from the stochastic isotopologue distribution, which is acceptable given our analytical precision (0.02‰ and 0.1‰ for $\delta^{13}C$ and δD, respectively) as well as the natural range of $\delta^{13}C$, δD, $\Delta^{13}CH_3D$ and $\Delta^{12}CH_2D_2$. The last two definitions have alternative forms: $R_{isotopologue}/R^{*}_{isotopologue}$, where R indicates [isotopologue]/[$^{12}CH_4$] ratios and * indicates such ratios at stochastic distribution). There is also a trivial difference between these two definitions (Wang et al., 2004) that is negligible in light of our precision.

We standardize our results into an absolute reference frame (Young et al., 2017; Eldridge et al., 2019) by scaling them with results from equilibrated methane gases created by C-H exchange on the surface of a heterogeneous metal catalysts at elevated temperature. We routinely prepare gas aliquots with a range of initial compositions ($\delta^{13}C$ and δD) and heat them in the presence of Ni/Al_2O_3 catalyst in a 500°C furnace for 24 hours for reaching

equilibrium distribution of methane isotopologues. Complementing these efforts, and in order to test our temperature scalability, we heated a separate gas in the presence of Ru/Al_2O_3 catalyst at 100°C for 11 days to reach full equilibration at this lower temperature. Long-term reproducibility is monitored by measuring a laboratory made standard mixture (spiked with $^{13}CH_4$ and $^{12}CH_3D$).

2.2. Methane generation and exchange modeling

We used a mathematical model to simulate the clumped isotope signatures of methane derived from the Upper Cretaceous Eagle Ford Shale. Methane generation in this model is simplified into two steps. The first step is homolytic cleavage of $C–CH_3$ bond in the precursor, and the second step is combining CH_3 with an H ('capping'). Each step is assigned with kinetic isotope effects that are specific to each isotopologue. We created basin burial histories for a mature and an immature Eagle Ford wells in our dataset (Virgina Fee 3H and Irvin Minerals 1S, respectively) with the PetroMod basin modeling software (See Appendix 5 for details), and used them as anchors to calculate temperature-time relationship and R_o-time relationship for other present-day maturities.

Rates of methane generation is constrained by pyrolysis experiments on Eagle Ford rock samples (Shao et al., 2018). The isotope compositions of instantaneously generated methane can be formulated into the analytical solutions (Xia and Gao, 2019):

$$\delta^{13}C = \delta^{13}C_{pre} + ln\alpha_{13CH3} * (1 + lnF)$$

$$\delta D = \frac{1}{4}\alpha_{cap}(1 + \delta D^{pre-cap}) + \frac{3}{4}ln\alpha_{12CH2D} * (1 + \delta D^{pre}) * F^{\alpha_{12CH_2D}-1} - 1$$

$$\Delta^{13}CH_3D = \frac{\alpha_{cap} + \frac{3\alpha_{13CH2D}}{\alpha_{13CH3}} * (1 + \Delta^{13}CH_2D^{pre}) * F^{\alpha_{13CH_2D}-\alpha_{13CH3}}}{\alpha_{cap} + 3 * \alpha_{12CH2D} * F^{\alpha_{12CH2D}-1}} - 1$$

$$\Delta^{12}CH_2D_2 = \frac{8(\alpha_{12CH2D}\alpha_{cap}\frac{(1 + \delta D^{pre-cap})}{(1 + \delta D^{pre})}F^{\alpha_{12CH_2D}-1} + \alpha_{12CHD2} * \left(1 + \Delta^{12}CHD_2^{pre}\right) * F^{\alpha_{12CHD_2}-1})}{\left[\alpha_{cap}\frac{(1 + \delta D^{pre-cap})}{(1 + \delta D^{pre})} + 3 * \alpha_{12CH2D} * F^{\alpha_{12CH_2D}-1}\right]^2} - 1$$

$\alpha_{cap}, \alpha_{12CH2D}, \alpha_{13CH3}, \alpha_{13CH2D}, \alpha_{12CHD2}$ — Kinetic isotope effects as in $\frac{k_{heavy\ isotopologue}}{k_{light\ isotopologue}}$, subscripts denotes the heavy isotopologue or capping hydrogen (cap). We use previous ab initio calculations for single isotope substitution (Tang et al., 2000; Ni et al., 2011), and assume an additional clumped isotope KIE to be 5‰ for α_{12CHD2} and 1‰ for α_{13CH2D}.

$\delta^{13}C_{pre}, \delta D^{pre}, \Delta^{13}CH_2D^{pre}, \Delta^{12}CHD_2^{pre}$ — Isotopic composition of the methyl (–CH_3) precursor.

$\delta D^{pre-cap}$ — Isotopic composition of the capping hydrogen precursor.

F — Fraction of residual methyl precursor.

A full list of kinetic parameters used in this model can be found in the Appendix 5. These instantaneous isotopic values are integrated over the burial history.

As discussed earlier, methane exchange can happen via either a free-radical mechanism or a substrate-catalyzed mechanism. We thus treat isotope exchange between any isotopologue pairs with this general equation:

$$\frac{dR}{dt} = k * (R_{eq} - R)$$

R denotes the isotopologue ratio of methane. R_{eq} is such ratio at thermodynamic equilibrium. k is the exchange rate constant (in s^{-1}), and $^{12}CH_2D_2$ exchanges two times faster than $^{13}CH_3D$ (Labidi et al., 2020; Giunta et al., 2021). We also account for the effect of gas expulsion from source by adding a loss term. It was estimated that between 40-60% of methane is lost due to expulsion from the Eagle Ford shale (Byrne et al., 2018).

2.3. Vitrinite reflectance analysis

Vitrinite reflectance data presented here is based on one of the following: 1) biomarker maturity indicators from co-produced oil or condensate, 2) direct Vitrinite measurements

on detrital fragments of continental macerals within the shale at the depth of production, and 3) conversion from $\delta^{13}C$ of methane using empirical calibrations. Depending on the context, one or two of these proxies might be unavailable. We use the term 'mapped R_o' for values determined from method (1) or (2), and 'equivalent R_o' for method (3). The use of R_o in each presentation is specified in figure captions or texts.

Many local and global relationships between source rock maturity and $\delta^{13}C$ of methane have been compiled over the years (Stahl and Carey, 1975; Schoell, 1980; Faber, 1987; Dai and Qi, 1989; Berner and Faber, 1996; Faber et al., 2015; Xia and Gao, 2019). They tend to differ a lot, especially in the early maturation (R_o<1.0%) and late maturation (R_o>2.0%) stages. We decide to apply the Xia and Gao (2019) relationship for gases sourced from Type I/II kerogens because its calculations are most consistent with Vitrinite reflectance determined from (1) and (2) where those data are available in our sample set of shale gas samples (Figure 5-A.4). Part of the gases presented in compound-specific isotope analysis source from Type III kerogens, and we use Dai and Qi (1989) calibration because it is shown to match source rock maturities in the Sichuan Basin (Dai et al., 2012; Dai et al., 2014), from where gases constitutes for a large proportion of our Type III kerogen gas compilation. Note that these relationships are established for most typical kerogens, whereas many hydrocarbon-producing materials often represent a mixing between these endmembers, which could possibly inflict possible uncertainty in

source maturity estimates. We decide to apply the Xia and Gao (2019) relationship for samples where the organic matter type is controversial or suggested to be mixed.

2.4. Natural gas samples

We collected and analyzed methane for 23 natural gas samples from eight different geological formations worldwide. Below lists a more detailed description of each sample source.

2.4.1. Shale gas samples

Eagle Ford Shale

Eight samples are collected from the Upper Cretaceous Eagle Ford Shale in Texas. The Eagle Ford Shale is a mixed siliciclastic/carbonate unit that is deposited in Upper Cretaceous. Well depth of our samples ranges between 2700-3800 meters.

Haynesville Shale

Two samples are collected from the Haynesville Shale, an Upper Jurassic-aged formation located in eastern Texas, southwestern Arkansas, and northwestern Louisiana. It was deposited in a marine environment. Our samples are collected from depths of 3398m and 4327m.

Marcellus Shale

Two samples are collected from the Marcellus Shale, a Middle Devonian-age organic-rich formation. The Marcellus Shale extends from northern New York State to northeastern Kentucky and southern Tennessee and is the most prolific natural gas-producing formation in the Appalachian basin. The Marcellus Shale is carbonaceous silty black shale that was deposited in a foreland basin. Our samples are collected at depths of 1054m and 1579m.

Bakken Shale

Two samples are from the Upper Devonian-Lower Mississippian Bakken Formation. The Bakken Shale is located in Williston Basin, North Dakota, and is deposited in a marine environment.

Longmaxi

Four shale gas samples are collected at the wellhead from Jiaoshiba field in the Sichuan Basin in China. These gases are produced from the Lower Silurian Longmaxi Formation. The Longmaxi Formation consists of organic-rich marine shale and is widely distributed across the Sichuan Basin. The formation thickness is 40–50m and vitrinite reflectance (R_o%) of the source rock is measured between 2.2 and 3.1%.

Doushantuo

Another shale gas sample was collected from a recently drilled well located in Yichang, China. This sample is sourced from the Precambrian Doushantuo Formation, which is deposited in marine environment during the Upper Sinian (Edicaran) period, between 635 – 551 Ma. The sample is retrieved from a depth of around 3800m.

2.4.2. Conventional gas samples

Sleipner Vest

One sample from a conventional hydrocarbon system was collected from the Sleipner Vest gas field located in the Norwegian sector of the North Sea petroleum province. Petroleum accumulations are found within Jurassic sandstone reservoirs in this area as reported in Barry et al. (2016).

Paris Basin

Three samples are collected from the Upper Triassic siliciclastic reservoirs of the Paris Basin. The well depths are between 1800-2200m and the present-day well temperature is between 90-110°C. Peak burial temperatures occurred in Upper Cretaceous with a range of 110-130 °C.

2.5 Compound-specific hydrogen isotope data collection and analysis

The readers can find C_1-C_3 stable hydrogen isotope data from a total of 17 publications and government reports. While most of them are thermogenic gases, we exclude some data if samples are suggested to 1) contain significant amounts of microbial gas; 2) have experienced microbial degradation; 3) have an abiotic (magmatic, hydrothermal) origin, or 4) is a mixture between two or more distinct endmembers. The last case, which often involves mixing between primary kerogen gas and secondary oil-cracked gas, can exhibit the so-called 'isotope reversal' or 'rollover' phenomena (Rodriguez and Paul Philp, 2010; Tilley and Muehlenbachs, 2013; Xia and Gao, 2018; Milkov et al., 2020), where the common trend of $\delta^{13}C_{C1} < \delta^{13}C_{C2} < \delta^{13}C_{C3}$ is changed. A list of all publications and reports together with our data filtering notes is included in the Appendix 5. Complete dataset is also available upon request to the corresponding author.

We calculate distance to the equilibrium plane for each sample (Figure A.5). The equilibrium plane is defined by equilibrium isotope effects between three compounds at a temperature range of 110-250 °C. Equilibrium isotope effects are calculated using Bigeleisen-Mayor theorem with vibrational frequencies computed using DFT (Thiagarajan et al., 2020b). Anharmonicity is approximated with zero point energy (ZPE) correction following suggestions of Liu et al. (2010).

3. Results

All samples presented in this study are of thermogenic origin (Figure 5-1). For the subset of gases with relatively low $\delta^{13}C$ (i.e., samples from the Bakken Shale, some of the Eagle Ford Shale samples, and those from the Paris Basin), significant microbial methane contribution can be ruled out by multiple lines of evidence. First, biodegradation of higher alkanes (that commonly associates with subsurface microbial methanogenesis (Jones et al., 2008)) could be ruled out by absence of typical indicators, such as anomalous $\delta^{13}C$ of propane and butane and pentane's isomer ratios (Table 5-1). Second, their $C_1/(C_2+C_3)$ ratios are low, placing them in the thermogenic field on a 'Bernard plot' (Figure 5-A.1; Bernard et al., 1978). Third, the current reservoirs for these gases are too deep and hot to host microbial life. The Eagle Ford shale gases are sampled from 2700-3800 meters with reservoirs temperatures ranging from 141 to 155 °C. The Paris Basin gases are from reservoirs between 1800 and 2200m, with temperatures ranging from 90 to 110°C. These are above the sustainable temperature ranges of bacteria and archaea that produce methane and/or degrade hydrocarbons (Head et al., 2003). Finally, carbon isotope data for alkanes from these gases form a straight line on the Chung plot (Chung et al., 1988), which is also consistent with a thermogenic origin and no subsequent biologic consumption of the larger volatile hydrocarbon compounds.

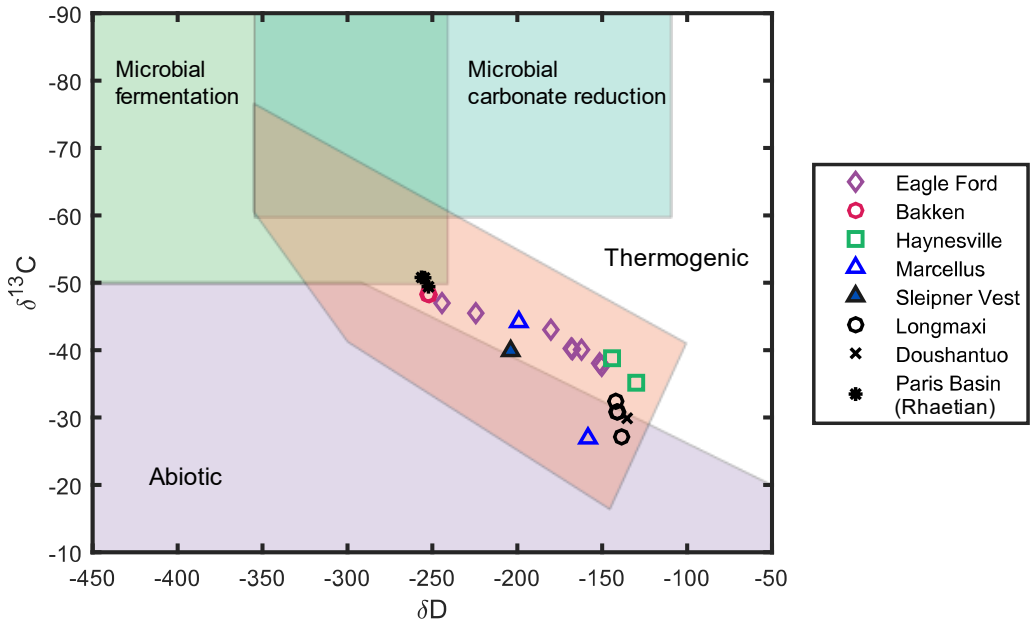

Figure 5-1: Stable isotope data of methane samples analyzed in this study, in a format often referred to as 'Schoell/Whiticar diagram' (Schoell, 1980). Genetic fields are mapped according to the suggestions of (Milkov and Etiope, 2018).

Table 5-1: Compositional, isotopic and other information of samples

Sample Info		Compositional data							Compound-specific carbon isotope data					Other information		
Field	Sample ID	C_1	C_2	C_3	iC_4	nC_4	iC_5	nC_5	$\delta^{13}CC_1$	$\delta^{13}CC_2$	$\delta^{13}CC_3$	$\delta^{13}CiC_4$	$\delta^{13}CnC_4$	Depth (ft)	Reservoir Temp (°C)	Mapped maturity (% Ro)
Haynesville	Hilltopper 1H	96.1	0.1	0.0	0.0	0.0			-35.1					14186	190	2.5
Haynesville	New Horizon E1H	94.0	3.2	0.4	0.1	0.1	0.0	0.0	-38.8	-19.9	-15.5			11142	163	1.7
EagleFord	Smith CC 3H	91.8	3.6	0.4	0.1	0.0	0.0	0.0						11838	155	1.1
Eagleford	Las Raices 21H	80.3	11.2	4.1	1.0	1.3	0.2	0.4	-40.7	-24.6	-22.7	-25.8	-23.3	9700	143	1.6
Eagleford	Irvin Mineral South 1H	77.8	12.6	5.3	0.6	1.3	0.3	0.3	-47.4	-32.2	-29.3	-31.2	-30.0	8838	141	1.1
Eagleford	Virginia Fee 3H	91.5	3.4	0.4	0.1	0.1	0.0	0.0	-39.2	-18.5	-15.2	-15.2	-16.7	12312	155	1.8
EagleFord	Las Raices 22H	80.7	10.6	3.8	1.0	1.3	0.5	0.4	-39.8	-24.2	-22.5	-26.0	-23.0	9792	143	1.6
EagleFord	Burks Ranch 2H	91.8	3.6	0.4	0.1	0.0	0.0	0.0	-37.8	-17.4	-14.0	-10.5	-13.6	12096	136	1.6
Eagleford	Virginia Fee 4H	83.0	9.2	2.1	0.7	0.6	0.3	0.2	-40.2	-23.3	-20.1	-22.0	-20.4	12351	155	1.8
Eagleford	Emma Tarrt 25H	77.9	11.9	4.9	0.5	1.0	0.2	0.2	-45.6	-33.6	-29.3	-31.6	-28.7	10169	143	1
Marcellus	Tome 8522H	98.4	1.1	0.0					-26.9	-33.1				3457	34	4.3
Marcellus	Forest / Warrant	78.6	14.3	4.4	0.4	1.0	0.2	0.2	-44.0	-34.3	-29.7			5176	48	1.5
Sleipner Vest	B14-T2								-39.8	-28.7	-27.1	-26.2	-27.6	11300 - 11710	123	
Paris basin	SDN 109	60.5	18.9	11.6	1.1	2.8										

We observed that the methane sample suite could be divided approximately evenly into samples with clumped isotope compositions consistent with thermodynamic equilibrium in $\Delta^{12}CH_2D_2$ vs. $\Delta^{13}CH_3D$ space (Figure 5-2; Table 5-2) and those that significantly violate equilibrium. Samples in equilibrium have clumped isotope compositions implying apparent equilibrium temperatures between 140 and 230 °C, generally within or below the thermogenic 'gas window'. Samples away from the equilibrium curve in Figure 5-2 consistently have very low $\Delta^{12}CH_2D_2$ values that are often negative. $\Delta^{13}CH_3D$ values vary from 1.9 to 3.2 ‰, which corresponds to apparent temperatures between 140 and 260 °C that are within extended gas window temperature.

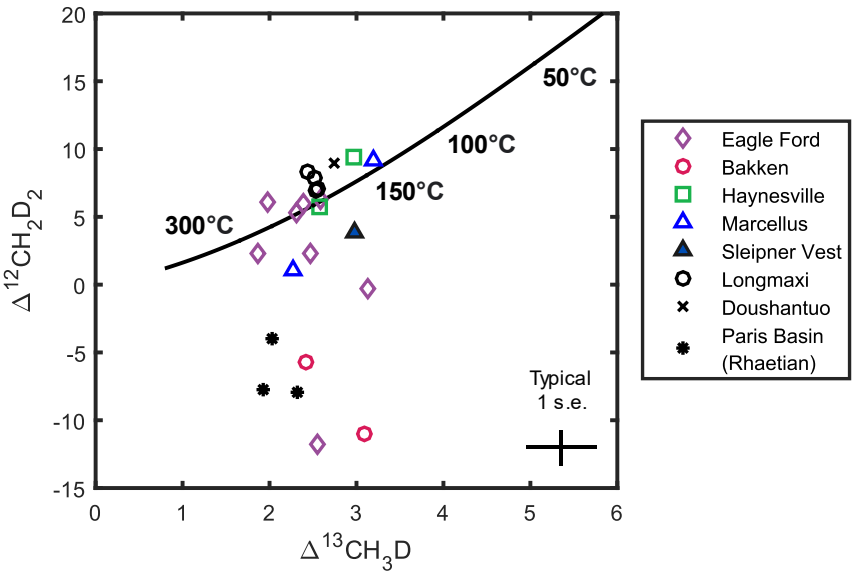

Figure 5-2: Cross-plot of $\Delta^{12}CH_2D_2$ vs. $\Delta^{13}CH_3D$ of all methane samples analyzed in this study. The curve represents thermodynamic equilibrium and dots mark equilibrium temperatures of 50, 100, 150, 200, 250, and 300 °C, from upper right to bottom left (Young et al., 2017).

Table 5-2: Methane clumped isotope results and reservoir types

Field	Sample ID	$\delta^{13}C$	$\sigma\delta^{13}C$	δD	$\sigma\delta D$	$\Delta^{12}CH_2D_2$	$\sigma\Delta^{12}CH_2D_2$	$\Delta^{13}CH_3D$	$\sigma\Delta^{13}CH_3D$	Note	Type
Haynesville	Hilltopper 1H	-35.15	0.02	-129.95	0.25	9.40	1.49	2.97	0.32	Merged Prototype data	Unconventional
Haynesville	New Horizon E1H	-38.83	0.02	-144.33	0.25	5.74	1.51	2.58	0.29	Merged Prototype data	Unconventional
EagleFord	Smith CC 3H	-43.03	0.02	-180.20	0.33	2.30	1.55	2.47	0.30	Prototype data	Unconventional
Eagleford	Las Raices 21H	-40.23	0.03	-168.20	0.15	2.30	1.39	1.87	0.31		Unconventional
Eagleford	Irvin Mineral South 1H	-46.97	0.02	-244.31	0.11	-11.77	1.51	2.55	0.36		Unconventional
Eagleford	Virginia Fee 3H	-38.05	0.02	-151.44	0.16	6.28	1.20	2.59	0.44		Unconventional
EagleFord	Las Raices 22H	-40.14	0.02	-167.43	0.17	5.31	1.29	2.31	0.28	Prototype data	Unconventional
EagleFord	Burks Ranch 2H	-37.66	0.03	-150.22	0.15	5.97	1.22	2.39	0.35		Unconventional
Eagleford	Virginia Fee 4H	-40.05	0.01	-162.18	0.12	6.08	1.20	1.98	0.37		Unconventional
Eagleford	Emma Tarrt 25H	-45.48	0.01	-224.38	0.11	-0.29	1.40	3.13	0.35		Unconventional
Marcellus	Tome 8522H	-26.91	0.02	-158.30	0.16	9.16	1.23	1.84	0.44		Unconventional
Marcellus	Forest / Warrant	-44.18	0.01	-199.10	0.13	1.06	1.36	1.79	0.43		Unconventional
Longmaxi	JY 9-2	-30.84	0.01	-141.39	0.15	6.96	1.23	2.53	0.36		Unconventional
Longmaxi	DJX15-11-20	-27.14	0.01	-138.66	0.18	7.08	1.17	2.55	0.34		Unconventional
Longmaxi	JY 85-1	-30.84	0.01	-140.91	0.14	7.88	1.26	2.52	0.33		Unconventional
Doushantuo	yy-1	-29.88	0.01	-135.32	0.15	8.96	1.26	2.74	0.34		Unconventional
Longmaxi	jy 54-6	-32.41	0.01	-142.02	0.18	8.33	1.20	2.44	0.39		Unconventional

Bakken	Rogney 17-8-1H treater 1	-48.29	0.02	-252.73	0.17	-5.71	1.84	2.39	0.31	Prototype data	Unconventional
Bakken	Rogney 17-8-1H backside	-48.21	0.02	-251.93	0.22	-10.99	1.66	3.06	0.36	Prototype data	Unconventional
Sleipner Vest	B14-T2	-39.89	0.02	-203.86	0.12	3.85	1.22	2.98	0.33		Conventional
Paris basin	CDM3-BP	-50.72	0.03	-254.60	0.12	-3.98	1.54	2.03	0.53		Conventional
Paris basin	DML1-BP	-50.78	0.01	-256.38	0.33	-7.94	1.66	2.32	0.62		Conventional
Paris basin	SDN 109	-49.40	0.01	-252.25	0.14	-7.74	1.25	1.93	0.46		Conventional

4. Discussion

4.1 Controls on clumped isotope signature

Gases from multiple geological formations and reservoirs exhibit methane clumped isotope compositions indicating a disequilibrium state of intramolecular isotopic ordering, demonstrating that isotope ordering in methane from these gases is frequently influenced by factors other than thermodynamic stability, possibly including kinetic isotope effects associated with irreversible chemical reactions. The gases furthest from an equilibrium methane clumped isotope composition are from the Bakken Shale, the Eagle Ford Shale, and the Paris Basin. Their isotope signatures depart from the equilibrium curve in Figure 5-2 vertically, with a substantial deficit in $\Delta^{12}CH_2D_2$ (-5 – -10‰) despite small to negligible offsets from equilibrium in $\Delta^{13}CH_3D$. This pattern resembles that for methane produced from laboratory pyrolysis of octadecane (Dong et al., 2020), though the low $\Delta^{12}CH_2D_2$ values of natural methanes are less extreme than those in experimental methanes. For this reason, we propose that irreversible thermal cracking chemistry, mechanistically similar to paraffin pyrolysis, is responsible for producing the disequilibrium clumped isotope signature in these natural methanes.

The typical clumped isotope pattern of both the natural methanes from this study and the octadecane pyrolysis products from Dong et al. (2020) — pronounced depletion in $\Delta^{12}CH_2D_2$ values and near-equilibrium $\Delta^{13}CH_3D$ values — coheres with the prediction

from a type of statistical clumped isotope effect known as the ‘combinatorial effect’ (Röckmann et al., 2016; Yeung, 2016; Xia and Gao, 2019; Cao et al., 2019). The combinatorial effect arises from forming a molecule with two or more indistinguishable chemical positions (e.g., the four H atoms in methane) that differ in probability of rare isotope substitution. Dong et al. (2020) argue that such an effect arises in the reactions associated with thermal cracking, where the step of forming methane combines a methyl radical with an H atom abstracted from an organic or water H source (propagation). And there is a large contrast in D/H ratio between hydrogen atoms from the reacting methyl group and the capping hydrogen atom that joins it to form methane. Three out of four H atoms come from a methyl group having D/H ratios of their alkyl source, modified by a secondary kinetic isotope effect associated with the reaction(s) that form the methyl group. The capping hydrogen atom has the D/H ratio of an alkyl or water sourced hydrogen modified by a primary isotope effect associated with hydrogen abstraction. Combination of these two reactants lead to relatively low $^{12}CH_2D_2$ abundance compared to the expected value based on the methane’s total D/H ratio, expressed as a negative anomaly in $\Delta^{12}CH_2D_2$. The combinatorial effect does not impact $\Delta^{13}CH_3D$ directly because the two rare isotopes in this species (^{13}C and D) occupy chemically distinguishable molecular sites and so their differences in relative probabilities of rare isotope substitution are accounted for in the molecular $\delta^{13}C$ and δD.

It is noteworthy that all methanes below the equilibrium curve in Figure 5-2 are oil-associated wet gases, which is a sign of primary cracking and oil-window catagenesis, and that most methanes on the equilibrium curve are non-associated dry gases, which is a sign of secondary cracking and gas-window catagenesis. Additionally, we found that the amplitude of a sample's departure from the equilibrium curve is correlated with the estimated thermal maturity of that sample's source rocks. Specifically, the vertical distance of a sample's offset from the equilibrium curve diminishes with increasing $\delta^{13}C$ of that methane and with increasing vitrinite reflectance index, R_o%, of its source rocks (Figure 5-3). Gas samples from source rocks with $R_o \geq 1.5\%$ are within error of equilibrium clumped isotope compositions.

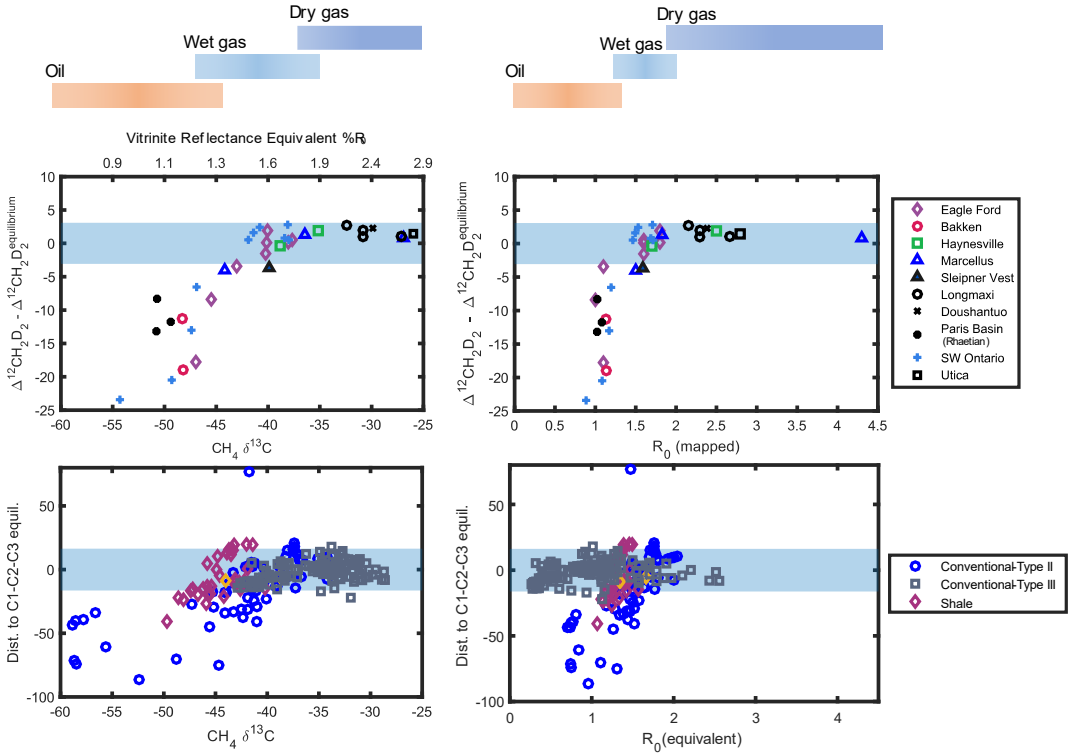

Figure 5-3: Distance to isotope equilibrium plotted versus carbon isotopes of methane and Vitrinite reflectance. The upper panels show distance to methane clumped isotope equilibrium as indicated by offset on $\Delta^{12}CH_2D_2$ axis. In the upper right panel's horizontal axis is Vitrinite Reflectance determined by method (1) or (2) (see Method and Materials section for details), or method (3) when (1) and (2) are not available. The lower panels show distance to the C1-C2-C3 compound-specific hydrogen isotope equilibrium. The lower right panel's horizontal axis is Vitrinite Reflectance determined by method (3), with respect to different types of source materials. The dataset is a compilation of

publications and reports. Band reflects error bar of equilibrium (0 on all four figures) with a 95% confidence interval, derived from each type of measurements and propagation. The dataset includes this study and previous publications. Data source: Eagle Ford, Bakken, Haynesville, Marcellus (2 out of 3), Sleipner Vest, Longmaxi, Doushantuo, Paris Basin (Rhaetian): this study; Marcellus (1 out of 3), Utica: Young et al., 2017; Southwest Ontario: Giunta et al., 2019.

The observed dichotomy of non-equilibrated low-maturity gases and equilibrated high-maturity gases suggests a fundamental change in the chemical mechanisms governing isotopic distributions in methane with thermal maturation. A straightforward interpretation of the attainment of equilibrium isotope distributions with increased thermal stress is that longer times at higher temperatures promote reversible hydrogen exchange reactions, although it is also possible that kinetic isotope effects of irreversible reactions coincidentally resemble the equilibrium clumped isotope signatures. For this latter possibility, observed clumped isotope compositions of methane will reflect both the isotope composition of the instantaneous product (which will reflect some combination of kinetic isotope effects associated with irreversible reactions and combinatorial effects associated with combining hydrogens from different sources) and the effects of accumulation of those instantaneous products. We note that natural gas from some of the

unconventional gas deposits, such as the Eagle Ford Shale studied here, are the residues left after partial loss (or expulsion) of mostly early-formed gas (e.g., Byrne et al., 2018), and thus we should expect them to have isotope compositions intermediate between instantaneous gas and cumulative gas (Rooney et al., 1995). Nevertheless, it is still useful to examine the hypothesis that apparently equilibrated gas actually formed by kinetically controlled mechanisms by evaluating these endmember scenarios.

The clumped isotope composition of the instantaneously formed methane is controlled by the clumped isotope composition of the precursor, kinetic isotope effects associated with formation of the methyl radical, and the strength of the combinatorial effect, which varies with the contrast in D/H ratio between the two H sources (methyl and capping H). This last factor is ultimately controlled by isotope ratios of their precursor substrates as well as the primary and secondary KIE's associated with their formation. KIEs could vary as a function of temperature, though temperature effects are not likely to be sufficiently large to account for all of the 20‰ range of the $\Delta^{12}CH_2D_2$ values seen in some natural methanes. For example, if the temperature changes from 150 to 200 °C, the shift in $\Delta^{12}CH_2D_2$ caused by the combinatorial effect (i.e., due to temperature effects on the fractionations controlling the D/H ratios of the methyl and capping H pools) is calculated to be 9‰, following the methods of Yeung (2016). High degrees of reaction progress can potentially distill reacting substrates toward isotopic contents that differ greatly from their initial compositions. The isotopic composition of instantaneously formed methane

influenced by this effect is expected to evolve continually with reaction progress, which contradicts the observed plateauing trend for methane at R_o>1.5. The accumulation process could potentially bring methane's clumped isotope composition closer to equilibrium when reaction progresses towards completion, assuming homolytic cleavage and hydrogen capping are the only isotopically fractionating mechanisms (Xia and Gao, 2019). In this scenario, the final clumped isotope composition of product methane could be similar to that of the methyl precursor, which might be fortuitously close to the equilibrium distribution for methane. However, this scenario can be ruled out in the case of our natural samples because it requires the near complete (95%+) transformation of precursors to methane, which is implausibly high for these thermogenic gases. For example, the most mature sample from the Eagle Ford Shale in this study is estimated to be the product of transformation of 53-58% of precursors to petroleum products (Byrne et al., 2018). Therefore, the existing kinetic mechanisms of methane formation (methyl+H) do not offer a satisfactory explanation for natural methane's clumped isotope evolution.

The transition from a non-equilibrium to equilibrium clumped isotope composition with rising thermal maturation is similar to the previously observed evolution of position-specific hydrogen isotopes of propane in shale gases (Liu et al., 2019; Zhao et al., 2020; Xie et al., 2020), which also reaches equilibrium at R_o>1.5. A parsimonious explanation of this common pattern for two different properties of two different molecules is that both methane clumped isotope signatures and propane site-specific hydrogen isotope

signatures are subject to equilibration by hydrogen exchange, which becomes faster at higher temperatures and progresses further with longer sustained heating (recognizing that the R_o value reflects both peak temperature and duration of heating). Hydrogen exchange of light alkanes is sluggish because alkyl C-H covalent bonds are relatively stable and inert, yet previous work demonstrates such exchange occurs over geological timescales (Sessions et al., 2004; Xie et al., 2020). The C-H bond in methane is the strongest C-H bond in alkanes (Bond Dissociation Energy=439 kJ/mol (Luo, 2007)). In the absence of any catalyst, hydrogen exchange can proceed with a free radical mechanism (Xia and Gao, 2019; Dong et al., 2020; Thiagarajan et al., 2020b). Previous experiments have shown that in a pure methane-water system hydrogen exchange between methane and water has a half-life of 6.3×10^5 years at 200°C and 8.7×10^3 years at 240°C (Koepp 1978). We compared these timescales with basin burial time-scales for the locations in this study using extrapolations of the Koepp (1978) estimates of exchange rates based on Arrhenius' law (Figure 5-4). This analysis shows that samples from the Haynesville Shale, Marcellus Shale, and Longmaxi Shale have resided for time-at-temperature that exceed the exchange timescales, while samples from the Bakken Shale and Paris Basin resided at depth for too short of time to reach exchange timescales at their burial temperatures. Our sampling of the Eagle Ford Shale includes both those that could have equilibrated by alkane-water hydrogen isotope exchange and those that could not have. This distribution of thermal histories experienced by the samples we studied

matches their distribution of observed equilibrium and disequilibrium clumped isotope signatures, i.e., samples that resided at elevated temperatures for longer than exchange timescales are in equilibrium and vice versa. Note that our use of the experimental constraints on isotope exchange rates assumes the absence of any catalytic materials that might have accelerated exchange. Many metal oxides and metals are capable of providing catalytic surfaces and promoting efficient hydrogen exchange (Sattler, 2018). For example, methane achieves full clumped isotope equilibration within days at room temperature in the presence of γ-alumina (Eldridge et al., 2019; Wang et al., 2020). Clay minerals such as montmorillonite and kaolinite that are more widespread in petroleum source rocks are also shown to be catalytic for such exchange (Alexander et al., 1984; Sessions et al., 2004). For these reasons, we recognize that exchange in nature could be swifter than estimated by our analysis of sample thermal histories due to the presence of these materials. Nevertheless, it is striking that this analysis leads to predictions that are well correlated with our findings.

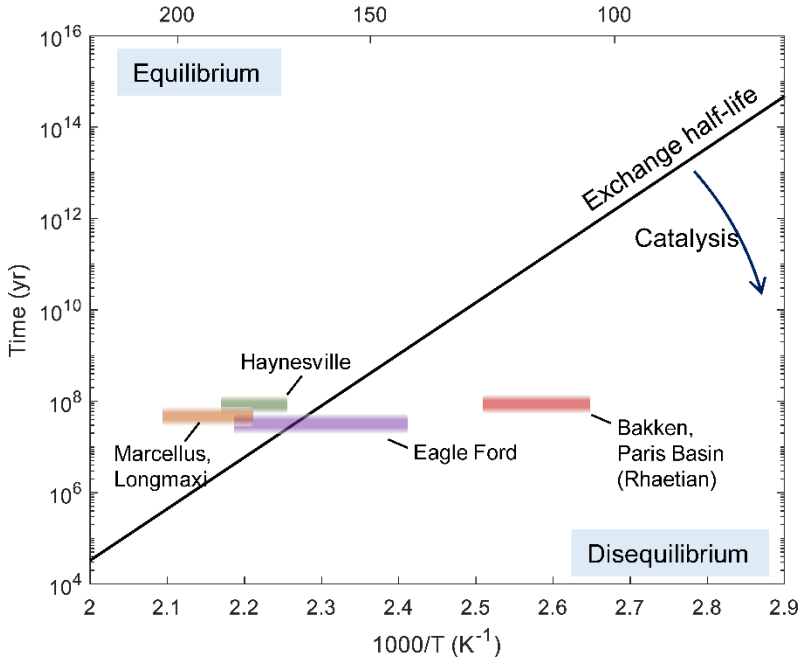

Figure 5-4: Comparing reconstructed temperature-time estimates of several formations in this study with hydrogen exchange rates from methane-water exchange experiments. The temperature of each formation is maximum burial temperature, and the time of each formation indicate the residence time at peak burial temperature with a 10% tolerance. Thermal history estimates from Eagle Ford, Haynesville, and Marcellus are based on Exxon Mobil's in-housing basin modeling. Thermal history of the Bakken shale is obtained from (Pitman et al., 2012).

A subset of the samples we consider come from the Eagle Ford Shale and encompass a large range in thermal maturation, from mainstage oil window to mainstage gas window.

The $\delta^{13}C_{VPDB}$ values of ethane from these samples range from -33.6 to -18.5 ‰ and their $C_1/(C_2+C_3)$ ratio (also known as the 'dryness' ratio) range from 3.6 to 23.7. Their clumped isotope signatures also cover the entire range we observe for other thermogenic gases. We attempted to interpret the chemical and isotopic properties of these samples using a forward numerical model for kinetic methane generation and hydrogen exchange in the Eagle Ford Shale, following the basic architecture of previous related models (Xia and Gao, 2019; Dong et al., 2020) and informed by 1-dimensional basin models for the samples' source rocks created with the Schlumberger PetroMod basin modeling package. Further details of this model are explained in the Method and Materials section. The model successfully reproduces the evolution of the clumped isotope signatures in the Eagle Ford Shale without significant parameter fitting (Figure 5-A.2). The success of this analysis suggests that the modeling framework we have used could be utilized as an inverse model to revise and calibrate basin thermal models using clumped isotope signatures as input.

Although hydrogen exchange equilibration offers a satisfactory interpretation of the clumped isotope trends, we still could not rule out alternative processes and factors that may also be responsible. It is possible that the results are influenced by alternative methane formation pathways besides methyl+H radical termination, such as transition metal catalysis (Mango, 1992) and carbonium ion mechanism catalyzed by clay minerals (Johns, 1979). In another example, low-temperature pyrolysis experiments have

demonstrated that water participation changes with temperature, indicating a shift in the chemical environment of methane formation (Wei et al., 2019). In addition, we also have to consider the role of isotope effects from phase transitions, particularly exsolution from oil. Phase separation of gas from liquid occurs during petroleum fluid migration, production and/or even laboratory gas extraction. Additionally, most samples that exhibit pronounced non-equilibrium $^{12}CH_2D_2$ deficits are oil-associated wet gases, whereas most samples that have near-equilibrium clumped isotope compositions are high-maturity non-associated dry gases, so that the substantial change in gas-to-oil ratio makes it reasonable to suspect a potential role of co-occurring oil in the creation of clumped isotope disequilibrium. Laboratory experiments demonstrated that non-trivial fractionation of Δ_{18} (isotope clumping notation of combined $^{13}CH_3D$ and $^{12}CH_2D_2$, dominantly driven by $\Delta^{13}CH_3D$) happens when wet gas is extracted from a high-pressure, condensate-bearing cylinder at room temperature (Douglas et al., 2017). However, no previous study has explored such effects on $\Delta^{12}CH_2D_2$, and we suggest this should be a subject of future work. We conclude that equilibration by thermally activated, hydrogen exchange of methane during prolonged residence at high temperatures provides a straightforward and parsimonious interpretation of our findings, but that more speculative hypotheses based on changes in methane formation pathway and environment might also succeed in explaining these data.

Many of the gases characterized by near-equilibrium clumped isotope compositions and relatively high thermal maturities lie just above the equilibrium curve in Figure 5-2 (i.e., higher in $\Delta^{12}CH_2D_2$), although this deviation is only 1-2× external precision of each measurement. It would be natural to suspect a systematic error such as an inaccurate calibration of laboratory working reference gases. However, data for thermogenic gases coming from both the Caltech lab and UCLA lab share this feature of slightly higher-than equilibrium $\Delta^{12}CH_2D_2$ values, making it less likely to be attributed to laboratory technical artifacts. We offer several other possible explanations: 1) the actual equilibrium curve for the natural form of methane at the condition of subsurface shale formations differs from the gas-phase equilibrium curve predicted by theory and calibrated in the laboratory. The pressure-temperature conditions of sources and reservoirs for these gases are usually in the stability field of supercritical methane, which has more intermolecular interactions than gas phase methane and could lead to changes in vibrational isotope effects. 2) This subtle $^{12}CH_2D_2$ enrichment is due to the nonlinear mixing effect that manifests for clumped isotopes when materials that differ in molecular-average isotopic content ($\delta^{13}C$ and δD) mix without intermolecular isotopic exchange (Eiler, 2007; Eiler, 2013). Here, we suggest this could be caused by post-generation mixing of gases of slightly different thermal maturity. This scenario would require that mixing post-dated gas generation and uplift, because the gas generation temperatures of these thermally mature gases were hot enough that our modeling above would lead us to expect post-mixing equilibration.

Therefore, gases that still reside in deep and hot reservoirs would not share this deviation in this case. This is supported by data from the Haynesville and Eagle Ford shales (both of which have not been uplifted significantly), where mature samples (R_o>1.5) do not show observable $^{12}CH_2D_2$ excess.

Our results indicate that direct conversion of methane clumped isotope signatures to temperatures assuming the known gas phase equilibrium calibrations (also known as apparent temperature) is only well-founded for equilibrated gases that form at higher thermal maturation (R_o>1.5%, or $\delta^{13}C$>-42‰ for gas sourced from type II kerogens) (Figure 5-5). If hydrogen exchange is the mechanism responsible for equilibration, the temperature derived from this proxy would record the temperature at which those gases were equilibrated, or a blocking temperature at isotope exchange ceased being rapid on geological timescales. We note that thermometry based on $\Delta^{13}CH_3D$ values from non-equilibrium samples (oil-window maturity) yield temperature very close to the formation temperature. This relationship likely reflects that ^{13}C-D clumping in the precursors (e.g., $\Delta^{13}CH_2D$ of the methyl group) are generally at or close to equilibrium, since the termination step (methyl + H) of methane formation does not cause significant deficits in $\Delta^{13}CH_3D$ (Xia and Gao, 2019; Dong et al., 2020). Similarly, Δ_{18} temperatures would also be relatable, although the large deficit in $\Delta^{12}CH_2D_2$ could decrease Δ_{18} values and increase apparent temperatures. Although we cannot rule out that these values still record meaningful temperature of precursors' equilibrium, people should be wary of

thermometry based on $\Delta^{13}CH_3D/\Delta_{18}$ values of thermogenic gases at oil-window maturity (R_o<1.5%). On the other hand, we propose that the deviation from $\Delta^{12}CH_2D_2$ equilibrium can serve as a new benchmark for thermal maturation of natural gases that form in the oil window and wet-gas window. Deviation from clumped isotope equilibrium is shown to be sensitive to maturation, shifting by ~25‰ over a R_o change of 0.5% in shale gas samples. The most likely explanation for this is the gradual erasing of kinetic isotope effects that occur during gas generation (mostly controlled by combinatorial effects) before it becomes completed removed by thermally activated isotope exchange equilibration.

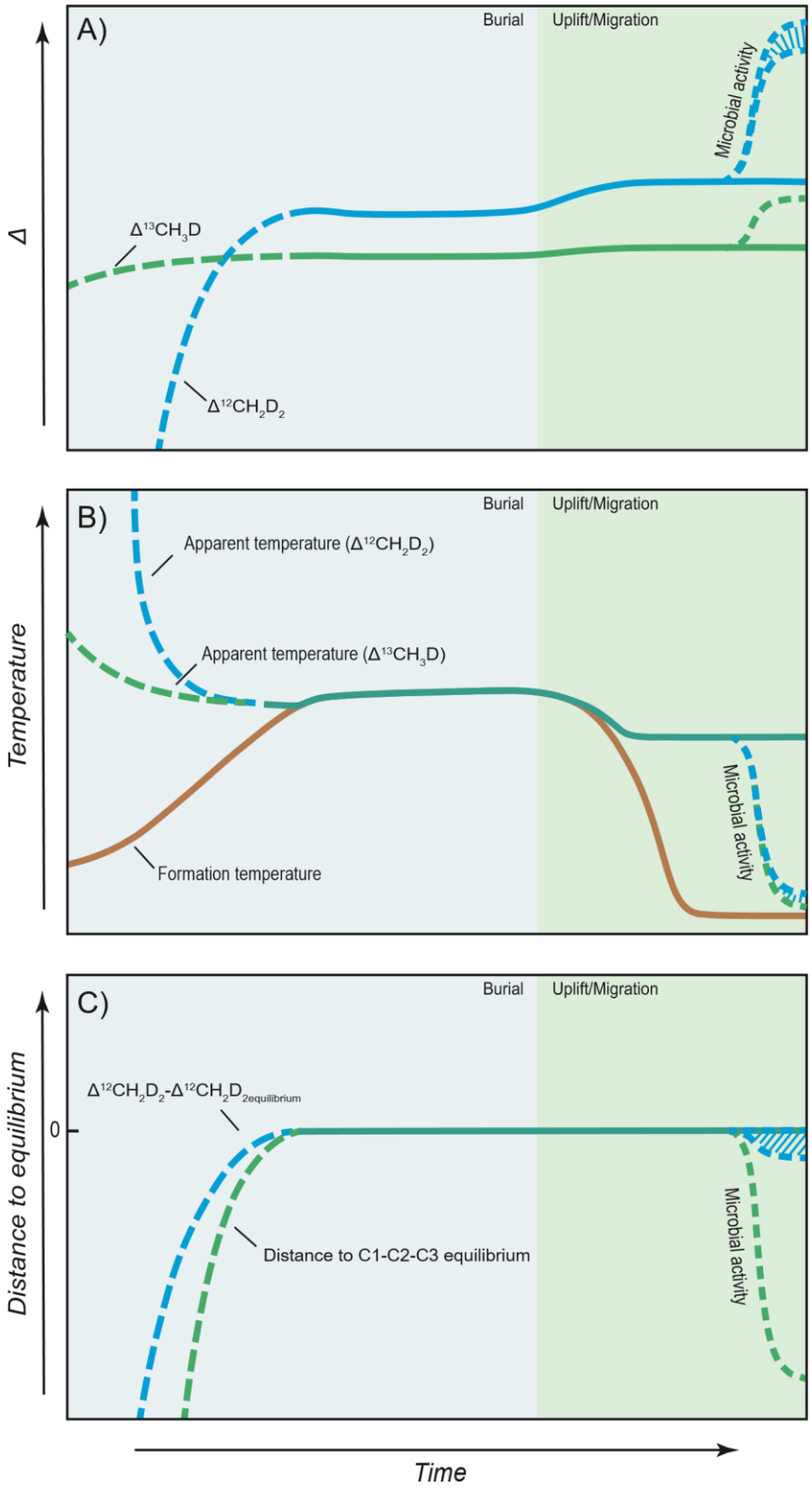
A)
Burial
Uplift/Migration
Microbial activity
Δ
Δ13CH3D
Δ12CH2D2
B)
Burial
Uplift/Migration
Apparent temperature (Δ12CH2D2)
Apparent temperature (Δ13CH3D)
Temperature
Formation temperature
Microbial activity
C)
Burial
Uplift/Migration
Δ12CH2D2-Δ12CH2D2equilibrium
0
Distance to equilibrium
Distance to C1-C2-C3 equilibrium
Microbial activity
Time

Figure 5-5: Schematic illustration of how geochemical signatures evolve in a typical basin burial-uplift process. A): evolution of methane clumped isotopes; B): evolution of apparent temperature derived from methane clumped isotopes; C): evolution of distance to equilibrium in methane clumped isotope system and C1-C2-C3 compound-specific hdyrogen isotope fractionation system. The range of effects of microbial activity (anaerobic oxidation of methane and methanogenesis) are estimated from prior studies of Stolper et al., 2015; Young et al., 2017; Giunta et al., 2019; Ash et al., 2019; Thiagarajan et al., 2020a.

4.2 Comparison to compound-specific hydrogen isotope fractionation

The exchange equilibration of intramolecular isotope ordering in methane and propane requires at least activation of C-H bond in both compounds regardless of its mechanism (radical chain or surface catalysis), which would also exchange hydrogen between methane, ethane and propane (C_1, C_2 and C_3, respectively). To test this idea, we compiled a global dataset of compound-specific (i.e., molecular average) hydrogen isotope compositions in natural gases from a variety of publications and reports (see the Methods and Materials Section for details). For each sample, we calculated the shortest distance from the sample's location in a δD_{C1} vs. δD_{C2} vs. δD_{C3} Cartesian space to a plane defined by mutual thermodynamic equilibrium among those gases. It was found that compound-

specific hydrogen isotope compositions exhibit a trend with thermal maturity similar to those exhibited by methane clumped isotopes (this study) and propane-site specific hydrogen isotopes (Liu et al., 2019; Xie et al., 2020). In the least mature gases, the compound specific hydrogen isotope composition is very distant from equilibrium and systematically concentrated on one side of the plane where δD_{C1} is lower than could be consistent with equilibrium with C_2 and C_3. A typical hydrogen isotope profile of these early maturity gases is very low δD_{C1} values (-250 – -300‰) and big gaps between C_1–C_2–C_3. This pattern resembles the predictions of kinetic models of hydrogen isotope fractionation during irreversible catagenetic reactions (Ni et al., 2011) and has been observed in pyrolysis experiments (Jin et al., 2009; Gao et al., 2014; Wei et al., 2019; Dong et al., 2020), suggesting that irreversible mechanisms in thermal cracking are responsible. The differences in hydrogen isotope composition between compounds get smaller as $\delta^{13}C_{C1}$ and gas maturity increase, eventually converging to thermodynamic equilibrium at thermal maturities corresponding to R_o>1.5 (Figure 5-3). Because the majority of our samples examined in this literature review are from conventional reservoirs instead of shale gases, we acknowledge that our evaluation of its maturity is prone to error and might be responsible for some of the scatter in Figure 5-3. Likewise, inter-laboratory inconsistencies in analytical techniques can also lead to errors in this analysis. Nevertheless, the similarities between this finding and our findings for methane clumped isotopes and propane positional preference are compelling and support both the

underlying mechanisms and potential applications. Specifically, we conclude that hydrogen exchange is plausibly responsible for the equilibrium isotope fractionations between these compounds, and we suggest that comparison of the compound-specific hydrogen isotope distribution among thermogenic gas components with the expected equilibrium distributions can be used to constrain thermal maturation in a manner resembling our suggested interpretation of methane clumped isotope and propane position-specific hydrogen isotope compositions.

Natural thermogenic gases derived from Type III kerogen (coal-derived gas) seem to show a different trend in Figure 5-3 than that defined by gases from Type II kerogens; in the case of the former samples, even the lower maturity samples of them can be close to or at equilibrium with respect to compound specific C_1–C_3 hydrogen isotope compositions. We suggest two possible explanations for this observation: (1) gas generation from Type III kerogens involves a kinetic effect that mimics the equilibrium fractionations (pseudo-equilibrium) and absence of combinatorial effects from methyl+H termination; or (2) enhanced exchange promotes equilibrium at lower maturities than those that permit equilibration of Type-II gases. Note that we cannot rule out an artifact of inaccurate calibration of the relationship between R_o and $\delta^{13}C_{C1}$ that was used to assign approximate thermal maturities to these gases. There is reason to suspect this as several publications report calibrations of this relationship that do not agree with each

other (See Method and Materials section for details). Future studies of methane clumped isotopes in Type III gases of variable thermal maturity might address this question.

It is possible to obtain the apparent temperature of thermogenic gas formations based on a nominally equilibrated sample's compound specific hydrogen isotope composition. We found that the apparent temperatures derived from this method of thermometry have a positive correlation with $\delta^{13}C_{C1}$ (Figure 5-A.3), suggesting the plausible result of increasing gas generation temperature with increasing thermal maturation. However, the data that define this trend are scattered for several reasons; most simply, the analytical precision for δD from the compiled literature data we have used in this exercise is usually around 5‰, which leads to relatively large variations in apparent temperature. For instance, if a typical equilibrated sample has 1σ=5‰ uncertainty on the δD of each of the three compounds (C_1, C_2, C_3), then the corresponding uncertainty in apparent temperature is +34°C and -33°C (at 95% confidence interval, based on a Monte-Carlo simulation), which is relatively large compared to the range of temperature evolution. There is also large uncertainty associated with estimation of equivalent R_o derived from gas isotopes (see Methods and Materials and Galimov (2006)). On the other hand, we note that the apparent temperature could also be influenced by post-generation equilibration. If a mature gas migrates to a reservoir or a host formation uplifts, the gas might continue to exchange hydrogen when the storage temperature is higher than blocking temperature

(Figure 5-4) and record a lower temperature than its generation (Figure 5-5). Nevertheless, this correlation between apparent temperature and empirical maturity supports the idea that the equilibria of hydrogen isotopes could be used to track the thermal history of gases.

5. Conclusion and further implications

We present several lines of evidence that intra- and inter-molecular hydrogen isotope distributions in methane, ethane and propane are controlled by chemical-kinetic isotope effects at early thermal maturities and equilibrium isotope effects at higher maturities. This is consistent with previous claims that increasing thermal maturity drives subsets of natural gas compounds toward metastable equilibrium (Xia and Gao, 2019; Thiagarajan et al., 2020b). We show this to be the case in fluids generated and stored at high temperatures in unconventional reservoirs, and in fluids that have migrated to cooler conventional reservoirs. If true, this observation has profound impacts on our understanding of the occurrence and evolution of petroleum, as it suggests that the major gas components of many systems exist in a dynamically reacting metastable equilibrium state. The crossover from disequilibrium to equilibrium isotopic distributions happens around a thermal maturity corresponding to R_o=1.5, which marks an important watershed for evaluating the chemistry governing natural gas speciation and isotope partitioning.

This maturity corresponds to temperature of 170–210 °C for typical burial time range of 1–100 Ma (Sweeney and Burnham, 1990).

According to this new scheme, both equilibrium and disequilibrium isotope distributions can be used to constrain thermal maturation of natural gas. In the early stages of thermal maturation, departure from equilibrium, reflected in both $\Delta^{12}CH_2D_2$ value and distance to C_1–C_2–C_3 hydrogen isotope equilibrium, correlates with integrated time-at-temperature of burial. A first-order estimation on the thermal maturation from the clumped isotope signature can be achieved with calibrated relationships of shale gases in this study. We also present a numerical model of the dynamics of kinetic gas generation and subsequent isotope exchange (based on data for samples from the Eagle Ford Shale), and this too could provide a process-based means of interpreting methane clumped isotope measurements of low maturity gases as constraints on their thermal maturity. In the case of gases with equilibrium clumped isotope compositions, this proxy can be used directly as a constraint on gas generation and/or storage temperatures.

Our analysis also highlights the value of compound-specific hydrogen isotope data of natural gas, which have received far less attention than compound-specific carbon isotopes. We show that thermal maturation of a gas can be assessed using δD values of C_1, C_2, and C_3, based on their departure from intermolecular equilibrium. Like the evolution of clumped isotope signatures, the evolution of compound-specific hydrogen

isotope fractionation has defined paths for geological processes of burial, uplift, and microbial activity (Figure 5-6), so that the combination of these signatures provides explicit interpretation of natural gas formations. The compound specific hydrogen isotope compositions can be measured more rapidly and in a larger number of labs than clumped isotopes of methane, suggesting this could be a fruitful approach to at least triaging natural gases to evaluate their thermal maturities. However, we acknowledge that the analysis performed in this study is limited to compound specific hydrogen isotope data compiled from previous publications and public reports (see details in the Method and Materials section and Appendix 5), which are limited in both amount and analytical precision. Further development of this concept may require more systematic studies that make use of higher precision methods (such as direct high-resolution mass spectrometry, which can achieve precisions in δD of 0.1 ‰).

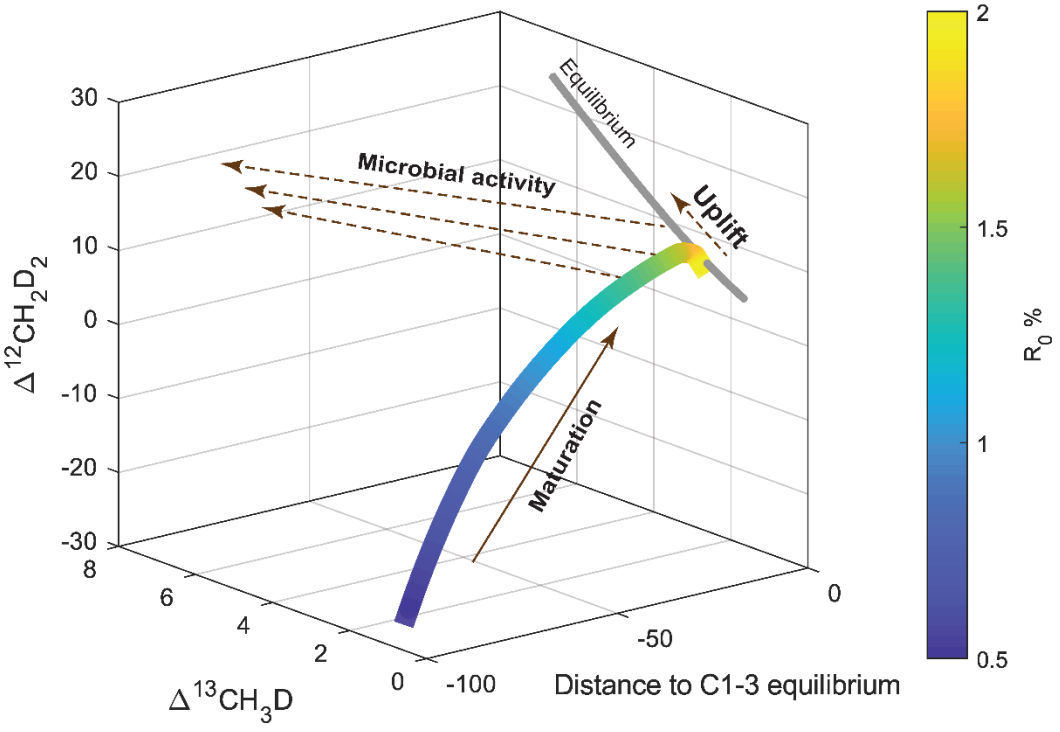

Figure 5-6: Schematic illustration of geological and microbial processes' trajectories on the isotope indices of methane clumped isotopes and C1–C2–C3 hydrogen isotopes. The range of effects of microbial activity (anaerobic oxidation of methane and methanogenesis) is estimated from prior studies of Stolper et al., 2015; Young et al., 2017; Giunta et al., 2019; Ash et al., 2019; Thiagarajan et al., 2020a.

Our results also indicate that low-maturity thermogenic gases and biogenic gases can potentially overlap in a $\Delta^{12}CH_2D_2$ vs. $\Delta^{13}CH_3D$ space, creating ambiguity in the interpretation of this proxy. However, we note that thermogenic gases have $\Delta^{13}CH_3D$ values confined to a tight range (1.5–3.5‰) for reasons explained above, whereas biogenic methane often varies greatly in this property (-2 – +10‰ for natural samples and -6 – +4‰ for lab cultures; Wang et al., 2015; Stolper et al., 2015; Douglas et al., 2016; Young, 2019). Therefore, the likelihood that microbial sourced methane will have both $\Delta^{13}CH_3D$ and $\Delta^{12}CH_2D_2$ within the thermogenic range remains low. Our study also redefines the clumped isotope compositions of pure thermogenic endmembers that might be considered in models of mixtures of thermogenic and biogenic gases. In cases where contribution from a low maturity thermogenic gas is suspected, other maturation indicators (e.g., gas wetness and compound-specific isotope compositions, biomarkers in co-existing oil, petrological proxies, basin modeling, etc.) might be used to pinpoint the isotopic signature of the thermogenic endmember.

Acknowledgements

This work was supported by Caltech, ExxonMobil Upstream Integrated Solutions, the Caltech Joint Industry Partnership for Petroleum Geochemistry, Thermo Fischer Scientific, and the Department of Energy BES program. We thank the ExxonMobil

Corporation, Sinopec, PetroChina and Lundin companies for collecting natural gas samples. We thank Nami Kitchen for laboratory assistance. We thank Alex Sessions and David Wang for helpful discussions. We thank Nina Albrecht, Ulrike Wacker, Darren Tollstrup, and Timothy Piles for advices on mass spectrometry.

References

Alexander R., Kagi R. I. and Larcher A. V. (1984) Clay catalysis of alkyl hydrogen exchange reactions-reaction mechanisms. *Org. Geochem.* **6**, 755–760.

Barry P. H., Lawson M., Meurer W. P., Warr O., Mabry J. C., Byrne D. J. and Ballentine C. J. (2016) Noble gases solubility models of hydrocarbon charge mechanism in the Sleipner Vest gas field. *Geochim. Cosmochim. Acta* **194**, 291–309.

Bernard B. B., Brooks J. M. and Sackett W. M. (1978) Light hydrocarbons in recent Texas continental shelf and slope sediments. *J. Geophys. Res.* **83**, 4053.

Berner U. and Faber E. (1996) Empirical carbon isotope/maturity relationships for gases from algal kerogens and terrigenous organic matter, based on dry, open-system pyrolysis. In *Organic Geochemistry* Pergamon. pp. 947–955.

Burnham A. K., Braun R. L., Gregg H. R. and Samoun A. M. (1987) Comparison of

Methods for Measuring Kerogen Pyrolysis Rates and Fitting Kinetic Parameters†. *Energy and Fuels* **1**, 452–458.

Burnham A. K., Braun R. L. and Samoun A. M. (1988) Further comparison of methods for measuring kerogen pyrolysis rates and fitting kinetic parameters. *Org. Geochem.* **13**, 839–845.

Byrne D. J., Barry P. H., Lawson M. and Ballentine C. J. (2018) Determining gas expulsion vs retention during hydrocarbon generation in the Eagle Ford Shale using noble gases. *Geochim. Cosmochim. Acta* **241**, 240–254.

Cao X., Bao H. and Peng Y. (2019) A kinetic model for isotopologue signatures of methane generated by biotic and abiotic CO2 methanation. *Geochim. Cosmochim. Acta* **249**, 59–75.

Chung H. M., Gormly J. R. and Squires R. M. (1988) Origin of gaseous hydrocarbons in subsurface environments: Theoretical considerations of carbon isotope distribution. *Chem. Geol.* **71**, 97–104.

Clog M., Lawson M., Peterson B., Ferreira A. A., Santos Neto E. V. and Eiler J. M. (2018) A reconnaissance study of 13C–13C clumping in ethane from natural gas. *Geochim. Cosmochim. Acta* **223**, 229–244.

Dai J., Ni Y. and Zou C. (2012) Stable carbon and hydrogen isotopes of natural gases sourced from the Xujiahe Formation in the Sichuan Basin, China. *Org. Geochem.* **43**, 103–111.

Dai J. and Qi H. (1989) Relationship of 13C-Ro of coal-derived gas in China. *Chinese Sci. Bull.* **34**, 690–692.

Dai J. X., Ni Y. Y., Hu G. Y., Huang S. P., Liao F. R., Yu C., Gong D. Y. and Wu W. (2014) Stable carbon and hydrogen isotopes of gases from the large tight gas fields in China. *Sci. China Earth Sci.* **57**, 88–103.

Dong G., Xie H., Kitchen N., Formolo M. J., Michael L., Sessions A. L. and Eiler J. M. (2020) Methane Clumped Isotope Effects during Hydrocarbon Cracking in Laboratory Experiments. *Submitt. to GCA*.

Douglas P. M. J., Stolper D. A., Eiler J. M., Sessions A. L., Lawson M., Shuai Y., Bishop A., Podlaha O. G., Ferreira A. A., Santos Neto E. V., Niemann M., Steen A. S., Huang L., Chimiak L., Valentine D. L., Fiebig J., Luhmann A. J., Seyfried W. E., Etiope G., Schoell M., Inskeep W. P., Moran J. J. and Kitchen N. (2017) Methane clumped isotopes: Progress and potential for a new isotopic tracer. *Org. Geochem.* **113**, 262–282.

Douglas P. M. J., Stolper D. A., Smith D. A., Walter Anthony K. M., Paull C. K., Dallimore S., Wik M., Crill P. M., Winterdahl M., Eiler J. M. and Sessions A. L. (2016a)

Diverse origins of Arctic and Subarctic methane point source emissions identified with multiply-substituted isotopologues. *Geochim. Cosmochim. Acta* **188**, 163–188.

Douglas P. M. J., Stolper D. A., Smith D. A., Walter Anthony K. M., Paull C. K., Dallimore S., Wik M., Crill P. M., Winterdahl M., Eiler J. M. and Sessions A. L. (2016b) Diverse origins of Arctic and Subarctic methane point source emissions identified with multiply-substituted isotopologues. *Geochim. Cosmochim. Acta* **188**, 163–188.

Eiler J. M. (2007) "Clumped-isotope" geochemistry-The study of naturally-occurring, multiply-substituted isotopologues. *Earth Planet. Sci. Lett.* **262**, 309–327.

Eiler J. M. (2013) The Isotopic Anatomies of Molecules and Minerals. *Annu. Rev. Earth Planet. Sci.* **41**, 411–441.

Eiler J. M., Clog M., Lawson M., Lloyd M., Piasecki A., Ponton C. and Xie H. (2018) The isotopic structures of geological organic compounds. *Geol. Soc. London, Spec. Publ.* **468**, 53–81.

Eldridge D. L., Korol R., Lloyd M. K., Turner A. C., Webb M. A., Miller T. F. and Stolper D. A. (2019) Comparison of Experimental vs Theoretical Abundances of 13 CH 3 D and 12 CH 2 D 2 for Isotopically Equilibrated Systems from 1 to 500 °C. *ACS Earth Sp. Chem.* **3**, 2747–2764.

Faber E. (1987) Zur isotopengeochemie gasförmiger Kohlenwasserstoffe. *Erdöl, Erdgas, Kohle* **103**, 210–218.

Faber Eckhard, Schmidt Mark, Feyzullayev A., Faber E, Schmidt M and Feyzullayev A. A. (2015) *Geochemical Hydrocarbon Exploration-Insights from Stable Isotope Models SMART-Sustainable Management of Offshore Groundwater Resources View project SFB574 View project Geochemical Hydrocarbon Exploration-Insights from Stable Isotope Models*.,

Galimov E. M. (2006) Isotope organic geochemistry. *Org. Geochem.* **37**, 1200–1262.

Galimov Ė. M. (1975) *Carbon isotopes in oil-gas geology*., National Aeronautics and Space Administration.

Gao L., Schimmelmann A., Tang Y. and Mastalerz M. (2014) Isotope rollover in shale gas observed in laboratory pyrolysis experiments: Insight to the role of water in thermogenesis of mature gas. *Org. Geochem.* **68**, 95–106.

Gilbert A., Lollar B. S., Musat F., Giunta T., Chen S., Kajimoto Y., Yamada K., Boreham C. J., Yoshida N. and Ueno Y. (2019) Intramolecular isotopic evidence for bacterial oxidation of propane in subsurface natural gas reservoirs. *Proc. Natl. Acad. Sci. U. S. A.* **116**, 6653–6658.

Gilbert A., Yamada K., Suda K., Ueno Y. and Yoshida N. (2016) Measurement of position-specific 13C isotopic composition of propane at the nanomole level. *Geochim. Cosmochim. Acta* **177**, 205–216.

Gilbert A., Yamada K. and Yoshida N. (2013) Exploration of intramolecular 13C isotope distribution in long chain n-alkanes (C11-C31) using isotopic 13C NMR. *Org. Geochem.* **62**, 56–61.

Giunta T., Labidi J., Kohl I. E., Ruffine L., Donval J. P., Géli L., Çağatay M. N., Lu H. and Young E. D. (2021) Evidence for methane isotopic bond re-ordering in gas reservoirs sourcing cold seeps from the Sea of Marmara. *Earth Planet. Sci. Lett.* **553**, 116619.

Giunta T., Young E. D., Warr O., Kohl I., Ash J. L., Martini A., Mundle S. O. C., Rumble D., Pérez-Rodríguez I., Wasley M., LaRowe D. E., Gilbert A. and Sherwood Lollar B. (2019) Methane sources and sinks in continental sedimentary systems: New insights from paired clumped isotopologues 13 CH 3 D and 12 CH 2 D 2. *Geochim. Cosmochim. Acta* **245**, 327–351.

Gonzalez Y., Nelson D. D., Shorter J. H., McManus J. B., Dyroff C., Formolo M., Wang D. T., Western C. M. and Ono S. (2019) Precise Measurements of 12CH2D2 by Tunable Infrared Laser Direct Absorption Spectroscopy. *Anal. Chem.* **91**, 14967–14974.

Head I. M., Jones D. M. and Larter S. R. (2003) Biological activity in the deep

subsurface and the origin of heavy oil. *Nature* **426**, 344–352.

Helgeson H. C., Knox A. M., Owens C. E. and Shock E. L. (1993) Petroleum, oil field waters, and authigenic mineral assemblages Are they in metastable equilibrium in hydrocarbon reservoirs. *Geochim. Cosmochim. Acta* **57**, 3295–3339.

Helgeson H. C., Richard L., McKenzie W. F., Norton D. L. and Schmitt A. (2009) A chemical and thermodynamic model of oil generation in hydrocarbon source rocks. *Geochim. Cosmochim. Acta* **73**, 594–695.

Hunt J. (1996) *Petroleum geology and geochemistry*., Freeman, New York.

James A. T. (1983) Correlation of Natural Gas By Use of Carbon Isotopic Distribution Between Hydrocarbon Components. *Am. Assoc. Pet. Geol. Bull.* **67**, 1176–1191.

Jin Y., Xiao X., Tang Y., Tian H. and Liu J. (2009) *Influence of water on yields and isotopic fractionations of gas hydrocarbons generated from oil cracking*.,

Johns W. D. (1979) Clay mineral catalysis and petroleum generation. *Annu. Rev. earth Planet. Sci. Vol. 7*.

Jones D. M., Head I. M., Gray N. D., Adams J. J., Rowan A. K., Aitken C. M., Bennett B., Huang H., Brown A., Bowler B. F. J., Oldenburg T., Erdmann M. and Larter S. R. (2008) Crude-oil biodegradation via methanogenesis in subsurface petroleum reservoirs.

Nature **451**, 176–180.

Koepp M. (1978) D/H isotope exchange reaction between petroleum and water : A contributory determinant for D/H-isotope ratios in crude oil? Short Pap. Fourth Int. Conf. Geochronology. Cosmochronol. Isot. Geol. 1978, 221–222.

Labidi J., Young E. D., Giunta T., Kohl I. E., Seewald J., Tang H., Lilley M. D. and Früh-Green G. L. (2020) Methane thermometry in deep-sea hydrothermal systems: Evidence for re-ordering of doubly-substituted isotopologues during fluid cooling. *Geochim. Cosmochim. Acta* **288**, 248–261.

Liu C., Liu P., McGovern G. P. and Horita J. (2019) Molecular and intramolecular isotope geochemistry of natural gases from the Woodford Shale, Arkoma Basin, Oklahoma. *Geochim. Cosmochim. Acta* **255**, 188–204.

Liu C., McGovern G. P., Liu P., Zhao H. and Horita J. (2018) Position-specific carbon and hydrogen isotopic compositions of propane from natural gases with quantitative NMR. *Chem. Geol.* **491**, 14–26.

Liu Q., Tossell J. A. and Liu Y. (2010) On the proper use of the Bigeleisen-Mayer equation and corrections to it in the calculation of isotopic fractionation equilibrium constants. *Geochim. Cosmochim. Acta* **74**, 6965–6983.

Luo Y. R. (2007) *Comprehensive handbook of chemical bond energies*., CRC press.

Mango F. D. (2013) Methane and carbon at equilibrium in source rocks. *Geochem. Trans.* **14**, 1–9.

Mango F. D. (1992) Transition metal catalysis in the generation of petroleum and natural gas. *Geochim. Cosmochim. Acta* **56**, 553–555.

Mango F. D., Jarvie D. and Herriman E. (2009) Natural gas at thermodynamic equilibrium implications for the origin of natural gas. *Geochem. Trans.* **10**, 1–12.

Milkov A. V. and Etiope G. (2018) Revised genetic diagrams for natural gases based on a global dataset of >20,000 samples. *Org. Geochem.* **125**, 109–120.

Milkov A. V., Faiz M. and Etiope G. (2020) Geochemistry of shale gases from around the world: Composition, origins, isotope reversals and rollovers, and implications for the exploration of shale plays. *Org. Geochem.* **143**, 103997.

Ni Y., Ma Q., Ellis G. S., Dai J., Katz B., Zhang S. and Tang Y. (2011) Fundamental studies on kinetic isotope effect (KIE) of hydrogen isotope fractionation in natural gas systems. *Geochim. Cosmochim. Acta* **75**, 2696–2707.

Ono S., Wang D. T., Gruen D. S., Sherwood Lollar B., Zahniser M. S., McManus B. J. and Nelson D. D. (2014) Measurement of a doubly substituted methane isotopologue,

13CH3D, by tunable infrared laser direct absorption spectroscopy. *Anal. Chem.* **86**, 6487–6494.

Piasecki A., Sessions A., Lawson M., Ferreira A. A., Santos Neto E. V., Ellis G. S., Lewan M. D. and Eiler J. M. (2018) Position-specific 13C distributions within propane from experiments and natural gas samples. *Geochim. Cosmochim. Acta* **220**, 110–124.

Pitman J. K., Price L. C. and LeFever J. A. (2012) *Diagenesis and fracture development in the bakken formation, williston basin: Implications for reservoir quality in the middle member*., U.S. Geological Survey.

Röckmann T., Popa M. E., Krol M. C. and Hofmann M. E. G. (2016) Statistical clumped isotope signatures. *Sci. Rep.*

Rodriguez N. D. and Paul Philp R. (2010) Geochemical characterization of gases from the Mississippian Barnett Shale, Fort Worth Basin, Texas. *Am. Assoc. Pet. Geol. Bull.* **94**, 1641–1656.

Rooney M. A., Claypool G. E. and Moses Chung H. (1995) Modeling thermogenic gas generation using carbon isotope ratios of natural gas hydrocarbons. *Chem. Geol.* **126**, 219–232.

Sackett W. M., Nakaparksin S. and Dalrymple D. (1966) *Advances in Organic*

Geochemistry: Proceedings of the Third International Congress. ed. G. Hobson, Pergamon.

Sattler A. (2018) Hydrogen/Deuterium (H/D) Exchange Catalysis in Alkanes. *ACS Catal.* **8**, 2296–2312.

Schoell M. (1980) The hydrogen and carbon isotopic composition of methane from natural gases of various origins. *Geochim. Cosmochim. Acta* **44**, 649–661.

Sessions A. L., Sylva S. P., Summons R. E. and Hayes J. M. (2004) Isotopic exchange of carbon-bound hydrogen over geologic timescales. *Geochim. Cosmochim. Acta* **68**, 1545–1559.

Shao D., Ellis G. S., Li Y. and Zhang T. (2018) Experimental investigation of the role of rock fabric in gas generation and expulsion during thermal maturation: Anhydrous closed-system pyrolysis of a bitumen-rich Eagle Ford Shale. *Org. Geochem.* **119**, 22–35.

Shuai Y., Douglas P. M. J., Zhang S., Stolper D. A., Ellis G. S., Lawson M., Lewan M. D., Formolo M., Mi J., He K., Hu G. and Eiler J. M. (2018) Equilibrium and non-equilibrium controls on the abundances of clumped isotopologues of methane during thermogenic formation in laboratory experiments: Implications for the chemistry of pyrolysis and the origins of natural gases. *Geochim. Cosmochim. Acta* **223**, 159–174.

Stahl W. J. and Carey B. D. (1975) Source-rock identification by isotope analyses of natural gases from fields in the Val Verde and Delaware basins, west Texas. *Chem. Geol.* **16**, 257–267.

Stolper D. A., Lawson M., Davis C. L., Ferreira A. A., Santos Neto E. V., Ellis G. S., Lewan M. D., Martini A. M., Tang Y., Schoell M., Sessions A. L. and Eiler J. M. (2014a) Formation temperatures of thermogenic and biogenic methane. *Science (80-.).* **344**, 1500–1503.

Stolper D. A., Lawson M., Formolo M. J., Davis C. L., Douglas P. M. J. and Eiler J. M. (2018) The utility of methane clumped isotopes to constrain the origins of methane in natural gas accumulations. *Geol. Soc. Spec. Publ.* **468**, 23–52.

Stolper D. A., Martini A. M., Clog M., Douglas P. M., Shusta S. S., Valentine D. L., Sessions A. L. and Eiler J. M. (2015) Distinguishing and understanding thermogenic and biogenic sources of methane using multiply substituted isotopologues. *Geochim. Cosmochim. Acta* **161**, 219–247.

Stolper D. A., Sessions A. L., Ferreira A. A., Santos Neto E. V., Schimmelmann A., Shusta S. S., Valentine D. L. and Eiler J. M. (2014b) Combined 13C-D and D-D clumping in methane: Methods and preliminary results. *Geochim. Cosmochim. Acta* **126**, 169–191.

Suda K., Gilbert A., Yamada K., Yoshida N. and Ueno Y. (2017) Compound– and position–specific carbon isotopic signatures of abiogenic hydrocarbons from on–land serpentinite–hosted Hakuba Happo hot spring in Japan. *Geochim. Cosmochim. Acta* **206**, 201–215.

Sweeney J. J. and Burnham A. K. (1990) Evaluation of a simple model of vitrinite reflectance based on chemical kinetics. *Am. Assoc. Pet. Geol. Bull.* **74**, 1559–1570.

Tang Y., Huang Y., Ellis G. S., Wang Y., Kralert P. G., Gillaizeau B., Ma Q. and Hwang R. (2005) A kinetic model for thermally induced hydrogen and carbon isotope fractionation of individual n-alkanes in crude oil. *Geochim. Cosmochim. Acta* **69**, 4505–4520.

Tang Y., Perry J. K., Jenden P. D. and Schoell M. (2000) Mathematical modeling of stable carbon isotope ratios in natural gases. *Geochim. Cosmochim. Acta* **64**, 2673–2687.

Thiagarajan N., Kitchen N., Xie H., Ponton C., Lawson M., Formolo M. and Eiler J. (2020a) Identifying thermogenic and microbial methane in deep water Gulf of Mexico Reservoirs. *Geochim. Cosmochim. Acta* **275**, 188–208.

Thiagarajan N., Xie H., Ponton C., Kitchen N., Peterson B., Lawson M., Formolo M., Xiao Y. and Eiler J. (2020b) Isotopic evidence for quasi-equilibrium chemistry in thermally mature natural gases. *Proc. Natl. Acad. Sci.* **117**, 3989–3995.

Tilley B. and Muehlenbachs K. (2013) Isotope reversals and universal stages and trends of gas maturation in sealed, self-contained petroleum systems. *Chem. Geol.* **339**, 194–204.

Tissot B. P., Pelet R. and Ungerer P. (1987) Thermal History of Sedimentary Basins, Maturation Indices, and Kinetics of Oil and Gas Generation. *Am. Assoc. Pet. Geol. Bull.* **71**, 1445–1466.

Tissot B. P. and Welte D. H. (1978) *Petroleum Formation and Occurrence*., Springer Berlin Heidelberg, Berlin, Heidelberg.

Ungerer P. (1990) State of the art of research in kinetic modelling of oil formation and expulsion. *Org. Geochem.* **16**, 1–25.

Wang D. T., Gruen D. S., Sherwood Lollar B., Hinrichs K. U., Stewart L. C., Holden J. F., Hristov A. N., Pohlman J. W., Morrill P. L., Könneke M., Delwiche K. B., Reeves E. P., Sutcliffe C. N., Ritter D. J., Seewald J. S., McIntosh J. C., Hemond H. F., Kubo M. D., Cardace D., Hoehler T. M. and Ono S. (2015) Nonequilibrium clumped isotope signals in microbial methane. *Science (80-.).* **348**, 428–431.

Wang D. T., Reeves E. P., McDermott J. M., Seewald J. S. and Ono S. (2018) Clumped isotopologue constraints on the origin of methane at seafloor hot springs. *Geochim. Cosmochim. Acta* **223**, 141–158.

Wang D. T., Sattler A., Paccagnini M. and Chen F. G. (2020) Method for calibrating methane clumped isotope measurements via catalytic equilibration of methane isotopologues on γ-alumina. *Rapid Commun. Mass Spectrom.* **34**.

Wang Z., Schauble E. A. and Eiler J. M. (2004) Equilibrium thermodynamics of multiply substituted isotopologues of molecular gases. *Geochim. Cosmochim. Acta* **68**, 4779–4797.

Wei L., Gao Z., Mastalerz M., Schimmelmann A., Gao L., Wang X., Liu X., Wang Y. and Qiu Z. (2019) Influence of water hydrogen on the hydrogen stable isotope ratio of methane at low versus high temperatures of methanogenesis. *Org. Geochem.* **128**, 137–147.

Wei L., Schimmelmann A., Mastalerz M., Lahann R. W., Sauer P. E., Drobniak A., Strąpoć D. and Mango F. D. (2018) Catalytic generation of methane at 60–100 °C and 0.1–300 MPa from source rocks containing kerogen Types I, II, and III. *Geochim. Cosmochim. Acta* **231**, 88–116.

Xia X. (2014) Kinetics of gaseous hydrocarbon generation with constraints of natural gas composition from the Barnett Shale. *Org. Geochem.* **74**, 143–149.

Xia X. and Gao Y. (2018) Depletion of 13C in residual ethane and propane during thermal decomposition in sedimentary basins. *Org. Geochem.* **125**, 121–128.

Xia X. and Gao Y. (2019) Kinetic clumped isotope fractionation during the thermal generation and hydrogen exchange of methane. *Geochim. Cosmochim. Acta* **248**, 252–273.

Xia X. and Gao Y. (2017) Mechanism of linear covariations between isotopic compositions of natural gaseous hydrocarbons. *Org. Geochem.* **113**, 115–123.

Xie H., Ponton C., Formolo M. J., Lawson M., Ellis G. S., Lewan M. D., Ferreira A. A., Morais E. T., Spigolon A. L. D., Sessions A. L. and Eiler J. M. (2020) Position-specific distribution of hydrogen isotopes in natural propane: effects of thermal cracking, equilibration and biodegradation. *Geochim. Cosmochim. Acta* **290**, 235–256.

Yeung L. Y. (2016) Combinatorial effects on clumped isotopes and their significance in biogeochemistry. *Geochim. Cosmochim. Acta* **172**, 22–38.

Young E. D. (2019) *A Two-Dimensional Perspective on CH4 Isotope Clumping: Distinguishing Process from Source.*,

Young E. D., Kohl I. E., Lollar B. S., Etiope G., Rumble D., Li (李姝宁) S., Haghnegahdar M. A., Schauble E. A., McCain K. A., Foustoukos D. I., Sutclife C., Warr O., Ballentine C. J., Onstott T. C., Hosgormez H., Neubeck A., Marques J. M., Pérez-Rodríguez I., Rowe A. R., LaRowe D. E., Magnabosco C., Yeung L. Y., Ash J. L. and Bryndzia L. T. (2017) The relative abundances of resolved l2CH2D2 and 13CH3D and

mechanisms controlling isotopic bond ordering in abiotic and biotic methane gases. *Geochim. Cosmochim. Acta* **203**, 235–264.

Zhao H., Liu C., Larson T. E., Mcgovern G. P. and Horita J. (2020) Bulk and position-specific isotope geochemistry of natural gases from the Late Cretaceous Eagle Ford Shale, south Texas. *Mar. Pet. Geol.*

Appendix 5

Appendix Figures

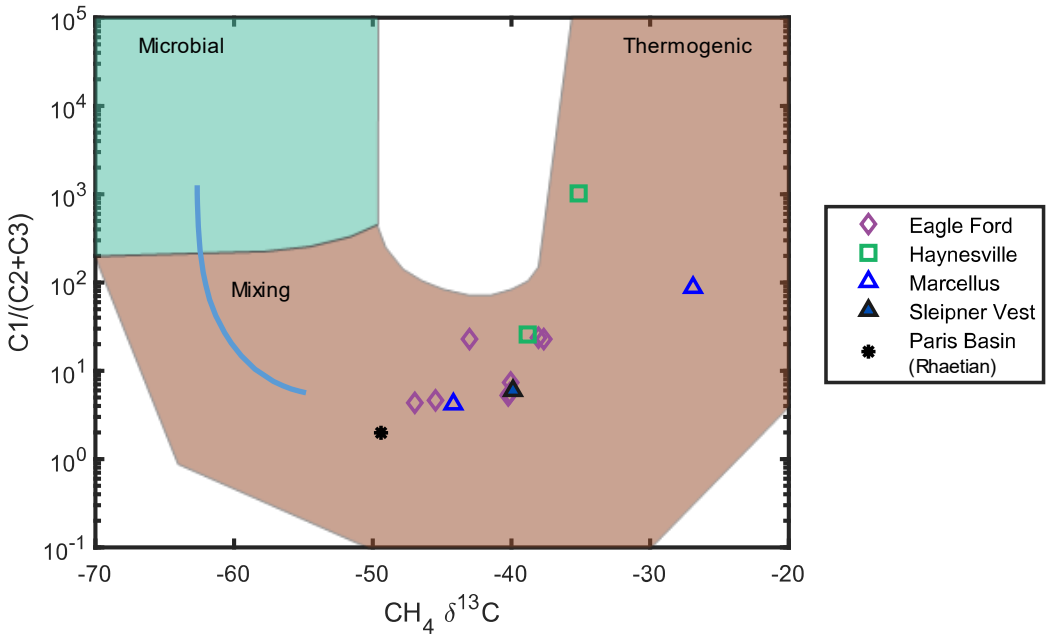

Figure 5-A.1: ‘Bernard diagram’ (Bernard et al., 1978) for natural gas samples of which methane are analyzed for clumped isotopes in this study. Due to limited availability of compositional measurements, some of the samples cannot be presented here. Genetic fields and trends are mapped according to the suggestions of (Milkov and Etiope, 2018).

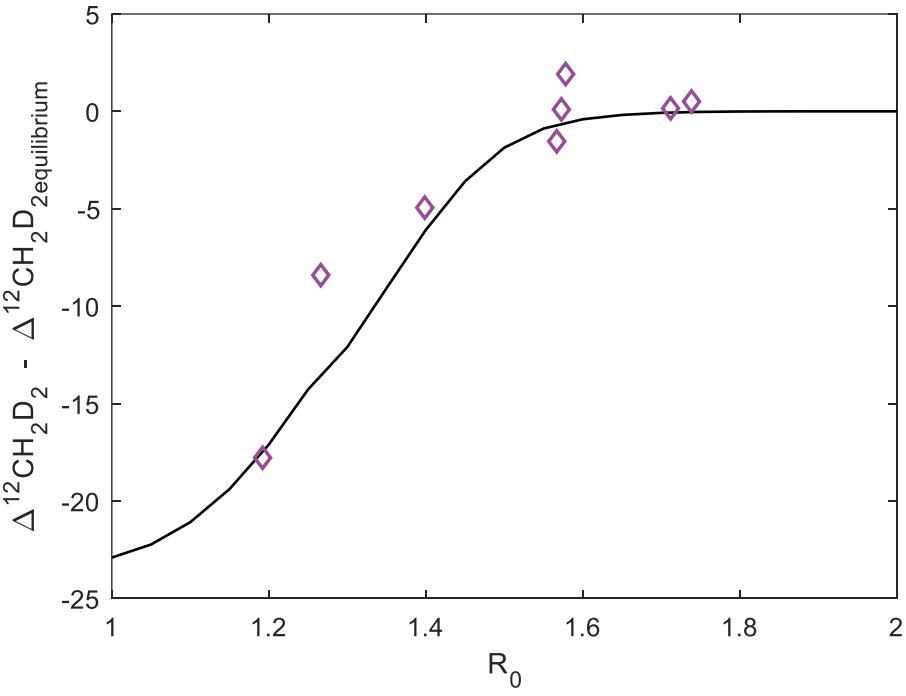

Figure 5-A.2: Modeling the trend of clumped isotope equilibration in Eagle Ford Shale samples. Here the R_o is equivalent R_o calculated with method (3) under the list of methods in Method and Materials section.

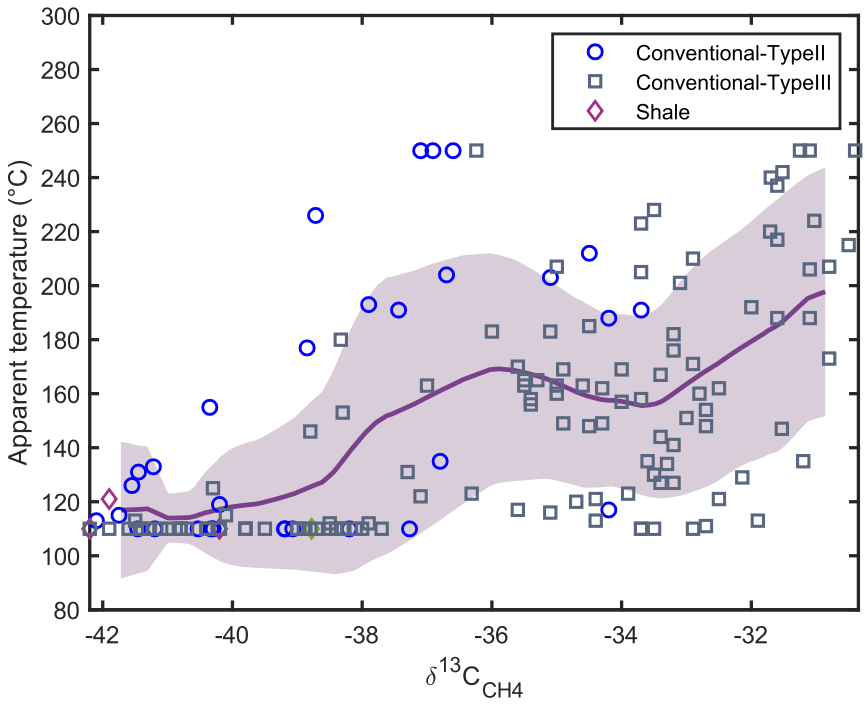

Figure 5-A.3: Apparent temperature derived from the C1-C2-C3 hydrogen isotope equilibrium proxy plotted vs. $\delta^{13}C$ of methane. The apparent temperature here is defined by the corresponding temperature of the nearest point from equilibrium plane to sample, in a δD_{C1} vs. δD_{C2} vs. δD_{C3} cartesian space. Only samples at equilibrium (within error) are used

in this analysis. The line and envelope area show a 3‰ moving average of apparent temperature and its standard deviation, respectively.

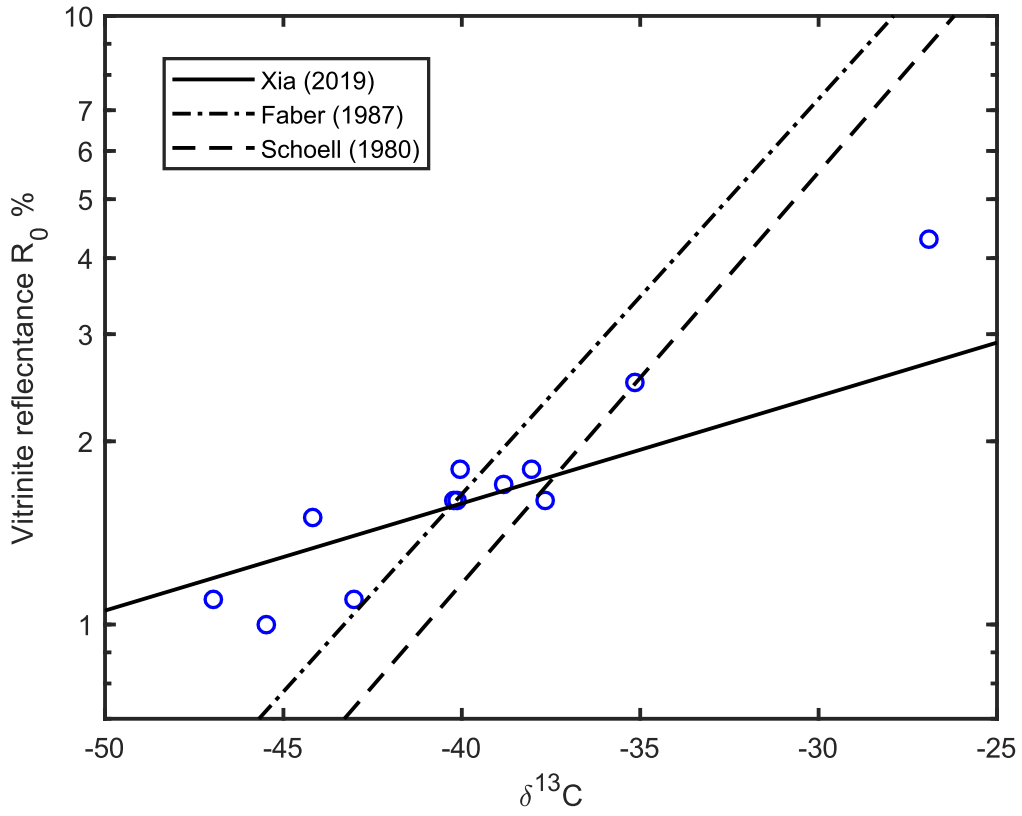

Figure 5-A.4: Mapped Vitrinite reflectance vs. $\delta^{13}C$ of methane for shale gas samples analyzed in this study, compared with several empirical relationships. Vertical axis is plotted on logarithmic scale. Note that these relationships are fitted for gas sourced from type I/II kerogen, from which all of our shale gas samples come as well.

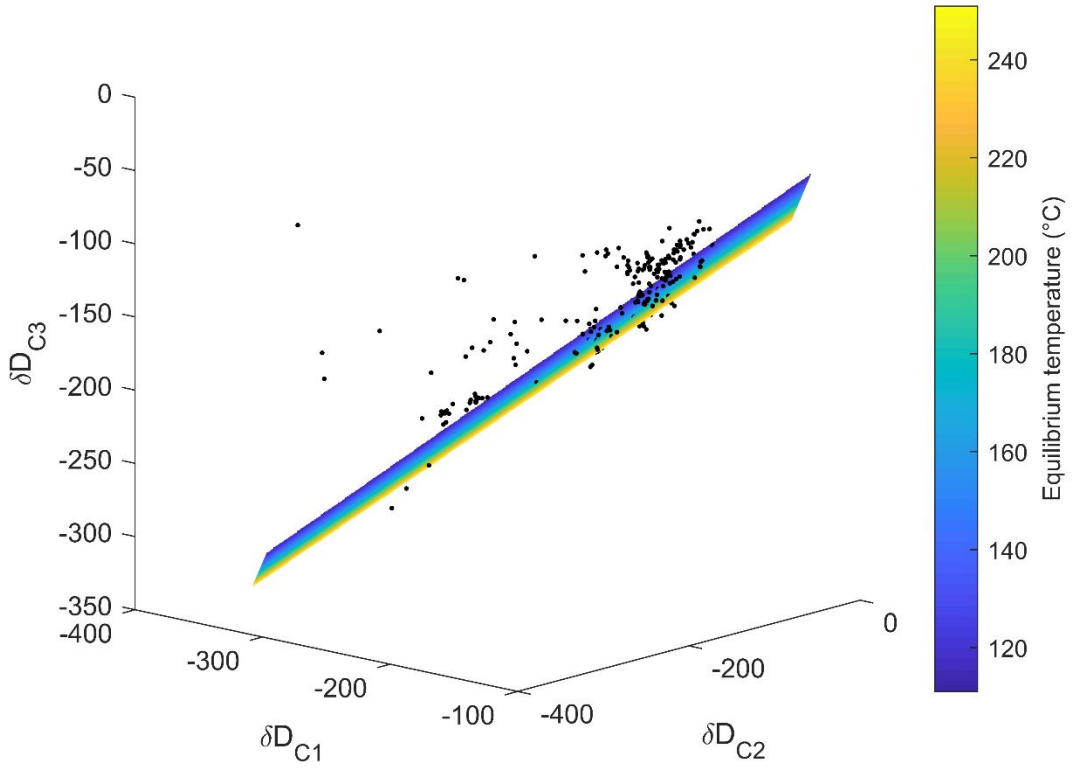

Figure 5-A.5: Compiled C1–C2–C3 hydrogen isotope data of thermogenic natural gases. This figure visualizes our definition of distance from equilibrium for the C1–C2–C3 hydrogen isotope system.

Kinetic parameters and kinetic isotope effects (KIE) used in methane generation-exchange modeling

Type	Parameter	Value	Source
KIE	$\alpha^{13}CH_3$	0.978	Tang et al. (2000)
	$\alpha^{12}CH_2D$	0.7	Ni et al. (2011)
	$\alpha^{13}CH_2D$	$0.999\alpha^{13}CH_3\,\alpha^{12}CH_2D$	Assumption
	$\alpha^{12}CHD_2$	$0.995(\alpha^{12}CH_2D)^2$	Assumption
	α_{cap}	0.33	Extrapolation to (Wang et al., 2009)
Precursor composition	$\delta^{13}C^{pre}$	-27‰	Eldrett et al. (2014)
	δD^{pre}	-100‰	Assumption
	$\Delta^{13}CH_2D^{pre}$	2‰	Assumption
	$\Delta^{12}CHD_2{}^{pre}$	6‰	Assumption
	$\delta D^{pre\text{-}cap}$	-100‰	Assumption
Exchange kinetics	A	$2.45\times10^{10}\ s^{-1}$	Experimental results from Sessions et al. (2004)
	Ea	200 kJ/mol	Experimental results from Sessions et al. (2004); Adjusted for catalysis

Basin modeling of selective wells in the Eagle Ford Shale

Virginia Fee 3H

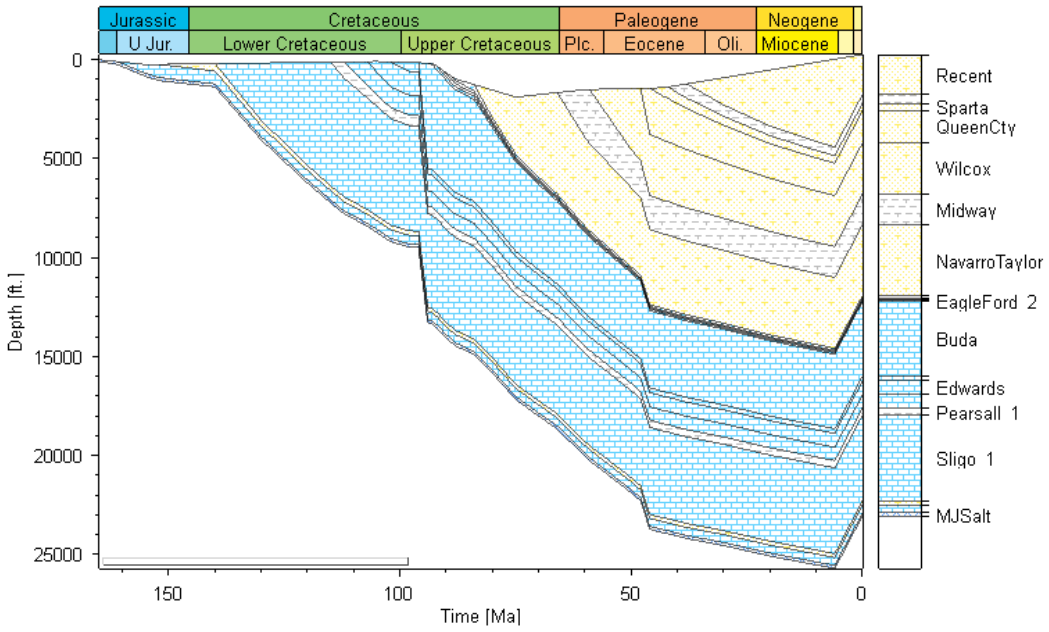

Irvin Minerals 1S

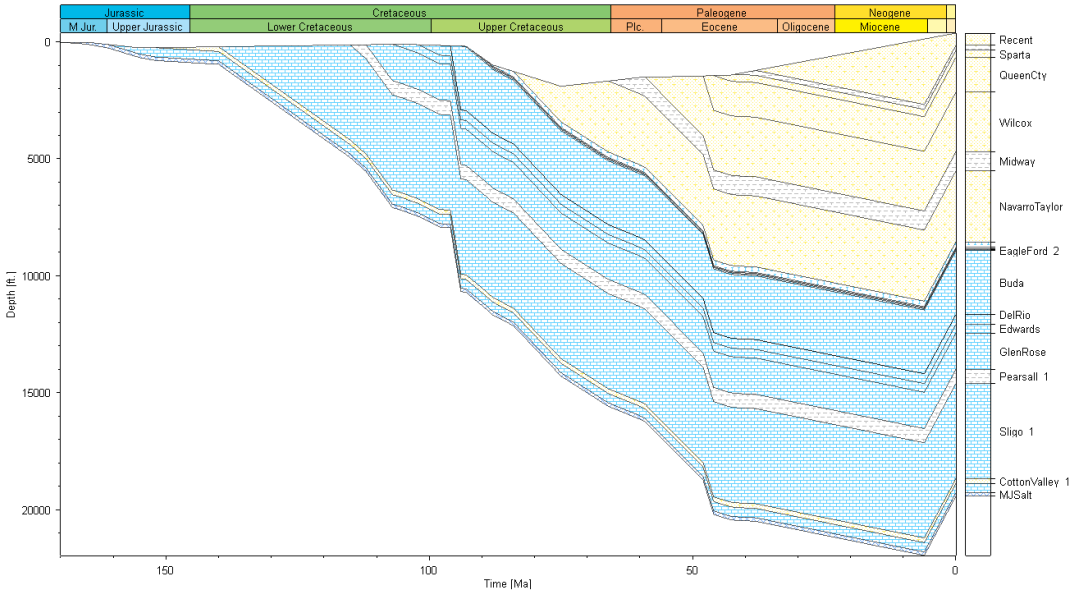

List of publications and reports with compound-specific hydrogen isotope data of C1, C2 and C3

Reference	Note
Krouse (1983)	Partially excluded – data with well depth shallower than 1700m are excluded due to microbial activity
Prinzhofer and Huc (1995)	Included
Rich et al. (1995)	Excluded due to biogenic methane

Hulston et al. (2001)	Included
Strapoć et al. (2007)	Excluded due to biogenic methane
Boreham and Edwards (2008)	Excluded due to biodegradation
Liu et al. (2008)	Excluded due to thermochemical sulfate reduction (TSR)
Jin et al. (2009)	Excluded due to the possibility of abiotic origin
Burruss and Laughrey (2010)	Included
Rodriguez and Paul Philp, (2010)	Included
Dai et al. (2012)	Included
Dai et al. (2014)	Partially excluded – some samples from the Sichuan Basin have the sample ID as Dai et al., (2012) yet hydrogen isotope data are different
Ni et al. (2015)	Included
Wang et al. (2015)	Partially excluded to avoid over-representation of the Sichuan Basin, Ordos Basin and Turpan-Hami Basin (as they have been presented in earlier studies)
Meng et al. (2017)	Excluded due to biodegradation
Thiagarajan et al., (2020)	Partially excluded; samples from Jen-Olla and Genesis are biogenic.
Geoscience Australia, 'ORGCHEM' database	Samples from the Browse Basin and Otway Basin.

References in the Appendix

Boreham C. J. and Edwards D. S. (2008) Abundance and carbon isotopic composition of neo-pentane in Australian natural gases. *Org. Geochem.* **39**, 550–566.

Burruss R. C. and Laughrey C. D. (2010) Carbon and hydrogen isotopic reversals in deep basin gas: Evidence for limits to the stability of hydrocarbons. *Org. Geochem.* **41**, 1285–1296.

Dai J., Ni Y. and Zou C. (2012) Stable carbon and hydrogen isotopes of natural gases sourced from the Xujiahe Formation in the Sichuan Basin, China. *Org. Geochem.* **43**, 103–111.

Dai J. X., Ni Y. Y., Hu G. Y., Huang S. P., Liao F. R., Yu C., Gong D. Y. and Wu W. (2014) Stable carbon and hydrogen isotopes of gases from the large tight gas fields in China. *Sci. China Earth Sci.* **57**, 88–103.

Eldrett J. S., Minisini D. and Bergman S. C. (2014) Decoupling of the carbon cycle during ocean anoxic event 2. *Geology* **42**, 567–570.

Hulston J. R., Hilton D. R. and Kaplan I. R. (2001) Helium and carbon isotope systematics of natural gases from Taranaki Basin, New Zealand. *Appl. Geochemistry* **16**, 419–436.

Jin Z., Zhang L., Wang Y., Cui Y. and Milla K. (2009) Using carbon, hydrogen and helium isotopes to unravel the origin of hydrocarbons in the wujiaweizi area of the Songliao Basin, China. *Episodes* **32**, 167–176.

Krouse H. R. (1983) *Stable isotope research in support of more effective utilization of gas fields in Alberta: Final report to the Alberta-Canada Energy Resource Research Fund.*,

Liu Q. Y., Dai J. X., Li J. and Zhou Q. H. (2008) Hydrogen isotope composition of natural gases from the Tarim Basin and its indication of depositional environments of the source rocks. *Sci. China, Ser. D Earth Sci.* **51**, 300–311.

Meng Q., Wang Xiaofeng, Wang Xiangzeng, Shi B., Luo X., Zhang L., Lei Y., Jiang C. and Liu P. (2017) Gas geochemical evidences for biodegradation of shale gases in the Upper Triassic Yanchang Formation, Ordos Basin, China. *Int. J. Coal Geol.* **179**, 139–152.

Ni Y., Zhang D., Liao F., Gong D., Xue P., Yu F., Yu J., Chen J., Zhao C., Hu J. and Jin Y. (2015) Stable hydrogen and carbon isotopic ratios of coal-derived gases from the Turpan-Hami Basin, NW China. *Int. J. Coal Geol.* **152**, 144–155.

Prinzhofer A. A. and Huc A. Y. (1995) Genetic and post-genetic molecular and isotopic fractionations in natural gases. *Chem. Geol.* **126**, 281–290.

Rich K., Muehlenbachs K., Uhrich K. and Greenwood G. (1995) Carbon isotope characterization of migrating gas in the heavy oil fields of Alberta, Canada. In *Proceedings - SPE International Heavy Oil Symposium* Society of Petroleum Engineers. pp. 215–224.

Rodriguez N. D. and Paul Philp R. (2010) Geochemical characterization of gases from the Mississippian Barnett Shale, Fort Worth Basin, Texas. *Am. Assoc. Pet. Geol. Bull.* **94**, 1641–1656.

Strapoć D., Mastalerz M., Eble C. and Schimmelmann A. (2007) Characterization of the origin of coalbed gases in southeastern Illinois Basin by compound-specific carbon and hydrogen stable isotope ratios. *Org. Geochem.* **38**, 267–287.

Thiagarajan N., Xie H., Ponton C., Kitchen N., Peterson B., Lawson M., Formolo M., Xiao Y. and Eiler J. (2020) Isotopic evidence for quasi-equilibrium chemistry in thermally mature natural gases. *Proc. Natl. Acad. Sci.*, 201906507.

Wang X., Liu W., Shi B., Zhang Z., Xu Y. and Zheng J. (2015) Hydrogen isotope characteristics of thermogenic methane in Chinese sedimentary basins. *Org. Geochem.* **83**–**84**, 178–189.

Wang Y., Sessions A. L., Nielsen R. J. and Goddard W. A. (2009) Equilibrium $^{2}H/^{1}H$ fractionations in organic molecules: II. Linear alkanes, alkenes, ketones, carboxylic acids, esters, alcohols and ethers. *Geochim. Cosmochim. Acta* **73**, 7076–7086.

Chapter 6

Predicting Isotopologue Abundances of The Products of Organic Catagenesis With a Kinetic Monte Carlo Model

Abstract

Recently developed analytical methods enable analysis of intramolecular stable isotope distributions of organic compounds in oil and gas, which can serve as signatures of the conditions and mechanisms of their formation and destruction. Previously published models of thermal cracking are incapable of predicting the wide range of intramolecular isotope patterns of products because they haven't integrated realistic precursors, elementary reactions, and patterns of inheritance. These deficits stem from the complexities of relevant reaction pathways and obscurity of kerogen/bitumen structures. In this study, we develop a kinetic Monte-Carlo model (kMC) to address this problem. We simulate thermal breakdown of different types of organic matter, including several molecular models of kerogens, representative oil compounds and oil mixtures. At the onset of each simulation, we initialize the model parent organic molecules with isotopic substitutions, and then subject them to 'cracking' reactions (catagenetic thermal decomposition) in a many-step process. For each time step of the model, we determine the rate constants of included reactions for all non-isotope-subsitituted atomic sites in the parent molecules using an external kinetic database (reaction mechanism generator), and then compute the rates of

those reactions for isotope-substituted sites using kinetic isotope effects (KIE) retrieved from either existing first-principle calculations or empirical models calibrated to those calculations. Every simulation captures a possible route of thermal degradation and tallies the numbers of each unique isotopomer of all product molecules at the end. We reach statistically meaningful results of isotopomer ratios by repeating a sufficient number of such simulations. Although this model produces data that contains information of all molecules and isotopic forms, we focus on the proportions of many of the isotopologues of every C1-C7 n-alkanes, in this study. We use two chemistry schemes that differ in complexity. The basic scheme (scheme A) includes only homolytic cleavage and capping of metastable radicals by hydrogen atoms. The more sophisticated model variant (scheme B) includes all reactions of importance in radical chain mechanism of thermal cracking. We examine the robustness of our model in an analytically-solvable system of reactions that describe thermal cracking of butane under scheme A — a scenario where all elementary model steps can be listed. Our model results generally resemble patterns of compound-specific and position-specific isotope measurements of C1-C5 alkanes in natural gases. We find that results from scheme B are more consistent with natural data than scheme A, suggesting that thermal cracking in natural hydrocarbon formation is mediated by not only homolytic cleavage, but also free radical chain mechanisms. Using our model, we provide mechanistic explanations for some of the existing observations, such as trend of intramolecular carbon isotope fractionation of propane with thermal maturity. Our study

also makes predictions on intramolecular isotope compositions of higher order alkanes (C4+) that could be further tested.

1. Introduction

Thermal cracking, the break down of organic compounds at elevated temperature, is thought to be responsible for forming most subsurface hydrocarbons, and is an essential part of the chemistry of the industrial refinement of heavy oil. Detailed description and computational simulation of thermal cracking is of great importance to understanding the origins and distributions of geological hydrocarbons, and is valuable to both the upstream exploration and downstream refinement sectors of petroleum industry. In petroleum exploration, predictive modeling of thermal cracking can yield the quantity and quality properties of oil and gas. It also allows people to relate hydrocarbon resources to their sources (kerogen or bitumen) and formation environment (burial history, fluid evolution). In this study, we present a new numeric model of thermal cracking that furthers our capabilities to make predictions of measurable geochemical signatures and enhance our understanding of the petroleum-forming chemistry.

2. Background

Stable isotope ratios of hydrocarbons are controlled by isotope ratios of precursor molecules and the chemical, physical and biological isotope effects associated with formation, transportation and destruction; for these reasons, they record valuable information regarding the origins and fates of these compounds. For several decades, bulk (material-average) and compound-specific (molecule-average) stable isotope compositions have been measured on geological hydrocarbons in efforts to understand their sources, thermal maturities, extent of biodegradation and other issues (Silverman and Epstein, 1958; Galimov, 1975; Schoell, 1980; Chung et al., 1988; Whiticar, 1996; Peters et al., 2004; Boreham et al., 2008; Dai et al., 2012). More recently, advances in several different analytical technologies have enabled study of abundances of individual isotopologues (i.e., compositionally and structurally unique isotopic forms) of hydrocarbon molecules. These measurements are often categorized into two types that measure different distinctive properties of isotopologues: position-specific and multiply-substituted. Such measurements can be approached using several different technologies, including include Nuclear Magnetic Resonance (NMR), High-Resolution Mass Spectrometry (HR–MS; using both sector and Fourier-transform instruments), Infrared (IR) Absorption Spectroscopy, Gas Chromatography – Pyrolysis – Gas Chromatography – Isotope Ratio Mass Spectroscopy (GC-p-GC-irMS) and chemical or biochemical degradation followed by Isotope Ratio Mass Spectrometry (Gilbert et al., 2013; Stolper et al., 2014; Ono et al., 2014; Julien et al., 2016; Gilbert et al., 2016; Young et al., 2016; Piasecki et al., 2016; L. Gao et al., 2016;

Clog et al., 2018; Li et al., 2018; Liu et al., 2018; Cesar et al., 2019; Gonzalez et al., 2019). Interpretation of these new signatures can help better trace the origins and fates of subsurface hydrocarbon.

The existing framework for kinetic modeling of the isotope geochemistry of catagenesis cannot predict abundances of specific isotopologues of hydrocarbons produced from thermal cracking of larger organic precursors. There is a relatively extensive and longstanding body of quantitative models that simulate oil and gas generation from thermal cracking of kerogen (e.g., Sweeney et al., 1987; Burnham and Braun, 1990; Behar et al., 1997; Lorant et al., 1998). These models represent a group of compounds by a general term (e.g., kerogen; oil; condensate; C1–C5 gas; coke). They then condense chemistry to a few 'conversion' reactions of those grouped compounds. Kinetics of these reactions can be parameterized by empirically-fitted distributions of activation energies. These models of reaction kinetics could be combined with quantum chemical calculations of associated isotope effects (Tang et al., 2000; Xiao, 2001; Tang et al., 2005) to model compound-specific isotope ratios of petroleum components. However, significant additional development would be needed to modify or upgrade these models to describe production of specific isotopologues of generated hydrocarbons because this would require explicit descriptions of the rates of elementary reactions for specific molecular and isotopic structures of precursors.

Describing the full reaction paths on the molecular level, where isotopic structure of precursor and product is specified and directly connected to reaction rate, demands an enormous amount of computational memory and processing power, beyond the capabilites of computers and programming during the period when the most well developed models of catagenesis were created (Ungerer, 1990; Behar et al., 1997). But, more recently kinetic modeling of explicit molecules and elementary reactions has been advanced to simulate more and more complicated reaction networks (Savage, 2000; You et al., 2009; Harper et al., 2011; C. W. Gao et al., 2016), especially for the systems of pyrolysis and combustion. These models represent the concentrations of species as variables and formulate relevant chemical reactions as components of ordinary differential equations of these variables. The differential equations are solved numerically (unless the model is simplistic enough) to provide time-evolving concentrations of all considered species. Ideally, we could follow this approach and introduce isotope labels to make these models describe the creation and destruction of specific isotopologues. However, there are two reasons that the methodologies used in these previous models of the kinetics of combustion can't undertake the problem of thermal cracking of macromolecular substrates. First, molecular models of kerogen are much bigger and more complex than the substrates that prior kinetic models typically consider. Second, specification of isotopologues and kinetic isotope effects increases the demand of computational resources dramatically. Concentrations of isotopologues need to be tracked and stored as variables, and the number of these variables

will be too large to be operated by any computer systems. For example, we can estimate the number of isotopologues for a kerogen molecule (typical substrate for catagenesis models) that has 5,000 carbon atoms (Bousige et al., 2016). Even if we only consider versions of this substrate molecule containing 0 to 3 ^{13}C-substitutions (clearly a simplification, given that on average ~50 ^{13}C's will be present in each formula unit), there will be 2E10 symmetrically non-equivalent isotopic forms of that substrate molecule. For reference, simulation of the isotope effects associated with the pyrolysis using propane as substrate (6 carbon-isotope isotopologues in total) takes 44 CPU hours (Goldman et al., 2019). Here we use a different approach of kinetic modeling, a statistical method known as the kinetic Monte Carlo method. The strength of this method is that it circumvents the obstacle of storing and modifying the concentrations and reactions of astronomical numbers of species. Instead, it initializes the system with a relatively large unit of molecular structures composed of atoms (with isotopic information labeled) and bonds that connects atoms. It allows the system to evolve via a stepwise execution of reactions, where a new reaction is stochastically selected from an automatically generated reaction list at each step, based on the permitted chemistry of the system at current state. Consequently, all isotopic forms of substrates and intermediates can be accounted for by randomized events, and we only extract information of interest (molecular and isotopic composition) from the system when the evolution ends. We define our methodology rigorously in the next section.

3. The Kinetic Monte Carlo Model

The kinetic Monte Carlo (kMC) method was developed in the 1960s and 1970s to provide a numerical solution to systems that evolve with time (Voter, 2007). The master equation for the evolving system can be formulated as (Fichthorn et al., 1991; Chatterjee and Vlachos, 2007):

$$\frac{\partial Pr(\sigma,t)}{\partial t} = \sum_{\sigma'} W(\sigma' \to \sigma, t)\, Pr(\sigma', t) - \sum_{\sigma'} W(\sigma \to \sigma', t)\, Pr(\sigma, t), \qquad (1)$$

where $Pr(\sigma, t)$ denotes the probability that the system (or an element of the system) is in state σ at time t, and $W(\sigma \to \sigma', t)$ is the probability per unit time (probability density function) of the system transitioning from σ to σ', and *vice versa*. In this system, both the next state and transition probabilities depend on the previous state. When dealing with a complex system with many interacting mechanisms, equation (1) cannot be solved analytically or by deterministic numerical differential equation methods. The kinetic Monte Carlo method provides a feasible numerical solution to this equation via sampling all possible paths and states stochastically. This method simulates the reactive system with atoms and bonds that are different from the 'concentration' or 'activity' description in deterministic formulations. The kMC method tracks a step by step evolution of the system, where it discretizes time into steps that jump the system from state to state. If the object of study progresses by chemical reactions, a jump is selected amongst all probable chemical reactions at that given time. If all probable reactions could be enumerated, the probability of a certain reaction happening in the next step is (Gillespie, 1976):

$$P(\tau, \mu) = W_\mu * \exp\left(-\sum_\nu W_\nu \tau\right). \quad (2)$$

$P(\tau, \mu)$ indicates the probability density (over time) that the next reaction would happen between times τ and $\tau + d\tau$ and would be reaction μ, where μ is an integer indexing the reaction number. W is the stochastic formulation of reaction rates in deterministic chemical kinetics. Using basic principles of probability, it could also be written as:

$$P(\tau, \mu) = P(\tau) * P(\mu \mid \tau). \quad (3)$$

Here $P(\tau)$ is the probability density that the next reaction would happen between times τ and $\tau + d\tau$ and $P(\mu \mid \tau)$ is the probability of that reaction being reaction μ, given that it is happening between τ and $\tau + d\tau$. Since the probability of more than one reaction happening over the time span of $d\tau$ is $o(d\tau)$, we could use the addition theorem of probabilities to get

$$P(\tau) = \sum_\nu P(\tau, \nu). \quad (4)$$

Combining equation (3) and (4) gives

$$P(\mu \mid \tau) = \frac{P(\tau, \mu)}{\sum_\nu P(\tau, \nu)}. \quad (5)$$

Substituting $P(\tau, \mu)$ and $P(\tau, \nu)$ from equation (2) yields:

$$P(\tau) = W_{tot} * \exp(-W_{tot}\tau) \quad (6)$$

$$P(\mu \mid \tau) = \frac{W_{\mu}}{W_{tot}}, \quad (7)$$

where $W_{tot} = \sum_{\nu} W_{\nu}$. Equation (6) and (7) provides the method for propagating chemical reactions. Equation (6) gives the probability density function of time for the next reaction, which allows a passing time length (time interval between the current reaction and the next reaction) to be generated randomly for a given reaction step. This means that the discretized series of events in the evolution could be projected to the continuous time vector.

Equation (7) indicates that the probability of a reaction to be selected is proportional to its rate (stoichiometric rate with unit of time^{-1}).

Peterson et al. (2018) firstly applied the kMC method to isotope fractionation in thermal cracking, where they studied carbon isotope fractionation of cracking n-C18 alkane (octadecane). In their model, the chemistry scheme is simplified to C-C bond cleavages only. Here we extend this concept to explore isotope effects involving multiple elements in thermal cracking of different substrates and with multiple reaction types. Specifically, we advance the notion of a kMC model catagenesis in four ways: Firstly, we consider a variety

of molecular models, including structural models of kerogens of different types and oil compounds as substrates. Secondly, we used reaction schemes that are more complete and realistic than homolytic cleavage of C–C bonds alone. Thirdly, we implemented accurate kinetic parameters, including rate constants of elementary reactions and kinetic isotope effects (KIE), derived from existing *ab initio* and empirical calculations. Finally, our model considers both ^{13}C and D substitution and provides abundances of site-specific and multiply-substituted isotopologues for C1-C7 product molecules. Note that Xie et al. (2020) presents a preliminary and simplified version of this model to calculate position-specific hydrogen isotope ratios of propane produced by catagenesis of kerogen and oil compounds. In the next few subsections, we detail the organization of our kMC model, which is also presented in Figure 6-1.

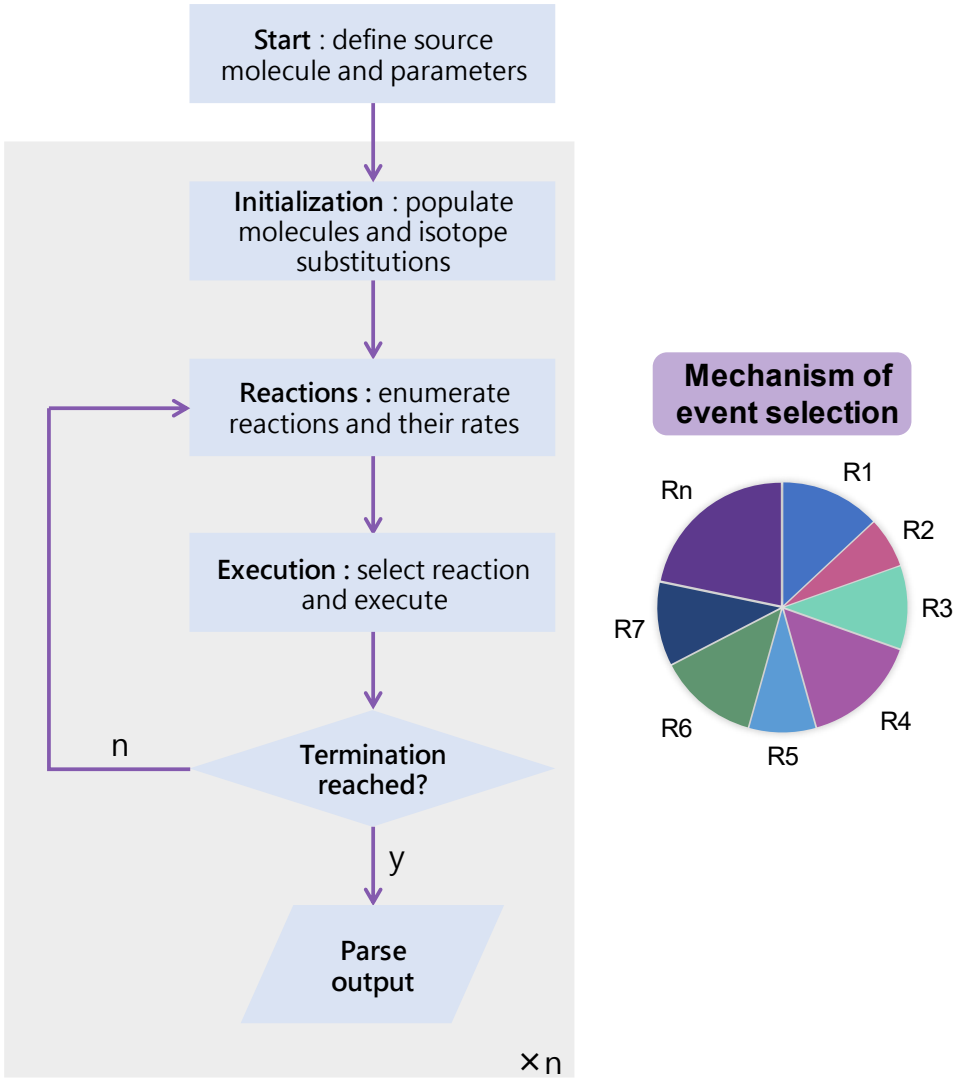

Figure 6-1: A flow-chart of the kMC model. R1, R2, R3… Rn on the wheel represent possible reactions in a time step.

3.1. Initialization

Structural modeling of kerogen and coal has a long history, as the earliest study to hypothesize representative molecular structure of coal is in the 1940s and of kerogen is in the 1960s (Vandenbroucke and Largeau, 2007). However, these works rely on very limited information provided by bulk organic matter analysis and pyrolysis and oxidative degradation experiments. The emergence and improvement of analytical techniques (e.g., infrared spectroscopy, nuclear magnetic resonance, X-ray) advanced chemical characterization of kerogen by providing richer information on bonding environments and moieties. Over this same period, advances in computational chemistry have enabled calculation of mechanical and thermodynamic properties of very large molecular models (Ungerer et al., 2015). Combination of various analytical observations and bottom-up molecular simulations result in more realistic molecular models. In this study, we use molecular models of kerogen and coal published in recent years (Bousige et al., 2016; Zhang et al., 2017). These model molecules have 5,000–15,000 carbon atoms.

In addition to these model kerogens and coals, we also created a model of mixed alkanes to mimic the saturated-hydrocarbon fraction of crude oil. The molecular model of saturated oil contains C10–C30 n-alkanes and pristane and phytane. Further details regarding the composition of this model can be found in the code and data availability section.

The kerogen molecular models from Bousige et al. (2016) contain free C1-C7 alkanes. We remove these preexisting C1–C7 alkanes prior to modeling of catagenetic reactions, because they might survive reactions and become tallied in the end to contaminate our results. We typically combine(repeat) many units of the molecular model in each system such that it contains around 10^5 to 10^7 carbon atoms. ^{13}C and D substitutions are populated randomly across the structure. In doing so, we assume that the isotopes in the precursor are distributed homogeneously. This might not be a realistic assumption, as we know that some biomolecule precursors of kerogen have heterogeneous stable isotope distributions (Abelson and Hoering, 1961; Monson and Hayes, 1980; Hayes, 2001). However, we are not aware of any measurements of natural materials, models or experiments that attempt to associate stable isotope compositions with structural moieties in kerogen molecules, so it is not possible to devise a credible mapping of the intramolecular isotope compositions of kerogens without some substantial body of new work. It is also possible that some of the heterogeneity in isotopic compositions of biomolecules does not lead to systematic site-specific isotopic variations in kerogens and oil compounds simply because the latter statistically average across many precursors sampled through many intermediate reactions; for example, the previous model of Xie et al. (2020), shows that differences in $\delta^{13}C$ between odd and even carbon sites in n-C17 alkane precursors has relatively little impact on position-specific isotope values of propane formed by thermal cracking (Xie et al., 2020). Yet we acknowledge that this problem is understudied and encourage future

research to provide better constraints on internal isotope distribution of kerogeneous organic matter.

3.2. Chemistry schemes

Despite the overwhelming complexity of the chemistry of catagenesis, it is possible to reduce it into schemes consisting of a limited number of elementary reaction types that act on one of the many structurally unique sites in the precursors. The most common description of the thermal cracking processes in the field of stable isotope petroleum geochemistry assumes that homolytic cleavage of single bonds dominates the formation of low molecular weight alkanes (Chung et al., 1988; Tang et al., 2000; Galimov, 2006). Considering only homolytic cleavage is parsimonious, yet it has been applied widely to explain molecular and isotopic compositions of natural gases (e.g., Waples and Tornheim, 1978; Tang et al., 2000). More sophisticated analysis of cracking chemistry identifies several types of reactions to be important: (1) homolytic cleavage, (2) β-scission, (3) H-abstraction, (4) radical recombination, and (5) radical isomerization (Ranzi et al., 1995; Xiao, 2001; Yuan et al., 2011). In this study, we explore thermal cracking modeling with two chemistry schemes: In scheme A, molecules break down via homolytic cleavage exclusively, and all radicals are immediately capped with H after cleavage events. In scheme B, we attempt to depict free radical chemistry more fully by implementing several

of the most important reaction types. Figures 2 and 3 and the following paragraphs detail these two schemes:

Scheme A

Under scheme A, each reaction 'event' is a single bond dissociation (homolytic cleavage). All single bonds between non hydrogen atoms are considered, including those with non-carbon atoms. Each bond dissociation event generates two radicals that are subsequently capped with a H atom.

Scheme B

We devise a free radical reaction network in scheme B, which includes six reaction types that can be broadly categorized into initiation, propagation and termination reactions.

Initiation: homolytic cleavage

Propagation: β-scission, radical isomerization, H-abstraction

Termination: radical recombination, capping.

Examples of theses reaction classes are shown in Figure 6-2. Reactions of homolytic cleavage are treated in the same way as scheme A, except that product radicals are not quenched immediately by hydrogen capping; instead, radicals produced by hemolytic

cleavage are retained in the model and subject to reactions in the next model time step. β-scission is the radical decomposition reaction where a second nearest (‘β’) ‘C—C’ single bond away from the radical position dissociates, and the nearest ‘C—C’ single bond becomes a double bond (e.g., 1-butyl→ethylene+ethyl). Radical isomerization reactions are intra-molecular hydrogen migration reactions. A H atom on an aliphatic chain containing an initial radical carbon site migrates to cap that initial radical, forming a new radical carbon site where that hydrogen came from (e.g., 1-octyl→5-octyl). Capping is a reaction that combines an external H atom with an existing radical (e.g., 1-octyl+H→octane). H abstraction reaction is a radical abstracting a H from another position on the substrate, forming a new radical carbon site where that hydrogen came from (e.g., 1-ethyl+octane→ ethane+2-octyl). Radical recombination is the combination reaction between two radicals (e.g., ethyl+ethyl→butane).

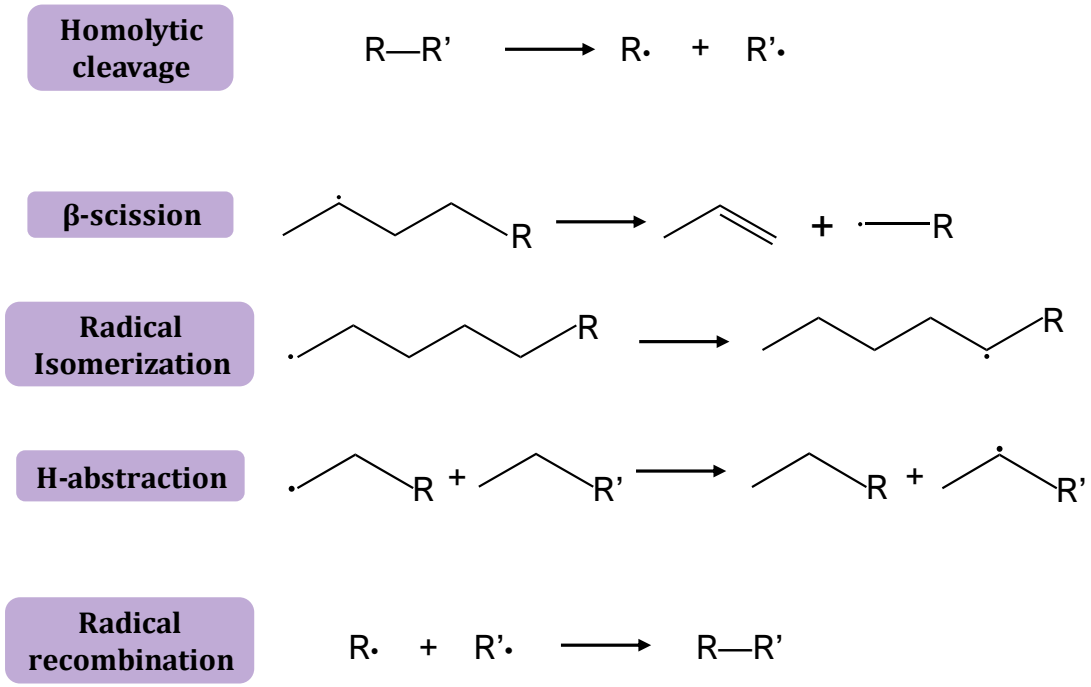

Figure 6-2: Illustration of reaction types included in our models.

The reaction networks of schemes A and B are displayed in Figure 6-3.

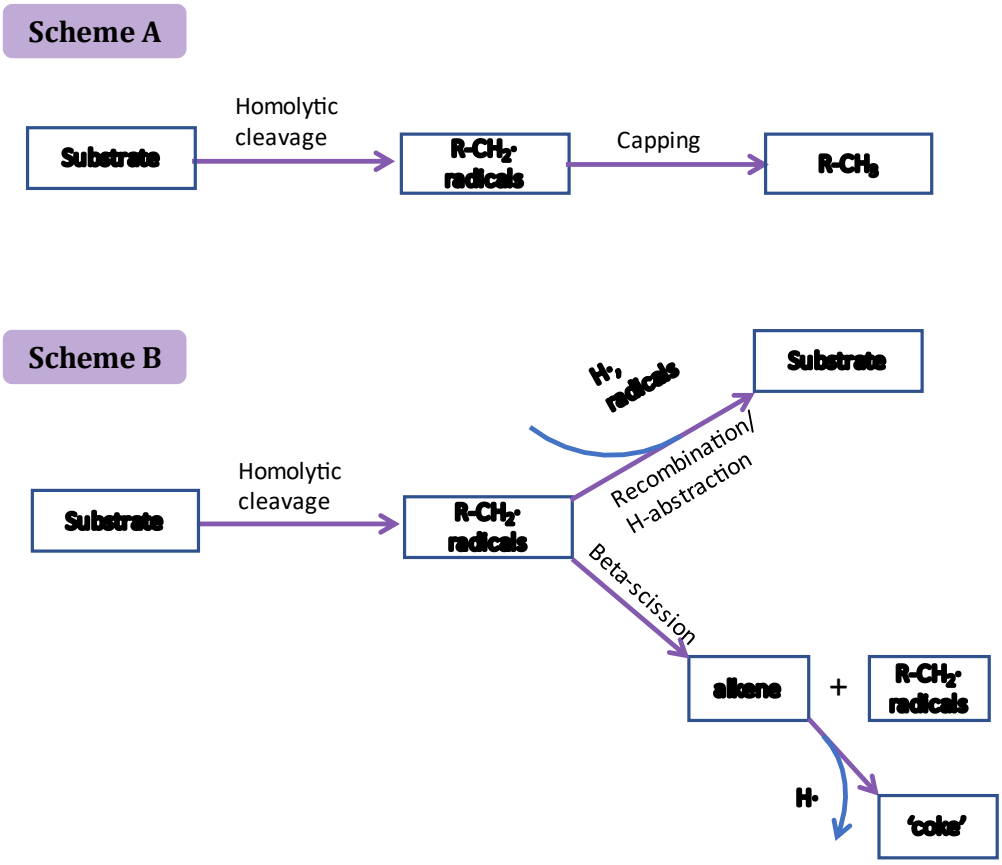

Figure 6-3: Chemical paradigm of scheme A and scheme B.

3.3. Iteration

Once the model system is initialized by defining the chemical and isotopic structure of its initial substrates, we then allow the system to evolve through chemical reactions that are

described in a series of distinct time steps. Every iteration step executes a single selected elementary reaction, or 'event', chosen randomly from the list of all possible elementary reactions determined by the system state at that time. The probability of an event being chosen for a given time step is equal to the reaction rate coefficients (in unit of time^{-1}) for that event divided by summation of all rate constants for all possible events, determined by the system state at that time. Rate coefficients of listed reactions are estimated with a modified Arrhenius form: $k = A\left(\frac{T}{T_0}\right)^n e^{-\frac{E_a}{RT}}$, where A is pre-exponential factor, T_0 is reference temperature and E_a is activation energy. Reactions in the event list are assigned with parameters retrieved from an embedded mini library, which is organized by reaction types (homolytic cleavage, β-scission, etc.) and reaction attributes (atoms, degree of atoms, etc.). The program processes the reaction information to classify it and acquire its designated parameters from the library. The mini kinetic library is established by obtaining parameters for different reaction types from the Reaction Mechanic Generator database, under RMG-Py rate rules (C. W. Gao et al., 2016). We detail our treatment for each reaction type in the next paragraph.

For kinetic treatment of homolytic cleavage, we divide all reactions to five categories: 'C(aliphatic) —C(aliphatic)', 'C(aliphatic) —C(aromatic)', 'C—O', 'C—N', 'C—S' and others (single bonds between two non-carbon atoms). 'C—H' bond is not considered here because its rate coefficient is around 5 orders of magnitude slower than 'C—C' bonds (at

180°C). We group all dissociation reactions of single bonds between two non-carbon atoms into the 'other' category because these reactions do not affect the model's generation of hydrocarbons directly. For β-scission, we apply a universal set of parameters for all reactions because studies have shown that kinetics of β-scission reactions do not vary very much for different radicals. Rate coefficients of β-scission reactions occurring on different chain lengths and carbon center degrees (1°, 2°, 3°) do not differ by more than an order of magnitude at relevant temperature (120—50°C) (Xiao, 2001; Ratkiewicz and Truong, 2012). This universal parameter is selected from scission of 1-octyl radical. For kinetic treatment of radical isomerization (H-migration), we assign parameters to reactions based on its migration distance. We allow migration from the radical position (1) to the 4,5 or 6 positions (number indexed by adjacency to the radical position), because the migration of other distances are at least 3 orders of magnitude slower (Ratkiewicz et al., 2010; Sirjean et al., 2012; Ratkiewicz, 2013). The library data contain sets kinetic parameters specific to migrations to the 4,5 and 6 positions. The reaction types illustrated so far are all unimolecular reactions, which have rate coefficients expressed in s^{-1}. H–abstraction, capping and radical recombination are bimolecular reactions that have rate coefficients in concentration^{-1}·s^{-1} (e.g., molecules·cm^3 • s^{-1}). We unify the rate expressions by multiplying the bimolecular rate coefficients with concentration of one of the reactants, which we specify here for each specific reaction types. In H-abstraction reactions, we start by assigning its elementary rate coefficient based on the degree of carbon at the radical

position (0°, 1°, 2°, 3°), and then multiply the rate coefficient with the concentration of aliphatic structures in the study. We retrieved kinetic parameters for typical radicals (0°, 1°, 2°, 3°) abstracting hydrogen from octane, so the concentration of aliphatic structure is normalized to equivalent octane concentration (converted by mol carbon). The position of the abstracted hydrogen is randomly selected from all possible positions across the system. We do not confine the geometrical locations of this abstracted hydrogen, because we do not keep track of the physical coordinates of atoms. However, we do not allow hydrogen on the carbon atom bonded to the radical position either, as these reactions are kinetically unfavorable. In capping reactions (only under scheme B because capping under scheme A is assumed to be instantaneous), concentration of the capping hydrogen radical (H·) is treated implicitly—we do not specify the origin of these H radicals, albeit we assume that they derive from water or other non-sapropelic hydrogen. Instead, we approximate that capping reaction for a radical has the same rate coefficient as the H-abstraction reaction. This approximation is based on low-temperature hydrous pyrolysis experiments (Wei et al., 2019), which found that around 10 – 14% of methane H derives from water at 140 and 200°C. I.e., same amount of hydrogen will be derived from water when we approximate that capping reactions are as common for a radical as H-abstraction reactions.

Homolytic cleavage, β-scission and radical isomerization are the unimolecular reactions in our model. We note that rate coefficients of these nominally unimolecular reactions can be pressure dependent. This stems from the requirement of an inert third body to collide with

the excited reactant and remove excess energy (e.g., Baulch et al., 2005). Multiple theoretical methods are available for estimating pressure-dependence on rate-coefficients (Allen et al., 2012), but we use the high-pressure limit kinetic data from RMG database because of the catagenetic environment of our application. We note that, there is a significant gap between typical conditions of oil and gas generation (120-250 °C and 1000-3000 bar) and what the RMG database is commonly intended for, which is industrial pyrolysis and combustion (500–2100°C and 0.01–50 bar). Albeit we import high pressure limit parameters from the database, there still might be non-trivial error of extrapolation of temperature and pressure. The full parameters used in this study is presented in the code and data availability section.

Following assignment of rate coefficients, reactions affected by isotope substitution on the substrate are modified with kinetic isotope effects (KIE). In this study, we concentrate our focus on ^{13}C and D(^{2}H) substitutions. For homolytic cleavage, we calculate KIE with the Arrhenius formula of $KIE = \frac{A^*}{A} * e^{-\frac{\Delta E_a}{RT}}$, where A^*/A and ΔE_a are the pre-exponential factor ratio and activation energy difference between substituted and unsubstituted reactions. We obtained sets of these parameters from previous density functional theory (DFT) calculations (Tang et al., 2000 and Tang et al., 2005 for carbon isotopes; Ni et al., 2011 for hydrogen isotopes). These preceding studies provided KIE parameters for a number of different reactions, showing that they are mainly influenced by three properties: 1) distance to substitution (primary, secondary and tertiary KIE) 2) bond types (‘C(aliphatic) —

C(aliphatic)', 'C(aliphatic) —C(aromatic)', 'C—O', 'C—N' and 'C—S') and 3) degree of carbon at the substituted position (0°, 1°, 2°, 3°). Each KIE calculation is examined for these properties in order to determine its KIE parameters. We neglect tertiary or higher order ^{13}C KIE and quaternary or higher order D KIE, because those are very small. I.e., if there is a ^{13}C or D substitution two bonds away from the dissociated bond, its KIE is neglected. If a homolytic cleavage reaction is influenced by multiple isotope substitutions, we multiply individual KIE from each substitution. For β-scission, we apply a similar approach to modify the rates if there is isotope substitution on the dissociated β bond at the atom that is further away from the radical site (hereinafter called 'the 3rd position'). Note that we neglect KIE on the closer atom of the dissociated β bond because that atom will be in a double bond, which will not be tallied at the end of the model (Scheme B does not allow pathways for unsaturated bonds to become saturated). We use Xiao (2001)'s quantum chemical estimates of carbon KIE's on the 3rd position for β-scission. Xiao (2001) does not report KIE for scission reactions other than on straight alkyl chains, so we use a universal set of carbon KIE parameter for all β-scission reactions. We are not aware of any literature data documenting hydrogen KIE's for β-scission reactions, so we approximate them using kinetic parameters from homolytic cleavage. In practice, we calculate D KIE with the homolytic cleavage parameters and apply it to the β-scission reaction if there is a D on the 3rd position. For the group of H-transfer reactions, including radical isomerization reactions, H-abstraction reactions, and capping reactions, we neglect carbon KIE and use a

primary hydrogen kinetic isotope effect on the transferred H atom. This primary KIE is estimated with higher limit of vibrational isotope effects, which is abstracting a free H· atom from its precursor. Under this scenario, the KIE equals to equilibrium isotope effect between an H· atom and the precursor hydrogen, which has been reported in previous studies (Wang et al., 2009). For radical isomerization and H-abstraction reactions, precursor of the H atom is assumed to be methylene groups (—CH_2—). For capping reactions, precursor of the H atom is assumed to be water. No KIE is implemented for radical recombination, as it does not have an energy barrier.

3.4. Model output

When step number reaches the target number chosen in the initialization of program, iteration is terminated and the system is parsed to tally the final product molecular constituents and their isotopologues. Note that we do not analyze or store information of molecules and isotopologues during the iteration steps. An example of a count of product molecules and isotopologues from the computed cracking of aliphatic oil is given in Table 6-1. The relative abundances of isotopologues of each compound are then converted into position-specific isotope ratios, clumped isotope values and compound-specific isotope ratios. For example, the position-specific isotope ratio for the m position is calculated with $R_m = \sigma_m C_m / \sigma_n C_n$, where σ_m, σ_n are symmetry numbers of m-substituted isotopologue

and non-substituted isotopologue, and C_m, C_n are concentrations of the m-substituted isotopologue and non-substituted isotopologue. In our current application, we focus on carbon and hydrogen isotopologues of C1–C7 n-alkanes, as they are the main components of natural gas and condensates, which has been characterized most widely. We note that our model could be easily modified to report information beyond these molecules, such as molecules of C4+ alkane's isomers, oil compounds and sulfur isotope substitutions.

Table 6-1. An example output of the model with saturated oil as substrate. T=180°C, chemistry is scheme A and progress=20%.

	Carbon Isotope Substitutions					Hydrogen Isotope Substitutions				
#	1	2	3	4	non	1	2	3	4	non
C1	1581294				28750112	548720				29298832
C2	2096666				19018488	731817				20434386
C3	1578930	797424			14260355	591748	261526			15902921
C4	1095297	1116017			9899771	426203	382795			11473092
C5	780675	794485	397807		7043656	315352	282755	141905		8483828
C6	540020	550779	551862		4879504	226458	205124	203384		6108489
C7	397767	404920	406871	204081	3592127	176207	155312	156034	77888	4673039

3.5. Temperature and Time

Temperature affects the rates of reactions, so it exerts important influence on the results of the kMC model. We enable the specification of the temperature followed over time in our model, allowing temperature to change during cracking in order to imitate burial conditions in a sedimentary basin. The rates of all reactions considered by the model are updated continuously as the temperature changes from one time-step to the next.

Based on equation 6, the time passed to a kMC time step can be estimated with the exponential function using another random number p_2 : $\tau = \ln(p_2) / \sum_v W_v$, where $p_2 \in (0, 1)$ and is uniformly distributed, and $\sum_v W_v$ is the summation of rates of all possible reactions (Fichthorn et al., 1991; Peterson et al., 2018). Integrating this function over the possibility range yields that the average time passed for such a step is $\tau = 1/\sum_v W_v$. Therefore, we could calculate the time increments per step with the average time equation and constrain the time flow during a kMC simulation.

3.6. Programming details

3.6.1. Program organization

A simulation of the kMC model is composed of initialization of system, iteration of time steps, and processing outputs. The total number of time steps is dependent on the size of the system as well as the extent of reaction. Under scheme A, this number can be converted to

a percentage ‘reaction progress’ by dividing by the total number of single bonds in the system (maximum number of steps that can be taken). It is more complicated to relate the total number of steps with reaction progress with scheme B due to the complexity of pathways, but we will discuss how we approach it in the results section. Single simulation does not produce enough n-alkane molecules to be statistically useful. A simulation starts with a system that has 10^5 to 10^7 carbon atoms, so only 10^2–10^4 $^{13}CH_4$ molecules will be formed if 10% carbon is turned into methane, which lead to unacceptable uncertainty on the isotope ratios. The uncertainty of the proportions of isotopologues in product molecules of interest computed by the model follows counting statistics (i.e., error scales with the reciprocal of the square root of the quantity of each isotopologue of interest). Reaching precisions that are useful for answering geochemical questions using this method demands counting a large number of each isotopologue of interest. E.g., one million of a given isotopologue must be observed to achieve a 1 ‰, 1 SE, relative uncertainty in its abundance.

Therefore, we repeat the simulation under the same settings (initialization and number of time steps) for many times and combine the outputs. Typically, 10^3–10^4 repetitions can result in satisfying precision. These repetitions allow us to parallelize the program for faster overall execution on a computation cluster facility. In this study, we use Caltech’s High-Performance Cluster. Each experiment uses 2,000–10,000 core hours. Implementing a Monte Carlo method in parallel computing can cause problems as the pseudorandom

number generator used to initialize each model and select reactions at each time step of each model can have seeding biases (Rosenthal, 2000). We avoid this problem by seeding the generator using current time at each computing thread.

3.6.2. Data structure

The topological molecular structures of chemical compounds in the model are stored as graphs. Each node represents an atom and each edge represents a covalent bond. Edge weights are assigned to reflect bond orders of their respective bonds. Properties associated with the atoms are stored in separate arrays, which include the element type (C, H, O, N or S), whether that site is a radical, and any isotope (^{13}C and ^{2}H) substitution.

When a simulation ends, we begin to process the computational output. The first step is to divide the system into separate molecules. This is operated by separating the system graph into subgraphs that are not in connection (covalent bonds) with other subgraphs. We extract and store these subgraphs from the original graph. Next, we examine the properties of these subgraphs for identification of compounds. These subgraphs are sorted by node size (number of nodes) and then we test whether each subgraph of a given size represents an n-alkane, as we are reporting data of n-alkanes in this study. We constructed a set of reference graphs representing C1–C7 n-alkanes. The target graph is then compared with one of the reference graphs (of same size) for graph isomorphism relationships. The graph isomorphism relationship here also restrict node atom elements and edge bond weights, i.e.,

the reference graph have to have identical atoms (all C) and bond weights (all single bonds) as the pre-constructed reference graphs. If graph isomorphism exists between the target subgraph and a reference graph, the subgraph is recognized as the n-alkane compound represented by reference graph (we only report n-alkanes in this study). We then examine the isotope substitutions present in each selected target subgraph to categorize its isotopologue identity.

3.6.3. Random event selection

An array of rates of all possible reactions is calculated at each iteration step: [r1,r2, …, rN]. A uniformly distributed random number $p \in (0, 1)$ is generated at each iteration step to select one of these reactions to occur, using the Mersenne Twister pseudorandom number generator. To do so, we calculate a cumulative summation array for the array of all possible reaction rates, by the order of the reaction list. The first reaction from the cumulative summation array to reach p*S, where S is the summation of all rates, is the selected reaction.

3.6.4. Algorithmic optimization

High demand for computational resources (both CPU and memory) is a disadvantage of the kMC model. We implemented numerous approaches to improve the computational efficiency. Here we report the most important ones.

First, we made hydrogen atoms implicit in the model. Numbers of hydrogen atoms are implied by the bonding of carbon (and presence or absence of radicals). This step reduces the number of nodes and edges of the molecular graph and therefore saves memory.

Second, we arbitrarily enriched the rare-isotope content in the starting model substrates, since most of the error is contributed by the uncertainty in counting product molecules that contain one or more minor isotope substitutions. We apply an enrichment factor relative to natural abundances of 5 for ^{13}C content and 50 for D content. We do not attempt higher level of enrichment to avoid doubly and multiply substituted isotopologues overwhelming the C2+ alkanes, as those isotopologues are identified in output processing. For example, if we use 10 times the natural abundance for ^{13}C content, the doubly substituted ^{13}C isotopologue of heptane would be as abundant as singly substituted isotopologue of heptane. We divide the isotope ratios of the output with these factors so that results can be compared with natural materials.

Third, for models that employ chemistry of scheme B, we divide the reactions types to three tiers: fast reactions, medium reactions and slow reactions. Fast reactions are radical isomerization reactions to the fourth and fifth position that have rate constants of 10^{4}–$10^{5}s^{-1}$ at 523K. Medium reactions include β-scission, radical re-combination, H-abstraction and capping. These reactions have radicals in the reactant and have rate constants of 10^{0}–$10^{3}s^{-1}$ at 523K. Slow reactions are homolytic cleavage reactions that have rate constants of 10^{-27}–$10^{-16}s^{-1}$ at 523K. Because fast reactions have orders of magnitude higher probability of happening, almost all the computational resources would be allocated to calculating fast reactions unless we intervened by artificially bypassing, suppressing or replacing them. However, repetitive propagation of the radical isomerization reactions does not promote the progress (measured by time passed) of thermal cracking, nor does it improve the quality of Monte Carlo results. We thereby place a limit of repetition number by introducing an 'inhibitor' on consecutive execution of radical isomerization steps. The length of a radical isomerization sequence is confined by a random integer between 1 and 6, which is generated at the first isomerization reaction of that sequence. When that integer is reached, the sequence is interrupted to execute a reaction from medium or slow reactions. On the other hand, it is not required to limit medium reactions. When a system keeps executing medium and fast reactions, radicals automatically quenches due to radical-loss medium reactions of capping and radical recombination, and homolytic cleavage (slow reaction) —

only reaction that do not require radical as reactant — becomes the only available reaction when the system has no radicals.

Last, we also modified models employing chemistry scheme B by representing molecular graphs with two matrices, a connection matrix and a bond matrix, during the chemical evolution of simulations in which graph size is big (>100,000 nodes). This is especially important for chemistry scheme B because the entire system in scheme B has to be stored in one graph in order to allow the two-body reaction of radical recombination. The computational costs of graph operations, such as addition/removal of edges and search for node neighbors, scale with the number of nodes and edges in a graph. We replace the graph data structure with two n × 4 matrices (where n=number of nodes). In the connection matrix, each row lists the indices of target nodes in connections with the row node (the maximum number of connections is 4 and any vacant element is left equal to 0). In the bond matrix, each row lists the bond orders (where aromatic bonds are assigned an order of 1.5) at the same position of the connection matrix. This representation is more efficient compared with the more common way of using an n × n adjacency matrix. For example, the complexity of a search algorithm (i.e., to find neighbors) using this method is $O(1)$, vs. $O(n)$ when using an adjacency matrix.

4. Results

4.1 Accuracy test of a simple system

The accuracy of results of kMC simulations can be tested by applying that simulation to an analytically solvable problem and comparing the simulation output to the corresponding analytical solution. Here we take this approach by simulating and analytically solving the outcome of cracking butane under chemistry scheme A, where the possible reaction paths are small in number and so relatively tractable to analytical description. We monitor the position-specific isotope distribution in residual butane, which is expected to evolve over time as homolytic cleavage reactions progress. In the following paragraph we derive the analytical solution to these predicted effects, which we then compare with results of our kMC simulation of this scenario.

Under chemistry scheme A, butane cracking initiates with dissociation of one of its three C—C bonds. Therefore, the concentration of non-isotope-substituted butane will evolve over time by the following loss equation:

$$\frac{dB(t)}{dt} = -R_{1,2} - R_{2,3} - R_{3,4} \tag{8}$$

$$B(t) = B(0)e^{-(R_{1,2}+R_{2,3}+R_{3,4})t} \tag{9}$$

$R_{a,b}$ denotes rate constants for homolytic cleavage of the bond between carbon atom a and carbon atom b.

Isotope effects modify this loss equation based on the primary, secondary and tertiary isotope effects involved. For example, in the case of 1-deuterium butane (butane containing a single deuterium substation on one of its first carbon positions, noted as B_{1-D}), cleavage of its carbon-carbon bond 1,2 will be affected by a secondary hydrogen kinetic isotope effect and cleavage of its carbon-carbon bond 2,3 will be affected by a tertiary hydrogen kinetic isotope effect. Therefore,

$$B_{1-D}(t) = B_{1-D}(0)e^{-({}^{D}_{2}KIE_1 R_{1,2} + {}^{D}_{3}KIE_1 R_{2,3} + R_{3,4})t} \tag{10}$$

where ${}^{D}_{2}KIE_1$ denotes a secondary deuterium KIE from a substituted 1° carbon. Similarly, we can define the rate of loss of 2-deuterium butane (singly-deuterium substituted at the second carbon position) as:

$$B_{2-D}(t) = B_{2-D}(0)e^{-({}^{D}_{2}KIE_2 R_{1,2} + {}^{D}_{2}KIE_2 R_{2,3} + {}^{D}_{3}KIE_2 R_{3,4})t} \tag{11}$$

Recognizing that the butane molecule is symmetrical, equations 10 and 11 provide enough information to solve for the evolution in the site-preference of the D/H composition of butane undergoing destruction by hemolytic cleavage:

$$\epsilon D_{2-1} = \frac{2}{3}\frac{B_{2-D}(t)}{B_{1-D}(t)} - 1$$

$$= \frac{2}{3}\frac{B_{2-D}(0)}{B_{1-D}(0)} e^{[-({}^{D}_{2}KIE_2 R_{1,2} + {}^{D}_{2}KIE_2 R_{2,3} + {}^{D}_{3}KIE_2 R_{3,4}) + {}^{D}_{2}KIE_1 R_{1,2} + {}^{D}_{3}KIE_1 R_{2,3} + R_{3,4}]t} - 1 \tag{12}$$

Assuming that the starting substrate butane has homogeneous deuterium distribution,

$$\epsilon D_{2-1} = e^{[-({}^{D}_{2}KIE_2R_{1,2}+{}^{D}_{2}KIE_2R_{2,3}+{}^{D}_{3}KIE_2R_{3,4})+{}^{D}_{2}KIE_1R_{1,2}+{}^{D}_{3}KIE_1R_{2,3}+R_{3,4}]t} - 1 \qquad (13)$$

Combining eqn. (9) and (13),

$$\epsilon D_{2-1} = f^{[-({}^{D}_{2}KIE_2R_{1,2}+{}^{D}_{2}KIE_2R_{2,3}+{}^{D}_{3}KIE_2R_{3,4})+{}^{D}_{2}KIE_1R_{1,2}+{}^{D}_{3}KIE_1R_{2,3}+R_{3,4}]/(-(R_{1,2}+R_{2,3}+R_{3,4}))} - 1, \quad (14)$$

where

$$f = \frac{B(t)}{B(0)}. \qquad (15)$$

Similarly, for ^{13}C,

$$\epsilon^{13}C_{2-1} = f^{[-({}^{13C}_{1}KIE_2R_{1,2}+{}^{13C}_{1}KIE_2R_{2,3}+{}^{13C}_{2}KIE_2R_{3,4})+{}^{13C}_{1}KIE_1R_{1,2}+{}^{13C}_{2}KIE_1R_{2,3}+R_{3,4}]/(-(R_{1,2}+R_{2,3}+R_{3,4}))} - 1. \quad (16)$$

The predictions of this analytical model of butane cracking are well matched by our kMC model. For example, for the case of 20% total reaction progress of C—C bond cracking at 180°C, the analytical model predicts that the residual butane will have site-specific H and C isotope structures characterized by values of ϵD_{2-1}=19.8 ‰ and $\epsilon^{13}C_{2-1}$= 6.38 ‰. kMC results of both carbon and hydrogen isotopes match the analytical values to within statistical uncertainty in the kMC model (Figure 6-4).

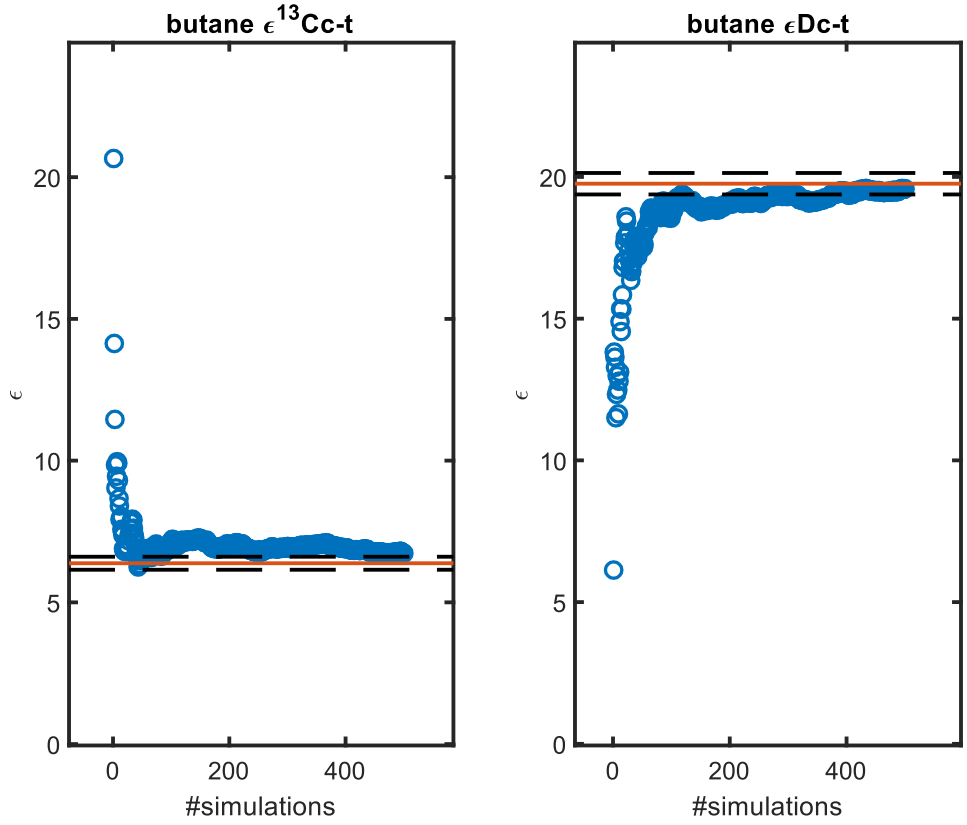

Figure 6-4: Cumulative average central-terminal isotope fractionation of residual butane in the accuracy test. X-axis is the number of simulations. The yellow line shows analytical solution. The dashed black lines are 1σ error envelopes (defined by counting statistics of the final result at n=500).

4.2. Isotope ratios of C1-C7 alkanes

In this section, we report the results of experiments in which the kMC model was run to a reaction progress of 20% (number of steps divided by total number of single bonds) for various substrates under chemistry scheme A. It is unclear how we should relate reaction progress in scheme A (20% completion) to that in scheme B, because scheme B has many more different reaction classes and the conversion from macromolecular substrate to gaseous hydrocarbons is not a linear function of the number of time steps or reaction events. Therefore, we compare calculated molecular isotopic compositions and structures for models run with chemistry scheme A and B at the same total yield of methane, which grows monotonically with reaction progress in both types of models. Initial isotopic compositions of the precursor are -25‰ for $\delta^{13}C$ and -100‰ for δD.

We note that the elapsed real time corresponding to 20% cleavage in scheme A, which could be estimated by methods illustrated in section 3.5, is between 10^{23} to 10^{24} s. This is almost 10 orders of magnitude longer than typical burial times of geological strata (10^{13}–10^{15}s or 3–300 Myr). This discrepancy exposes the problem of over-simplification of chemistry. Thermal cracking is likely accelerated by reactions other than homolytic cleavage, such as those we include under chemistry scheme B. Although part of the reason that kinetic constants from high temperature experiments do not apply to low temperature conditions well, its misfit is unlikely to account for the large gap between model time and realistic time. Under scheme B, the estimated time length of 20% (equivalent) reaction progress is between 10^{17} to 10^{18}s, which is much closer to realistic burial time scale. We

suggest two possible reasons for this discrepancy. (1) The kinetic database that we are using (RMG rate rules) might not be accurate in the temperature range of catagenesis. (2) Our chemistry schemes might not represent the whole picture of catagenetic chemistry. They might have omitted the significance of potential catalysts such as clay minerals, transition metals and water (Seewald, 2003). They might have not treated sulfur radical reactions properly, which have also been suggested to be catalytic for hydrocarbon generation (Lewan, 1998). These issues will be examined in further iterations of the kMC model.

Position-specific isotope ratios of C3–C7 alkanes from chemistry scheme A are shown in Figure 6-5. Alkanes produced from cracking of oil (saturated fraction) have distinctive intramolecular stable isotope patterns characterized by heavy-isotope depletion on the terminal methyl group and relatively uniform values across the internal positions. This pattern is consistent from propane to heptane. The terminal groups have $\delta^{13}C$ values lower than the rest of the molecule by 10–20‰ and δD values lower by 230 – 250‰.

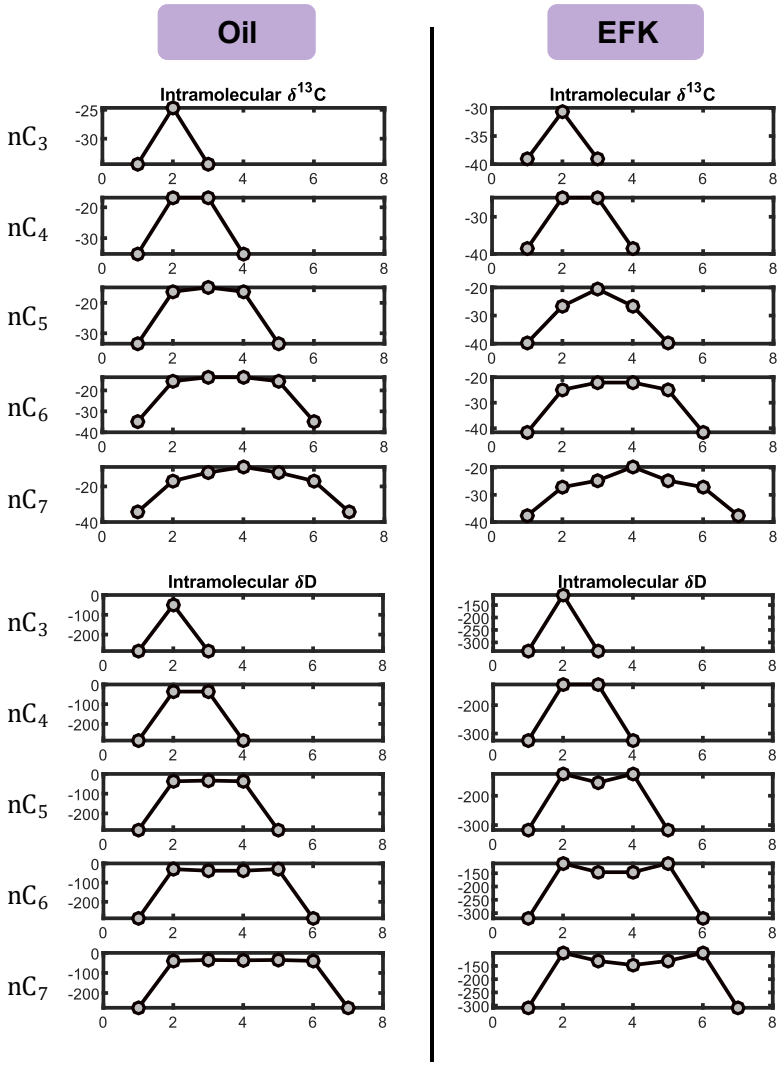

Figure 6-5: Position-specific carbon and hydrogen isotope values of n-alkanes produced from substrates under scheme A, scaled in VPDB and VSMOW respectively. Oil: saturated fraction of oil; EFK: Eagle Ford shale kerogen model. Temperature is at 180°C. Precursor material is hypothesized to have $\delta^{13}C$= -25 ‰ and δD= -100 ‰.

At equivalent reaction progress, results from models run using chemistry scheme B are more diverse in site-specific carbon isotope structures than those generated with scheme A (Figure 6-6). For cracking of oil (saturated fraction) using scheme B, the second positions of C5, C6 and C7 alkanes are also slightly depleted in carbon isotopes compared to the inner positions. For cracking of the Eagle Ford Shale kerogen using scheme B, C6 and C7 alkanes have the second carbons being most depleted in ^{13}C, although this experiment produces so little C6 and C7 hydrocarbons that the precision in calculated isotope ratios approaches the sizes of calculated site-specific variations. The hydrogen isotope structures of these compounds have the same terminal depletion pattern as those from scheme A.

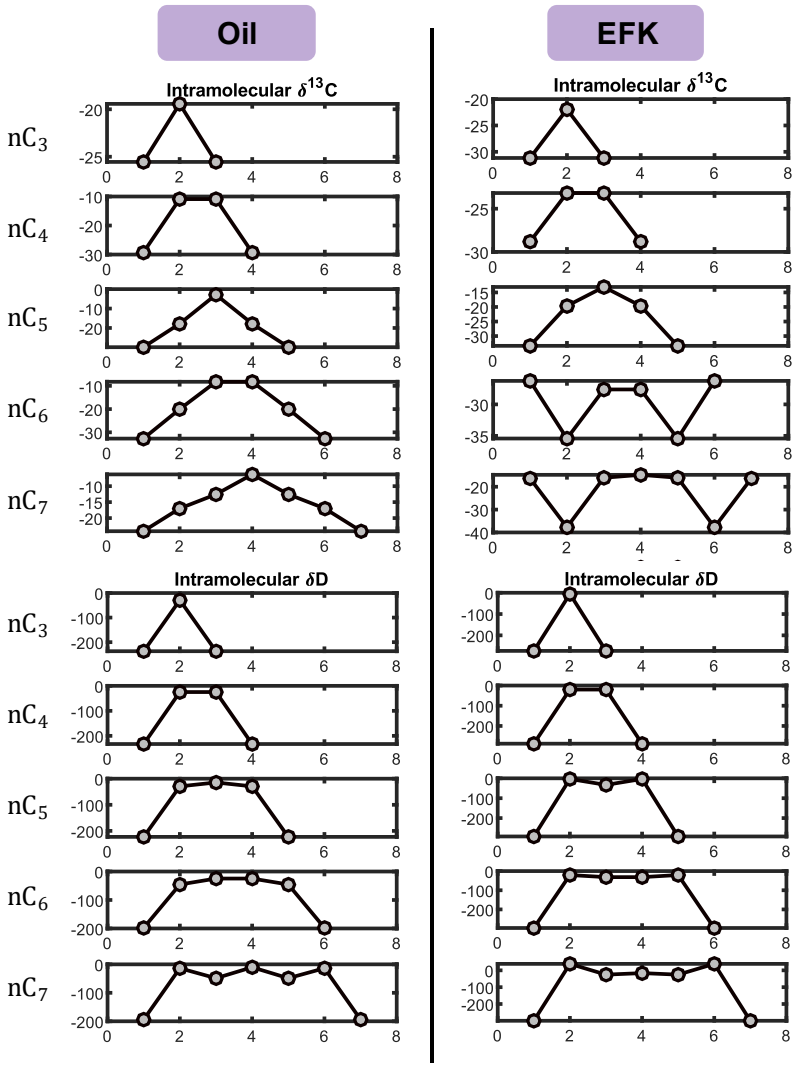

Figure 6-6: Position-specific carbon and hydrogen isotope values of n-alkanes produced from substrates under scheme B, scaled in VPDB and VSMOW respectively. Precursor material is hypothesized to have $\delta^{13}C$= -25 ‰ and δD= -100 ‰.

We present compound-specific carbon and hydrogen isotope compositions calculated for C1 through C5 n-alkanes produced by our kMC model of cracking; these data are illustrated using the 'Chung plot' (Figure 6-7). Chung et al. (1988) devised this classic $\delta^{13}C$ vs 1/n diagram (where n=chain length) based on the hypothesis that one site per alkane is isotopically fractionated by KIE's associated with bond dissociation reactions by which these compounds were generated. The chemistry of either of the schemes in our model is more varied than this simplifying assumption, so that there are many possible numbers and locations of sites in product molecules that can be influenced by bond-dissociation KIE's. However, the Chung diagram is widely used to interpret measured isotopic compositions of natural gas components, so it is useful to examine our model outputs in this plot.

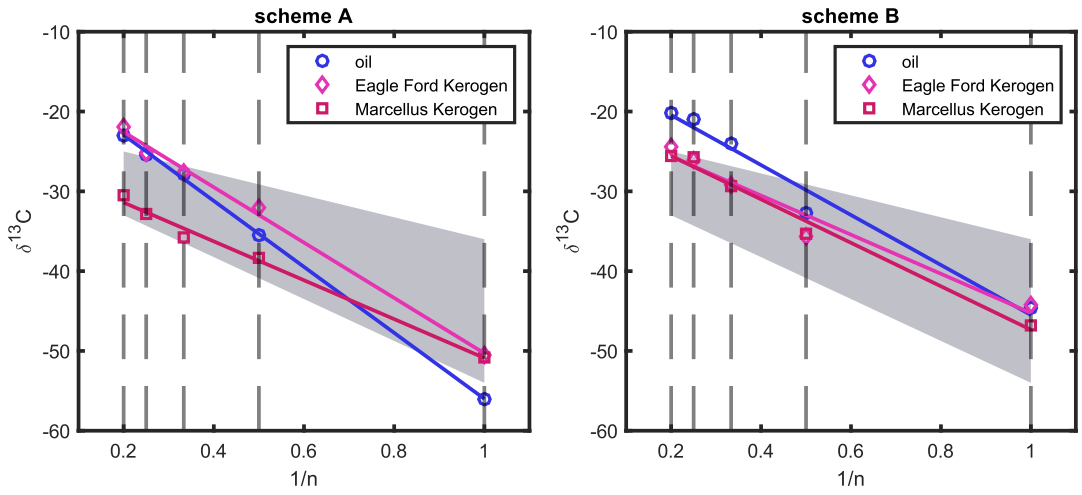

Figure 6-7: Compound-specific carbon isotope plot for natural gas cracked from different substrates under scheme A and scheme B. Gray area shows common isotope composition of natural gas derived from type II kerogen (Zou et al., 2007). Precursor material is hypothesized to have $\delta^{13}C$= -25 ‰ and δD= -100 ‰.

Results calculated by our kMC model using both chemistry schemes form relatively straight lines on the 'Chung plot' (Figure 6-7). The reported results here are from the same model executions in the previous section, so $\delta^{13}C$=-25‰ and δD=-100‰ in the initial substrate. The reaction progress is breaking 20% of all single bonds for scheme A and at equivalent methane yield to scheme A for scheme B. Under scheme A, $\delta^{13}C$ of methane ranges from -60 to -50‰. The slope ranges from -41 to -24‰ (per unit of the X-axis quantity, 1/n). Under scheme B, $\delta^{13}C$ of methane ranges from -44 to -47‰ and the slope ranges from -31 to -27‰ (per unit of the X-axis quantity, 1/n). The positions of the trends for model output in Figure 6-7 are consistent with the empirical field of natural gas generated from sapropelic substrates, suggesting our model captures first order features of measured isotopic properties of natural gases — an encouraging result given that our model was not tuned in any way to match isotopic data for natural gases or catagenesis experiments.

4.3. Effects of reaction progress

We examined the computed isotopic compositions and intramolecular isotopic structures of product compounds of interest (C1–C7 n-alkanes) at several different stages of reaction progress for a model using the Eagle Ford shale kerogen molecule a substrate and either chemistry scheme A or B (Table 6-2). This exercise allowes us to examine what the kMC model predicts for the trend in gas isotope chemistry over the course of natural burial and thermal maturation. We find that the $\delta^{13}C$ values of ethane and higher order alkanes increase with reaction progress, while the compositional proportions of them decrease In contrast, the $\delta^{13}C$ of methane and C1/(C2+C3) ratio do not change monotonically. Instead, both variables decrease slightly in the early stages of reaction progress and then increase in the later stages. Under chemistry scheme A, the intramolecular carbon and hydrogen isotope differences of propane (i.e., center-terminal fractionation, $\varepsilon^{13}C_{C\text{-}T}$) increases with reaction progress; specifically, $\varepsilon^{13}C_{C\text{-}T}$ rises from 9‰ at 20% reaction completion to 30‰ at 80% reaction completion (Figure 6-8). Again, the reaction progress here is expressed as percentage of bond broken for scheme A, and at equivalent methane yield to scheme A for scheme B. Under chemistry scheme B, the center-terminal carbon isotope fractionation of propane remained relatively constant (total range of 4 ‰, with no consistent temporal trend) over the course of reaction, and similar to the value observed in scheme A at low total reaction progress (i.e., early in the model, or low in thermal maturity).

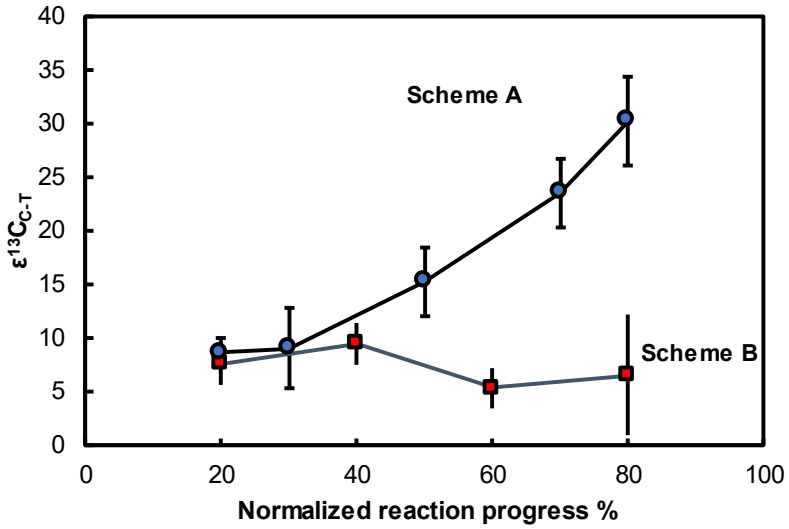

Figure 6-8: Carbon isotope fractionation between the central and terminal positions of propane vs. reaction progress.

Table 6-2: Molecular and isotopic output at different extent of reaction, using the Eagle Ford Shale kerogen as substrate.

			Compound-specific δ13C							Compound-specific δD							Position-specific C3	
Scheme	Normalized progress	Dryness	C1	C2	C3	C4	C5	C6	C7	C1	C2	C3	C4	C5	C6	C7	$\varepsilon^{13}C_{C\text{-}T}$	1 σ
A	20	2.67	-46.4	-40.2	-36.3	-31.7	-30.6	-29.5	-28.4	-354	-262	-198	-162	-140	-123	-102	8.7	1.3
	30	2.12	-46.3	-39.3	-34.0	-30.5	-26.7	-32.2	-27.9	-369	-269	-202	-172	-145	-126	-98	9.1	3.8
	50	1.88	-50.5	-32.0	-27.6	-25.2	-21.9	-16.0	-13.7	-415	-271	-197	-158	-137	-117	-85	15.3	3.2
	70	2.54	-47.3	-19.8	-8.1	-0.2	-1.9			-439	-225	-136	-95	-62	-50	-42	23.6	3.2
	80	3.56	-44.4	-5.2	2.6	8.4				-440	-168	-81	-23	4			30.3	4.1
	90	6.47	-37.9	9.6	9.8					-427	-68	-17					25.9	6.2
	95	12.71	-33.5	23.0	66.1					-411	35							
B	20	2.46	-47.6	-40.7	-32.8	-29.3	-26.5	-26.3	-33.3	-278	-179	-135	-110	-94	-89	-50	7.7	2.1
	40	3.04	-46.0	-36.3	-28.1	-26.0	-23.8	-29.8	-22.1	-279	-172	-118	-90	-59	-47	-12	9.5	2.0
	60	4.83	-40.9	-29.7	-19.4	-14.6	-21.0			-274	-144	-65	-28	13			5.4	1.9
	80	25.00	-35.0	-12.5	-3.3	-5.3				-270	-31	77	149				6.6	5.7

5. Discussion

5.1. Position-specific isotope distribution of C3-C7 alkanes

When the aliphatic fraction of the substrate is dominantly composed of linear unbranched alkyl chains instead of branched ones, such as the saturated oil model and Eagle Ford kerogen model, a strong depletion of both carbon and hydrogen isotopes on the terminal groups of product C3-7 n-alkanes is observed. Such depletion is caused by the preferential expression of KIE's associated with bond dissociation reactions on the terminal sites of products. The dissociation of single bonds in hydrocarbon chain moieties of substrates selects for ^{12}C over ^{13}C and for H over D at the bond dissociation site, which ends up being the terminal positions of products.

For models using chemistry scheme A, the internal positions become more heavy-isotope enriched relative to terminal positions with increasing reaction progress (Figure 6-8). We recognize two main causes for this trend. (1) Secondary cracking of the product n-alkane molecules increases residual molecules' heavy isotope value, and does so unevenly across the non-equivalent molecular sites. This is because internal positions have two C—C bonds, thus have higher probability of participating in bond dissociation events and being affected by KIE's. (2) The hydrocarbons produced early in the catagenetic process (at low reaction progress) are more commonly formed via one bond dissociation event. Because n-alkane is symmetrical, the isotope ratio of terminal position averages one fractionated

position and one unaffected position, such that the average heavy-isotope depletion of terminal sites is diluted by about a factor of 2 relative to the actual KIE. The late stage C3-7 hydrocarbons (those still present after high overall reaction progress) are often products of two bond dissociation events, enhancing the overall magnitude of heavy-isotope depletion in the terminal positions. In contrast, in models that use chemistry scheme B, the center-terminal fractionations vary little over a range of reaction progress. This discrepancy likely stems from the addition of radical chemistry in scheme B, although the specific mechanism is not clear. One of the possible mechanisms for moderating the development of stronger site-specific fractionations as reaction progress increases is reformation of propane via radical recombination (e.g., methyl+ethyl → propane). These reactions provide a source of propane that do not have high central-terminal isotopic value differences. Central-terminal fractionation for propane increases slightly or does not change with thermal maturity in natural gas samples (Liu et al., 2019; Zhao et al., 2020; Julien et al., 2020; Xie et al., 2020) and pyrolysis experiments (Piasecki et al., 2018; Gilbert et al., 2019). The maximum range of $\varepsilon^{13}C_{C\text{-}T}$ of propane is less than 5‰ in these pyrolysis experiments and natural samples, but is 23‰ in our simulation of the Eagle Ford kerogen model under scheme A. Therefore, the trend in scheme B is much closer to real samples.

5.2. Compound-specific isotope signatures and molecular compositions

Compound-specific carbon isotope compositions of C1 – C5 alkanes from our model agree reasonably well with data for samples of natural gases (Figure 6-7). The carbon isotope values we calculate for alkanes produced after 20% reaction progress under chemistry scheme B are also consistent with compound specific isotopic measurements of early maturity gas from the Eagle Ford Shale (e.g., Byrne et al., 2018). An exception is that the 'Chung plot' slope of results from scheme A are higher than those from scheme B and those from natural samples. We notice that this slope also increases with reaction progress (Table 6-2). The change of slope is mostly driven by enrichment of ^{13}C in higher alkanes. In fact, ethane and propane become progressively enriched in ^{13}C rapidly and their $\delta^{13}C$ values exceed typical range of natural gas at later stages (>0‰). The same phenomenon was discovered in Peterson et al. (2018). We think this is likely caused by self-cracking of non-methane alkanes that leave the residual pool more heavy-isotope enriched, which has been hypothesized for longer alkanes (Tang et al., 2005). Under chemistry scheme A, cracking is a unidirectional process of breaking larger molecules to smaller fragments. Near completion of each model experiment, longer alkanes are decomposed to high extents, so their heavy isotope contents of the remaining fractions become significantly elevated by distillation. The carbon isotopes of these alkanes in the maturation sequence of scheme B do not increase as much as scheme A—they do not turn positive even at the end of the examined maturity range. This is likely a result of alkane inter-conversion mediated by radical reactions. For example, a methyl radical can be formed from a methane molecule

via H-abstraction by another radical, and the methyl radical can recombine with another radical to form a higher-order alkane molecule. This reformed alkane inherits carbon from the isotopically lighter smaller alkanes. Therefore, this mechanism can potentially 'buffer' the carbon isotope composition of higher order alkanes.

Natural gas produced using chemistry scheme A is wetter (lower in C1/C2+ mole proportions) than that produced using scheme B, and both are wetter than most real natural gas samples (Figure 6-9). The discrepancy between scheme A and scheme B could be explained by the unbiased bond-breaking behavior of homolytic cleavage under scheme A. A simple scenario, thermal cracking of a nC_6 molecule under scheme A, illustrates this phenomenon. Consider hydrocarbon composition after the first reaction, which corresponds to 20% completion (1 out of 5 bonds). Listing all possibilities of the first reaction and their weights, we found that the output is 20% C_1, 20% C_2, 20% C_3, 20% C_4, and 20% C_5. This one-step product has a C1/(C2+C3) ratio of 0.5. This value is exceptionally low compared to data of global natural gas samples. For example, Milkov and Etiope (2018) shows that C1/(C2+C3) ratios of 99% of all published natural gas samples are greater than 1. Therefore, homolytic cleavage of linear alkyl structures tends to produce higher proportions of wet components than natural gas formations. Conversely, molecular breakdown under scheme B has other paths that might not produce wet gas. Some of the possible reaction events will favor production of methyl radical, which can be capped to form methane. For example, propyl radicals could undergo β-scission to form a

methyl radical. Similarly, a 1-hexyl radical has a very high rate constant to isomerize into a 3-hexyl radical, which could undergo β-scission to form a methyl radical. Another important reason for scheme B to produce methane-rich gases is that methyl radicals have higher reactivity with an alkyl-H or H atom (compared to other alkyl radicals), so it is more favorably de-radicalized than longer radicals. The fact that both schemes produce natural gas with more wet components than natural gas probably reflects the role of alternative pathways (to thermal cracking) in natural gas formation, such as metal catalysis or quasi-equilibrium chemistry (Mango, 1992; Helgeson et al., 2009; Mango et al., 2009).

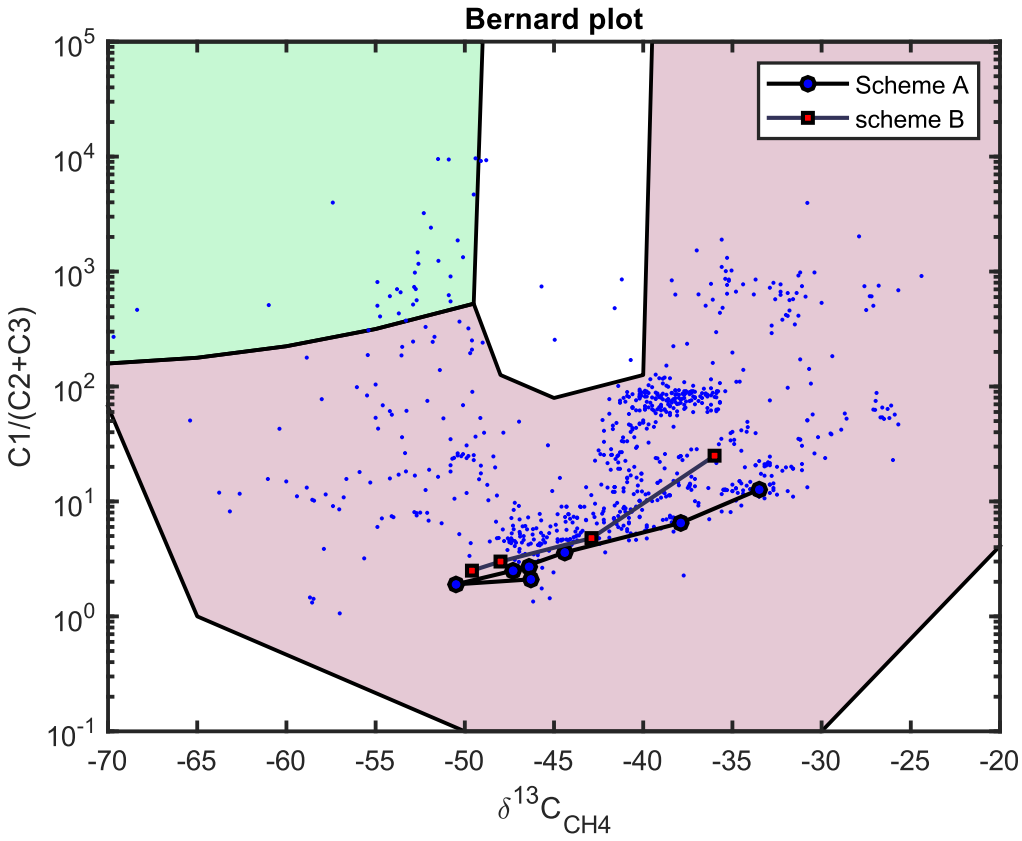

Figure 6-9: Evolution of C1/(C2+C3) ratio and methane $\delta^{13}C$ with reaction progress. Background data in blue represent global natural gas data compiled from literature (Dai et al., 2014; Sherwood et al., 2017; Thiagarajan et al., 2020). Genetic fields (thermogenic vs. microbial) are redrawn from (Milkov and Etiope, 2018). Precursor material is hypothesized to have $\delta^{13}C$= -25 ‰ and δD= -100 ‰.

6. Conclusion

Realistic modeling of explicit reaction networks in thermal cracking are valuable to many research fields. For research in petroleum geochemistry, it could help us build a forward model to calculate proportions of isotopologues of hydrocarbons in oil and natural gas. In this study, we employ the kinetic Monte Carlo method to overcome the challenge of system complexity in conventional models. We designed a model that directly take molecular structure of precursor organic matter as input, temperature and time as condition variables, and outputs the composition and isotopic values (both intra- and intermolecular) of hydrocarbon products. We verified the reliability and accuracy of our model in a confined system of butane cracking.

Our model provides rich information, including carbon and hydrogen isotope values of every position in all alkanes. Our results generally agree observational data of natural hydrocarbons. For intra-molecular carbon and hydrogen isotope data of C4+ alkanes, we provide predictions that can be used in future analytical studies.

We tested the performance of two chemistry schemes, a relatively simple one that only considers homolytic cleavage and capping and a more complicated one that further includes β-scission, radical isomerization, and H-abstraction. Our overall results indicate that results from the more complicated model are more similar to real data from natural gases in many aspects, including gas wetness, trend of intramolecular isotope fractionation, compound-specific isotope compositions, and time. This shows that the radical reactions

other than homolytic cleavage play important roles in the thermal cracking chemistry of petroleum formation.

Acknowledgements

The computations were conducted on the Caltech High Performance Cluster, partially supported by a grant from the Gordon and Betty Moore Foundation. We thank David Wang, Michael Lawson, Thomas F. Miller for valuable discussions.

Code and data availability

All scripts and data used in this chapter are available at https://github.com/1995123xh/kMC.

References

Abelson P. H. and Hoering T. C. (1961) Carbon isotope fractionation in formation of amino acids by photosynthetic organisms. *Proc. Natl. Acad. Sci. U. S. A.* **47**, 623–632.

Allen J. W., Goldsmith C. F. and Green W. H. (2012) Automatic estimation of pressure-dependent rate coefficients. *Phys. Chem. Chem. Phys.* **14**, 1131–1155.

Baulch D. L., Bowman C. T., Cobos C. J., Cox R. A., Just T., Kerr J. A., Pilling M. J., Stocker D., Troe J., Tsang W., Walker R. W. and Warnatz J. (2005) Evaluated kinetic data for combustion modeling: Supplement II. *J. Phys. Chem. Ref. Data* **34**, 757–1397.

Behar F., Vandenbroucke M., Tang Y., Marquis F. and Espitalie J. (1997) Thermal cracking of kerogen in open and closed systems: Determination of kinetic parameters and stoichiometric coefficients for oil and gas generation. *Org. Geochem.* **26**, 321–339.

Bousige C., Ghimbeu C. M., Vix-Guterl C., Pomerantz A. E., Suleimenova A., Vaughan G., Garbarino G., Feygenson M., Wildgruber C., Ulm F. J., Pellenq R. J. M. and Coasne B. (2016) Realistic molecular model of kerogen's nanostructure. *Nat. Mater.* **15**, 576–582.

Burnham A. K. and Braun R. L. (1990) Development of a detailed model of petroleum formation, destruction, and expulsion from lacustrine and marine source rocks. *Org. Geochem.* **16**, 27–39.

Byrne D. J., Barry P. H., Lawson M. and Ballentine C. J. (2018) Determining gas expulsion vs retention during hydrocarbon generation in the Eagle Ford Shale using noble gases. *Geochim. Cosmochim. Acta* **241**, 240–254.

Cesar J., Eiler J., Dallas B., Chimiak L. and Grice K. (2019) Isotope heterogeneity in ethyltoluenes from Australian condensates, and their stable carbon site-specific isotope analysis. *Org. Geochem.* **135**, 32–37.

Chatterjee A. and Vlachos D. G. (2007) An overview of spatial microscopic and accelerated kinetic Monte Carlo methods. *J. Comput. Mater. Des.* **14**, 253–308.

Chung H. M., Gormly J. R. and Squires R. M. (1988) Origin of gaseous hydrocarbons in subsurface environments: Theoretical considerations of carbon isotope distribution. *Chem. Geol.* **71**, 97–104.

Clog M., Lawson M., Peterson B., Ferreira A. A., Santos Neto E. V. and Eiler J. M. (2018) A reconnaissance study of 13C–13C clumping in ethane from natural gas. *Geochim. Cosmochim. Acta* **223**, 229–244.

Dai J. X., Ni Y. Y., Hu G. Y., Huang S. P., Liao F. R., Yu C., Gong D. Y. and Wu W. (2014) Stable carbon and hydrogen isotopes of gases from the large tight gas fields in China. *Sci. China Earth Sci.* **57**, 88–103.

Fichthorn K. A., Weinberg W. H. and Carlo M. (1991) Theoretical foundations of dynamical Monte Carlo simulations. *J. Chem. Phys.* **95**, 1087.

Galimov E. M. (2006) Isotope organic geochemistry. *Org. Geochem.* **37**, 1200–1262.

Gao C. W., Allen J. W., Green W. H. and West R. H. (2016) Reaction Mechanism Generator: Automatic construction of chemical kinetic mechanisms. *Comput. Phys. Commun.* **203**, 212–225.

Gao L., He P., Jin Y., Zhang Y., Wang X., Zhang S. and Tang Y. (2016) Determination of position-specific carbon isotope ratios in propane from hydrocarbon gas mixtures. *Chem. Geol.* **435**, 1–9.

Gilbert A., Lollar B. S., Musat F., Giunta T., Chen S., Kajimoto Y., Yamada K., Boreham C. J., Yoshida N. and Ueno Y. (2019) Intramolecular isotopic evidence for bacterial oxidation of propane in subsurface natural gas reservoirs. *Proc. Natl. Acad. Sci. U. S. A.* **116**, 6653–6658.

Gilbert A., Yamada K., Suda K., Ueno Y. and Yoshida N. (2016) Measurement of position-specific 13C isotopic composition of propane at the nanomole level. *Geochim. Cosmochim. Acta* **177**, 205–216.

Gilbert A., Yamada K. and Yoshida N. (2013) Exploration of intramolecular 13C isotope distribution in long chain n-alkanes (C11-C31) using isotopic 13C NMR. *Org. Geochem.* **62**, 56–61.

Gillespie D. T. (1976) A general method for numerically simulating the stochastic time evolution of coupled chemical reactions. *J. Comput. Phys.* **22**, 403–434.

Goldman M. J., Vandewiele N. M., Ono S. and Green W. H. (2019) Computer-generated isotope model achieves experimental accuracy of filiation for position-specific isotope analysis. *Chem. Geol.* **514**, 1–9.

Gonzalez Y., Nelson D. D., Shorter J. H., McManus J. B., Dyroff C., Formolo M., Wang D. T., Western C. M. and Ono S. (2019) Precise Measurements of 12CH2D2 by Tunable Infrared Laser Direct Absorption Spectroscopy. *Anal. Chem.* **91**, 14967–14974.

Harper M. R., Van Geem K. M., Pyl S. P., Marin G. B. and Green W. H. (2011) Comprehensive reaction mechanism for n-butanol pyrolysis and combustion. *Combust. Flame* **158**, 16–41.

Hayes J. M. (2001) Fractionation of Carbon and Hydrogen Isotopes in Biosynthetic Processes. *Rev. Mineral. Geochemistry* **43**, 225–277.

Helgeson H. C., Richard L., McKenzie W. F., Norton D. L. and Schmitt A. (2009) A chemical and thermodynamic model of oil generation in hydrocarbon source rocks. *Geochim. Cosmochim. Acta* **73**, 594–695.

Julien M., Goldman M. J., Liu C., Horita J., Boreham C. J., Yamada K., Green W. H., Yoshida N. and Gilbert A. (2020) Intramolecular 13C isotope distributions of butane from natural gases. *Chem. Geol.* **541**, 119571.

Julien M., Nun P., Höhener P., Parinet J., Robins R. J. and Remaud G. S. (2016) Enhanced forensic discrimination of pollutants by position-specific isotope analysis using isotope ratio monitoring by 13C nuclear magnetic resonance spectrometry. *Talanta* **147**, 383–389.

Lewan M. D. (1998) Sulphur-radical control on petroleum formation rates. *Nature* **391**, 164–166.

Li Y., Zhang L., Xiong Y., Gao S., Yu Z. and Peng P. (2018) Determination of position-specific carbon isotope ratios of propane from natural gas. *Org. Geochem.* **119**, 11–21.

Liu C., Liu P., McGovern G. P. and Horita J. (2019) Molecular and intramolecular isotope geochemistry of natural gases from the Woodford Shale, Arkoma Basin, Oklahoma. *Geochim. Cosmochim. Acta* **255**, 188–204.

Liu C., McGovern G. P., Liu P., Zhao H. and Horita J. (2018) Position-specific carbon and hydrogen isotopic compositions of propane from natural gases with quantitative NMR. *Chem. Geol.* **491**, 14–26.

Lorant F., Prinzhofer A., Behar F. and Huc A. Y. (1998) Carbon isotopic and molecular constraints on the formation and the expulsion of thermogenic hydrocarbon gases. *Chem. Geol.* **147**, 249–264.

Mango F. D. (1992) Transition metal catalysis in the generation of petroleum and natural gas. *Geochim. Cosmochim. Acta* **56**, 553–555.

Mango F. D., Jarvie D. and Herriman E. (2009) Natural gas at thermodynamic equilibrium implications for the origin of natural gas. *Geochem. Trans.* **10**, 1–12.

Milkov A. V. and Etiope G. (2018) Revised genetic diagrams for natural gases based on a global dataset of >20,000 samples. *Org. Geochem.* **125**, 109–120.

Monson K. D. and Hayes J. M. (1980) Biosynthetic control of the natural abundance of carbon 13 at specific positions within fatty acids in Escherichia coli. Evidence regarding the coupling of fatty acid and phospholipid synthesis. *J. Biol. Chem.* **255**, 11435–11441.

Ni Y., Ma Q., Ellis G. S., Dai J., Katz B., Zhang S. and Tang Y. (2011) Fundamental studies on kinetic isotope effect (KIE) of hydrogen isotope fractionation in natural gas systems. *Geochim. Cosmochim. Acta* **75**, 2696–2707.

Ono S., Wang D. T., Gruen D. S., Sherwood Lollar B., Zahniser M. S., McManus B. J. and Nelson D. D. (2014) Measurement of a doubly substituted methane isotopologue, 13CH3D, by tunable infrared laser direct absorption spectroscopy. *Anal. Chem.* **86**, 6487–6494.

Peterson B. K., Formolo M. J. and Lawson M. (2018) Molecular and detailed isotopic structures of petroleum: Kinetic Monte Carlo analysis of alkane cracking. *Geochim. Cosmochim. Acta* **243**, 169–185.

Piasecki A., Sessions A., Lawson M., Ferreira A. A., Neto E. V. S. and Eiler J. M. (2016) Analysis of the site-specific carbon isotope composition of propane by gas source isotope ratio mass spectrometer. *Geochim. Cosmochim. Acta* **188**, 58–72.

Piasecki A., Sessions A., Lawson M., Ferreira A. A., Santos Neto E. V., Ellis G. S., Lewan M. D. and Eiler J. M. (2018) Position-specific 13C distributions within propane from experiments and natural gas samples. *Geochim. Cosmochim. Acta* **220**, 110–124.

Ranzi E., Gaffuri P., Faravelli T. and Dagaut P. (1995) A wide-range modeling study of n-heptane oxidation. *Combust. Flame* **103**, 91–106.

Ratkiewicz A. (2013) First-principles kinetics of *n* -octyl radicals. *Prog. React. Kinet. Mech.* **38**, 323–341.

Ratkiewicz A., Bankiewicz B. and Truong T. N. (2010) Kinetics of thermoneutral intermolecular hydrogen migration in alkyl radicals. *Phys. Chem. Chem. Phys.* **12**, 10988–10995.

Ratkiewicz A. and Truong T. N. (2012) Kinetics of the C-C bond beta scission reactions in alkyl radical reaction class. *J. Phys. Chem. A* **116**, 6643–6654.

Rosenthal J. S. (2000) *Parallel computing and Monte Carlo algorithms*.,

Savage P. E. (2000) Mechanisms and kinetics models for hydrocarbon pyrolysis. *J. Anal. Appl. Pyrolysis* **54**, 109–126.

Seewald J. S. (2003) Organic-inorganic interactions in petroleum-producing sedimentary basins. *Nature* **426**, 327–333.

Sherwood O. A., Schwietzke S., Arling V. A. and Etiope G. (2017) Global inventory of gas geochemistry data from fossil fuel, microbial and burning sources, version 2017. *Earth Syst. Sci. Data* **9**, 639–656.

Sirjean B., Dames E., Wang H. and Tsang W. (2012) Tunneling in hydrogen-transfer isomerization of n -alkyl radicals. *J. Phys. Chem. A* **116**, 319–332.

Stolper D. A., Sessions A. L., Ferreira A. A., Santos Neto E. V., Schimmelmann A., Shusta S. S., Valentine D. L. and Eiler J. M. (2014) Combined 13C-D and D-D clumping in methane: Methods and preliminary results. *Geochim. Cosmochim. Acta* **126**, 169–191.

Sweeney J. J., Burnham A. K. and Braun R. L. (1987) MODEL OF HYDROCARBON GENERATIAON FROM TYPE I KEROGEN: APPLICATION TO UINTA BASIN, UTAH. *Am. Assoc. Pet. Geol. Bull.* **71**, 967–985.

Tang Y., Huang Y., Ellis G. S., Wang Y., Kralert P. G., Gillaizeau B., Ma Q. and Hwang R. (2005) A kinetic model for thermally induced hydrogen and carbon isotope fractionation of individual n-alkanes in crude oil. *Geochim. Cosmochim. Acta* **69**, 4505–4520.

Tang Y., Perry J. K., Jenden P. D. and Schoell M. (2000) Mathematical modeling of stable carbon isotope ratios in natural gases. *Geochim. Cosmochim. Acta* **64**, 2673–2687.

Thiagarajan N., Xie H., Ponton C., Kitchen N., Peterson B., Lawson M., Formolo M., Xiao Y. and Eiler J. (2020) Isotopic evidence for quasi-equilibrium chemistry in thermally mature natural gases. *Proc. Natl. Acad. Sci.* **117**, 3989–3995.

Ungerer P. (1990) State of the art of research in kinetic modelling of oil formation and expulsion. *Org. Geochem.* **16**, 1–25.

Ungerer P., Collell J. and Yiannourakou M. (2015) Molecular modeling of the volumetric and thermodynamic properties of kerogen: Influence of organic type and maturity. *Energy and Fuels* **29**, 91–105.

Vandenbroucke M. and Largeau C. (2007) Kerogen origin, evolution and structure. *Org. Geochem.* **38**, 719–833.

Voter A. F. (2007) Introduction To the Kinetic Monte Carlo Method. In *Radiation Effects in Solids* Springer Netherlands, Dordrecht. pp. 1–23.

Wang Y., Sessions A. L., Nielsen R. J. and Goddard W. A. (2009) Equilibrium 2H/1H fractionations in organic molecules. II: Linear alkanes, alkenes, ketones, carboxylic acids, esters, alcohols and ethers. *Geochim. Cosmochim. Acta* **73**, 7076–7086.

Waples D. W. and Tornheim L. (1978) Mathematical models for petroleum-forming processes: n-paraffins and isoprenoid hydrocarbons. *Geochim. Cosmochim. Acta* **42**, 457–465.

Wei L., Gao Z., Mastalerz M., Schimmelmann A., Gao L., Wang X., Liu X., Wang Y. and Qiu Z. (2019) Influence of water hydrogen on the hydrogen stable isotope ratio of methane at low versus high temperatures of methanogenesis. *Org. Geochem.* **128**, 137–147.

Xiao Y. (2001) Modeling the kinetics and mechanisms of petroleum and natural gas generation: A first principles approach. *Rev. Mineral. Geochemistry* **42**, 382–436.

Xie H., Ponton C., Formolo M. J., Lawson M., Ellis G. S., Lewan M. D., Ferreira A. A., Morais E. T., Spigolon A. L. D., Sessions A. L. and Eiler J. M. (2020) Position-specific

distribution of hydrogen isotopes in natural propane: effects of thermal cracking, equilibration and biodegradation. *Geochim. Cosmochim. Acta* **290**, 235–256.

You X., Egolfopoulos F. N. and Wang H. (2009) Detailed and simplified kinetic models of n-dodecane oxidation: The role of fuel cracking in aliphatic hydrocarbon combustion. *Proc. Combust. Inst.* **32 I**, 403–410.

Young E. D., Rumble D., Freedman P. and Mills M. (2016) A large-radius high-mass-resolution multiple-collector isotope ratio mass spectrometer for analysis of rare isotopologues of O2, N2, CH4 and other gases. *Int. J. Mass Spectrom.* **401**, 1–10.

Yuan T., Zhang L., Zhou Z., Xie M., Ye L. and Qi F. (2011) Pyrolysis of n-Heptane: Experimental and Theoretical Study. *J. Phys. Chem. A* **115**, 1593–1601.

Zhang Z., Kang Q., Wei S., Yun T., Yan G. and Yan K. (2017) Large Scale Molecular Model Construction of Xishan Bituminous Coal. *Energy and Fuels* **31**, 1310–1317.

Zhao H., Liu C., Larson T. E., Mcgovern G. P. and Horita J. (2020) Bulk and position-specific isotope geochemistry of natural gases from the Late Cretaceous Eagle Ford Shale, south Texas. *Mar. Pet. Geol.*

Zou Y. R., Cai Y., Zhang C., Zhang X. and Peng P. (2007) Variations of natural gas carbon isotope-type curves and their interpretation - A case study. *Org. Geochem.* **38**, 1398–1415.